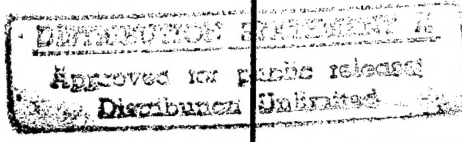


REPORT DOCUMENTATION PAGE

Form Approved
OMB No. 0704-0188

Public reporting burden for this collection of information is estimated to average 1 hour per response, including the time for reviewing instructions, searching existing data sources, gathering and maintaining the data needed, and completing and reviewing the collection of information. Send comments regarding this burden estimate or any other aspect of this collection of information, including suggestions of reducing this burden, to Washington Headquarters Services, Directorate for Information Operations and reports, 1215 Jefferson Davis Highway, Suite 1204, Arlington, VA 22202-4302, and to the Office of Management and Budget, Paperwork Reduction Project (0704-0188), Washington, DC 20503.

1. AGENCY USE ONLY (Leave blank)	2. REPORT DATE	3. REPORT TYPE AND DATES COVERED
	April 1995	Final
4. TITLE AND SUBTITLE The Source and Evolution of Turbulence in Trailing Vortex Pairs		5. FUNDING NUMBERS N00014-90-J-1909 N00014-91-J-1773
6. AUTHOR(S) C. M. Vogel and W. J. Devenport		
7. PERFORMING ORGANIZATION NAME(S) AND ADDRESS(ES) Virginia Polytechnic Institute and State University Blacksburg, VA 24061-0203		8. PERFORMING ORGANIZATION REPORT NUMBER VPI-AOE-217
9. SPONSORING / MONITORING AGENCY NAME(S) AND ADDRESS(ES) Defense Advanced Research Projects Agency Submarine Technology Division 1400 Wilson Blvd. Arlington, VA 22209		10. SPONSORING / MONITORING AGENCY REPORT NUMBER
11. SUPPLEMENTARY NOTES		
12a. DISTRIBUTION / AVAILABILITY STATEMENT Unclassified Unlimited		12b. DISTRIBUTION CODE 
13. ABSTRACT (Maximum 200 words) The reanalysis of data obtained from the experimental studies of trailing vortex pairs has been conducted to obtain a more complete understanding of the turbulence structure of these flows. The results of these studies are compared with those of an isolated vortex to distinguish between the structure and effects of the separate vortices from that of vortex interaction. The analysis of a counter-rotating vortex pair reveal that, initially, the vortices develop in a manner similar to an isolated vortex. The cores appear laminar and the turbulence structure outside them is dominated by the spiral wakes. After some distance, flow inside and outside the cores becomes much more turbulent. The results indicate that this change may be a result of wave instabilities developed in the cores. The analysis of the co-rotating pair reveals that turbulence is present in the cores as they spiral about each other and move downstream. After a certain distance, the cores merge into a single core, which contains more turbulence and is over twice the size of the pair that created it. As merger comes to (over)		
4. SUBJECT TERMS Trailing Vortices Vortex Interaction Turbulence		15. NUMBER OF PAGES 234
17. SECURITY CLASSIFICATION OF REPORT Unclassified		16. PRICE CODE
18. SECURITY CLASSIFICATION OF THIS PAGE Unclassified		19. SECURITY CLASSIFICATION OF ABSTRACT Unclassified
20. LIMITATION OF ABSTRACT		

THE SOURCE AND EVOLUTION OF TURBULENCE IN TRAILING
VORTEX PAIRS

by

C.M. Vogel and W.J. Devenport

Department of Aerospace and Ocean Engineering
Virginia Polytechnic Institute and State University

April 1995

THE SOURCE AND EVOLUTION OF TURBULENCE IN TRAILING VORTEX PAIRS

by

Christine M. Vogel

Committee Chairman: Dr. William J. Devenport

Department of Aerospace and Ocean Engineering

(Abstract)

The reanalysis of data obtained from the experimental studies of two different trailing vortex pairs has been conducted to obtain a more complete understanding of the turbulence structure of these flows. Statistical and spectral results, as well as filtered results and estimates of the effects of vortex wandering on the characteristics of the flows are presented. The results of the vortex pair are compared with the data from the experimental study of an isolated vortex conducted under similar testing conditions and model configuration to distinguish between the structure and effects of the separate vortices from those of vortex interaction.

The analysis of a counter-rotating vortex pair reveals that initially the vortices develop in a manner similar to an isolated vortex. The cores appear laminar and the turbulence structure outside them is dominated by the spiral wakes. After some distance, flow inside and outside the cores becomes much more turbulent. The cores begin to grow and decay. The results indicate that this change may be a result of wave instabilities developed in the cores.

The analysis of the co-rotating vortex pair reveal that turbulence is present in the cores as they spiral about each other and move downstream. After a certain distance, the cores merge into a single core, which contains more turbulence and is over twice the size of the pair that created it. As merger comes to completion, a symmetric core is formed which has much less turbulence. Merger appears to cause an increased rate of vortex decay.

Acknowledgment:

The author would like to thank Jeffery Zsoldos for making the measurements used in the following analysis and Michael Rife and Gautam Sharma for their assistance in these measurements. Special thanks to Dr. William Devenport whose guidance and encouragement throughout this research are greatly appreciated. The financial support of ARPA, administered by Mr. Gary W. Jones and the Office of Naval Research, through ONR contracts N00014-90-J-1909 and N00014-91-J-1773 is also gratefully acknowledged.

Table of Contents

List of Tables	vi
List of Figures	vii
List of Nomenclature	xix
1. Introduction	1
1.1. Studies of Counter-rotating Vortex Pairs	2
1.2. Studies of Co-rotating Vortex Pairs	8
1.3. Aims	12
2. Description of Experiments and Data Reduction	14
2.1. Trailing Vortex Pair Experiments of Zsoldos(1992).....	14
2.1.1 Configuration.....	14
2.1.2 Flow Visualizations.....	16
2.1.3 Single Hot-wire Measurements.....	16
2.1.4 Quad Hot-wire Measurements.....	17
2.1.5 Probe Interference.....	18
2.2. Data Reduction and Analysis Methods Used in the Present Study.....	19
2.2.1 Wandering Analysis.....	19
2.2.2 Quad Hot-wire Reduction Equations.....	21
2.3. Isolated Vortex Experiment of Devenport et al(1995).....	24
3. Data Analysis Results/Discussion	25
3.1. A Parallel Study of an Isolated Trailing Vortex	25
3.2. Counter-rotating Vortex Pair	31
3.2.1. Measurements at $x/c=10$	31
3.2.2. Measurements at $x/c=30$	41
3.3. Co-rotating Vortex Pair	49

3.3.1. Measurements at $x/c=10$	49
3.3.2. Measurements at $x/c=15$	57
3.3.3. Measurements at $x/c=22$	63
3.3.4. Measurements at $x/c=30$	69
4. Conclusions	75
4.1. Isolated Trailing Vortex.....	75
4.2. Counter-rotating Vortex Pair	76
4.3. Co-rotating Vortex Pair	77
5. References	79
Tables	84
Figures	90

List of Tables

Table 1. Vortex pair wing trailing edge characteristics.....	84
Table 2. Quad hot-wire uncertainties in measurements	84
Table 3. Flow conditions, vortex core parameters and characteristics of wandering motions for quad hot-wire measurement cases of vortex pair experiments.....	85
Table 4. Vortex pair far wake characteristics.....	86
Table 5. Flow conditions, vortex core parameters and characteristics of wandering motions for quad hot-wire measurement cases of isolated vortex experiments.....	87
Table 6. Comparison between conclusions of isolated vortex study and the vortex pair studies.....	88

List of Figures

Figure 1. View of aircraft generating vortex pairs.....	90
Figure 2. (a) View of aircraft generating a counter-rotating vortex pair.....	91
(b) View of aircraft generating a co-rotating vortex pair.....	92
Figure 3. Schematic of the test section showing the coordinate system for (a) vortex pair experiments of Zsoldos(1992).....	93
(b) isolated vortex experiment of Devenport et al(1995).....	94
Figure 4. Schematic of the quad hot wire probe showing dimensions and wire configuration in the measurement plane.....	95
Figure 5. Photo-mosaic of vortex pairs at $\Delta y=c/4c$, $\alpha=5^\circ$, $Re_c=130,000$ from Zsoldos(1992) (a) counter-rotating vortex pair.....	96
(b) co-rotating vortex pair.....	97
Figure 6(a). Flow visualization of dummy hot-wire probe in the lower core of the counter-rotating pair at $\Delta y=c/4c$, $\alpha_e=5^\circ$, $Re_c=400,000$ at streamwise location $x/c=22$	98
(b). Flow visualization of quad hot-wire probe in isolated vortex core at $\alpha=5^\circ$, $Re_c=130,000$ from Engel(1995).....	98
Figure 7. Contours of turbulence axial normal stress of isolated vortex at (a) $x/c=10$, (b) $x/c=15$, (c) $x/c=20$, and (d) $x/c=30$ from Devenport et al (1995).....	99
Figure 8. Contours of streamwise vorticity normalized on U_{ref} and c of the isolated vortex at $x/c=10$ from Devenport et al(1995).....	103
Figure 9. Color contours of axial normal stress at $x/c=10$ and 30 of isolated vortex from Devenport et al(1995).....	104
Figure 10. Rates of strain and turbulence stress on the spiral wake centerline at $x/c=10$ of isolated vortex. Strain rates normalized on the maximum axial velocity gradient in the two-dimensional portion of the wake from Devenport et al(1995).....	105

Figure 11. V+W velocity autospectra at selected locations along the spiral wake centerline at $x/c=10$ of isolated vortex from Devenport et al(1995).....	106
Figure 12. Vertical mean tangential and axial velocity profiles through the core of the isolated vortex (a) uncorrected and (b) corrected for the effects of wandering from Devenport et al(1995).....	107
Figure 13. Variation in wandering amplitude, core radius, and peak tangential velocity with streamwise distance for isolated vortex from Devenport et al(1995).....	108
Figure 14. Axial velocity autospectra along a z-wise profile from the spiral wake to the core center at $x/c=10$ of isolated vortex from Devenport et al(1995).....	109
Figure 15. Variation of axial velocity autospectra at the core center normalized on U_{ref} and c with streamwise distance of isolated vortex from Devenport et al(1995).....	110
Figure 16. Velocity autospectra at the core center for all streamwise locations normalized on parameters of the two-dimensional wake of isolated vortex, (a)U spectra, and (b) V+W spectra from Devenport et al(1995).....	111
Figure 17. Contours of axial normal stress \bar{u}^2/U_{ref}^2 filtered at $fc/U_{ref}=3$ at $x/c=10$ of isolated vortex from Devenport et al(1995).....	112
Figure 18. Contours of axial normal stress \bar{u}^2/U_{ref}^2 filtered at $fc/U_{ref}=40$ at $x/c=10$ of isolated vortex from Devenport et al(1995).....	113
Figure 19. Contours of axial normal stress of flow field \bar{u}^2/U_{ref}^2 at $x/c=10$ of counter-rotating vortex pair.....	114
Figure 20. Mean cross-flow velocity vectors at $x/c=10$ of counter-rotating vortex pair.....	115
Figure 21. Contours of mean axial velocity U/U_{ref} at $x/c=10$ of counter-rotating vortex pair.....	116
Figure 22. Contours of mean streamwise vorticity normalized on U_{ref} and c at $x/c=10$ of counter-rotating vortex pair.....	117
Figure 23. Contours of axial normal stress \bar{u}^2/U_{ref}^2 at $x/c=10$ of counter-rotating	

vortex pair.....	118
Figure 24. Contours of cross-flow normal stress sum ($\bar{v}^2 + \bar{w}^2$)/ U_{ref}^2 at $x/c=10$ of counter-rotating vortex pair.....	119
Figure 25. Profiles of axial normal stress \bar{u}^2/U_{ref}^2 at selected locations along the spiral wake centerline at $x/c=10$ of counter-rotating vortex pair.....	120
Figure 26. Profiles of normal stress \bar{v}_s^2/U_{ref}^2 parallel to the wake centerline at selected locations along the spiral wake centerline at $x/c=10$ of counter-rotating vortex pair.....	121
Figure 27. Profiles of normal stress \bar{v}_n^2/U_{ref}^2 normal to the wake centerline at selected locations along the spiral wake centerline at $x/c=10$ of counter-rotating vortex pair.....	122
Figure 28. Velocity autospectra in coordinates aligned with the spiral wake centerline at $x/c=10$ of counter-rotating vortex pair, (a) U spectra, (b) V_s spectra, (c) V_n spectra.....	123
Figure 29. Normal stress profiles along the plane of symmetry between the vortices at $x/c=10$ of counter-rotating vortex pair.....	124
Figure 30. Rates of strain and turbulence stress on the spiral wake centerline at $x/c=10$ of counter-rotating vortex pair. Strain rates normalized on maximum axial velocity gradient in the two-dimensional portion of the wake.....	124
Figure 31. Mean tangential and axial velocity profiles through the right-hand core of counter-rotating pair (a) uncorrected and (b) corrected for the effects of wandering.....	125
Figure 32. Autospectra of U velocity fluctuations at various spanwise locations along a horizontal profile through the right-hand core center at $x/c=10$ of counter-rotating vortex pair.....	126
Figure 33. Autospectra of V velocity fluctuations at various spanwise locations along a horizontal profile through the right-hand core center at $x/c=10$ of counter-rotating vortex pair.....	127
Figure 34. Autospectra of W velocity fluctuations at various spanwise locations along a horizontal profile through the right-hand core center at $x/c=10$	

of counter-rotating vortex pair.....	128
Figure 35. Autospectra at the centerline of the two-dimensional portion of the spiral wake of the counter-rotating pair at (a) $x/c=10$ and (b) $x/c=30$	129
Figure 36. Autospectra at locations moving from the edge of the turbulent region into the free-stream along a vertical profile through the right-hand core center at $x/c=10$ of counter-rotating vortex pair, (a)U spectra, (b)V spectra, (c) W spectra.....	130
Figure 37. Autospectra of U velocity fluctuations at core center normalized on two-dimensional wake parameters for isolated vortex cases and counter-rotating pair at $x/c=10$.Solid line is right-hand core and dashed line is left-hand core.....	131
Figure 38. Autospectra of V+W velocity fluctuations at core center normalized on two-dimensional wake parameters for isolated vortex cases and counter-rotating pair at $x/c=10$.Solid line is right-hand core and dashed line is left-hand core.....	132
Figure 39. Contours of axial normal stress \bar{u}^2/U_{ref}^2 filtered at $fc/U_{ref}=3$ at $x/c=10$ of counter-rotating vortex pair.....	133
Figure 40. Contours of axial normal stress \bar{u}^2/U_{ref}^2 filtered at $fc/U_{ref}=40$ at $x/c=10$ of counter-rotating vortex pair.....	134
Figure 41. Contours of axial normal stress \bar{u}^2/U_{ref}^2 of flow field at $x/c=30$ of counter-rotating vortex pair.....	135
Figure 42. Mean cross-flow velocity vectors at $x/c=30$ of counter-rotating vortex pair.....	136
Figure 43. Contours of mean axial velocity U/U_{ref} at $x/c=30$ of counter-rotating vortex pair.....	137
Figure 44. Contours of mean streamwise vorticity normalized on U_{ref} and c at $x/c=30$ of counter-rotating vortex pair.....	138
Figure 45. Contours of axial normal stress \bar{u}^2/U_{ref}^2 at $x/c=30$ of counter-rotating vortex pair.....	139
Figure 46. Contours of cross-flow normal stress sum ($\bar{v}^2 + \bar{w}^2$)/ U_{ref}^2 at $x/c=30$ of counter-rotating vortex pair.....	140

Figure 47. Color contours of axial normal stress at $x/c=10$ and 30 of the counter-rotating pair.....	141
Figure 48. Profiles of axial normal stress \bar{u}^2/U_{ref}^2 at selected locations along the curve about right-hand core at $x/c=30$ of counter-rotating vortex pair.....	142
Figure 49. Profiles of normal stress \bar{v}_s^2/U_{ref}^2 parallel to the curve about the right-hand core at selected locations along this line at $x/c=30$ of counter-rotating vortex pair.....	143
Figure 50. Profiles of normal stress \bar{v}_n^2/U_{ref}^2 normal to the curve about the right-hand core at selected locations along this line at $x/c=30$ of counter-rotating vortex pair.....	144
Figure 51. Velocity autospectra in coordinates aligned with the curve about the right-hand core at $x/c=30$ of counter-rotating vortex pair, (a) U spectra, (b) V_s spectra, (c) V_n spectra.....	145
Figure 52. Rates of strain and turbulence stress on the curve about the right-hand core at $x/c=30$ of counter-rotating vortex pair. Strain rates normalized on maximum axial velocity gradient in the two-dimensional portion of the wake.....	146
Figure 53. Normal stress profiles along the plane of symmetry between the vortices at $x/c=30$ of counter-rotating vortex pair.....	146
Figure 54. Autospectra of U velocity fluctuations at various spanwise locations along a horizontal profile through the right-hand core center at $x/c=30$ of counter-rotating vortex pair.....	147
Figure 55. Autospectra of V velocity fluctuations at various spanwise locations along a horizontal profile through the right-hand core center at $x/c=30$ of counter-rotating vortex pair.....	148
Figure 56. Autospectra of W velocity fluctuations at various spanwise locations along a horizontal profile through the right-hand core center at $x/c=30$ of counter-rotating vortex pair.....	149
Figure 57. Autospectra at locations moving from the edge of the turbulent region into the free-stream along a vertical profile through the right-hand core center at $x/c=30$ of counter-rotating vortex pair, (a) U spectra, (b) V spectra, (c) W spectra.....	150

Figure 58. Autospectra of U velocity fluctuations at core center normalized on two-dimensional wake parameters for isolated vortex cases and counter-rotating pair at $x/c=30$. Solid line is right-hand core and dashed line is left-hand core.....	151
Figure 59. Autospectra of V+W velocity fluctuations at core center normalized on two-dimensional wake parameters for isolated vortex cases and counter-rotating pair at $x/c=30$. Solid line is right-hand core and dashed line is left-hand core.....	152
Figure 60. Variation of velocity autospectra at core center with streamwise distance of counter-rotating pair.....	153
Figure 61. Contours of axial normal stress \bar{u}^2/U_{ref}^2 filtered at $fc/U_{ref}=3$ at $x/c=30$ of counter-rotating vortex pair.....	154
Figure 62. Contours of axial normal stress \bar{u}^2/U_{ref}^2 filtered at $fc/U_{ref}=40$ at $x/c=30$ of counter-rotating vortex pair.....	155
Figure 63. Variation in wandering amplitude, core radius, and peak tangential velocity with streamwise distance for counter-rotating pair.....	156
Figure 64. Contours of turbulence axial normal stress \bar{u}^2/U_{ref}^2 at $x/c=10$ of co-rotating vortex pair.....	157
Figure 65. Mean cross-flow velocity vectors at $x/c=10$ of co-rotating vortex pair.....	158
Figure 66. Contours of mean axial velocity U/U_{ref} at $x/c=10$ of co-rotating vortex pair.....	159
Figure 67. Contours of mean streamwise vorticity normalized on U_{ref} and c at $x/c=10$ of co-rotating vortex pair.....	160
Figure 68. Contours of axial normal stress \bar{u}^2/U_{ref}^2 at $x/c=10$ of co-rotating vortex pair.....	161
Figure 69. Contours of cross-flow normal stress sum ($\bar{v}^2 + \bar{w}^2$)/ U_{ref}^2 at $x/c=10$ of co-rotating vortex pair.....	162
Figure 70. Profiles of axial normal stress \bar{u}^2/U_{ref}^2 at selected locations along the curve about upper at $x/c=10$ of co-rotating vortex pair.....	163
Figure 71. Profiles of normal stress \bar{v}_s^2/U_{ref}^2 parallel to the curve about the upper	

core at selected locations along this line at $x/c=10$ of co-rotating vortex pair.....	164
Figure 72. Profiles of normal stress \bar{v}_n^2/U_{ref}^2 normal to the curve about the upper core at selected locations along this line at $x/c=10$ of co-rotating vortex pair.....	165
Figure 73. Velocity autospectra in coordinates aligned with the curve about the upper core at $x/c=10$ of co-rotating vortex pair, (a) U spectra, (b) V_s spectra, (c) V_n spectra.....	166
Figure 74. Rates of strain and turbulence stress on the curve about the upper core at $x/c=10$ of co-rotating vortex pair. Strain rates normalized on maximum axial velocity gradient in the two-dimensional portion of the wake.....	167
Figure 75. Normal stress profiles along the plane of antisymmetry between the vortices at $x/c=10$ of co-rotating vortex pair.....	167
Figure 76. Mean tangential and axial velocity profiles through the upper core of the co-rotating pair at $x/c=10$ and the lower core at $x/c=15$ and through the single cor at $x/c=22$ and 30 (a) uncorrected and (b) corrected for the effects of wandering.....	168
Figure 77. Autospectra of U velocity fluctuations at various spanwise locations along a horizontal profile through the upper core center at $x/c=10$ of co-rotating vortex pair.....	169
Figure 78. Autospectra of V velocity fluctuations at various spanwise locations along a horizontal profile through the upper core center at $x/c=10$ of co-rotating vortex pair.....	170
Figure 79. Autospectra of W velocity fluctuations at various spanwise locations along a horizontal profile through the upper core center at $x/c=10$ of co-rotating vortex pair.....	171
Figure 80. Autospectra at centerline of two-dimensional portion of the wake of co-rotating pair at $x/c=10, 15, 22$, and 30.....	172
Figure 81. Autospectra of U velocity fluctuations at core center normalized on two-dimensional wake parameters for isolated vortex cases and co-rotating pair at $x/c=10$. Solid line is upper core and dashed line is lower core.....	173

Figure 82. Autospectra of V+W velocity fluctuations at core center normalized on two-dimensional wake parameters for isolated vortex cases and co-rotating pair at $x/c=10$. Solid line is upper core and dashed line is lower core.....	174
Figure 83. Contours of axial normal stress \bar{u}^2/U_{ref}^2 filtered at $fc/U_{ref}=3$ at $x/c=10$ of co-rotating vortex pair.....	175
Figure 84. Contours of axial normal stress \bar{u}^2/U_{ref}^2 filtered at $fc/U_{ref}=40$ at $x/c=10$ of co-rotating vortex pair.....	176
Figure 85. Contours of turbulence axial normal stress \bar{u}^2/U_{ref}^2 at $x/c=15$ of co-rotating vortex pair.....	177
Figure 86. Mean cross-flow velocity vectors at $x/c=15$ of co-rotating vortex pair.....	178
Figure 87. Contours of mean axial velocity U/U_{ref} at $x/c=15$ of co-rotating vortex pair.....	179
Figure 88. Contours of mean streamwise vorticity normalized on U_{ref} and c at $x/c=15$ of co-rotating vortex pair.....	180
Figure 89. Contours of axial normal stress \bar{u}^2/U_{ref}^2 at $x/c=15$ of co-rotating vortex pair.....	181
Figure 90. Contours of cross-flow normal stress sum ($\bar{v}^2 + \bar{w}^2$)/ U_{ref}^2 at $x/c=15$ of co-rotating vortex pair.....	182
Figure 91. Profiles of axial normal stress \bar{u}^2/U_{ref}^2 at selected locations along the curve about the upper core at $x/c=15$ of co-rotating vortex pair.....	183
Figure 92. Profiles of normal stress \bar{v}_s^2/U_{ref}^2 parallel to the curve about the upper core at selected locations along this line at $x/c=15$ of co-rotating vortex pair.....	184
Figure 93. Profiles of normal stress \bar{v}_n^2/U_{ref}^2 normal to the curve about the upper core at selected locations along this line at $x/c=15$ of co-rotating vortex pair.....	185
Figure 94. Velocity autospectra in coordinates aligned with the curve about the upper core at $x/c=15$ of co-rotating vortex pair, (a) U spectra, (b) V_s spectra, (c) V_n spectra.....	186

Figure 95. Rates of strain and turbulence stress on curve about the upper core at $x/c=15$ of co-rotating vortex pair. Strain rates normalized on maximum axial velocity gradient in the two-dimensional portion of the wake.....	187
Figure 96. Normal stress profiles along the plane of antisymmetry between the vortices at $x/c=15$ of counter-rotating vortex pair.....	187
Figure 97. Autospectra of U velocity fluctuations at various spanwise locations along a horizontal profile through the lower core center at $x/c=15$ of co-rotating vortex pair.....	188
Figure 98. Autospectra of V velocity fluctuations at various spanwise locations along a horizontal profile through the lower core center at $x/c=15$ of co-rotating vortex pair.....	189
Figure 99. Autospectra of W velocity fluctuations at various spanwise locations along a horizontal profile through the lower core center at $x/c=15$ of co-rotating vortex pair.....	190
Figure 100. Autospectra of U velocity fluctuations at core center normalized on two-dimensional wake parameters for isolated vortex cases and co-rotating pair at $x/c=15$. Solid line is lower core and dashed line is upper core.....	191
Figure 101. Autospectra of V+W velocity fluctuations at core center normalized on two-dimensional wake parameters for isolated vortex cases and co-rotating pair at $x/c=15$. Solid line is lower core and dashed line is upper core.....	192
Figure 102. Contours of axial normal stress \bar{u}^2/U_{ref}^2 filtered at $fc/U_{ref}=3$ at $x/c=15$ of co-rotating vortex pair.....	193
Figure 103. Contours of axial normal stress \bar{u}^2/U_{ref}^2 filtered at $fc/U_{ref}=40$ at $x/c=15$ of co-rotating vortex pair.....	194
Figure 104. Contours of turbulence axial normal stress \bar{u}^2/U_{ref}^2 at $x/c=22$ of co-rotating vortex pair.....	195
Figure 105. Mean cross-flow velocity vectors at $x/c=22$ of co-rotating vortex pair.....	196
Figure 106. Contours of mean axial velocity U/U_{ref} at $x/c=22$ of co-rotating vortex pair.....	197

Figure 107. Contours of mean streamwise vorticity normalized on U_{ref} and c at $x/c=22$ of co-rotating vortex pair.....	198
Figure 108. Contours of axial normal stress \bar{u}^2/U_{ref}^2 at $x/c=22$ of co-rotating vortex pair.....	199
Figure 109. Contours of cross-flow normal stress sum ($\bar{v}^2 + \bar{w}^2$)/ U_{ref}^2 at $x/c=22$ of co-rotating vortex pair.....	200
Figure 110. Profiles of axial normal stress \bar{u}^2/U_{ref}^2 at selected locations along the curve about the core at $x/c=22$ of co-rotating vortex pair.....	201
Figure 111. Profiles of normal stress \bar{v}_s^2/U_{ref}^2 parallel to the curve about the core at selected locations along this line at $x/c=22$ of co-rotating vortex pair.....	202
Figure 112. Profiles of normal stress \bar{v}_n^2/U_{ref}^2 normal to the curve about the core selected locations along this line at $x/c=22$ of co-rotating vortex pair....	203
Figure 113. Velocity autospectra in coordinates aligned with curve about the core at $x/c=22$ of co-rotating vortex pair, (a) U spectra, (b) V_s spectra, (c) V_n spectra.....	204
Figure 114. Rates of strain and turbulence stress on curve about the core at $x/c=22$ of co-rotating vortex pair. Strain rates normalized on maximum axial velocity gradient in the two-dimensional portion of the wake.....	205
Figure 115. Autospectra of U velocity fluctuations at various spanwise locations along a horizontal profile through the core center at $x/c=22$ of co-rotating vortex pair.....	206
Figure 116. Autospectra of V velocity fluctuations at various spanwise locations along a horizontal profile through the core center at $x/c=22$ of co-rotating vortex pair.....	207
Figure 117. Autospectra of W velocity fluctuations at various spanwise locations along a horizontal profile through the core center at $x/c=22$ of co-rotating vortex pair.....	208
Figure 118. Autospectra of U velocity fluctuations at core center normalized on two-	

dimensional wake parameters for isolated vortex cases and co-rotating pair at $x/c=22$	209
Figure 119. Autospectra of $V+W$ velocity fluctuations at core center normalized on two-dimensional wake parameters for isolated vortex cases and co-rotating pair at $x/c=22$	210
Figure 120. Contours of axial normal stress \bar{u}^2/U_{ref}^2 filtered at $fc/U_{ref}=3$ at $x/c=22$ of co-rotating vortex pair.....	211
Figure 121. Contours of axial normal stress \bar{u}^2/U_{ref}^2 filtered at $fc/U_{ref}=40$ at $x/c=10$ of co-rotating vortex pair.....	212
Figure 122. Contours of turbulence axial normal stress \bar{u}^2/U_{ref}^2 at $x/c=30$ of co-rotating vortex pair.....	213
Figure 123. Mean cross-flow velocity vectors at $x/c=30$ of co-rotating vortex pair.....	214
Figure 124. Contours of mean axial velocity U/U_{ref} at $x/c=30$ of co-rotating vortex pair.....	215
Figure 125. Contours of mean streamwise vorticity normalized on U_{ref} and c at $x/c=30$ of co-rotating vortex pair.....	216
Figure 126. Contours of axial normal stress \bar{u}^2/U_{ref}^2 at $x/c=30$ of co-rotating vortex pair.....	217
Figure 127. Contours of cross-flow normal stress sum $(\bar{v}^2 + \bar{w}^2)/U_{ref}^2$ at $x/c=30$ of co-rotating vortex pair.....	218
Figure 128. Profiles of axial normal stress \bar{u}^2/U_{ref}^2 at selected locations along the curve about the core at $x/c=30$ of co-rotating vortex pair.....	219
Figure 129. Profiles of normal stress \bar{v}_s^2/U_{ref}^2 parallel to the curve about the core at selected locations along this line at $x/c=30$ of co-rotating vortex pair.....	220
Figure 130. Profiles of normal stress \bar{v}_n^2/U_{ref}^2 normal to the curve about the core at selected locations along this line at $x/c=30$ of co-rotating vortex pair.....	221

Figure 131. Velocity autospectra in coordinates aligned with curve about the core at $x/c=30$ of co-rotating vortex pair, (a) U spectra, (b) V_s spectra, (c) V_n spectra.....	222
Figure 132. Rates of strain and turbulence stress on the curve about the core at $x/c=30$ of co-rotating vortex pair. Strain rates normalized on maximum axial velocity gradient in the two-dimensional portion of the wake.....	223
Figure 133. Autospectra of U velocity fluctuations at various spanwise locations along a horizontal profile through the core center at $x/c=30$ of co-rotating vortex pair.....	224
Figure 134. Autospectra of V velocity fluctuations at various spanwise locations along a horizontal profile through the core center at $x/c=30$ of co-rotating vortex pair.....	225
Figure 135. Autospectra of W velocity fluctuations at various spanwise locations along a horizontal profile through the core center at $x/c=30$ of co-rotating vortex pair.....	226
Figure 136. Autospectra of U velocity fluctuations at core center normalized on two-dimensional wake parameters for isolated vortex cases and co-rotating pair at $x/c=30$	227
Figure 137. Autospectra of $V+W$ velocity fluctuations at core center normalized on two-dimensional wake parameters for isolated vortex cases and co-rotating pair at $x/c=30$	228
Figure 138. Variation of core center velocity autospectra with streamwise distance of co-rotating pair.....	229
Figure 139. Contours of axial normal stress \bar{u}^2/U_{ref}^2 filtered at $fc/U_{ref}=3$ at $x/c=30$ of co-rotating vortex pair.....	230
Figure 140. Contours of axial normal stress \bar{u}^2/U_{ref}^2 filtered at (a) $fc/U_{ref}=15.12$ at $x/c=30$ and (b) $fc/U_{ref}=18.24$ at $x/c=22$ of co-rotating pair.....	231
Figure 141. Variation in wandering amplitude, core radius, and peak tangential velocity with streamwise distance for co-rotating vortex pair.....	232
Figure 142. Variation of core size with streamwise distance for co-rotating pair at (a) $x/c=10$, (b) $x/c=15$, (c) $x/c=22$, and (d) $x/c=30$	233

List of Nomenclature

a_c	effective core radius
b_c	separation distance between vortex core centers
c	wing chord
d	radial scale of axial profile corrected for wandering
d_c	cutoff distance of vortex filament
d_m	radial scale of axial profile in presence of wandering
d_1	vortex core diameter
e	correlation coefficient between amplitudes of wandering
f	frequency in Hertz
G_{ii}	one sided autospectral density function in the i th direction
h	hot-wire yaw factor
k	hot-wire pitch factor
L_w	local wake width of two-dimensional portion of wake
n	direction normal to wake width
Q	magnitude of mean velocities
Q_e	magnitude of estimated velocities
Re_c	Reynolds number based on free-stream velocity and wing chord
r_1	true core radius corrected for core wandering

r_{1m}	core radius measured in the presence of wandering
s	direction along spiral wake
U, V, W	mean velocity components in the x, y, z directions
U, V_s, V_n	mean velocity components in the x, s, n directions
U_D	axial velocity deficit corrected for core wandering
U_{Dm}	axial velocity deficit in the presence of wandering
U_e, V_e, W_e	hot-wire estimates of mean velocities
U_{eff}	effective hot-wire velocity
U_{ref}	free-stream velocity
$\bar{u}^2, \bar{v}^2, \bar{w}^2$	turbulence normal stresses in x, y, z directions
$\bar{u}^2, \bar{v}_s^2, \bar{v}_n^2$	turbulence normal stresses in x, s, n directions
u_w	maximum axial turbulence intensity in two-dimensional wake
$V_{\theta 1}$	true peak tangential velocity corrected for wandering
$V_{\theta 1m}$	peak tangential velocity in the presence of wandering
x	streamwise direction depicted in Figure 3
y	spanwise direction depicted in Figure 3
z	transverse direction depicted in Figure 3
y_1	rotated spanwise direction depicted in Figures 66 and 87
z_1	rotated transverse direction depicted in Figures 66 and 87

Greek Symbols

α	constant in wandering analysis
α_e	angle of attack counter-rotating pair
α_o	angle of attack co-rotating pair

κ	constant in short-wave instability analysis
δ	boundary layer thickness where $U/U_e=0.99$
δ^*	boundary layer displacement thickness
Δy	separation distance between two wing tips
Γ_1	core circulation
Γ_0	wing root circulation
θ	boundary layer momentum thickness
σ_y	wandering amplitude in y direction
σ_z	wandering amplitude in z direction
σ_{y1}	wandering amplitude in y_1 direction
σ_{z1}	wandering amplitude in z_1 direction
ν	kinematic viscosity
ω	vorticity

1. Introduction

Vortical flows are of great interest in the aerodynamic world. In this area, there is a special interest in the interaction of vortices generated by lifting surfaces for many practical reasons. The vortical wakes produced by large military and commercial aircraft are extremely hazardous to smaller aircraft flying in the vicinity. This requires aircraft to be spaced a larger distance apart for take-off and landing, greatly reducing the efficiency of most airports. Vortices produced by the bow plane on a submarine interact with the rear of the vessel resulting in large acoustic signals. This increases the detection of the vessel and reduces its overall capability. In addition, helicopter blades produce vortices which interact with each other resulting in noise and vibration problems. Thus, there is a desire to simulate the interaction of vortices through the use of computers to analyze and understand their effects. This cannot be accomplished without an understanding of the turbulence structure of these vortical flows. Providing this knowledge is the motivation for this study.

In general, a vortex is generated from a vortex sheet shed from a finite lifting surface as a consequence of the nonuniform spanwise lift distribution on that surface. The sheet rolls up into a discrete vortex at the tip. The vortex produced by the wing tip is characterized by two distinct regions of flow. In the inner region, called the core, the mean tangential velocity varies approximately proportionally with the radius from zero at the center to a maximum at the edge of the core. The circulation varies approximately proportionally with the radius squared. In the outer region, the mean tangential velocity varies approximately inversely with the radius and asymptotically approaches a value of zero. The circulation is more constant with radius in the outer region.

In reality, an aircraft generates vortical wakes from its wing and flap tips which form pairs and groups of vortices, Figure 1. The evolution of the flow field as a couple of vortex pairs move downstream is depicted in Figure 2. Two different types of vortex pairs can be created, a counter-rotating pair consisting of two vortices rotating in opposite directions, or a co-rotating pair of vortices with the same rotational direction. Previous investigations have revealed that three regions of flow can be characterized for the interaction of counter-rotating vortices. The first region is roll-up, as described above, which takes place at the wing and flap tips. As the vortices move away from the generating surface, they begin to interact which leads to the development of instabilities in the core regions. However, their flow field structure and strength remain relatively the same. This is called the plateau region. Much further downstream, the vortices begin to decay and die out. The latter two regions constitute the two stage decay that has been observed in vortical flow studies. The interaction of co-rotating vortices is characterized by three regions of flow. Again there is initial roll-up followed by a region where the vortices spiral about each other in their mutual rotational direction as they move downstream. After some distance, the vortices merge creating a single more diffuse vortex core.

1.1. Studies of Counter-rotating Vortex Pairs

There has been little research into the turbulence structure of counter-rotating trailing vortex pairs, although much theoretical and experimental work has been conducted in other areas. The most in-depth theoretical studies have centered around the development of instabilities in the vortex cores. Crow(1970) showed that a pair of infinite line vortices of opposite sign with finite cores are unstable to sinusoidal disturbances of specific wavelength along planes that lie at 45° to that joining the vortices. Crow instability is a primary mechanism causing the dissipation and breakdown of a counter-rotating vortex pair. As the amplitude of Crow instability

grows, it starts to become non-linear. Ultimately, at low background turbulence levels, the vortex cores link together and a series of ring vortices is formed. At higher turbulence levels, vortex bursting may diffuse the cores before linking can occur.

Crow instability is a long wave core instability, Widnall(1975) has observed the effects of short wave core instability. More specifically, she studied the effects of short wave instability on trailing vortices and vortex rings. Unlike Crow instability, with Widnall instability the presence of another vortex, i.e. vortex interaction, plays a dominant role rather than the perturbation of a single vortex core. She found that short waves occur in a vortex core for a value of the ratio of core size to wavelength for which long-wave self-induction theory predicts an angular velocity about the core axis of zero. She developed a stability diagram for a counter-rotating vortex pair indicating the most unstable long wavelength and the most unstable short wavelength for a given ratio of core size to core separation distance. Widnall et al(1971) found that the presence of strong axial velocity in the vortex core has a significant effect on its wave motion. Axial flow slows down the vortex filament rotation requiring a balancing Coriolis force which induces traveling waves upon the filament to provide the necessary lift to turn the internal core axial flow. The amplification rate for short waves is greater than for long waves as long as the core size is less than half of the separation distance. Above this value, their amplification rates are equal and decrease as core size approaches separation distance. The flow field of a vortex ring near the vortex core is a quasi-stagnation-point flow. Thus, the study of vortex ring stability is related to that of a vortex pair if the self-induced rotation can be overcome or is zero because then the filament will diverge, i.e. become unstable, in the stagnation point flow. Researchers have observed that under some conditions even with instabilities, the vortex rings continue to propagate. Widnall(1975) postulates that the instabilities act to produce turbulence in the core, causing the core to grow. This also may be applicable to the development of vortex pair flow structure.

Thomas and Auerbach(1994) observed long and short wave instabilities on a counter-rotating vortex pair generated from a flapping flat plate. They found that the characteristic wavelength for both short and long wave instabilities remains constant in time. However, while the wavelength for the short wave instability is independent of vortex length, the wavelength for the long wave instability grows with vortex length. They developed an analysis to obtain a prediction of the most unstable wavelengths and found that for long waves this value is 8.6 times the separation distance between the vortex cores, b_c , and for short waves this value is 0.25 b_c . Thomas and Auerbach(1994) found that their results agreed well with Crow(1970) for long wave instability. However, they did not agree well with Widnall et al(1974) for short wave instability. This may be a consequence because the vortices were not generated at the same time. Thus, one vortex was further in its development when vortex interaction occurred. Another reason for this difference could be that the estimate of the ratio of core separation distance to core diameter was cited from previous studies and not measured directly from the vortex pairs investigated in their study.

Some of the earliest experimental studies of counter-rotating vortex pairs were full scale flight tests. Kerr and Dee(1959) assessed the severity of rolling moments imposed on a follower aircraft from the vortical wake of the generating aircraft. They found that the trailing vortices undergo a two stage vortex decay and that more severe atmospheric turbulence will cause the vortices to decay more rapidly becoming less of a hazard. Treddenick(1968) observed an apparent constant eddy viscosity decay of the vortices generated behind a Convair 880 aircraft. McCormick et al(1968) obtained farfield measurements of tangential velocity and core radius and observed that the maximum tangential velocity decreases and the core size increases with downstream distance indicating vortex decay. The circulation of the core was found to be constant with downstream distance while its distribution was found to be logarithmic with radius. Scorer and Davenport(1970) made observations of the contrails from an aircraft and found that vorticity is generated outside the vortex pair flow field which causes the flow

pattern of the vortex pair to be altered to produce detrainment of external fluid and stable vortices. Further downstream, the upper stagnation point in the motion relative to the vortices moves upward so that some mixed fluid is entrained into the vortex circulation and the vortices go unstable. Thus, Crow instability and vortex bursting occur in the vortex cores.

In 1971, the FAA sponsored flight tests to investigate vortex wake turbulence. The test included follower aircraft flights through the marked wakes of larger generating aircraft, in-flight probes on the follower, and tower hot-wire measurements. They observed a trailing vortex system with two counter-rotating cylindrical air masses which start to descend after roll-up and then level off with the onset of decay. The breakdown of the vortices was affected by atmospheric turbulence and the start of decay was identified by the sinusoidal oscillation of one of the vortices. Garodz(1971) performed studies similar to the FAA and observed that the wakes of aircraft are initially laminar. However, as they move downstream Crow instability develops in the cores and they break up into vortex rings accompanied by considerable turbulence. Tombach(1973) made observations of the atmospheric effects on vortex wakes and showed that vortical wakes break down due to instabilities and not dissipation in the cores. He concluded that core bursting is independent of Crow instability and that it is observed at all levels of atmospheric turbulence. Chevalier(1973) performed flight tests to observe the dissipation of trailing vortices. He found that three types of vortex breakdown occur which include vortex core bursting resulting in turbulence dispersion, non-turbulent vortex core stretching until dissipation and turbulent dissipation. Crow instability and vortex bursting both have the same wavelength, however, bursting will occur in stronger background turbulence.

Other experimental studies on counter-rotating vortices have been conducted in the laboratory. Lezius(1974) conducted a study in a towing tank, taking measurements downstream of a rectangular foil using a hydrogen bubble technique. He observed that decay is signaled by an increase in core size and a decrease in maximum tangential

velocity and that a flow field decays everywhere simultaneously with higher rates of decay for higher levels of turbulence. Tombach et al(1973) made observations of the effects of atmospheric turbulence on vortex wakes and concluded that core bursting will occur in one vortex without necessarily affecting the other vortex while Crow instability occurs in both vortices and causes vortex linking. The lifetime of the wake is decreased significantly in the presence of free-stream turbulence and the mechanism of decay does not change the lifetime. Ciffone et al(1975) used a scanning LDA in a towing tank to obtain velocity measurements through the trailing vortices of a swept wing. Their results show two stages of vortex decay. There is a region that extends from roll-up to about 100 spanlengths downstream in which the maximum tangential velocity remains constant. This is called the plateau region. In the decay region, peak tangential velocity, $V_{\theta\max}$, decreases at a rate proportional to an inverse 1/2 power. They also found that tailoring the wingspan loading will reduce $V_{\theta\max}$ by a factor of two, broadening the vortex core. Eliason et al(1975) made wind tunnel observations of Crow instability of a rectangular wing wake using a helium bubble technique that agree well with Crow(1970). Barker and Crow(1977) conducted a flow visualization study of low Reynolds number counter-rotating vortex pairs in ground effect. The vortices were generated by the unsteady motion of a flat plate and transition was observed to occur around the core and propagate into the core which subsequently relaminarizes into a small but growing subcore. Sarpkaya(1983) conducted towing tank experiments of trailing vortices in density stratified fluid and observed Crow instability with and without linking. Bursting occurred when the axial velocity in a vortex became equal to the maximum tangential velocity at the core edge. Sarpkaya et al(1987) conducted further testing in the towing tank for flow behind rectangular models with varying free-stream turbulence. They found that Crow instability with linking occurs in weak free-stream turbulence and vortex core bursting occurs in strong free-stream turbulence.

Sarpkaya(1992) performed flow visualizations in a water tunnel on a hydrofoil to study the interactions of vortices with a free surface. He observed that numerous

tentacle like vortex sheets of finite length, resulting from helical instabilities, stretch out or are thrown away from the outer edges of the vortex core. The vortex sheets peel off randomly and the vortex sheds vorticity along its length. Exchange of momentum between the core and the outer region leads to oscillation of the vortex core. Studies with a free surface are relevant to trailing vortex pairs because the surface will create a straining field near the vortex similar to the presence of another vortex. Liu et al(1992) conducted towing tank experiments of ground effect on vortex pair drift and separation and found that the vortices will separate and rebound. Liu(1992) also conducted tests on the effects of free-stream turbulence on the decay of trailing vortices. He found that vortex linking occurs for large scale weak free-stream turbulence and bursting occurs when small scale free-stream turbulence is present and the rate of decay increases with free-stream dissipation rate. Sarpkaya et al(1994) investigated the coherent structures in the interaction of a vortex and a free surface. Through flow visualizations and LDA measurements, they found that the turbulent kinetic energy of the vertical velocity fluctuations is redistributed among the lateral and streamwise motions of the vortex rendering the turbulence anisotropic.

Numerical studies have been conducted to augment the experimental studies of counter-rotating vortex pair interaction. Costen(1972) performed a numerical study on the drift of buoyant wing-tip vortices. He found that buoyancy accelerates vortex breakup and nonuniform buoyancy causes vortices to approach unevenly which triggers Crow instability. Hackett and Evans(1977) performed numerical studies of three dimensional breakdown of trailing vortices in which they found that there is a lower limit to the wavelength at which Crow instability can occur and below this limit the self-induction causes the plane of disturbance waves to rotate counter to the vortex direction. Disturbance waves in a horizontal plane are several times more stable than Crow instability waves. Hecht et al(1981) used a second order turbulence model to observe the effects of density stratification on trailing vortices. They concluded that the vortex pair descent in the fluid is halted by a diffuse region of countersign vorticity

primarily outside the vortex cores. The characteristics of the vortex pair do not change significantly during descent. Thus, smaller core size and large turbulence macroscale cause a shorter descent and more rapid dissipation. Bliss(1982) studied the effects of forcing on Crow instability in the vortex cores and found that forcing causes the rate of interaction to increase. Greene(1986) conducted a numerical study with point vortices and he found that if a buoyant vortex begins to rise, then both viscous and asymmetry effects act together to reduce the concentration of vorticity and rapidly enlarge the core. Liu et al(1987) and Robins and Delisi(1993) performed numerical simulations of a vortex pair in ground effect. They found that the vortices will separate and rebound when they interact with the ground without cross wind. However, in the presence of cross wind the vortices separate and do not rebound.

Previous investigations, both experimental and numerical, have looked at specific parameters to obtain some characteristics of the flow field structure of the vortices of a counter-rotating pair. They have mainly concentrated on the decay of the vortex pair without uncovering the physical mechanisms that cause this decay. Researchers have also had a difficult time obtaining detailed measurements over the entire cross-plane of the flow field, especially in the core region experimentally as a result of such problems as seeding the flow in LDV and probe interference when using hot-wires. Thus, the turbulence structure of the cross-plane of a counter-rotating pair has not been revealed in detail. A physical understanding of this turbulence structure is also lacking. Previous studies have not clearly shown the characteristics of the two stage decay of a counter-rotating pair that some have discovered and distinguished the effects and structure due to vortex interaction separate from that of an isolated vortex.

1.2. Studies on Co-rotating Vortex Pairs

The following review shows that little research has been conducted into the turbulence structure of co-rotating vortex pairs. Perhaps the most studied of such flows

is generated by the split-wing configuration, Figure 3(a). Here, a single stable vortex is generated from the merger of two wing tip vortices shed from two wings placed tip to tip at equal and opposite angles of attack. The split-wing vortex is different from an isolated vortex generated from a half wing in that it lacks the same initial turbulence or mean flow structure. Hoffman and Joubert(1963) used a split-wing to analyze the circulation distribution of the single merged vortex. They found a region where the circulation is proportional to the logarithmic radius for various conditions. They also developed a circulation defect law in the inner region of the vortex analogous to a turbulent boundary layer. Phillips and Graham(1984) used a split-wing to generate a single vortex. They obtained mean velocities and Reynolds stresses for all three directions. Their vortex appeared to be axisymmetric with solid body rotation in the core region. Bandyopadhyay et al(1990) made turbulence measurements using a split-wing in various amounts of free-stream turbulence. Through smoke flow visualization and hot-wires, they observed that momentum transfer occurs between the core and the outer region. These studies emphasize the structure of the flow after core merger.

Other experimental research has been conducted which gives results before, during, and after core merger. Corsiglia et al(1976) and Bilanin et al(1976) performed flow visualizations in the wind tunnel to determine the effect of span loading on aircraft wakes. Investigations into the change in wing loading through such means as the deflection of flaps are pertinent because wing loading has a direct effect on the strength, number, and location of co-rotating vortices that are created behind the aircraft. In conjunction with these studies, rolling moment data was obtained for the follower aircraft to determine the least hazardous vortical wake formation from the generating aircraft. Corsiglia et al(1976) found that certain span loading configurations created three co-rotating vortices behind each wing which effectively dispersed the vorticity of the wake and merged to form one large diffuse vortex behind each wing. They also observed a reduction in rolling moment of the follower aircraft as a result of merger. Ciffone(1977) performed similar tests in a towing tank and came to the same conclusion

that alleviation of the wake vorticity is obtained by causing wake vortices to interact and merge. Brandt et al(1977) performed hot-wire and rolling moment measurements. They presented correlation of merger location with their development of circulation and momentum defect diameter scales, as 'universal' normalizing reference diameters in order to compare merging characteristics of various vortex pair circulation profiles. They found through flow visualization that a decrease in initial vortex separation distance causes a decrease in length for merger. Their circulation and tangential velocity profiles show a broader core and lower peak tangential velocity values after merger. Corsiglia et al(1978) used a laser Doppler velocimeter(LDV) to measure velocity of the flow fields generated from a split wing configuration. They presented contours of stream function, vorticity, and cross-flow velocity before, during, and after merger. Before core merger, they observed a muticell pattern of streamwise vorticity for each vortex which they perceived as incomplete roll-up of the vorticity from each wing. Through a comparison of circulation and vorticity between an isolated vortex and a co-rotating vortex pair, they found a decrease in vorticity for the pair indicating decay downstream while the isolated vortex remained the same. Iversen et al(1979) obtained velocity measurements from hot-wire and LDV systems. They observed that the turbulent energy within the merged vortex was about four times as great as that of each vortex before merger. Thus, merger is responsible for turbulent energy production and the outward diffusion of vorticity. Smits and Kumer(1985) examined a split-wing vortex at various downstream locations. However, unlike previous split-wing studies, they observed the flow before merger and found that the two vortices rotated about each other and eventually merged to produce a dominant single vortex. Their circulation profiles varied logarithmically with radius at all streamwise locations similar to Hoffman and Joubert(1963). They developed a first order turbulence model to obtain a relationship between mean flow gradients and shear stresses and conclude that it may successfully predict the merger process if a variable eddy viscosity is used.

Numerical studies have been conducted to gain some insight into the behavior of co-rotating vortex pairs. Bilanin et al(1977) performed inviscid computations to show merging sensitivity to small changes in spanwise load distribution, and turbulent flow calculations showing co-rotating vortex merger of equal strength vortices. They found that the vortices produce turbulent convection and diffusion of vorticity during merger and that the influence of the vortices upon each other destroys their axial symmetry. Thus, turbulence may be produced in the cores. Rossow(1977) performed two dimensional inviscid calculations of vortex core merger with a variation of vortex strengths and numbers . He concluded that merger does not occur for large vortex separations. He also established merger criteria based upon core separation, relative strength, and vorticity distribution. Steger and Kutler(1977) performed similar viscous computations for co-rotating vortex pairing in lifting surface wakes. Their results agree qualitatively with experiment and their codes allow the use of initial conditions obtained experimentally. Overman and Zabusky(1982) and Melander et al(1988) performed numerical simulations to determine the causes and conditions for merger of symmetric co-rotating vortex structures and found that merger can result only for certain initial conditions. Overman and Zabusky(1982) developed criteria that predict which initial conditions will lead to vortex core merger. Mitchell et al(1992) performed a numerical simulation of sound coming from a co-rotating vortex pair merger in both the near field and far flow field regions. They used two incompressible, inviscid point vortices which rotate about each other and merge and showed that sound is propagated outward from the cores as they merge and this sound is diminished as merger comes to completion.

Many of the previous studies have concentrated on the characteristics of the single vortex core after merger and the criteria that will lead to core merger. They have not investigated in detail the flow structure and motion of the cores before merger and uncovered the physical mechanisms that lead to merger. Again, detailed measurements of the entire cross-plane of a co-rotating vortex pair have been difficult to obtain. Thus, the details of the turbulence structure of the development of a co-rotating pair before

and throughout core merger are lacking. A more complete physical understanding of this turbulence structure is needed to simulate this flow. Previous studies have not made a clear distinction between the effects and structure associated with a co-rotating vortex pair and an isolated vortex to obtain the effects of vortex pair interaction.

1.3. AIMS

A review of previous studies of counter-rotating and co-rotating vortex pairs has uncovered areas that have not been researched before. A better understanding of the turbulence structure of these two flows as they develop with streamwise distance is lacking, as well as a clear distinction between the structure and effects associated with the interaction of vortices separate from those of an isolated vortex. Thus, in 1992, Zsoldos conducted an experimental study to obtain detailed turbulence measurements of the cross-plane of a counter-rotating pair and a co-rotating pair of vortices generated from a split-wing model. He used a miniature quad hot-wire to obtain statistical and spectral results and performed a preliminary analysis where he revealed for the first time the turbulence structure of the development of the two different vortex pairs with streamwise distance over the entire cross-plane of the flow field. In this analysis, Zsoldos did not have the time or data processing capabilities to conduct a more in-depth study of the structure of the vortex pairs. The unique nature of the data obtained by Zsoldos(1992) has allowed for a reanalysis to attain the following aims:

- to reveal in detail the turbulence structure of the development of a counter-rotating vortex pair with streamwise distance.
- to uncover the physical mechanisms of the vortex decay of a counter-rotating vortex pair.
- to observe a defined two stage decay of a counter-rotating vortex pair.
- to reveal in detail the turbulence structure of the development of a co-rotating vortex pair with streamwise distance.

- to uncover the physical mechanisms associated with vortex core merger.
- to observe the structure of the flow field before and throughout core merger.
- to distinguish between the structure and effects of vortex pair interaction and those of an isolated vortex.

To meet the last aim, the results of an experimental study of an isolated vortex conducted by Devenport et al(1995) are used as a control in the present analysis. They obtained quad hot-wire measurements under similar conditions to Zsoldos(1992) with one wing removed. Through statistical and spectral results, they have revealed the turbulence structure of an isolated vortex which are used for comparison with the vortex pair results to reveal the effects of vortex pair interaction.

This report is organized into four chapters. The experimental configurations and procedures used in Zsoldos' and the isolated vortex studies and modifications employed in the present study are covered in chapter two. The present data analysis and discussion are presented in chapter three with conclusions covered in chapter four.

2. Description of Experiments and Data Reduction

This chapter contains a summary of the trailing vortex pair experiments conducted by Zsoldos(1992) which produced the data analyzed in the present investigation. It explains the hot-wire data reduction process for the data reanalysis, as well as the issues of probe interference and vortex wandering which are of great importance in establishing the validity of the results. A summary of the parallel experimental study of an isolated vortex, which is relevant to the data analysis, is also included.

2.1. Trailing Vortex Pair Experiments of Zsoldos(1992)

2.1.1 Configuration

Zsoldos(1992) conducted his experiments in the Virginia Tech Stability Wind Tunnel, which is a continuous, single return, closed-circuit wind tunnel. It is powered by a 600 horse power dc motor allowing a maximum speed of 56 m/s. The test section used for the experiment is square with a cross section of 1.83m x 1.83m and a length of 7.33m. Seven anti-turbulence screens are located in the settling chamber just ahead of the nozzle which has a contraction ratio of 9:1. The diffuser angle is 3° with large vortex generators located at the entrance to prevent separation as the flow decelerates. Flow in the empty test section is closely uniform with a turbulence intensity of less than 0.05% at 20 m/s, Choi and Simpson(1987).

The vortex pairs were generated using two identical half-wings mounted tip to tip, Figure 3(a). Both had a rectangular planform and NACA 0012 section and blunt tip with a chordlength c of 0.203m and an effective half span of 0.879m. The separation distance between the wing tips was $0.25c$. Both wings were equipped with effective boundary layer trips covering locations from 20% to 40% of the chordlength of the wing surface to eliminate possible unsteadiness and nonuniformity that might result from natural transition. The wings were introduced from the ceiling and floor of the test section and mounted with their quarter chord lines collinear and perpendicular to the free-stream, Figure 3(a). The wings were both set at a 5° angle of attack (measured according to the right hand rule for the negative y axis, Figure 3(a)) to generate a pair of counter-rotating vortices. The wings were set at opposite angles of attack (top wing at 5° , lower wing at -5°) to generate a pair of co-rotating vortices.

In most engineering applications, a single wing generates the vortex pair. The present configuration was used instead because it allows significant interaction between the vortices generated at the wing tips without sacrificing Reynolds number. To obtain significant interaction between a vortex pair, they must be allowed to develop over a streamwise distance equal to many times the distance separating them. Given the length of most wind tunnel test sections, this means that if the vortices are generated from the opposing tips of the same wing, only a very small wing can be used and Reynolds numbers will be correspondingly low.

Zsoldos performed flow visualizations, single hot-wire, and quad hot-wire measurements on the co and counter-rotating vortex pair flows. All measurements referred to here were performed at a Reynolds number based on wing chord and free-stream velocity, $Re_c = cU_{ref}/v$, of 260,000. The coordinate system to be used in presenting measurements is defined in Figure 3(a). The origin of the system (x, y, z) is at the leading edge of the wings and half way between the wing tips, with x in the streamwise direction, y in the spanwise direction, and z in the transverse direction.

2.1.2 Flow Visualizations

Flow visualizations were performed using the helium bubble technique with the wings at equal and opposite angles of attack, generating counter and co-rotating vortices of equal strength respectively. The pictures, Figure 5, are time averaged exposures from Zsoldos(1992) of a counter-rotating vortex pair and a co-rotating vortex pair generated at the angles of attack and wing tip separation given in the previous section at a chord Reynolds number of 130,000. The vortex cores appear as two bright streaks generated by the helium bubbles trapped there. Here, the flow is from the right of the page to the left. Notice that the vortices of the counter-rotating pair move apart as they flow downstream and the vortices of the co-rotating pair spiral about each other and merge into a single core within the length of the test section. The streamwise locations chosen for detailed velocity measurements are highlighted in the flow visualization pictures in Figure 5. Measurements were taken at 10 and 30 chordlengths downstream of the wing leading edges (see Figure 3) for the counter-rotating vortex pair case. Measurements were taken at $x/c=10, 15, 22$, and 30 downstream of the wing leading edges for the co-rotating vortex pair case. The testing conditions for the measurements of these cases were given in the previous section and they are summarized in Table 3.

2.1.3 Single Hot-Wire Measurements

Zsoldos(1992) performed measurements using a single hot-wire probe 1mm downstream of the trailing edge of each airfoil to reveal the properties of the trailing edge boundary layers. Profiles of mean velocity, turbulence intensity, and frequency spectra were measured at spanwise locations, $y/c=1.3, 0.73, -0.73$, and -1.73 (see Figure 3(a)) for both counter-rotating and co-rotating cases. Results are summarized in Table 1. Zsoldos(1992) concluded that on either side of the wing trailing edges, the flow was

similar to a two-dimensional, fully turbulent, boundary layer. Velocity profiles showed that the boundary layer was not separated.

2.1.4. Quad Hot-Wire Measurements

Zsoldos(1992) made measurements in the two vortex pair flows using a miniature quad hot-wire probe. The probe consists of four wires arranged to form two orthogonal x-wire arrays with each wire inclined at a normal angle of 45° to the probe axis, Figure 4. The 0.4 mm³ sensing volume gives high spatial resolution and minimizes probe interference effects. Each wire is made of tungsten and is 0.8mm in length and 5µm in diameter. The quad wire probe was mounted in a probe holder of 23.6mm diameter steel tubing attached to the traverse mechanism and aligned with the flow as shown in Figure 3. The holder positioned the probe 0.7m upstream of the traverse mechanism. Two 6.2mm diameter rods were used to offset the probe from the holder by 105mm.

Velocity measurements were made using a quad hot-wire probe in conjunction with a Dantec anemometer system. This system consisted of four Dantec 56C17 bridges and four Dantec 56C01 constant temperature anemometers housed in a Dantec 56B12 main frame. The output voltages from the anemometer bridges were then sent to a 'buck and gain' amplifier system. The amplifiers subtracted an offset voltage from the anemometer output voltage, typically 1.95 volts, and multiplied the result by a factor of 10. The frequency response of the amplifiers were flat out to 100kHz. Voltages were sent to an Analog 12 bit HSDAS-12 A/D converter with a voltage range of 0-5 volts. The A/D converter can sample four channels simultaneously at a maximum rate of 100kHz per channel. The quad hot-wire probe is capable of simultaneous measurements of all 3 velocity components. For more details see Zsoldos(1992).

A large amount of data was taken using the quad hot-wire to obtain a detailed view of the physics of the two different trailing vortex pairs. Over 70 traverses were

made with an average of 70 points per traverse. At a sampling rate of 30 kHz, 100 blocks of 6144 samples were taken at each measurement point on the four quad wire channels resulting in a total of over 33 gigabytes of raw data taken for this experiment. The raw data consists of full time scales of voltages on all four sensors which provides a full numerical record of the experiments, providing a unique opportunity in which the raw data could be reprocessed for the present analysis. Optical disk cartridges holding up to 940 megabytes each were used to store the raw data of Zsoldos(1992) and the processed data.

2.1.5 Probe Interference

Trailing vortices have a reputation for being unusually sensitive to probe interference. Establishing the amount of interference was a key prerequisite of Zsoldos' measurements. Zsoldos used helium bubble flow visualization to do this. A dummy hot-wire probe of the same size and shape as the quad hot-wire was used in the flow visualization in Figures 6(a). The flow was captured with the probe in the lower core of the counter-rotating pair at a streamwise location x/c of 22, a wing tip separation of $0.25c$, and a chord Reynolds number of 400,000. Here the light streaks represent the vortex cores and the dummy probe is pointing out from the left side of the picture. If the probe was interfering with the vortex core structure, the streaks would waver. He concluded, as shown, that the small quad hot-wire probe did not interfere with the flow field of the vortices at this streamwise location. Further investigation of miniature quad hot-wire probe interference was performed by Engel(1995). Figure 6(b) shows a probe in the core of an isolated vortex generated from a half wing model, with the same characteristics as the wings used by Zsoldos(1992), at an angle of attack of 5° and a chord Reynolds number of 130,000 in a smaller wind tunnel. He also found that the probe does not interfere with the vortex flow.

2.2. Data Reduction and Analysis Methods of the Present Study

The data set generated by Zsoldos(1992) is the first extensive set of detailed turbulence measurements made of counter and co-rotating vortex pairs. Zsoldos(1992) performed the basic reduction of this data validating the measurements and plotting most of the measured turbulence quantities. However, because of limitations on time and data processing capabilities, he was unable to reveal in detail the turbulence structure of the vortex cores or the flow immediately surrounding them. The same limitations prevented extensive filtering of the measurements to remove the effects of vortex wandering.

Since Zsoldos' work, data processing capabilities have improved substantially. There has also been time to perform a much deeper analysis of the data that has revealed in detail the mean flow and turbulence structure of the vortex cores and the flow surrounding them. This analysis, which also includes filtering of the measurements to eliminate wandering effects and provide information about the turbulence structure scales that constitute the flow, has led to a much deeper physical understanding of these flows. In addition, a second experiment performed on an isolated vortex has become available. This experiment provides a control in the present analysis in that it gives the turbulence structure and characteristics of an isolated vortex which through comparison can reveal the effects of interaction between the vortices in a vortex pair. This study also provides additional knowledge on vortex wandering that has been implemented in the present data analysis. A summary of the experiment is therefore given below.

2.2.1. Wandering Analysis

Vortex wandering is an issue that needs to be explored when working with vortical flow measurements made by a fixed probe. Wandering causes a fixed probe to greatly overestimate turbulence stresses in regions where there are significant mean velocity gradients across the vortex. It may also smooth mean velocity profiles

significantly. Baker et al(1974) conducted experiments on a trailing vortex generated by a rectangular wing in a water tunnel using LDV. They found that vortex wandering decreased the maximum tangential velocities by 30% and increased the measured core radius by a factor of 2.2. Baker attributed the wandering to free-stream turbulence. Chigier and Corsiglia(1972) and Corsiglia et al(1973) conducted triple hot-wire measurements on a trailing vortex in the NASA Ames 40x60 wind tunnel. They observed a spanwise wandering of about $\pm 2c$. As a result, mean velocity measurements made with a fixed hot-wire probe underestimated the peak tangential velocity by as much as 50%. Zsoldos(1992) acknowledged the presence of core wandering in the vortex pair measurements. However, he did not investigate its effects on the pair flows in detail.

Since vortex wandering is unavoidable, its effects on the turbulence structure of the flows under investigation are desirable. Devenport et al(1995) developed a theory for vortex wandering and applied it to a single vortex. In their preliminary analysis, they developed a theory based on the assumption that the measured axial velocity and streamwise vorticity profiles through the core are Gaussian (q-vortex profiles). Defining the measured profile, axial velocity or streamwise vorticity, as a convolution of values at all possible vortex core locations times a weighting function which is assumed to be an isotropic Gaussian, one finds these values by taking the Fourier transform of the convolution. The assumptions of this theory make it very specific. However, Devenport et al(1995) developed some rules of thumb to obtain the true core parameters corrected for the effects of core wandering from the measured values from this theory which are given below.

$$r_1/r_{1m} = \sqrt{1 - 2\alpha\sigma^2/r_{1m}^2} \quad (3)$$

$$V_{\theta 1}/V_{\theta 1m} = r_{1m}/r_1 \quad (4)$$

$$U_D = U_{Dm}/\sqrt{(1 - 2\alpha\sigma^2/d_m^2)} \quad (5)$$

where $\sigma = \sqrt{0.5 * (\sigma_y^2 + \sigma_z^2)}$ is the upper bound for the amplitude of core motions and σ_y and σ_z are the amplitudes in the cross-plane directions, $\alpha = 1.25643$, and the subscript m indicates measured quantities with r_1 , $V_{\theta 1}$, and U_D defined as the core radius, peak tangential velocity, and axial velocity deficit respectively. The ratio between d and d_m , which is the radial scale of the axial profile, is the same as that between r_1 and r_{1m} .

Devenport et al(1995) have developed another theory in which they assume that the axial velocity and streamwise vorticity profiles used in the convolution are a sum of Gaussians(q-vortices). For the theory to be applicable, the unwandered profiles must be axisymmetric. They assumed a general correlated Gaussian for the weighting function which is a function of $p = p(y, z, \sigma_y, \sigma_z, e)$, where σ_y , σ_z , and e are the rms amplitudes of core motions in the cross-plane directions and e is the correlation between these components ($e = \sigma_{yz}/\sigma_y\sigma_z$). Thus, the axial velocity or streamwise vorticity profiles are estimated as a summation where σ_y , σ_z , and e are varied until these profiles match the measured profiles. The profiles obtained are essentially the unwandered profiles multiplied by some constant coefficients which form a curve fit of the measured data with the original wandering. Knowing the constant coefficients and given the measured data, the profiles corrected for the effects of wandering can be obtained. This vortex wandering theory was implemented in the present analysis of the vortex pairs. The data can also be high-pass filtered to remove the low frequency velocity fluctuations that are assumed to be mostly a result of vortex wandering leaving intact the bulk of the fluctuations due to coherent wake structures and other core motions to estimate the effects of core wandering motions on the turbulence stress fields.

2.2.2. Quad Hot-Wire Reduction Equations

Zsoldos(1992) used a miniature quad hot-wire probe to measure mean velocities and Reynolds stresses at various planes downstream of the wings. The quad hot-wire is capable of simultaneous measurements of all three velocity components. These

components were determined from the four instantaneous effective velocities output in a two stage process. First estimates of the instantaneous velocity components were obtained using a Jorgenson(1971) type analysis. These estimates were then coupled using the results of a direct angle calibration. As part of the present investigation, improvements were made to this procedure which will be highlighted in the summary given below.

Consider the probe shown in Figure 4. Using Jorgenson's approximation, equations for the effective cooling velocities experienced by each wire are:

$$U_{\text{eff1}}^2 = (U_e \cos \theta_1 + V_e \sin \theta_1)^2 + k_1^2 (V_e \cos \theta_1 - U_e \sin \theta_1)^2 + h_1^2 W_e^2 \quad (6)$$

$$U_{\text{eff2}}^2 = (U_e \cos \theta_2 + W_e \sin \theta_2)^2 + k_2^2 (W_e \cos \theta_2 - U_e \sin \theta_2)^2 + h_2^2 V_e^2 \quad (7)$$

$$U_{\text{eff3}}^2 = (U_e \cos \theta_3 - V_e \sin \theta_3)^2 + k_3^2 (U_e \cos \theta_3 + V_e \sin \theta_3)^2 + h_3^2 W_e^2 \quad (8)$$

$$U_{\text{eff4}}^2 = (U_e \cos \theta_4 - W_e \sin \theta_4)^2 + k_4^2 (U_e \cos \theta_4 + W_e \sin \theta_4)^2 + h_4^2 V_e^2 \quad (9)$$

where in the present analysis, U_e , V_e , and W_e were considered only as first estimates of the velocity components. Zsoldos(1992) estimated the pitch and yaw factors k and h for each wire by making measurements over a range of pitch and yaw angles in a uniform flow of known direction. Effective wire angles were determined using the angle calibration mechanism in the uniform flow. Splitting the velocity components into mean and fluctuating terms and ignoring higher order terms, equations (6) through (9) may be rewritten explicitly for the estimated velocities U_e , V_e , and W_e .

$$V_e = [(U_{\text{eff3}}/\sqrt{A_3}) - (U_{\text{eff1}}/\sqrt{A_1})]/[(D_3/A_3) - (D_1/A_1)] \quad (10)$$

$$W_e = [(U_{\text{eff4}}/\sqrt{A_4}) - (U_{\text{eff2}}/\sqrt{A_2})]/[(D_4/A_4) - (D_2/A_2)] \quad (11)$$

$$U_e = [(U_{\text{eff1}} - (D_1/\sqrt{A_1})V_e)/\sqrt{A_1} + (U_{\text{eff2}} - (D_2/\sqrt{A_2})V_e)/\sqrt{A_2}]/2 \quad (12)$$

where

$$A_1 = 1 - \cos^2 \theta_1 \quad A_2 = 1 - \cos^2 \theta_2 \quad A_3 = 1 - \cos^2 \theta_3 \quad A_4 = 1 - \cos^2 \theta_4$$

$$D_1 = \sin 2\theta_1/2 \quad D_2 = \sin 2\theta_2/2 \quad D_3 = \sin 2\theta_3/2 \quad D_4 = \sin 2\theta_4/2$$

Note that equation (12) is an improvement upon Zsoldos' reduction procedure in that it takes into account the streamwise effective velocity U_e measured in the UV plane, as well as the value measured in the UW plane. This makes the measurements less sensitive to velocity gradients in the measurement volume, especially those with streamwise vorticity.

The results of a direct angle calibration were then used to correct the velocity component estimates. The direct calibration involved pitching and yawing the quad wire in a uniform flow of known velocity and direction and comparing the actual velocity components experienced by the probe, deduced from the flow velocity and pitch and yaw angles, with those estimates obtained using the above analysis and constructing tables of corrections of the form:

$$V - V_e/Q = f_1(V_e/Q_e, W_e/Q_e) \quad (13)$$

$$W - W_e/Q = f_2(V_e/Q_e, W_e/Q_e) \quad (14)$$

$$Q - Q_e/Q_e = f_3(V_e/Q_e, W_e/Q_e) \quad (15)$$

where $Q = \sqrt{U^2 + V^2 + W^2}$

$$Q_e = \sqrt{U_e^2 + V_e^2 + W_e^2}$$

These correction tables were then used point by point to reduce the velocity measurements made in the vortices, yielding instantaneous simultaneous measurements of U , V , and W accurate to much larger values of flow angle than the original estimates. Another adjustment that was made in the data reduction process of the present analysis deals with the direct calibration. An error in the relations for the geometric and measured angles Zsoldos used in the creation of the direct calibration files, which was especially evident when large pitch and yaw angles were combined, was corrected in the present procedure.

2.2.3 Isolated Vortex Experiment of Devenport et al(1995)

One of the objectives of the present analysis is to distinguish between the structure and effects of vortex pair interaction separate from those of an isolated vortex. To accomplish this, the experimental results from a study of an isolated trailing vortex conducted by Devenport et al(1995) are compared with the results of the vortex pairs. These particular results were chosen because Devenport et al(1995) conducted their tests at conditions very close to that of Zsoldos(1992) making a valid comparison reasonable. Devenport et al(1995) conducted experiments in the Virginia Tech Stability Wind Tunnel, which has been described above. The model configuration was the same as that of Zsoldos(1992) with one wing removed, Figure 3(b). It consisted of a rectangular planform half wing with a NACA 0012 airfoil section, a chordlength c of 0.203m and a blunt tip. It was mounted vertically as a half wing at the center of the test section ceiling with 0.879m protruding into the flow. For the measurements referenced in this report, the boundary layer on the wing was tripped between the 20% and 40% chord locations. The wing model was set at an angle of 5° and tests were run at a chord Reynolds number of 530,000. The test conditions as well as flow parameters for the cases of interest are given in Table 5. Devenport et al performed fixed quad hot-wire probe measurements on an isolated vortex over a range of conditions to obtain the necessary statistical and spectral information to reveal its turbulence structure. This study also offers filtered results which eliminate the effects of vortex wandering. As mentioned above, Devenport et al(1995) developed a vortex wandering theory and applied it to a single vortex. The isolated vortex results are used as a reference in the present report.

3. Data Analysis Results/Discussion

The Cartesian coordinate system shown in Figure 3(a), will be used to present the vortex pair data. The origin of the coordinate system lies at the leading edge of the wing models half way between the wing tips. The coordinate system shown in Figure 3(b), will be used to present the isolated vortex data of Devenport et al(1995). The origin of this system lies at the wing model leading edge at the wing tip. Most of the results of both studies have been normalized on the wing chord c of 0.203m and the free-stream velocity U_{ref} . Measurements were made at a chord Reynolds number $Re_c = U_{ref}c/v$ of 260,000 corresponding to a free-stream velocity of about 20 m/s for the vortex pair studies. Measurements for the isolated vortex study that will be considered below were made at $Re_c = 530,000$ which corresponds to a free-stream velocity of about 44 m/s. Reynolds averaged statistics, spectral results, and high-pass filtered statistics are presented. Uncertainties in Reynolds averaged statistics of the vortex pair results are listed in Table 2.

3.1 A Parallel Study of an Isolated Trailing Vortex

We begin by summarizing some of the results of Devenport et al(1995). They studied the evolution and structure of an isolated trailing vortex generated under similar conditions to that of Zsoldos(1992) (i.e. with one wing removed). Devenport et al's results therefore provide a control enabling us to distinguish between structure generated individually by the present vortices and structure generated by their

interaction. The cases of the isolated vortex study that will be used for comparison in the present analysis include what Devenport et al(1995) refers to as the baseline cases at streamwise locations $x/c=10, 15, 20$, and 30 behind the wing model, which coincide as close as possible with the test locations of the pairs. The details of the experimental setup and procedure of the isolated vortex study were covered in the previous chapter. The wing model was set at an angle of attack of 5° and a boundary layer trip was placed on the model surface between the 20% and 40% chord locations to ensure uniform transition to turbulent flow over the wing. These conditions are the same as those of the vortex pair experiments. The only difference between the two experimental studies is the testing speed. The isolated vortex study was conducted at a free-stream velocity, U_{ref} , of 44 m/s which corresponds to a chord Reynolds number $Re_c=cU_{ref}/\nu$ of $530,000$. The vortex pair experimental tests were conducted at a lower speed of 20 m/s corresponding to a chord Reynolds number of $260,000$. Devenport et al(1995) showed that Reynolds number has little significant effect on the evolution and structure of the isolated vortex. They compared velocity autospectra of data taken at a Reynolds number of $530,000$ and $260,000$ at streamwise location $x/c=30$. They found that the only difference due to a decrease in Reynolds number is a small decrease in high frequency spectral levels, i.e. small scale turbulence energy. Thus, a valid qualitative comparison can be made between the isolated vortex study of Devenport et al(1995) and the vortex pair studies of the present analysis.

Figure 7 illustrates the roll up of the isolated vortex in terms of contours of turbulence axial normal stress, \bar{u}^2/U_{ref}^2 and its variation with streamwise distance. Contours of streamwise vorticity, $\omega_x c/U_{ref}$, in Figure 8 give an additional view of the flow structure outside the core region at $x/c=10$. The turbulence stress contours clearly show a decay in turbulence stress which appears to have a linear rate of variation with streamwise distance. Thickening of the spiral wake occurs at a rate of $1/2$ power. This decay in turbulence axial normal stress with streamwise distance is depicted through color contours at $x/c=10$ and 30 in Figure 9.

Turbulence levels vary along the spiral wake centerline, which is defined as the locus of peak axial normal stress and is denoted by the dashed line in Figure 7(a). Far from the core, in the flat part of the wake, Devenport et al(1995) showed through mean velocity and Reynolds stress profiles and velocity autospectra that the structure of the flow is much like that of a two-dimensional wake. Three dimensional effects take over as one moves from the flat portion of the spiral wake into the curved part. First, peak turbulence levels rise, reaching a maximum near where the wake begins to curve. They then fall monotonically as the core is approached along the spiral wake centerline. Devenport et al(1995) concluded that these variations were a consequence of the rates of strain and lateral curvature suffered by the wake turbulence. Figure 10 shows rates of wake turbulence stretching and skewing on the spiral wake centerline at $x/c=10$. They are defined as $\partial V_s / \partial s$ and $\partial V_s / \partial n$ respectively, where the velocity component V_s is in the direction aligned with spiral wake centerline, s , and n is the direction normal to the wake centerline, normalized on the maximum mean axial velocity gradient, $\partial U / \partial z$, in the two-dimensional portion of the wake far from the wing tip. It shows that stretching is smaller than skewing at most locations and is diminished as the wake curves above the vortex core. Skewing increases passing through zero and shoots upward as the wake curves above the core. The positive skewing and stretching are generated by the rotational velocity field of the vortex. The negative skewing is associated with streamwise vorticity embedded within the wake, Figure 8.

The additional rates of strain and the curvature of the wake appear to influence turbulence levels by inhibiting the large scale turbulence structures. Devenport et al(1995) showed through velocity autospectra measured at points along the spiral wake centerline, Figure 11, that a substantial decrease in low-frequency energy levels, below $fc/U_{ref}=10$, occurs as the rates of strain increase, i.e. as one progresses inward along the spiral wake tail. Spectral levels at frequencies above $fc/U_{ref}=20$, however, remain at almost the same absolute values along the outer part of the spiral wake. Closer to the

core they rise slightly, possibly as a result of additional small scale turbulence created by the break up of larger scales in the high strain rates here.

Moving our attention from the spiral wakes to the turbulence structure of the vortex core region, the turbulence axial normal stress results, Figure 7, show that levels rise to a maximum at the core center which Devenport et al(1995) indicated was mostly an effect of vortex core wandering. They applied their wandering theory summarized in Chapter 2 to obtain estimates of wandering amplitudes of core motions in the flow cross-plane and their correlation, σ_y , σ_z , and e , and correct the mean velocity profiles for the effects of wandering. Profiles of mean axial and tangential velocity of their measured data and this data corrected for wandering are shown in Figure 12. These profiles were used by Devenport et al(1995) to obtain the isolated vortex core parameters given in Table 5.

Figure 13 shows the variation in wandering amplitude, core radius, and peak tangential velocity with streamwise distance, where the core parameters are corrected for wandering. Core radius, r_1/c , varies only slightly from 0.037c and the core regions are closely circular at all streamwise locations of interest. Peak tangential velocity, $V_{\theta 1}$, decreases slightly with streamwise distance. Devenport et al(1995) took these trends to be indicative of laminar flow because of the absence of significant core growth and decay, i.e. increase in core size and decrease in peak tangential velocity. Vortex core wandering amplitude increases linearly from $x/c=10$ to 20 and by 1.5 times from $x/c=20$ to 30. The upper bound for the rms amplitude of core motions is 34% of the core radius at $x/c=30$. The Rossby number, which is defined as the ratio of axial velocity deficit to peak tangential velocity, $U_D/V_{\theta 1}$, varies around 0.5 for streamwise locations between $x/c=10$ and 20 and it increases to 0.6 at $x/c=30$ which indicate according to Mayer and Powell(1992) that the isolated vortex is stable at the baseline locations. The core circulation normalized on root circulation, Γ_1/Γ_0 , for the isolated vortex varies slightly around 0.27 and decreases to 0.248 at $x/c=30$. Finally, the axial velocity deficit, U_D/U_{ref} , varies slightly around 0.15 with streamwise distance.

Autospectra of axial velocity fluctuations are plotted as G_{uu}/cU_{ref} vs. fc/U_{ref} in Figure 14, where f is frequency in Hertz, at various z locations from the spiral wake to the core center at $x/c=10$ to show the turbulence energy distribution of the vortex. The locations of the spectra are given relative to the core center at $z/c=0.0$. At frequencies less than $fc/U_{ref}=20$, spectral levels rise as the core center is approached from the spiral wake in part due to vortex core wandering. At frequencies greater than $fc/U_{ref}=20$, where one would expect to see the influence of smaller turbulence structures, spectral levels fall becoming an order of magnitude smaller at the core center than they are in the wake. Even in the region just outside the core edge, where the mean tangential and axial rates of strain generated by the core reach their maxima as a result of the rotation of the vortex core, spectral levels in this frequency range are substantially lower than in the spiral wake. According to Devenport et al(1995), this suggested that the velocity field of the vortex core was not generating any turbulence of its own.

Figure 15 shows the autospectrum at the core center, G_{uu} , and there is a shift in the spectrum to lower frequency and energy with distance downstream but little change in shape. To find the origin of the velocity fluctuations at the core center, Devenport et al(1995) scaled the core center autospectra on various velocity and length scales. They found that spectral levels above $fc/U_{ref}=1$ collapsed when scaled on parameters of the flat portion of the wake, u_w and L_w , Figure 16. Devenport defined u_w and L_w as the maximum axial turbulence intensity and the local half width of the flat part of the spiral wake tail measured in the z direction at $1/2u_w$, respectively. Devenport et al indicated that this scaling implied the absence of turbulence generated by core motions. It also indicated the absence of any turbulence in the core region because if turbulence were diffused in from the wake, it would be stabilized and controlled by the rotational motion of the core and would not scale. Devenport et al(1995) therefore concluded that the vortex core was laminar and velocity fluctuations here were produced by inactive motions as the core was buffeted by surrounding spiral wake turbulence.

The data of the isolated vortex study was high-pass filtered to distinguish the various sources of velocity fluctuations. Figures 17 and 18 show data at $x/c=10$ filtered at normalized frequencies of $fc/U_{ref}=3$ and 40, respectively. Assuming Taylor's hypothesis these frequencies correspond to streamwise length scales of $0.33c$ and $0.025c$ respectively. Figure 17 shows contours of \bar{u}^2/U_{ref}^2 at $x/c=10$ filtered at $fc/U_{ref}=3$, where the core edge is denoted by the dark line. Filtering at this normalized frequency should eliminate most of the velocity fluctuations associated with wandering leaving intact the bulk of the fluctuations associated with coherent wake structures and other core motions. The flow structure is similar to that revealed by the unfiltered results. Filtered turbulence stress levels still rise to a maximum at the core center. Devenport et al presumed this was a result of inactive motion of the core as it was buffeted by the wake. Figure 18 shows contours of \bar{u}^2/U_{ref}^2 filtered at $fc/U_{ref}=40$ with the core edge denoted by the dark line. Filtering at this frequency should eliminate all affects except those of the smallest scale turbulence. Notice the intensity of small scale turbulence fluctuations remains almost unchanged along the outer part of the spiral wake, despite the varying rates of strain imposed by the vortex at $x/c=10$. There is an increase in small scale turbulence levels in the vicinity of the core presumably as a result of the break up of large scale structures in the high strain rates here. Moving into the core, the small scale turbulence levels drop dramatically. Inside the core, levels are very low compared to the surrounding wake and almost constant, which is consistent with laminar flow. Decay of the turbulence stress field was evidenced in the data at $x/c=30$ filtered at $fc/U_{ref}=40$ which revealed very low small scale turbulence levels in comparison with the results at other streamwise locations. They have not been included here because of the large uncertainty as a result of excessive noise present with these high frequency motions.

The isolated vortex results of Devenport et al(1995) reveal that the turbulence structure of this vortex is dominated by the spiral wake wound about the core and the core appears to be laminar at all streamwise locations. The following sections will reveal the results of generating two vortices in close proximity to each other on the turbulence

structure of the flow. They will distinguish between the effects and structure that are a result of vortex interaction and a result of the separate vortices through a comparison of the vortex pair results with the results of the isolated vortex presented above.

3.2. Counter-rotating Vortex Pair

3.2.1. Measurements at $x/c=10$

Figure 19 reveals the entire flow structure at $x/c=10$ in terms of contours of turbulence axial normal stress \bar{u}^2/U_{ref}^2 . Figures 20 through 24 show the flow structure in and around the cores in terms of mean cross-flow velocity vectors, contours of mean axial velocity U/U_{ref} , mean streamwise vorticity $\omega_x c/U_{ref}$, axial normal stress \bar{u}^2/U_{ref}^2 , and cross-flow normal stress sum $(\bar{v}^2 + \bar{w}^2)/U_{ref}^2$. The sum of the cross-flow stresses is presented because it is invariant to rotation in the cross-flow plane.

At $x/c=10$, the vortex cores have drifted in the negative z direction and are centered at $z/c=-0.66$. The vortex cores have moved apart from $0.25c$ at the wing tips to $0.45c$ here. This presumably is a result of Betz's conservation laws governing the inviscid roll-up of each vortex which state that the centroid of the vorticity distribution shed by each wing must remain fixed during the roll-up. Since the centroid is inboard of the tip, the vortex cores move apart.

The effects of the rotational velocity field of one vortex core upon the other, i.e. mutual induction, result in a strong upwash of fluid between the vortex cores and a relatively weak downwash to either side of them. This rotational motion is shown through mean cross-flow velocity vectors of variable length in Figure 20. Thus, the cores ascend in the direction of wing lift pulling the spiral wakes with them due to their mutual induction¹. We refer to the wakes as spiral wakes here because they have a distinct turbulence structure similar to that seen in the isolated vortex results, Figure 7.

¹We use the terms upward or ascend to refer to the direction parallel to the wing lift, regardless of the actual directions in the wind tunnel.

A view of the entire flow field, Figure 19, clearly shows the spiral wakes wound about their respective cores as a result of the individual rotation of the cores. The spiral wakes are pulled upward into the region between the cores and they wind toward the outside of the cores as they converge upon the core regions. They appear to merge in the region between the cores as evidenced by the maximum in turbulence stress levels here.

Through examination of the turbulence stress contours, it appears that the flow field has been captured just after initial contact between the spiral wakes is made because the spiral wakes are still well defined. There are heightened turbulence stress levels along the spiral wake centerlines, which are defined as the loci of maximum axial normal stress and denoted by the dashed lines in Figures 23 and 24.

In the flat portion of the spiral wakes far from the vortex cores, at $y/c=2.5$, the characteristics of the flow resemble those of a two-dimensional turbulent wake. Profiles of turbulence normal stresses in coordinates aligned with the spiral wake centerline, Figures 25 through 27, give the profiles of this portion of the spiral wake. The coordinate system directions and profile locations are highlighted in Figure 19. The turbulence stress profiles in the flat portion of the spiral wake show that the turbulence stress in the n direction (which is parallel to the z direction here) remain constant across the inner part of the spiral wake tail width compared to that in the streamwise direction and s direction (which is parallel to the y direction here). These results agree with those of Wygnanski et al(1986) for a two-dimensional turbulent wake. The characteristics of this portion of the spiral wake, which is referred to as the flat part, are used for comparison throughout the analysis at $x/c=10$.

The spiral wakes appear to suffer lateral curvature as they wind about the cores. The contours of turbulence axial normal stress, Figures 19 and 23, show suppression of turbulence levels at the points of greatest curvature above and below the cores. As the spiral wakes curve to the outside of the cores and straighten out, the turbulence levels increase forming a local maximum. This suppression of turbulence stress may also be a

result of rates of strain due to spiral wake turbulence stretching and skewing which will be discussed below.

Lateral curvature of the spiral wakes appears to cause breakdown of coherent wake structures above the cores. Profiles of turbulence normal stress in coordinates aligned with the spiral wake centerline are presented in Figures 25 through 27 to investigate the effects of curvature on the spiral wake turbulence. To clarify, the velocity component U is in the streamwise direction, V_s is aligned with the spiral wake centerline, and V_n is normal to the wake centerline. The numbers in the figures indicate the profile locations along the spiral wake centerline shown in Figure 19. The results show that turbulence stress peak values in the spiral wake tail below the cores, location 1, resemble the flat part of the spiral wake far from the cores for all three components which indicates that the spiral wakes retain their character here. The peak values reach a maximum in the middle of the region between the cores, location 4, where wake merger occurs, for all three components. This suggests that coherent wake structures aligned with the wake centerline are being intensified in this region because peak values of \bar{u}^2 and \bar{v}_n^2 which are associated with these structures reach peak values at least 1.5 times that of the flat portion of the spiral wake. Peak values past this point remain constant at levels the same as the flat part of the spiral wake for \bar{u}^2 and slightly higher than these values for \bar{v}_n^2 . Peak values of \bar{v}_s^2 fall to half that of the flat portion of the wake as the spiral wake curves above the right-hand core. The last two results suggest that coherent wake structures are broken down as a result of the severe lateral curvature in the portion of the wake above the right-hand core.

Autospectra of the U , V_s , and V_n velocity fluctuations normalized on U_{ref} and c at locations along the spiral wake centerline highlighted in Figure 19 are shown in Figure 28. They indicate that coherent wake structures are intensified in the region between the cores as evidenced by the heightened peaks at low frequencies, $1 < f_c/U_{ref} < 10$, at locations 3 and 4 of autospectra of velocity components in the streamwise direction and normal to the spiral wake centerline, U and V_n . The turbulence energy levels of the

peaks in these two autopsectra decrease significantly as the spiral wake winds about the right-hand core past location 4 suggesting a break down of coherent wake structures as a consequence of the curvature and possibly rates of strain here. At higher frequencies, above $fc/U_{ref}=10$, spectral levels of autospectra of U and V_n increase along the spiral wake centerline from the spiral wake tail and converging upon the core indicating an increase in small scale turbulence energy presumably as a result of the break down of larger scales due to lateral curvature. The autospectrum of V_s velocity fluctuations show a suppression of turbulence energy levels at locations 6 and 7 where the spiral wake curves above the right-hand core over the entire frequency range which appears to be a result of lateral curvature. Spectral levels at location 3 are also suppressed however, this does not appear to be a result of curvature.

The intensification of coherent wake structures aligned with the spiral wake centerline appears to be the result of stretching of the spiral wake turbulence in the region between the cores. This is consistent with the observations made by Keffer(1965) of a uniformly distorted turbulent wake. He observed that the large scale coherent structures aligned in the straining direction are intensified while the rate of viscous dissipation of randomly oriented small scale structures is augmented by the strain which results in a wake structure almost entirely dominated by large scale motions. The autospectra of U and V_n , Figure 28, show lower spectral levels at frequencies above $fc/U_{ref}=10$, at locations 3 and 5 in the region between the cores than at locations further about the core. Peak levels of \bar{v}_s^2 fall to about half that of the flat portion of the wake at these two locations. These results indicate an increase in dissipation presumably due to wake turbulence stretching.

Further evidence of distortion of the wake turbulence in the wake merger region between the cores is the anisotropy of the turbulence normal stresses shown by profiles of these stresses along the plane of symmetry between the cores, Figure 29. The peaks in \bar{u}^2 and \bar{v}^2 indicate an intensification of coherent structures aligned with the wake centerline in the wake merger region due to stretching. However, values of \bar{w}^2 do not

show a peak in this region and are as low as 1/7th of \bar{V}^2 indicating that stretching is not as great in this direction.

Rates of spiral wake turbulence stretching and skewing defined as $\partial V_s / \partial s$ and $\partial V_s / \partial n$, respectively, normalized on the maximum mean axial velocity gradient $\partial U / \partial z$ of the flat part of the spiral wake are shown as a function of profile location in Figure 30. Stretching is accelerated along the spiral wake centerline from the spiral wake tail into the region between the cores. It then decelerates moving out of this region and accelerates curving above the core. Skewing accelerates to location 3 as well and then it remains low through the region between the cores. It accelerates again as the spiral wake curves to the outside of the core where stretching diminishes. Thus, suppression of turbulence energy levels seen in autospectrum of V_s , at locations 6 and 7 is a result of increased rates of stretching and skewing as well as lateral curvature. The suppression of spectral levels at location 3 is presumably a result of increased rates of stretching and skewing here.

Moving our attention from the spiral wakes to the structure of the vortex core regions, the normal stress contours, Figures 23 and 24, show turbulence fluctuations rising to a maximum at the core centers. This is assumed to be mostly an effect of small amplitude core wandering. Using the method developed by Devenport et al(1995), upper bounds for the rms amplitudes of core motions in the flow cross-plane were obtained. The method produced good agreement between the mean velocity and turbulence normal stress profiles in the core regions estimated using the wandering theory of Devenport et al(1995) and those of the measured data, with the result that wandering has a smaller effect on the axial normal stress than the spanwise and transverse components. At this streamwise location, the wandering amplitudes in the cross-plane, σ_y and σ_z , and the correlation coefficient, e , defined as $\sigma_{yz} / \sigma_y \sigma_z$, are equal to $0.1027 r_{im}$, $0.1068 r_{im}$, and 0.3097 respectively, where r_{im} is the core radius obtained from the measured data. The angle of the principle direction of wandering, defined from the y axis to the negative z axis, is 41.4° . This is a result of the fact that the magnitude

of core wandering is very similar in both directions. According to Devenport et al's correction formulae, the present measurements should overestimate the true core radius and underestimate the true peak tangential velocity by 2.7%. Figure 31 which presents mean tangential and axial velocity profiles of both the measured (with wandering) results and this data corrected for wandering agree with this estimate. The shaded regions in Figures 23 and 24 indicate the areas where more than 30% of the levels of the Reynolds stresses are due to wandering. This value is used with reference to the fact that 30% is approximately the contribution that inactive motion makes to the streamwise normal stress in an attached boundary layer. For \bar{u}^2/U_{ref}^2 , Figure 23, these regions cover the cores and extend about half a radius beyond the core edges denoted by the thick lines. For $(\bar{v}^2 + \bar{w}^2)/U_{ref}^2$, Figure 24, the regions of wandering are larger. They engulf the cores and extend about 1.5 radii beyond the core edges. These results show that measurements outside the core regions are free of wandering.

The mean flow characteristics of the vortex cores can be obtained from various core parameters. Since the mean velocity profiles of Figure 31 show that there is only a small difference between the measured data and this data corrected for the effects of wandering, we will only discuss the core parameters obtained from the corrected profiles which are given in Table 3. The thick lines in Figure 23 represent the core edges which are defined by the loci of peak tangential velocity. The cores are closely circular with corrected radii of 0.044c. The core is symmetric about the core center and the velocity profiles through the right-hand core center in Figure 31 show that the mean tangential velocity values are 40% U_{ref} at the core edges. The axial velocity deficit is symmetric about the core center and the profile of mean axial velocity through the right-hand core shows a double peak structure. The axial velocity deficit is about 14.8% U_{ref} . The contours of mean axial velocity, Figure 21, show irregularities that are a result of this double peak structure which appears antisymmetric without taking into account the fact that the cores lie at an angle to the free-stream and measurement plane. The Rossby number, which is defined as the maximum axial velocity deficit, U_D , divided by the peak

tangential velocity, $V_{\theta 1}$, is 0.368 for the counter-rotating pair at $x/c=10$. The ratio of core circulation to root circulation, Γ_1/Γ_0 , is 0.208. The contours of mean streamwise vorticity in Figure 22 are approximately circular in the core regions and concentric with the core edges outside them. The vorticity field of each vortex at this stage of flow development is similar to that of an isolated vortex, Figure 8, with low levels in the spiral wake and levels rising to a maximum at the core centers.

Focusing on the turbulence structure of the cores, velocity autospectra are presented to give more insight into the turbulence energy of the counter-rotating vortex pair, especially in the core regions. Figures 32 through 34 show autospectra of U, V, and W velocity fluctuations normalized on U_{ref} and c for various spanwise locations, y/c , moving from the spiral wake into the core center, which are indicated by the dots in Figure 23. The locations are given relative to the core center at $y/c=0.25$. The spectra at $y/c=0.176$ and 0.126 show the character of the velocity fluctuations in the spiral wake. They resemble the spectra in the flat (two-dimensional) portion of the spiral wake, Figure 35, which indicates that the turbulence structure at this location in the wake flow is not that different despite the strong distorting effects of the nearby vortex. Outside the core, the autospectrum of U, Figure 32, show an inertial subrange indicating a well developed energy cascade outside the core region.

Moving from the spiral wake into the vortex core, spectral levels in the low frequency range, below $f_c/U_{ref}=2$, rise mostly as a consequence of wandering. At low frequencies, the motion of the vortex cores could be a result of Crow(1970) long wave instability. Thus, an estimate for the most unstable long wavelength was obtained. A major factor in the analysis of wave instabilities for the counter-rotating vortex pair is the definition of the core diameter. The general analysis of wave instability uses a vortex filament which in turn means that a cutoff method must be used to avoid singularities. Crow(1970) in his theory of long wave instability, makes the assumption that vorticity is distributed uniformly within the cores and is zero outside so that the cores rotate like solid bodies, which is an idealized situation. In order for Crow's cutoff method to agree

with Kelvin's result that a very long wave will rotate around a vortex at a specific angular frequency in a direction opposite the circulatory motion, he defines a ratio of cutoff distance to core diameter $d_c/d_1=0.321$. The estimate for the ratio of core diameter to vortex separation distance for this method is $d_1/b_c=0.197$ which is similar to the value for the present vortex pair at $x/c=10$ of 0.196. Thus, the cutoff distance, setting the core diameter equal to $0.088c$ from the peak tangential velocity, is $0.0282c$. With knowledge of this value and that the vortex separation distance is $0.45c$, a value for the ratio of cutoff distance to separation distance, which is 0.0628, can be used to find the most unstable long wavelength. Using Crow's results, this implies a most unstable long wavelength of $3.3c$ which corresponds to a normalized frequency $fc/U_{ref}=0.3$. The spectra do not show a distinct peak here, Figures 32 through 34. It appears that Crow instability may not be present or that the amplitude of the wave motion is very small at this point in the flow development.

Another type of instability could be present whose effects would appear at higher frequencies, above $fc/U_{ref}=1$. Widnall, Bliss, and Tsai(1974) studied theoretically the presence of short wave instability in a vortex pair and they found that this instability will occur in a vortex core for a value of the wavenumber times the effective core radius, ka_e , for which long wave self-induction theory predicts an angular velocity about the core axis of zero. For this to occur, the wavenumber of the most unstable short wavelength is defined as $k=\kappa/a_e$ where $\kappa=1.44$. Crow(1970) demonstrates in his analysis that a vortex with a given core size and distribution of vorticity is kinetically equivalent to a vortex filament of the same circulation with constant vorticity and of a core size a_e . Since the vorticity distribution in the cores of the present study is not constant but closer to a continuous distribution (i.e. $\xi(r)=(r^2-a^2)^2$ where a is the core radius) then a_e is estimated as $0.7a$. Thus, in the present analysis the values for a and a_e are $0.044c$ and $0.0308c$ respectively. Using the theory of Widnall et al(1974), this gives a most unstable short wavelength of $0.134c$ which corresponds to a normalized frequency $fc/U_{ref}=7.44$.

Examining the autospectra, Figures 32 through 34, in the mid frequency range, $2 < f_c/U_{ref} < 20$, which should be dominated by wave motions, the autospectra of both V and W velocity fluctuations show peaks at f_c/U_{ref} of 5.0 and 8.0. The second peak could be an indication of Widnall instability taking into account the uncertainty in the estimate given above especially because of the uncertainty in the definition of core size. Previous experiments that examined the effects of short wave instability show that short waves effect the entire vortex flow field not only the core region. Thomas and Auerbach(1994) made flow visualizations of a counter-rotating vortex pair and observed wave instabilities acting upon one of the vortices and the entire flow field of that vortex appeared to move. Didden(1977) observed short wave instability on a vortex ring, and he found that the turbulence of the entire flow grows dramatically as a result of this instability. Thus, further evidence of the possibility of the presence of short wave instability is shown in the velocity autospectra at locations moving from the edge of the turbulent region of the wake out into the free-stream above the cores in Figure 36. These spectra show peaks around $f_c/U_{ref}=10$ for all three velocity components. Peaks are also seen at $f_c/U_{ref}=8.0$ of G_{vw} and $f_c/U_{ref}=7.0$ of G_{ww} which suggest that a short wave instability may be present.

The peak at $f_c/U_{ref}=5.0$ may be the result of the passage of large scale wake structures near the cores. Devenport et al(1995) have demonstrated in their results that, at frequencies above $f_c/U_{ref}=1$, velocity fluctuations in the core scale on parameters of the two-dimensional portion of the spiral wake. Thus, the velocity fluctuations in the isolated vortex core are presumably a result of the inactive motions of the core buffeted by the surrounding wake fluid. Figures 37 and 38 show that core center spectra at $x/c=10$ of the counter-rotating pair also scale on parameters of the flat portion of the spiral wake above $f_c/U_{ref}=1$. However, peaks at $f_c/U_{ref}=5$ also appear in the isolated vortex results at the core center at all streamwise locations suggesting that they might be a result of the effects of the model wing tip. The spectral scaling indicate that the cores

of the counter-rotating pair are laminar at $x/c=10$ for reasoning along the same lines as that of the isolated vortex analysis.

At higher frequencies, above $fc/U_{ref}=20$, in Figures 32 through 34, which shows the small scale turbulence energy contribution to the flow, spectral levels fall by as much as an order of magnitude as the core is approached from the spiral wake. Even in the region at the core edge where the mean tangential and axial rates of strain reach their maxima, spectral levels in this frequency range are substantially lower than in the spiral wake. Like the isolated vortex results, these suggest that the velocity field of the cores may not be generating any of its own turbulence further substantiating our conclusions from the spectral scaling. Notice that the spectra at the core center show no inertial subrange indicating that the turbulence energy cascade is severely disrupted here.

Filtered statistics have been included in this analysis to provide more detailed information about the different turbulence scales that comprise the flow field. The data were high-pass filtered at $fc/U_{ref}=3$ and 40 corresponding to length scales of $0.33c$ (7.3 core radii) and $0.025c$ (0.56 core radii) respectively given Taylor's hypothesis. Filtering at $fc/U_{ref}=3$ should eliminate the velocity fluctuations due to core wandering leaving intact the bulk of the turbulence wake structures and other core motions. Figure 39 shows that the axial normal stress field of the filtered data is similar to that of the unfiltered data suggesting that wandering does not have a large effect on the axial normal stresses coinciding with the wandering analysis above. Notice stress levels in the cores still rise to a maximum suggesting that the cores are being buffeted by the surrounding wake fluid and possibly waves are acting upon the cores. Filtering at $fc/U_{ref}=40$ should eliminate all effects except those due to the small scale turbulence. Figure 40 shows the absence of any small scale turbulence in the wake merger region between the cores which is expected because from the analysis it has been shown that stretching causes an increased rate of dissipation here. In the core regions, seen as depressions, the contours show constant levels of turbulence lower than the regions immediately surrounding them suggesting that the cores are laminar. The lobes on the

diagonals above and below the core regions could be a result of small scale turbulence created by the break down of larger scales of the wakes due to high strain rates. They appear at places of severe lateral curvature of the spiral wake turbulence. These lobes could also be the effects observed by Locke et al(1993) in a counter-rotating pair. They found that due to disturbances present during initial vortex sheet roll-up, a pair of vortices weaker than the primary vortices were formed which orbit the primary vortices. After roll-up was completed, these weak vortices were no longer distinct filaments but regions surrounding the cores.

Comparing the counter-rotating vortex pair results with those of the isolated vortex at $x/c=10$ should allow us to distinguish between the structure and effects of the separate vortices and their interaction. The turbulence structure of the vortex pair flow field is dominated by the spiral wakes winding about the cores which is also observed in the isolated vortex flow. At this point in flow development, the spiral wakes are still distinct structures similar to two isolated vortices. However, the presence of a second vortex of the pair flow allows the spiral wakes to interact and merge between the vortices altering their structure slightly from that of the isolated vortex. The vortex cores of the pair appear to be laminar as indicated by the spectral scaling, like the isolated vortex core.

3.2.2. Measurements at $x/c=30$

At $x/c=10$, the turbulence structure is similar to that of an isolated vortex with the structure outside the cores dominated by the spiral wakes and spectral scaling at the core centers suggesting laminar flow. The following analysis will show that a significant change in the turbulence structure occurs between $x/c=10$ and 30. The vortices appear to have passed through the plateau region in which the characteristics of the flow field and the overall structure remain constant. The results show that the vortices have begun

to decay as a result of the creation of turbulence and development of instabilities in the cores.

Figure 41 shows the entire flow structure in terms of axial normal stress \bar{u}^2/U_{ref}^2 . Figures 42 through 46 show the characteristics in and around the vortex cores in terms of mean cross-flow velocity vectors, contours of mean axial velocity U/U_{ref} , mean streamwise vorticity $\omega_x c/U_{ref}$, axial normal stress \bar{u}^2/U_{ref}^2 , and cross-flow normal stress sum $(\bar{v}^2 + \bar{w}^2)/U_{ref}^2$. The vortex cores have moved further apart with streamwise distance. At $x/c=30$, the separation distance between the vortex cores is $0.52c$ which is a 13.5 % increase from $x/c=10$. They have also drifted under their mutual induction to $z/c=-1.73$, Figure 41.

The mean rotational motion of the flow field is similar to that seen at $x/c=10$, Figure 42. However, a view of the entire flow field in terms of axial normal stress contours, Figure 41, shows that the wake turbulence structure surrounding the core regions has changed significantly. At $x/c=10$, turbulence normal stress results, Figure 19, revealed that distinct spiral wakes are wound about the core regions. The stress levels were heightened along the spiral wake centerline curving from the spiral wake tails into the region between the cores and then about the core regions. The lower stress levels in the regions directly above the cores gave clarity to this flow structure. At $x/c=30$, looking at the region of the wakes enclosing the cores, turbulence stress levels increase gradually from the outer edge of this region into the vortex cores. It appears that the organized turbulence structure of the spiral wakes at $x/c=10$ has become disorganized at $x/c=30$ revealing significantly more wake turbulence immediately surrounding the cores. These differences in wake structure are shown in the comparison of color contours of axial normal stress with streamwise distance for the counter-rotating pair in Figure 47. Presumably, the wake coherent structures are being distorted as they are continuously swept around the cores by the individual rotation of the vortex cores and this leads to large scale turbulence structure breakdown causing a change in the stress fields of the wakes. The local maximum in stress levels in the region between

the cores seen at $x/c=10$ has disappeared at $x/c=30$. In contrast, a comparison over the same streamwise distance of color contours of axial normal stress of the isolated vortex, Figure 9, show a significant decrease in stress levels of the spiral wake indicating a decay of turbulence stress with streamwise distance. Thus, the observed change in turbulence structure of the counter-rotating pair flow field appears to be a result of vortex interaction.

To obtain more information about the organization of the turbulence in the portions of the wake surrounding the cores and below them, turbulence normal stress profiles are plotted at locations along a curve spiraling about the right-hand core in Figures 48 through 50, similar to the spiral wake centerline at $x/c=10$. The coordinate directions and profile locations are highlighted in Figure 41. The profiles in the portions of the wake tails far from the vortex cores show characteristics of a two-dimensional turbulent wake similar to the results at $x/c=10$. The profiles of the three stress components in the remnants of the wake tails below the cores, location 1, show peak levels similar to those of the two-dimensional portion of the wakes. The profiles in the region between the cores, locations 2 and 3, show little humps with highly elevated levels in the middle of the region for \bar{u}^2 and \bar{v}_n^2 . The profiles at location 4, above the region between the cores, show peaks in \bar{u}^2 and \bar{v}_n^2 mainly because there is a slight depression in turbulence stress levels here. Profiles of \bar{v}_s^2 and \bar{v}_n^2 at locations 6, 7, and 8 in the portion of the wake curving to the outside of the right-hand core, show distinct peaks suggesting that some organization of wake turbulence exists in the portions surrounding the cores. This could be turbulence that has been recently swept into the region surrounding the cores from the tails as opposed to wake turbulence that has circulated about the core many times which distorts its coherent structures.

Autospectra of U , V_s , and V_n velocity fluctuations, normalized on U_{ref} and c , at the same locations as the profiles are plotted in Figure 51. Spectral levels are similar above $fc/U_{ref}=10$ at all locations in the portion of the wake surrounding the core for autospectra of U and V_n . Spectral levels for the two-dimensional portion of the wake

far from the cores and in the wake tail below the cores are lower than at other locations over the entire frequency range. These results indicate that a majority of the turbulence energy of the wakes is contained in the portion surrounding the cores. The small scale turbulence energy is the same following the wake curving about the core in contrast to the results at $x/c=10$ where lateral curvature and rates of strain had an effect on this energy.

Rates of strain on the curve about the right-hand core, defined the same as in the previous sections, are shown in Figure 52. Stretching accelerates along the dashed line in Figure 41, moving into the region between the cores and decelerates moving out of this region. Both stretching and skewing accelerate curving to the outside of the right-hand core. Then stretching diminishes and skewing levels off at locations 7 and 8. These strain rates have similar trends but are much higher than at $x/c=10$ which presumably affects the organization of the wake turbulence surrounding the cores. The normal stress profiles along the plane of symmetry in Figure 53 show strong anisotropy in the region between the vortex cores reinforcing the profiles of rates of strain here.

Moving our attention from the turbulence structure of the wakes to that of the core regions, the turbulence stress contours, Figures 45 and 46, show velocity fluctuations rising to a maximum at the core centers which presumably is mostly a result of vortex core wandering. Using the wandering theory of Devenport et al(1995), the upper bound for the rms amplitudes of core motions and their correlation coefficient in the flow field cross-plane, defined in the previous section, are found to be $\sigma_y=0.3357r_{1m}$, $\sigma_z=0.32r_{1m}$ and $e=0.5624$ respectively, where r_{1m} is the core radius obtained from the measured data. There is a 300% increase in wandering amplitude from $x/c=10$. The angle of the principle direction of wandering defined from the y axis to the negative z axis, is 47.43° indicating that the magnitude of core wandering motions is similar in both directions. According to the correction formulae of Devenport et al, the present measurements should overestimate the true core radius and underestimate the true peak tangential velocity by 14.6%. Comparing mean tangential and axial velocity profiles of

the measured data and this data corrected for wandering, Figure 31, they show a 12% decrease in core radius, a 14.5% increase in peak tangential velocity, and a 8.8% increase in axial velocity deficit with correction. The shaded regions in the turbulence normal stress contours show where vortex core wandering contributes more than 30% to these stresses. The regions for \bar{u}^2/U_{ref}^2 , Figure 45, cover the core regions and extend almost a radius beyond the core edges. For $(\bar{v}^2 + \bar{w}^2)/U_{ref}^2$, the regions extend further than at $x/c=10$ to 3 core radii beyond the core edge, Figure 46. These results show that a significant area of the flow field is affected by wandering and other means of analysis such as spectral and filtering are needed to reveal the details of the turbulence structure of the flow.

The mean flow characteristics of the vortex core regions have been obtained from the mean velocity profiles presented in Figure 31. Since there is a significant difference in the core parameters obtained from the data corrected for core wandering, both the uncorrected and the corrected parameters will be given. However, only the core parameters obtained from the corrected profiles given in Table 3 will be used for comparison with the results at $x/c=10$. The thick lines in the turbulence stress contours show that the core regions remain closely circular with core radii of 0.054c. The true core radius is about 0.0473c which is a 7% increase in core size from $x/c=10$. The profiles of peak tangential velocity, Figure 31, indicate that the core region is axisymmetric with a value of 29% U_{ref} at the core edge uncorrected and a corrected value of 33.7% U_{ref} which is a 16% decrease from $x/c=10$. The profiles of mean axial velocity through the right-hand core, Figure 31, show an uncorrected axial velocity deficit of 14.8% U_{ref} and a corrected value of 16.2% U_{ref} which appears symmetric about the core center and is a 8.9% increase from $x/c=10$. The Rossby number of the flow at $x/c=30$ is 0.482. The ratio of core circulation to root circulation is 0.183 here. The contours of streamwise vorticity calculated from the measured data in Figure 44 remain circular in the core regions and concentric with the core edges with streamwise distance. However, maximum levels in the cores have decreased by about 39% from

$x/c=10$. Taking into account that as a consequence of core wandering, peak tangential velocity values are underestimated by a greater amount at $x/c=30$ than at $x/c=10$, the difference in maximum streamwise vorticity is probably less than this estimate.

The turbulence structure of the core regions has changed from $x/c=10$ to 30 with high turbulence normal stress levels extending beyond these regions at the latter location, Figure 47. Velocity autospectra are plotted to obtain an understanding of the distribution of turbulence energy of the vortex pair, especially in the cores. Figures 54 through 56 show the autospectra of U , V , and \bar{W} velocity fluctuations normalized on U_{ref} and c for various spanwise locations moving from the wake into the core center, which are indicated by the dots in Figure 45. The locations are relative to the core center at $y/c=0.275$. The autospectra of U and V velocity fluctuations above $fc/U_{ref}=1$ at $y/c=0.214$ and 0.167 , resemble the two-dimensional portion of the wake far from the vortex cores, Figure 35, indicating that even at this late stage in flow development, the wake has retained its characteristics toward the outer edge of the region surrounding the cores. The spectra G_{ww} in the wake show a peak at $fc/U_{ref}=2.7$ which is close to the peak in the spectra of the two-dimensional portion of the wake at $fc/U_{ref}=2$. Moving from the wake into the core center, spectral levels rise by more than two orders of magnitude at frequencies below $fc/U_{ref}=1$, partially as a result of core wandering. In contrast to spectral results at $x/c=10$, the autospectra here show distinct peaks at $fc/U_{ref}=0.36$ for G_{ww} which is close to the frequency predicted by Crow's long wave instability theory. More evidence of wave motions on the cores appears in the contours of axial normal stress in Figure 45 where the core regions are set at about 45° from the plane of symmetry and the double peak distributions are present that would appear as a result of oscillations of a near axial velocity deficit along an axis coincident with a line joining the two peaks. Thus, there is strong evidence of the presence of Crow instability on the cores at $x/c=30$.

In the mid frequency range, $2 < fc/U_{ref} < 20$, Figures 54 through 56, there is a peak in the autospectra G_{uu} and G_{ww} at $fc/U_{ref}=4.5$ at the core center and edge. This is close to

the value of the peak seen at $x/c=10$ of unknown origin. Even though the peak seen at $x/c=10$ at $fc/U_{ref}=8.0$ does not appear at this location, the presence of Widnall instability should not be ruled out. The velocity autospectra at locations moving from the edge of the turbulent region into the free-stream, Figure 57, show peaks at $fc/U_{ref}=7$ and 10 in G_{vv} and G_{ww} , similar to the results at $x/c=10$. The first peak is close to the frequency of the most unstable short wavelength. It seems plausible that the change in turbulence structure of the flow is a result of the development of short wave instabilities on the cores. Widnall(1975) found that theoretically, the decay of, as well as the production of turbulence in vortex rings is a result of short wave instability and the same results can be expected for vortex pairs. As mentioned in the analysis at $x/c=10$, Didden(1977) experimentally observed the dramatic change in turbulence structure very similar to what is observed in the counter-rotating pair here of a vortex ring which he attributed to the development of short wave instability.

At high frequencies, above $fc/U_{ref}=20$, spectral levels at the core center fall below those at all other locations for all three velocity components, Figures 54 through 56. Spectral levels at the core edge and the portion of the wake immediately surrounding the core are as much as a magnitude higher than at the core center. However, this difference is not as great as that seen at $x/c=10$ indicating that higher small scale turbulence energy levels are present at $x/c=30$ in the region of the wake immediately surrounding the cores similar to the trends in turbulence stress levels shown in the contours of Figure 47. Figures 58 and 59 show that the autospectra at $x/c=30$ do not scale on the parameters of the two-dimensional portion of the wake far from the cores which suggests that the cores are generating turbulence because the velocity fluctuations here do not have the characteristic length and velocity scales of the wake. This is in direct contrast to the results at $x/c=10$ and of the isolated vortex. A comparison of velocity autospectra at the core center with streamwise distance, Figure 60, indicates that there is more large scale turbulence energy present at $x/c=30$ which is mostly due to wandering. However, the level of small scale turbulence energy is comparable at $x/c=10$.

and 30. This is in contrast to the isolated vortex results in which there was a shift to lower frequencies for the spectra above $fc/U_{ref}=1$ with streamwise distance, Figure 15. Thus, the change in turbulence structure of the counter-rotating pair is a result of vortex interaction.

Further evidence of the change in turbulence structure of the vortex pair can be supplied by analyzing filtered results. Figure 61 shows contours of axial normal stress filtered at $fc/U_{ref}=3$ which should remove the effects of wandering and Crow instability. The filtered structure is similar to the unfiltered results except that the double peaks in the cores have disappeared. Filtering at $fc/U_{ref}=40$, Figure 62, should reveal the small scale turbulence structure. Outside the core regions, the turbulence structure is similar to that seen at $x/c=10$. The two local maxima are present. The small scale turbulence levels immediately outside the cores are much higher at $x/c=30$ and penetrate much deeper into the core region. Turbulence stress levels in the cores are much greater than at $x/c=10$ suggesting that the cores are no longer laminar and decay is occurring.

The increase in core size and the decrease in peak tangential velocity shown in Figure 63 indicate a growth and decay of the vortex cores with streamwise distance. Vortex pair growth and decay are greater than that seen in the isolated vortex results, Figure 13. Thus, the increased rate of vortex decay is a result of vortex interaction. The apparent breakdown of wake turbulence organization about the core regions and the increase in turbulence immediately surrounding these regions appear to be a result of vortex pair interaction, which is especially evidenced in the color contours of turbulence axial normal stress of the isolated vortex and the counter-rotating vortex pair, Figures 9 and 47. The spectral scaling results indicate that the cores of the vortex pair at $x/c=30$ contain turbulence in contrast to the laminar core of the isolated vortex at this streamwise location.

In summary, the mean flow field structures at $x/c=10$ and 30 are similar. However, the turbulence structures of the counter-rotating vortex pair at these locations is very different. Through analysis, it is observed that the vortex cores appear to be

laminar and the turbulence of the flow field is dominated by the spiral wakes curving about the cores at $x/c=10$. At $x/c=30$, a more homogeneous turbulence structure is observed in the wakes and the cores contain turbulence indicating that a transition has occurred. The results show that Crow instability is present at this location. However, the presence of Widnall instability can not be confirmed by the results because the uncertainties involved in predicting and observing short wave instability make detection difficult. The characteristics of this flow indicate that the growth and decay of the vortex cores seen in the farfield wakes of aircraft may be a result of vortex pair interaction.

3.3. Co-rotating Vortex Pair

The characteristics of the mean flow and turbulence structure of a counter-rotating vortex pair were revealed in the previous section. The analysis in the following section will show that the flow field development of a co-rotating vortex pair is significantly different. The flow visualizations, Figure 5, presented earlier show that initially the vortices move apart. Further downstream, the separation distance between the vortices decreases as they rotate about their common center winding the wing wakes with them and merge into a single core approximately twice the size of each vortex core of the pair that created it by $x/c=22$.

3.3.1. Measurements at $x/c=10$

Figure 64 reveals the entire flow field structure at $x/c=10$ in terms of contours of axial normal stress \bar{u}^2/U_{ref}^2 . Figures 65 through 69 show the flow structure in and around the core regions in terms of mean cross-flow velocity vectors, contours of mean axial velocity U/U_{ref} , mean streamwise vorticity $\omega_x c/U_{ref}$, axial normal stress \bar{u}^2/U_{ref}^2 , and cross-flow normal stress sum ($\bar{v}^2 + \bar{w}^2$)/ U_{ref}^2 .

At $x/c=10$, the vortices have rotated 135° about the midpoint of the line joining the core centers as a result of mutual induction. Notice that the change in rotational direction of one vortex of a pair has a significant effect on the structure of the flow field, Figure 64. Remember the counter-rotating vortices drifted upward as a result of their mutual induction. The separation distance between the vortices at $x/c=10$ is $0.27c$ which is slightly greater than the wing tip separation of $0.25c$. The vortices are moving back toward each other after initially moving apart as shown in the flow visualizations in Figure 5(b).

The individual rotation of the vortices, as well as the rotation of the cores about the midpoint of the line joining their centers (their common center) contributes to the flow field structure shown in Figure 64. The mean rotational motion of the flow field is shown by mean cross-flow velocity vectors in Figure 65. This motion is significantly different than that of the counter-rotating vortex pair which produced a strong upwash of wake fluid between the cores, causing the wakes to be stretched and thinned as they were pulled upward. Here, the individual rotation of the vortex cores in the same direction causes the wakes to spiral about their respective cores from locations to the outside of the cores into the region between them. The turbulence axial normal stress contours, Figure 64, show that the wake structure is similar to that of the spiral wake at $x/c=10$ of the counter-rotating pair with heightened stress levels along the wake centerline denoted by the dashed line. This applies in the portions of the wakes above and below the region immediately surrounding the cores just after the wakes begin to curve as they converge on the cores, i.e. before location 5 in Figure 64. We will refer to these portions as the spiral wake tails. However, past this location, in the portion of the wakes curving about the cores, stress levels rise from the outer edge of the wakes to the core edges and the spiral wake structure is not present here. The orientation of the spiral wake tails is a result of the rotation of the cores about their common center. The winding of the wakes about the cores results in a large spiral flow field structure.

The wakes merge in the regions above and below the cores and along the plane of antisymmetry between the cores shown by the overlapping velocity vectors in Figure 65. This is a result of both the rotation of the cores about their common center and their individual rotation. To examine the effects of curvature on the wake turbulence structure and obtain some greater understanding of the change in the wake turbulence from the spiral wake tail into the region surrounding the cores, turbulence normal stress profiles in coordinates aligned with the spiral wake centerline in the spiral wake tail and the dashed line curving about the upper core are presented in Figures 70 through 72. The directions of the coordinate system and the profile locations are highlighted in Figure 64. Profiles in the spiral wake tail far from the cores, $y/c=2.5$, show that unlike \bar{u}^2 and \bar{v}_s^2 , values of \bar{v}_n^2 do not vary across the inner part of the spiral wake width, indicating that the spiral wake tail is closely two-dimensional here. The profiles show that peak stress values are elevated above those of the two-dimensional part of the spiral wake in the spiral wake tail, locations 1 and 2. These results suggest an intensification of coherent wake structures here. Peak values of \bar{u}^2 and \bar{v}_s^2 fall at locations 3 and 4. This appears to be a consequence of wake curvature. Peak values of \bar{u}^2 increase again attaining levels slightly below those in the two-dimensional portion of the spiral wake tail as the wake curves about the upper core. Peak values of \bar{v}_n^2 fall slightly from location 5 as the wake curves about the core. The peaks of the turbulence stress profiles become less distinct at locations 6 and 7 which shows the change in organization of turbulence in the portion of the wake curving about the core.

Velocity autospectra of U , V_s , and V_n velocity fluctuations normalized on U_{ref} and c at the profile locations are presented in Figure 73. At low frequencies, below $fc/U_{ref}=1$, the highest spectral levels occur at locations 1 and 2 in the spiral wake tail for autospectra of all three components. In the mid frequency range, $1 < fc/U_{ref} < 8$, spectral levels decrease moving from locations in the spiral wake tail and then curving about the upper core for autospectra of U and V_s . The peak in autospectra of V_s is the highest in the spiral wake tail, locations 1 and 2. In this frequency range, for autospectra of V_n , the

peak is the highest at locations 2 and 3 as the wake begins to curve and it is suppressed at locations 5, 6, and 7 curving about the core. At frequencies above $f_c/U_{ref}=10$, spectral levels increase moving from the spiral wake tail to the portion converging upon the upper core for autospectra of U and V_n . These spectral results indicate the intensification of large scale wake structures and increased dissipation of smaller scales in the spiral wake tails. It appears that large scale structures are breaking down into smaller scales presumably in part due to the curvature of the wake turbulence in the portion of the wake curving about the core, locations 5, 6, and 7.

The rates of strain that the wake turbulence experiences could also be a cause of the turbulence stress and spectral results presented above. Rates of stretching and skewing, defined as $\partial V_x/\partial s$ and $\partial V_y/\partial n$ normalized on the maximum mean velocity gradient in the two-dimensional portion of the spiral wake tail, on the dashed curve in Figure 64 are shown in Figure 74. Stretching accelerates from location 2 in the spiral wake tail along the curve converging upon the upper core. Skewing accelerates until location 3 and then decelerates as the wake begins to curve at locations 3 and 4. Finally, it accelerates greatly as the wake curves about the core. The decrease in large scale and increase in small scale wake turbulence energy as the wake curves about the upper core from the spiral wake tail appear to be a result of both wake curvature and the increasing rates of strain suffered by the wake turbulence.

In the region between the cores, along the plane of antisymmetry, the wakes come in contact and some wake fluid merger occurs at regions above and below the core regions where the vectors from the two velocity fields overlap, Figure 65. Turbulence normal stress profiles along the plane of antisymmetry between the cores are shown in Figure 75, where the center peak is associated with the wake turbulence immediately between the cores and the peaks to either side are associated with the turbulence in the spiral wake tails above and below the cores. The turbulence stresses are almost isotropic in the center peak suggesting that little straining of wake turbulence occurs

here. The anisotropy in the spiral wake tails presumably is a result of curvature the wakes suffer as they wind about the cores.

Changing our focus to the core regions, turbulence normal stress contours, Figures 68 and 69, show that levels rise to a maximum at the core centers which presumably is mostly a result of small amplitude core wandering. The wandering theory of Devenport et al(1995) was used to estimate the amplitudes of core motions and the mean velocity profiles corrected for the effects of this wandering. The measured data was rotated about the midpoint of the line joining the core centers into the system (y_1 , z_1) shown in Figure 66 so that this line was parallel to the y axis for these calculations. The values for the amplitudes and their correlation as defined in previous sections are $\sigma_{y_1}=0.2139r_{1m}$, $\sigma_{z_1}=0.2751r_{1m}$, and $e=-0.1963$. These values indicate that core wandering motions are larger in the z_1 direction. This may explain the shape of the core regions obtained from the values of peak tangential velocity which define the core edges from the measured data (with wandering). The dark lines of Figure 68 represent the core edges and show they are elliptical with major axes of $0.09c$ at a slight angle to the plane of antisymmetry and minor axes of $0.08c$. The estimated angle of the principle direction of wandering motion defined from the y_1 axis to positive z_1 axis is 108.8° which shows that the cores are wandering mostly in the z_1 direction.

The mean velocity profiles of both the measured data with wandering and this data corrected for the effects of wandering, Figure 76, show that the present measurements overestimate the core radius by 12% and they underestimate the peak tangential velocity by 3.3% and the axial velocity deficit by 5%. These results are along the lines of the correction formulae of Devenport et al(1995) which predict that as a result of wandering the measurements should overestimate the core radius and underestimate the peak tangential velocity by 7.9%. The shaded regions presented in the contours of turbulence normal stress, Figures 68 and 69, indicate regions where wandering contributes more than 30% to the normal stresses. For \bar{u}^2/U_{ref}^2 , Figure 68, the regions cover the core regions. For $(\bar{v}^2 + \bar{w}^2)/U_{ref}^2$, Figure 69, the regions extend

about one core radius beyond the core edges. These estimates show that a majority of the turbulence structure outside the core regions is unaffected by vortex wandering. In the core regions, other means such as spectral analysis and filtering can be used to obtain their turbulence structure.

The mean flow vortex core parameters were obtained from both the uncorrected and the corrected mean velocity profiles for comparison. The corrected core parameters are given in Table 3. As mentioned above, the core regions obtained from the uncorrected data show that they are elliptical which could be a result of wandering. However, the inviscid computations of Rossow(1971) and the viscous computations of Melander et al(1988) show the merging process of two co-rotating vortices where each core deformed into an elliptical shape as a result of the individual rotation of the vortices. The shape of the cores could also be a result of the fact that the cores lie at an angle of about 3° to the free-stream and the cross-plane in which the data was measured. The measured core radii are about $0.0417c$ and the corrected (true) core radii are $0.0366c$. The measured axial velocity deficit is $12.1\% U_{ref}$ and the corrected value is $12.8\% U_{ref}$. The axial velocity is symmetric about the core center. The measured peak tangential velocity is $15.9\% U_{ref}$ and the corrected value is $16.4\% U_{ref}$. The Rossby number, defined in the previous sections, for this flow is 0.776. The ratio of core circulation to root circulation is 0.144. Contours of streamwise vorticity in Figure 67 are relatively circular in the core regions. However, they are distorted away from the cores showing the effects of strong rotation on the flow structure with contours contracting in the regions immediately surrounding the cores and expanding out into the spiral wake tails. These contours are in contrast to the counter-rotating pair, where they were concentric with the circular core edges at this streamwise location.

With reference to the wandering analysis above, velocity autospectra are presented to give more insight into the turbulence energy of the co-rotating pair, especially in the core regions. Figures 77 through 79 show autospectra of U , V , and W velocity fluctuations normalized on U_{ref} and c for various spanwise locations, y_1/c , in the

rotated coordinate system moving from the wake into the core center of the upper core. These locations are indicated by the dots in Figure 68 and are relative to the core center at $y_1/c=0.129$. The results show that the spectra at $y_1/c=0.27$ and 0.15 resemble the two-dimensional portion of the wakes, Figure 80, for all three components with the peak in G_{ww} not as strong as in the two-dimensional portion of the wake. This is surprising because of the strong distorting effects of the vortices. At low frequencies, below $fc/U_{ref}=2$, spectral levels rise moving from the wake into the core region for all three components, mostly as a result of vortex wandering. Notice that spectral levels in the core region are significantly higher than those of the wake for all three components. At higher frequencies, above $fc/U_{ref}=20$, the core center spectra levels fall slightly below those in the portion of the wake immediately surrounding the core region, $y_1/c=0.09$, in G_{uu} and G_{ww} , and spectral levels at the core edge match those at the core center. Spectral levels at the location in the wake furthest from the core in this frequency range are about an order of magnitude smaller than at the core center for all three components. For G_{ww} , spectral levels at the core center are slightly higher than at the core edge which match those at $y_1/c=0.09$ and 0.15 in the wake. These results suggest that the cores may be producing their own turbulence, since levels in the core region are not much lower than in the wake. It appears that the amount of small scale turbulence energy in the wake increases significantly as the core is approached which presumably is an effect of the higher rates of strain closer to the cores. Figures 81 and 82 show that the core center spectra at $x/c=10$ scale on parameters of the two-dimensional portion of the spiral wake tail which suggests that the cores are not generating their own turbulence. However, the cores do not appear to be laminar as evidenced by the spectral levels at the core center which are high in comparison to the results of the counter-rotating pair at $x/c=10$ and the isolated vortex where they fell below levels in the surrounding wake.

The data was high-pass filtered to continue the analysis of the turbulence structure of the core regions. Figure 83 shows data filtered at $fc/U_{ref}=3$ to remove the effects of wandering and leave a majority of the stresses due to coherent wake structures

and other core motions. The filtered results are similar to the unfiltered results with low stress levels in the spiral wake tails and levels rising to a maximum at the core centers. The higher levels in the core regions are presumably partially a result of buffeting of the cores by the surrounding wakes because of the spectral scaling results. Figure 84 shows data filtered at $fc/U_{ref}=40$ which should eliminate all effects except those of the small scale turbulence. The contours of \bar{u}^2/U_{ref}^2 do not show distinct core regions only slight depressions with lobes of higher stress levels outside them. There is an elongated region of maximum stress between the cores which coincides with observations made from the results in the wake above which suggest that large scale wake structures are breaking down creating smaller scales due to the rates of strain they suffer as they approach the core regions from the spiral wake tail. Thus, the wake fluid that is swept into the region between the cores consists of much small scale turbulence. The slant of the elongated region coincides with the direction of rotation of the vortices about their common center. Notice that the lobes appear at locations where the wake turbulence curvature is the most severe. Since similar lobes appear in the counter-rotating pair filtered results, they could be a result of the theory developed by Locke et al(1993) described in section 3.2.1. It is interesting to note that small scale turbulence dominates in the region between the cores at this location for the co-rotating pair, while large scale turbulence dominates in this region for the counter-rotating pair.

Comparing the results of the co-rotating pair with the isolated vortex results of Devenport et al(1995) at $x/c=10$, the turbulence stress contours show that the stress field of the pair resembles that of the isolated vortex with spiral wake tails. However, the spiral wake structure of the wakes disappears as the wakes curve about their respective cores which is a result of vortex interaction. The streamwise vorticity contours of the pair are significantly different than those of the isolated vortex showing the effects of two different rotations with the rotation of the cores about their common center a result of vortex interaction. The spectral results of the vortex pair show that the core regions have small scale turbulence energy comparable to the wakes immediately

surrounding them unlike the isolated vortex results where spectral levels of the core center fell far below those of the wake. The core center spectra of both cases scale on parameters of the two-dimensional portion of the wakes. However, unlike the isolated vortex core, the cores of the co-rotating pair at $x/c=10$ do not appear to be laminar.

3.3.2. Measurements at $x/c=15$

At $x/c=10$, the analysis revealed that the turbulence structure of the pair is dominated by the structure of the core regions and the portions of the wakes immediately surrounding them. The spectral analysis and filtered results indicate that the cores contain some turbulence. The following section will show that at $x/c=15$, the vortices have rotated further about their common center and the origin of the velocity fluctuations in the cores has changed.

Figure 85 shows the entire flow structure at $x/c=15$ in terms of turbulence axial normal stress \bar{u}^2/U_{ref}^2 . Figures 86 through 90 show the structure in and around the cores in terms of mean cross-flow velocity vectors, mean axial velocity U/U_{ref} , mean streamwise vorticity $\omega_x c/U_{ref}$, axial normal stress \bar{u}^2/U_{ref}^2 , and cross-flow normal stress sum ($\bar{v}^2 + \bar{w}^2)/U_{ref}^2$. At $x/c=15$, the vortex cores have rotated about their common center through 252° and the separation distance between the cores has decreased by 27% to $0.2c$.

The vortices spiral toward each other due to their mutual induction. The mean cross-flow velocity vectors, Figure 86, show by their variable length that the rotational velocity of the flow fields away from the cores has increased in magnitude indicating that the rotation rate of the vortex cores about their common center has increased from $x/c=10$. A view of the entire flow field structure, Figure 85, shows that the wake turbulence structure is similar to that at $x/c=10$ with spiral wake tails above and below the cores and levels rising from the outer edges of the wakes to the core edges in the portions of the wakes immediately surrounding the cores. Turbulence normal stress

levels have decreased in the spiral wake tails and increased in the portions of the wakes immediately surrounding the cores from $x/c=10$. However, this increase in stress could be a result of increased core wandering which will be investigated below. The wakes spiral further about the cores at $x/c=15$ and the increase in curvature of the wake turbulence in the spiral wake tails from $x/c=10$ could be the cause of the decrease in turbulence stress here.

To investigate the effects of curvature and rates of strain on the structure of the wakes, profiles of turbulence normal stress in coordinates aligned with the spiral wake centerline and the dashed line in the portion of the wake immediately surrounding the lower core are presented in Figures 91 through 93. The coordinate system directions and profile locations are highlighted in Figure 85 where the dashed line denotes the spiral wake centerline in the spiral wake tail. Profiles of the stresses in the portion of the spiral wake tail far from the cores, $y/c=2.5$, show that this part is similar to a two-dimensional turbulent wake for the same reasoning presented in previous sections. Peak stress values are elevated above those of the two-dimensional portion of the spiral wake tail at location 1 and they fall as the spiral wake tail curves below the cores, location 5, for all three components where they are lower than the two-dimensional portion of the wake for \bar{u}^2 and \bar{v}_s^2 . Peak values increase past this location as the wake curves about the lower core attaining levels above the two-dimensional portion of the wake at location 8 for the three components. These results show a decrease in turbulence stress with increase in curvature of the wake, especially at locations 4, 5, and 6. The peaks are less distinct at location 8 where the spiral wake tail structure no longer appears, Figure 85.

Velocity autospectra of U , V_s , and V_n velocity fluctuations normalized on U_{ref} and c at the locations of the profiles are presented in Figure 94 to continue the analysis of the wake turbulence. At low frequencies, below $fc/U_{ref}=1$, spectral levels are the lowest at locations 4, 5, and 6 where the spiral wake tail curves below the cores for all three velocity components. In the mid frequency range, $1 < fc/U_{ref} < 10$, the peak in

autospectra of V_s is the highest in the beginning of the spiral wake tail, locations 1 and 2, and in the portion of the wake curving about the lower core, locations 7 and 8 and the lowest at locations 3, 4, and 5 in the spiral wake tail. For autospectra of V_n fluctuations in this frequency range, the peak is the highest at locations 1, 2, and 8. However, it is suppressed at all other locations. At higher frequencies, above $fc/U_{ref}=10$, spectral levels at 3, 4, 5, and 6 are lower than locations curving about the core for the three components where levels increase along the curve. The spectral levels in the spiral wake at locations 1 and 2 are similar to those at location 6 in the portion of the wake curving below the cores. These results suggest that wake turbulence structures are broken down and there is also an increase in dissipation of smaller scales in the portion of the spiral wake tail curving below the cores, locations 4 through 6 in part due to the increase in curvature of the wake turbulence here.

The turbulence stress and spectral results may also be a result of the rates of strain suffered by the wake turbulence. Rates of stretching and skewing on the dashed line in Figure 85 defined the same as in previous sections are shown in Figure 95. Stretching and skewing decelerate moving from locations 1 to 3 in the spiral wake tail. They remain low between locations 3 and 5. However from locations 5 to 7 both stretching and skewing accelerate. Thus, the decrease in turbulence stress and the low spectral levels in the spiral wake tail curving below the cores and converging upon the lower core, locations 4 through 7, show the effects of curvature and rates of strain on the wake turbulence.

In the region between the cores, an increase in straining of the wake fluid should occur because the size of the region has decreased. Thus, turbulence stress levels in this region should increase from $x/c=10$. The profiles of turbulence normal stress along the plane of antisymmetry, Figure 96, show that at the center peak which is located in the region between the cores, maximum values of \bar{v}^2 and \bar{w}^2 have increased from $x/c=10$. The peaks to either side of the center which show turbulence stress levels in the spiral wake tails above and below the cores have decreased significantly from $x/c=10$ which is

a result of increased wake turbulence curvature and rates of strain here. The increase in turbulence stress in the region between the cores could be partially a result of vortex core wandering.

The normal stress contours, Figures 89 and 90, show turbulence fluctuations rising to a maximum at the core centers which is assumed to be mostly an effect of small amplitude core wandering. Using the method developed by Devenport et al(1995), the rms amplitudes of core motions and their correlation in the flow cross-plane are estimated to be $\sigma_{y1}=0.2228r_{1m}$, $\sigma_{z1}=0.3595r_{1m}$, and $e=-0.4093$. These estimates were made using data profiles rotated into the coordinate system (y_1, z_1) shown in Figure 87. Similar to the results at $x/c=10$, the core motions are larger in the z_1 direction. The angle of the principle direction of core wandering defined from the y_1 axis to the positive z_1 axis is 109.7° which is close to that at $x/c=10$. This could explain the shape of the core regions obtained from the loci of peak tangential velocity of the measured (wandered) data. The dark lines in Figure 89 represent the core edges which are elliptical with major axes of $0.1c$ at a slight angle to the plane of antisymmetry and minor axes of $0.09c$. The core wandering is greater at $x/c=15$ than at $x/c=10$. However, because the amplitudes and their correlation are large, the wandering estimates are more uncertain at $x/c=15$.

Mean velocity profiles of the measured data and this data corrected for the effects of wandering are shown in Figure 76. They indicate that the measured data overestimates the core radius by 30% and underestimates the peak tangential velocity by 3.5% and the axial velocity deficit by 7.7%. The shaded regions in Figures 89 and 90 indicate regions where wandering contributes more than 30% to the turbulence normal stresses. For \bar{u}^2/U_{ref}^2 , the regions cover the cores and extend about one core radius beyond the core edges. For $(\bar{v}^2 + \bar{w}^2)/U_{ref}^2$, the regions extend about three core radii past the core edges. These results indicate that much more of the flow field is affected by core wandering at $x/c=15$ than at $x/c=10$ and that other means such as spectral

analysis and filtering must be used to reveal the turbulence structure of the flow, especially in the core regions.

The vortex core parameters have been obtained from the mean velocity profiles of the measured data and this data corrected for wandering. Both will be presented here and the corrected core parameters are given in Table 3. The measured core radii are about $0.0475c$ and the corrected value is $0.0333c$ which suggests that the core regions have decreased in size by 11%. The measured peak tangential velocity is 15.25% U_{ref} and the corrected value is 15.78% U_{ref} which is only a 3.9% decrease from $x/c=10$. The measured axial velocity deficit is 11.6% U_{ref} and the corrected value is 12.6% U_{ref} which is similar to the value at $x/c=10$. The Rossby number, defined in previous sections, is 0.797 for this location. The ratio of core circulation to root circulation is 0.126. The contours of streamwise vorticity show that the rotation of the vortex cores about their common center has a strong effect on this field as evidenced by the distortion of the contours. Maximum levels at the core centers have decreased by 25% from $x/c=10$ which indicates that vorticity is being diffused at $x/c=15$.

Focusing on the turbulence structure of the core regions, the velocity autospectra of U, V, and W velocity fluctuations are presented, Figures 97 through 99, at various locations along the rotated axis y_1 in Figure 87 moving from the wake into the lower core center. These locations, indicated by the dots in Figure 89 are referenced from the core center at $y_1/c=0.0847$. The spectra at $y_1/c=0.61$ give the characteristics of the flow in the spiral wake tail. The spectra at $y_1/c=0.21$ and 0.11 give the characteristics of the flow in the portion of the wake immediately surrounding the vortex cores. The spectra at $y_1/c=0.61$ resemble the two-dimensional portions of the wakes, Figure 80, including the peak at $fc/U_{ref}=2.6$ in G_{ww} which presumably is associated with the passage of large scale structures. These results indicate that despite the curvature that the wakes suffer they retain their characteristics. In the low frequency range, below $fc/U_{ref}=2$, spectral levels at $y_1/c=0.61$ are higher than at $y_1/c=0.21$ and lower than $y_1/c=0.11$, which is expected because $y_1/c=0.61$ is at the spiral wake centerline(i.e. location of peak axial

normal stress) and $y_1/c=0.21$ is at the outer edge of the portion of the wake near the core. However, at higher frequencies, above $fc/U_{ref}=20$ spectral levels at $y_1/c=0.6$ fall slightly below those at $y_1/c=0.21$ for autospectra of U and W velocity fluctuations.

The autospectra of all three components at the core center, core edge, and in the portion of the wake immediately surrounding the core regions attain levels above locations in the outer portions of the wake over the entire frequency range. At low frequencies, below $fc/U_{ref}=1$, this is mostly a result of core wandering. At higher frequencies, spectral levels at the core center remain the same from $x/c=10$ to 15 and spectral levels in the core region are about an order of magnitude higher than in the spiral wake in all three directions at $x/c=15$. These results show that small scale turbulence energy in the core regions has not changed from $x/c=10$. However, these energy levels fall more quickly moving from the core to the spiral wake tail here then at $x/c=10$. These results indicate the presence of turbulence in the core regions, especially the difference in levels between the core region and the wake. The velocity autospectra at the core center are scaled on parameters of the two-dimensional portion of the wakes to obtain the origin of these turbulence levels. Figures 100 and 101 show that the core center spectra do not scale on two-dimensional wake parameters, in contrast to the results at $x/c=10$, suggesting that the cores are generating turbulence.

The data has been high-pass filtered to obtain more information about the turbulence structure of the flow, especially in the core regions which is necessary at this streamwise location according to the wandering analysis above. Figure 102 shows contours of $\overline{u^2}/U_{ref}^2$ filtered at $fc/U_{ref}=3$ which should remove the low frequency velocity fluctuations due to core wandering. The filtered flow structure is similar to that of the unfiltered data indicating at least that core wandering does not have an overwhelming effect on the turbulence axial normal stresses. Figure 103 shows contours of $\overline{u^2}/U_{ref}^2$ filtered at $fc/U_{ref}=40$ to eliminate the effects of all except the small scale turbulence structures. The filtered flow structure is similar to the filtered results at $x/c=10$ with the elongated region of maximum stress between the cores and lobes outside the core

regions. Notice again there is little small scale turbulence present in the spiral wake tails. The region between the cores has increased in intensity from $x/c=10$. These results coincide with the spectral results presented above which indicated that the small scale turbulence energy of the flow has not changed from $x/c=10$ to 15. However, at this streamwise location, the spectra do not scale on wake parameters indicating that the velocity fluctuations in the core regions are a result of turbulence generated by the cores.

Comparing the results of the co-rotating pair with those of the isolated vortex at $x/c=15$ from Devenport et al(1995), the spiral wake structures are similar for the two flows. Turbulence stresses have decreased with streamwise distance in the spiral wake tails for both flows. The core center autospectra do not scale on parameters of the two-dimensional wake for the vortex pair in contrast to the isolated vortex results where the core is laminar at $x/c=15$. The generation of turbulence in the cores of the co-rotating pair at $x/c=15$ appears to be a result of vortex interaction.

3.3.3. Measurements at $x/c=22$

At $x/c=15$, the spectral and filtered results revealed a small scale turbulence structure similar to that at $x/c=10$. However, the origin of the turbulence in the core regions had changed. The following section will present the mean flow and turbulence structure at $x/c=22$, most significantly a single core created from the merger of the two vortex cores seen at $x/c=15$. The results will show that the process of merger is accompanied by an increase in turbulence and a diffusion of vorticity.

Figure 104 shows the entire flow structure at $x/c=22$ in terms of contours of axial normal stress \bar{u}^2/U_{ref}^2 . Figures 105 through 109 show the flow structure in and around the core in terms of mean cross-flow velocity vectors, contours of mean axial velocity U/U_{ref} , mean streamwise vorticity $\omega_x c/U_{ref}$, axial normal stress \bar{u}^2/U_{ref}^2 , and cross-flow normal stress sum ($\bar{v}^2 + \bar{w}^2$)/ U_{ref}^2 . At $x/c=22$, a single core has formed from

the two separate vortex cores seen at $x/c=15$. A significant change in the flow field structure has occurred.

The mean cross-flow velocity vectors in Figure 105 reveal a rotational flow that has a single center, however, it is not symmetric at this stage of merger. A view of the entire flow structure, Figure 104, shows that the wakes form a large spiral structure enclosing the single core as they are wound about it. The portions of the wakes above and below the cores are similar in structure to the spiral wakes at $x/c=15$ with heightened stress levels along the wake centerline until location 5, denoted by the dashed line in Figure 104. These portions will be referred to as the spiral wake tails. As the wake curves about the core, past this location, turbulence stress levels increase from the outer edge of this region to the core edge denoted by the dark line, Figure 104. Turbulence stress levels in the spiral wake tails have decreased from $x/c=15$ to 22. Levels have also decreased in the portions of the wakes immediately surrounding the core and in the core region from $x/c=15$. However, this may be a result of a decrease in core wandering which will be investigated below.

The effects of curvature and rates of strain on the wake turbulence of this new flow field structure with a single core are investigated through profiles of turbulence normal stress in coordinates aligned with the wake centerline in the spiral wake tail and along the dashed line in the portion of the wake converging upon the core, Figures 110 through 112. The coordinates and profile locations are highlighted in Figure 104. The profiles in the portion of the spiral wake tail far from the core, $y/c=2.5$, show that this region is closely two-dimensional. The profiles show that peak stress values are elevated above those of the two-dimensional portion of the wake at location 1 in the spiral wake tail and they fall following along the spiral wake tail to location 5 for all three components. Peak values increase at locations 7 and 8 in the portion of the wake curving above the core. The profiles at locations 7 and 8 show distinct peaks indicating that the wake turbulence has some organization here where the spiral wake structure is

no longer present. These results show a decrease in turbulence stress with increase in curvature. However, the effects of curvature are not as large as at $x/c=15$.

Velocity autospectra of U , V_s , and V_n velocity fluctuations normalized on U_{ref} and c are presented in Figure 113 to examine the levels of turbulence energy in the wake. At low frequencies, below $fc/U_{ref}=1$, spectral levels at location 6 fall below those at all other locations for autospectra of U and V_s fluctuations. In the mid frequency range, $1 < fc/U_{ref} < 10$, the peak in autospectra of V_s is the highest for locations 1 through 4 in the spiral wake tail and it is totally suppressed at location 6. The peak in autospectra of V_n is the highest for locations 1 and 2 and the same at all other locations in this frequency range. At higher frequencies, above $fc/U_{ref}=10$, levels increase slightly from location 4 to location 8 in the wake for autospectra of all three velocity components. These results show a decrease in large scale turbulence energy and an increase in small scale turbulence energy with increase in wake turbulence curvature suggesting breakdown of large scale wake structures into smaller scales. The turbulence stress and spectral results could also be the result of rates of stretching and skewing of the wake turbulence. Figure 114 shows that stretching and skewing, which are defined in previous sections, accelerate slightly from location 1 to location 4 along the spiral wake tail. From locations 4 to 5 both rates decelerate as the wake begins to curve directly upward. From locations 5 to 6 both rates accelerate. Stretching and skewing only change slightly past this location. The increased rates of stretching and skewing along with curvature of the wake turbulence cause the results seen at location 6.

Moving our attention from the wakes to the core regions, the normal stress contours show turbulence fluctuations rising to a maximum at the core centers. This is assumed to be mostly an effect of small amplitude wandering. Using the method developed by Devenport et al(1995), the rms amplitudes of core motions and their correlation in the flow cross-plane are estimated to be $\sigma_y=0.06775r_{1m}$, $\sigma_z=0.08232r_{1m}$, and $e=0.1816$. These estimates indicate that wandering is about the same in both directions and relatively small, especially in comparison to the results at $x/c=15$, which is

assumed to be a direct result of vortex core merger. The wandering theory of Devenport et al(1995) makes the assumption that the core is axisymmetric. However, the core edge obtained from the measured data defined as the locus of peak tangential velocity shows a nonaxisymmetric structure, Figure 108. This is partially a result of the fact that the core lies at an angle to the free-stream. Mean velocity profiles of the measured data and this data corrected for the effects of wandering are presented in Figure 76. The profiles indicate that the measured data overestimates the core radius and underestimates the peak tangential velocity and axial velocity deficit by less than 1.5%. The analysis also shows that the entire flow field is free of wandering that contributes more than 30% to the turbulence normal stresses. Note the data was low-pass filtered to remove the large amount of fluctuations due to turbulence to obtain the wandering estimates at $x/c=22$ and 30 of the co-rotating pair.

The vortex core parameters that will be covered here are taken from the mean velocity profiles corrected for the effects of wandering to be consistent with the values presented at the previous streamwise locations. The core radius is $0.099c$ which is a 66% increase in core size from each of the cores at $x/c=15$. This suggests that the core region not only contains turbulence from the two vortex cores, it has also engulfed wake turbulence from the region between the cores seen at $x/c=15$. The peak tangential velocity is 13.4% U_{ref} which is a 14.8% decrease from $x/c=15$. The axial velocity deficit at $x/c=22$ is 7.7% U_{ref} which is a 38.6% decrease from $x/c=15$. The Rossby number at this location is 0.575. The ratio of core circulation to root circulation is 0.32. The contours of mean streamwise vorticity, Figure 107, show the effects of strong rotation on core merger. They are elliptical in the core region and resemble the core edge away from the core region. Maximum levels of vorticity in the core region have decreased by 50% from $x/c=15$. However, the cores at $x/c=15$ were heavily wandered so this difference is presumably larger when the measured data is correct for the effects of wandering.

The characteristics of the turbulence structure at $x/c=22$ reveal significant information about the merger process. The normal stress contours show that levels at the core center have decreased by 53% in \bar{u}^2 and 80% in $(\bar{v}^2 + \bar{w}^2)$ from $x/c=15$ to 22. However, the cores are heavily wandered at $x/c=15$ and this wandering contributes to the normal stress levels in the core regions here. Thus, the change in turbulence stress levels due to merger are not as significant. However, the large increase in core size and the decrease in peak tangential velocity from $x/c=15$ to 22 indicate vortex core decay. The isolated vortex results of Devenport et al(1995) do not show as significant an increase in core size or decrease in peak tangential velocity between $x/c=10$ and 20.

Velocity autospectra have been plotted to learn about the turbulence energy associated with the process of vortex core merger. Figures 115 through 117 show the autospectra of U, V, and W velocity fluctuations at various spanwise locations moving from the wake into the core center normalized on U_{ref} and c . The spectra at $y/c=0.55$, 0.37, and 0.21 are located in the wake outside the core region. Over the entire frequency range, spectral levels in the wake increase as the core is approached for autospectra of all three velocity components. The autospectra of U and V fluctuations in the wake surrounding the core resemble those of the two-dimensional portion of the wake, Figure 80, indicating that the wakes have retained their character despite the distorting effects of the core. The core center spectra of the three velocity components have the highest levels over the entire frequency range with levels at the core edge falling slightly below those at the core center. Spectral levels at the core center are a magnitude greater than in the portion of the wake just outside the core edge $y/c=0.21$. The core center spectral levels are higher than at $x/c=15$ indicating an increase in small scale turbulence energy here. These results suggest that turbulence is being produced in the cores as a result of the merger process because the high core center spectral levels are not observed in the isolated vortex results. Figures 118 and 119 show velocity autospectra at the core center scaled on parameters in the two-dimensional portion of the wakes far from the core. They reveal that the core center spectra at $x/c=22$ do not

scale on two-dimensional wake parameters indicating that the turbulence velocity fluctuations in the core are not controlled by the wakes. The spectral results are evidence that merger increases the turbulence energy of the flow and appears to be a mechanism of vortex decay. Here a single highly turbulent core is created.

The data was high-pass filtered to observe the distribution of turbulence scales at this stage of vortex core merger. Figure 120 shows contours of \bar{u}^2/U_{ref}^2 filtered at $fc/U_{ref}=3$ to remove the effects of core wandering which according to the analysis above should be very small. The filtered flow structure is similar to the unfiltered structure indicating that wandering does not have an overwhelming effect on the axial normal stress. Notice a majority of the turbulence is contained in the core region and the portion of the wakes immediately surrounding the core. Figure 121 shows contours of \bar{u}^2/U_{ref}^2 filtered at $fc/U_{ref}=40$ which should eliminate the effects of the large scale turbulence. The contours show that a significant amount of small scale turbulence is present in the core region as well as immediately surrounding it. However, there does not appear to be any significant amount of small scale turbulence in the spiral wake tails which coincides with the spectra results where turbulence energy decreases moving away from the core region due to their natural decay. These filtered results indicate that turbulence is produced by the core. It appears that the elongated region of maximum stress between the cores seen in filtered results at $x/c=15$ has been engulfed by the core.

Comparing the results of the co-rotating vortex pair with the isolated vortex results of Devenport et al(1995) to distinguish the effects of core merger, the turbulence stress in the spiral wake tails has decreased with streamwise distance for the two flows. The turbulence stress in the portion of the wakes immediately surrounding the core have also decreased with streamwise distance for the pair. However, this is presumably more a result of the great amount of wandering estimated at $x/c=15$. The major difference between the two flows is that the core center spectra of the pair show there is significant small scale turbulence energy present and these spectra do not scale on parameters of the two-dimensional wake indicating that the core is not laminar unlike the isolated vortex at

$x/c=20$. It appears that merger, i.e. vortex interaction results in the generation of turbulence in the core. The core also shows signs of decay, i.e. increase in core size and decrease in peak tangential velocity, greater than those seen in the isolated vortex results.

3.3.4. Measurements at $x/c=30$

The characteristics of the turbulence structure at vortex merger were revealed through the analysis at $x/c=22$. It was shown that merger causes an increase in turbulence energy in the core region and an increased rate of vortex core decay. The analysis in the present section will show that another significant change in turbulence structure occurs at $x/c=30$ as merger comes to completion.

Figure 122 shows the entire flow structure at $x/c=30$ in terms of contours of axial normal stress \bar{u}^2/U_{ref}^2 . Figures 123 through 127 show the structure in and around the core region in terms of mean cross-flow velocity vectors, contours of mean axial velocity U/U_{ref} , mean streamwise vorticity $\omega_x c/U_{ref}$, axial normal stress \bar{u}^2/U_{ref}^2 , and cross-flow normal stress sum $(\bar{v}^2 + \bar{w}^2)/U_{ref}^2$.

The mean rotational field shown through velocity vectors in Figure 123 reveals that the mean flow is symmetric and resembles an isolated vortex. A view of the entire flow field, Figure 122, shows that the wakes have formed a relatively circular region about the vortex core. The size of this region has increased from $x/c=22$ as a result of the rotation of the wakes further about the core. The wake structure is similar to that seen at $x/c=22$. However, the spiral wake tails reach further around the core region, from locations 1 to 4 in Figure 122. Past this location, stress levels increase from the outer edge of the region of the wakes surrounding the core to the core edge. Turbulence stress levels in both portions of the wakes described here have decreased from $x/c=22$. Axial normal stress levels in the core region have decreased by about 30% from $x/c=22$.

Examining the structure of the wakes at this stage of vortex merger, profiles of turbulence normal stresses in coordinates aligned with the spiral wake centerline in the spiral wake tail and the dashed line curving above the core, Figure 122, are presented in Figures 128 through 130. The coordinate directions and stress profile locations are highlighted in Figure 122. The profiles in the portion of the spiral wake tail far from the core, $y/c=2.5$, show that the wake here is closely two-dimensional. The stress profiles show trends similar to those seen at $x/c=22$, however, peak stress values fall and never increase again following the spiral wake tail and converging upon the core. The peaks at locations 5, 6, 7, and 8 are not distinct indicating that the wake turbulence structure does not have specific organization like the spiral wake tails. The results indicate that peak turbulence stress levels decrease with increase in wake turbulence curvature.

Velocity autospectra of U , V_s , and V_n velocity fluctuations normalized on U_{ref} and c at locations along the dashed line in Figure 122 are presented in Figure 131. At low frequencies, below $fc/U_{ref}=1$, spectral levels decrease from the spiral wake tail into the portion of the wakes surrounding the core for all three velocity components. In the mid frequency range, $1 < fc/U_{ref} < 10$, the peaks in autospectra of V_s and V_n and levels of autospectra of U are the highest at locations 1 and 2 in the spiral wake tail and they are similar at all other locations. At higher frequencies, above $fc/U_{ref}=10$, spectral levels increase from the spiral wake into the portion of the wake surrounding the core for autospectra of U and V_n and they are similar at all locations for autospectra of V_s . These results indicate that decrease in large scale turbulence energy and increase in small scale turbulence energy is a result of an increase in wake curvature which suggests a breakdown of large scale wake structures into smaller scales. Rates of wake turbulence stretching and skewing are shown in Figure 132. Stretching is accelerated and skewing is decelerated from locations 2 to 3. Skewing and stretching decelerate from locations 3 to 4 and accelerate from locations 4 to 6 and then decelerate again from locations 6 to 8. The rates of strain and wake turbulence curvature are much less severe than at $x/c=22$.

Examining the core regions, the normal stress contours show turbulence fluctuations rising to a maximum at the core centers. This is assumed to be mostly an effect of small amplitude wandering. Using the method developed by Devenport et al(1995) the rms amplitudes of core motions and their correlation in the flow cross-plane are estimated to be $\sigma_y=0.06827r_{1m}$, $\sigma_z=0.06871r_{1m}$, and $e=0.1626$. Similar to the wandering estimates seen at $x/c=22$, the motions of the core appear to be small and symmetric. The estimated angle of the principle direction of wandering defined from the y axis to the positive z axis is 43.87° which is close to the wandering direction of the cores of the counter-rotating pair at $x/c=30$. These estimates coincide with shape of the core region defined by the locus of peak tangential velocity which is circular. Mean velocity profiles of the measured data and this data corrected for the effects of wandering are presented in Figure 76. These profiles show that the measured(wandered) data overestimates the core radius and underestimates the peak tangential velocity and axial velocity deficit by less than 1%. The turbulence stress contours, Figures 126 and 127, show that the flow field is free of wandering which contributes more than 30% to the turbulence normal stresses similar to the results at $x/c=22$.

Looking at the mean flow characteristics of the core regions, only the vortex core parameters obtained from the mean velocity profiles corrected for wandering will be given because they are close to the measured values and they are compared with the parameters at other streamwise locations corrected for wandering. The core radius is $0.105c$ which is a 5.7% increase from $x/c=22$. The peak tangential velocity is 13% U_{ref} which is a slight decrease from $x/c=22$. The axial velocity deficit is 7.7% U_{ref} which is the same as at $x/c=22$. The Rossby number at this location is 0.591. The ratio of core circulation to root circulation is 0.329. The contours of streamwise vorticity, Figure 125, show a symmetric flow field with contours concentric with the core edge similar to those of the counter-rotating vortex pair at this streamwise location. Values of maximum vorticity in the core region have increased slightly from $x/c=22$.

The change in turbulence energy of the core region from $x/c=22$ to $x/c=30$ is highlighted in the velocity autospectra. Figures 133 through 135 show autospectra of U , V , and W velocity fluctuations normalized on U_{ref} and c for various spanwise locations moving from the wake into the core center. These locations are relative to the core center at $y/c=0.076$. Autospectra at $y/c=0.62$ give the characteristics of the turbulence in the spiral wake. Autospectra at $y/c=0.38$ and 0.21 give the characteristics of the portion of the wakes immediately surrounding the core. The spectra at these locations do not resemble the two-dimensional portion of the spiral wakes indicating that the wakes do not retain their structure as they wind about the core. In the low frequency range, below $fc/U_{ref}=2$, core center spectral levels are significantly higher than at locations outside the core including the core edge in the autospectra of all three velocity components. However, at higher frequencies, above $fc/U_{ref}=20$, the core center spectra fall attaining levels lower than the spectra at the core edge and in the portion of the wake immediately surrounding the core region. It appears from these results that small scale turbulence is being suppressed in the core region. The core center spectra are scaled on parameters of the two-dimensional wake in Figures 136 and 137. They show that these spectra scale on wake parameters suggesting that the core is not producing turbulence. These results indicate that a significant amount of turbulence in the core region has been either diffused or destroyed as merger comes to completion. The variation of core center autospectra with streamwise distance, Figure 138, shows that small scale turbulence energy levels have decreased by about an order of magnitude from $x/c=22$ to 30 signaling a significant change in turbulence energy as merger comes to completion. Notice small scale turbulence levels are only slightly greater at $x/c=22$ than at $x/c=10$ and 15 .

The data has been high-pass filtered to obtain more information about the turbulence structure of the flow, especially in the core region. Figure 139 shows contours of \bar{u}^2/U_{ref}^2 filtered at $fc/U_{ref}=3$ to remove the effects of core wandering which should be small. The filtered structure is similar to the unfiltered data. Small scale

turbulence stress levels are low at $x/c=30$ and because there is significant noise at high frequencies here the results are nonphysical when filtered at $fc/U_{ref}=40$. Thus, Figure 140 shows contours of \bar{u}^2/U_{ref}^2 filtered at a frequency scaled on parameters of the two-dimensional wake at $x/c=22$ and 30, which are $fc/U_{ref}=15.12$ and 18.24, respectively. The filtered results reveal the small scale turbulence structure of the flow at $x/c=30$ which shows that the core region is a slight depression between two lobes. It appears that small scale turbulence has been diffused out into the wake immediately surrounding the core region. Comparing the filtered results at this location with those at $x/c=22$, stress levels in the core region have decreased significantly and the region of small scale turbulence has expanded moving downstream. Note that similar lobes appear in the filtered results at $x/c=30$ for the counter-rotating pair. The variation in core parameters, Figure 141, show that the core size grows significantly and the peak tangential velocity decreases with streamwise distance indicating core decay. Similar to the results of the counter-rotating pair, vortex core merger, i.e. vortex interaction causes an increased rate of vortex core decay in comparison to the isolated vortex results.

In summary, the changes in turbulence structure throughout the merger process have been revealed above. At $x/c=10$, the individual rotation of the vortex cores causes the wakes to spiral about them and come in contact with each other. These two different rotations are significant to the merger process. The cores contain turbulence at this location. The core center spectra scale on parameters of the two-dimensional wake indicating that the core is not generating this turbulence. At $x/c=15$, the rotation rate of the cores about their common center has increased as the separation distance between them has decreased. The wakes have spiraled further about the cores. Turbulence is present in the cores at this stage. Even though their small scale turbulence energy levels and stress fields are the same as at $x/c=10$, spectral scaling here indicates that the cores are generating turbulence. The cores have merged and created a single core at $x/c=22$. Merger has caused the an increase of turbulence in the core as well as engulfment of

wake turbulence from the region between the cores as evidenced by the core size. The high spectral levels in the core confirm these findings. Finally at $x/c=30$, the core region is circular. The spectral and filtered results indicate that turbulence of the core has decreased from $x/c=22$ to 30. Core center spectra scale on parameters of the two-dimensional wake at $x/c=30$. The merger process which is an effect of vortex interaction has increased vortex core decay.

4. Conclusions

The interaction between the two vortices of a counter-rotating vortex pair and a co-rotating vortex pair have been analyzed to reveal and understand the turbulence structure of these flow fields. The effects of this interaction are revealed through a comparison of the vortex pair results with those of a parallel study of an isolated vortex. The main conclusions for the three flow fields are presented here. A comparison between the three flows is given in Table 6.

4.1. Isolated trailing vortex

1. The turbulence structure outside the core of an isolated trailing vortex is dominated by the spiral wake curving about the core.
2. Turbulence levels in the wake decrease as the core is approached as a result of rates of strain and lateral curvature suffered by the wake turbulence.
3. Turbulence levels in the spiral wake decrease approximately linearly with streamwise distance.
4. There is a shift to lower frequency and turbulence energy of the velocity autospectra with streamwise distance.
5. Velocity spectra measured at the core center for all streamwise locations scale on the velocity and length scales of the two-dimensional wake, but not on core parameters. This is strong evidence that the cores are laminar.
5. There is evidence of small decay of the isolated vortex core between $x/c=10$ and 30.

4.2. Counter-rotating vortex pair

1. The vortex cores ascend pulling the wing wakes which are wound about the cores with them as a result of mutual induction at $x/c=10$ and 30 .
2. The spiral wakes retain a distinct turbulence structure curving about their respective cores at $x/c=10$.
3. Coherent wake structures aligned with the spiral wake centerline are intensified in the region between the cores, where the wakes merge, as a result of wake turbulence stretching at $x/c=10$.
4. Rates of strain and lateral curvature suffered by the wake turbulence cause a breakdown of coherent wake structures as the wakes curve about the cores at $x/c=10$ and 30 .
5. Similar to an isolated vortex, velocity autospectra measured at the core center scale on parameters of the two-dimensional wake at $x/c=10$. Results of filtering at $fc/U_{ref}=40$ also show that the cores appear laminar, and turbulence structure outside the cores is dominated by the spiral wakes.
6. The wake turbulence stress fields change with streamwise distance. The wakes no longer have the distinct structure seen at $x/c=10$. Turbulence levels in the portions of the wakes immediately surrounding the cores are much more turbulent at $x/c=30$.
7. The turbulence structure of the vortex cores changes with streamwise distance. Core center velocity autospectra do not scale on parameters of the two-dimensional wake indicating the cores are producing turbulence. Compared to the isolated vortex, the flow inside and outside the cores becomes much more turbulent at $x/c=30$.
8. A greater rate of vortex core growth and decay with streamwise distance is observed

for the counter-rotating vortex pair than for the isolated vortex.

9. The present experiment appears to demonstrate that this change in flow field turbulence is a consequence of the interaction between the vortices. It may be produced by Crow and Widnall wave instabilities.
10. The development of Crow long-wave instability is observed in the vortex cores.

4.3. Co-rotating vortex pair

1. The rotation of the vortex cores about their common center as a result of mutual induction and their individual rotation which causes the wakes to wind about them produces a large spiral flow field structure at $x/c=10$ and 15 .
2. Coherent wake structures are intensified in the spiral wake tails. These structures are broken down as the wakes curve about their respective cores due to increased lateral curvature and rates of strain at all streamwise locations.
3. Core center velocity autospectra scale on parameters of the two-dimensional wake indicating that the cores are not producing turbulence at $x/c=10$. However, high spectral levels in the cores show they are not laminar, unlike the isolated vortex.
4. Results filtered at $fc/U_{ref}=40$ show that most of the small scale turbulence is contained within the core regions and portions of the wake immediately surrounding them at all streamwise locations of the co-rotating pair.
5. At $x/c=15$, the cores have spiraled closer together as they rotate further about their common center and turbulence stress decreases in the spiral wake tails.
6. Small scale energy levels indicated by the spectral results and small scale turbulence stress fields from the filtered results at $fc/U_{ref}=40$ are similar at $x/c=10$ and 15 .
7. Core center velocity autospectra at $x/c=15$ do not scale on parameters of the two-dimensional wake suggesting they are producing turbulence.
8. At $x/c=22$, the two vortex cores seen at $x/c=15$ have merged into a single core. This core is over twice the size of each core that created it indicating that the core

also contains some wake turbulence.

9. Velocity autospectra show that turbulence energy in the core has increased and filtered results at $fc/U_{ref}=40$ show the small scale turbulence stress in the core has increased from $x/c=15$ to 22. Spectral scaling suggests that the core is producing turbulence.
10. At $x/c=30$, the core region is symmetric and velocity autospectra indicate that turbulence energy levels in the core have decreased significantly from $x/c=22$ to 30. Filtered results indicate that the small scale turbulence stress has also decreased.
11. Core center velocity autospectra scale on parameters of the two-dimensional wake. The core contains some turbulent velocity fluctuations at $x/c=30$ with spectral levels at the core center slightly lower than in the portions of the wakes immediately surrounding it.
12. Rate of core decay is greater for the co-rotating pair than the isolated vortex.

The experimental data presented in this report is available on the World Wide Web from URL <http://www.aoe.vt.edu/flowdata.html>

5. References

Baker GR, Barker SJ, Bofah KK, and Saffman PG, 1974, "Laser anemometer measurements of trailing vortices in water", *Journal of Fluid Mechanics*, vol. 65 pp.325-336.

Bandyopadhyay P, Stead D, and Ash R, 1990, "The organized nature of a turbulent trailing vortex", *AIAA 21st Fluid Dynamics, Plasma Dynamics and Lasers Conference*, June 18-20, Seattle, WA, Paper AIAA-90-1625

Barker SJ, and Crow SC, 1977, "The motion of two-dimensional vortex pairs in a ground effect", *Journal of Fluid Mechanics*, vol. 82, pp.659-671

Bilanin AJ, Teske ME, and Williamson GG, 1976, "Viscous effects in aircraft trailing vortices", *Wake-Vortex Minimization*, NASA SP409

Bilanin AJ, Teske ME, and Williamson GG, 1977, "Vortex interactions and decay in aircraft wakes", *AIAA Journal*, vol 15, no. 2, pp.250-260

Bliss DB, 1982, "Effects of unsteady forcing on the sinusoidal instability of vortex wakes", *Journal of Aircraft*, vol. 19, no. 9, pp.713-721

Brandt SA, and Iversen JD, 1977, "Merging of aircraft trailing vortices", *Journal of Aircraft*, vol. 14, no. 12, pp.1212-1230

Chevalier H, 1973, "Flight test studies of the formation and dissipation of trailing vortices", *Society of Automotive Engineers, Business Aircraft Meeting*, Wichita, KS, April 30, 1973

Chigier NA, and Corsiglia VR, 1972, "Wind tunnel studies of wing wake turbulence", *Journal of Aircraft*, vol. 9, pp.820-825.

Choi K, and Simpson RL, 1987, "Some mean-velocity, turbulence, and unsteadiness characteristics of the VPI&SU Stability Wind Tunnel", *Report VPI-AOE-161*, VPI&SU, Blacksburg, VA

Ciffone DL, 1977, "Vortex interactions in multiple vortex wakes behind aircraft",

Ciffone DL, and Orloff KL, 1975, "Far-field wake-vortex characteristics of wings", Journal of Aircraft, vol. 12, no. 5, pp.464-470

Corsiglia VR, Schwind RG, and Chigier NA, 1973, "Rapid scanning, three-dimensional hot-wire anemometer surveys of wing-tip vortices", Journal of Aircraft, vol. 10, pp.752-757

Corsiglia VR, Rossow VJ, and Ciffone DL, 1976, "Experimental study of the effects of span loading on aircraft wakes", Journal of Aircraft, vol. 13, no. 12, pp.968-973

Corsiglia VR, Iversen JD, and Orloff KL, 1978, "Laser-velocimeter surveys of merging vortices in a wind tunnel", Journal of Aircraft, vol. 15, no. 11, pp.762-768

Costen RC, 1972, "Drift of buoyant wing-tip vortices", Journal of Aircraft, vol. 9, no. 6, pp.320-406

Crow SC, 1970, "Stability theory for a pair of trailing vortices", AIAA Journal, vol. 8, no. 12, pp. 2172-2179

Devenport WJ, Rife MC, Liapis, SI, and Miranda JA, 1994, "Turbulent trailing vortices", 32nd Aerospace Sciences Meeting and Exhibit, Jan. 10-13, 1994, Reno, NV, Paper AIAA-94-0404

Devenport WJ, Rife MC, Liapis SI, and Follin GJ, 1995, "Turbulence structure and scaling in trailing vortices", 33rd Aerospace Sciences Meeting and Exhibit, Jan. 9-12, 1995, Reno, NV, Paper AIAA-95-0588

Didden N, 1977, from Van Dyke M, 1982, An Album of Fluid Motion, Parabolic Press, Stanford, CA, pp.66-67.

Eliason BG, Gartshore IS, and Parkinson GV, 1975, "Wind tunnel investigation of Crow instability", Journal of Aircraft, Vol. 12, no. 12, pp.985-988

Engel, M, 1995, "A wind tunnel investigation of a trailing vortex", Report No. VPI-AOE-218, AOE Dept., VPI&SU, Blacksburg, VA

FAA, 1971, "Vortex wake turbulence", Report No. FAA-FS-71-1

Garodz LJ, 1971, "Federal Aviation Administration full-scale aircraft vortex wake turbulence flight test investigation: past, present, and future", AIAA 9th Aerospace Sciences Meeting, New York, NY, Jan 25-27, 1971 Paper AIAA-71-97

Greene, 1986, "An approximate model of vortex decay in the atmosphere", *Journal of Aircraft*, vol. 23, no. 7, pp.566-573

Hackett JE, and Evans PF, 1977, "Numerical studies of three-dimensional breakdown in trailing vortex wakes", *Journal of Aircraft*, vol. 14, no. 11, pp.1093-1101

Hecht AM, Bilanin J, and Hirsh JE, 1981, "Turbulent trailing vortices in stratified fluids", *AIAA Journal*, vol.19, no. 6, pp.691-698

Hoffmann EF and Joubert PN, 1963, "Turbulent line vortices", *Journal of Fluid Mechanics*, vol. 16, pp.395-411

Iversen JD, Corsiglia VR, Park S, Backhus DR, and Brickman RA, 1979, "Hot-wire, laser-anemometer and force measurements of interacting trailing vortices", *Journal of Aircraft*, vol. 16, no. 7, pp.448-454

Jorgenson FE, 1971, "Directional sensitivity of wire and fiber-film probes", *DISA Information*, No. 11, pp.6-10

Keffer JF, 1965, "The uniform distortion of a turbulent wake", *Journal of Fluid Mechanics*, vol. 22, pp.135-159

Kerr TH, and Dee FW, 1959, "A flight investigation into the persistence of trailing wake vortices behind large aircraft", *ICAO Circular 92-AN/76*, pp.13-34

Lezius DK, 1974, "Water tank study of the decay of trailing vortices", *AIAA Journal*, vol. 12, no. 8, pp.1154-1155

Lui CH, and Ting L, 1987, "Interaction of decaying trailing vortices in spanwise shear flow", *Computers and Fluids*, vol. 15, no. 1, pp.77-92

Liu HT, 1992, "Effects of ambient turbulence on the decay of a trailing vortex wake", *Journal of Aircraft*, vol. 29, no. 2, pp.255-263

Liu HT, Hwang PA, and Srnsky RA, 1992, "Physical modeling of ground effects on vortex wakes", *Journal of Aircraft*, vol. 29, no. 6, pp.1027-1034

Locke CA, Hirsa A, and Rubin MD, 1993, "Short-wave instability in a laminar vortex pair", *ASME FED*, Vol. 157, pp. 73-81.

Mayer EW, and Powell KG, 1992, "Similarity solutions for viscous vortex cores", *Journal of Fluid Mechanics*, vol. 238, pp.487-507.

McCormick BW, Tangler JL, and Sherrieb HE, 1968, "Structure of trailing vortices", Journal of Aircraft, vol. 5, no. 3, pp.260-267

Melander MV, Zabusky NJ, and McWilliams JC, 1988, "Symmetric vortex merger in two dimensions: causes and conditions", Journal of Fluid Mechanics, vol. 195, pp.303-340

Mitchel BE, Lele SK, and Moin P, 1992, "Direct computation of the sound from a compressible co-rotating vortex pair", AIAA 30th Aerospace Sciences Meeting and Exhibit, Reno, NV, Jan 6-9, 1992, Paper AIAA-92-0374

Overman EA, and Zabusky NJ, 1982, "Evolution and merger of isolated vortex structures", Physics of Fluids, vol. 25, no. 8, pp.1297-1305

Phillips WRC, and Graham JAH, 1984, "Reynolds stress measurements in a turbulent trailing vortex", Journal of Fluid Mechanics, vol. 147, pp.353-371

Robins RE, and Delisi DP, 1993, "Potential hazard of aircraft wake vortices in ground effect", Journal of Aircraft, vol. 30, no. 2, pp.201-206

Rossow VJ, 1977, "Convective merging of vortex cores in lift-generated wakes", Journal of Aircraft, vol. 14, no. 3, pp.283-290

Sarpkaya T, 1983, "Trailing vortices in homogenous and density-stratified media", Journal of Fluid Mechanics, vol. 136, pp.85-109

Sarpkaya T, and Daly JJ, 1987, "Effects of ambient turbulence on trailing vortices", Journal of Aircraft, vol. 24, no. 6, pp.399-404

Sarpkaya T, 1992, "Three-dimensional interactions of vortices with a free surface", AIAA 30th Aerospace Sciences Meeting and Exhibit, Reno, NV, Jan 6-9, 1992, Paper AIAA-92-0059

Sarpkaya T, Merrill C, and Carroll J, 1994, "Coherent structures in vortex/free surface interaction", AIAA 32nd Aerospace Sciences Meeting and Exhibit, Reno, NV, Jan. 10-13, 1994, Paper AIAA-94-0530

Scorer RS, and Davenport LJ, 1970, "Contrails and aircraft downwash", Journal of Fluid Mechanics, vol. 43, part 3, pp.451-464

Smits AJ, and Kummer RP, 1985, "The interaction and merging of two turbulent line vortices", AIAA 23rd Aerospace Sciences Meeting, Reno, NV, Jan. 14-17, 1985, Paper AIAA-85-0046

Steger JL, and Kulter P, 1977, "Implicit finite-difference procedures for the computation of vortex wakes", Paper AIAA-76-385

Thomas PJ, and Auerbach D, 1994, "The observation of the simultaneous development of a long- and a short-wave instability mode on a vortex pair", Journal of Fluid Mechanics, vol. 265, pp.289-302

Tombach I, 1973, "Observations of atmospheric effects on vortex wake behavior", Journal of Aircraft, vol. 10, no. 11, pp.641-647

Treddenick DS, 1968, "Flight measurements of the vortex wake behind a convair 880", ICAO, Circular 92-AN/76, pp.3-12

Widnall SE, Bliss DB, 1971, "Slender-body analysis of the motion and stability of a vortex filament containing an axial flow", Journal of Fluid Mechanics, vol. 50

Widnall SE, Bliss DB, and Tsai C, 1974, "The instability of short waves on a vortex ring", Journal of Fluid Mechanics, vol. 66, part 1, pp.35-47

Widnall SE, 1975, "The structure and dynamics of vortex filaments", Journal of Fluid Mechanics, pp. 141-164

Zsoldos JS, 1992, "An experimental investigation of interacting wing-tip vortex pairs", Report No. VPI-AOE-191, AOE Dept., VPI&SU, Blacksburg, VA

Table 1. Vortex pair wing trailing edge characteristics from Zsoldos(1992).

Case	δ/c	δ^*/c	θ/c	Re_θ
α_o y/c=1.3 pressure	0.03564	0.00797	0.00453	1060.0
α_o y/c=1.3 suction	0.05482	0.01349	0.00732	1712.6
α_o y/c=.73 pressure	0.04028	0.00958	0.00533	1289.1
α_o y/c=.73 suction	0.05631	0.01344	0.00742	1796.1
α_o y/c=-.73 pressure	0.04770	0.01005	0.00615	1486.9
α_o y/c=-.73 suction	0.06275	0.01500	0.00835	1953.9
α_o y/c=-1.3 pressure	0.04889	0.01066	0.00618	1445.9
α_o y/c=-1.3 suction	0.06378	0.01568	0.00856	2004.15
α_e y/c=1.3 pressure	0.03364	0.00734	0.00419	979.76
α_e y/c=1.3 suction	0.05843	0.01477	0.00778	1819.7
α_e y/c=.73 pressure	0.03834	0.00850	0.00488	1180.1
α_e y/c=.73 suction	0.05949	0.01535	0.00822	1986.4
α_e y/c=-.73 pressure	0.04544	0.00960	0.00579	1400.2
α_e y/c=-.73 suction	0.06232	0.01552	0.00857	2072.4

Table 2. Quad hot-wire uncertainties from Zsoldos(1992).

	Wake region	Core edge	Core center
Quantity	Uncertainty	Uncertainty	Uncertainty
U/U_{ref}	0.015	0.015	0.014
V/U_{ref}	0.025	0.025	0.024
W/U_{ref}	0.025	0.024	0.023
u^2/U_{ref}^2	3.1×10^{-6}	1.4×10^{-5}	4.3×10^{-5}
v^2/U_{ref}^2	9.5×10^{-6}	1.5×10^{-5}	1.7×10^{-4}
w^2/U_{ref}^2	9.9×10^{-6}	2.0×10^{-5}	1.6×10^{-4}
uv/U_{ref}^2	4.3×10^{-6}	1.4×10^{-5}	5.2×10^{-5}
vw/U_{ref}^2	4.5×10^{-6}	2.3×10^{-5}	5.2×10^{-5}
uw/U_{ref}^2	2.9×10^{-6}	8.5×10^{-6}	1.0×10^{-4}

Table 3. Flow conditions, vortex core parameters, and characteristics of wandering motions for quad hot-wire measurement cases of vortex pair experiment. The core parameters are deduced from mean velocity profiles corrected for wandering using the method of Devenport et al(1995). The angle of principle axis of wandering is measured from y axis toward the negative z axis for counter-rotating pair and toward the positive z axis for the co-rotating pair.

Counter-rotating vortex pair			Vortex core parameters						Wandering		
Conditions			r_1/c	$V_{\theta 1}/U_{\infty}$	U_D/U_{ref}	Γ_1/Γ_0	$U_D/V_{\theta 1}$	σ_y/c	σ_z/c	Angle	
x/c	$U_{\infty}c/v$	α_e	Trip								
10	260000	5°	20-40%	0.044	0.402	0.148	0.208	0.368	0.0047	0.0049	41.4°
30	260000	5°	20-40%	0.047	0.337	0.162	0.183	0.482	0.0181	0.0172	47.4°
Co-rotating vortex pair			Vortex core parameters						Wandering		
Conditions			r_1/c	$V_{\theta 1}/U_{\infty}$	U_D/U_{ref}	Γ_1/Γ_0	$U_D/V_{\theta 1}$	σ_y/c	σ_z/c	Angle	
x/c	$U_{\infty}c/v$	α_o	Trip								
10	260000	5°	20-40%	0.037	0.164	0.128	0.144	0.776	0.0089	0.0115	108.8°
15	260000	5°	20-40%	0.033	0.158	0.126	0.126	0.797	0.0105	0.0171	109.7°
22	260000	5°	20-40%	0.099	0.134	0.077	0.320	0.575	0.0068	0.0083	21.4°
30	260000	5°	20-40%	0.105	0.130	0.077	0.329	0.592	0.0073	0.0074	43.9°

Table 4. Vortex pair far wake characteristics.

Counter-rotating pair					
Case	$(\bar{u}^2/U_{ref}^2)_{max}$	$(\bar{v}^2/U_{ref}^2)_{max}$	$(\bar{w}^2/U_{ref}^2)_{max}$	u_w/U_{ref}	L_w/c
x/c=10	2.265×10^{-4}	2.139×10^{-4}	2.621×10^{-4}	0.01702	0.1313
x/c=30	6.730×10^{-5}	5.592×10^{-5}	7.615×10^{-5}	0.009378	0.2125
Co-rotating pair					
Case	$(\bar{u}^2/U_{ref}^2)_{max}$	$(\bar{v}^2/U_{ref}^2)_{max}$	$(\bar{w}^2/U_{ref}^2)_{max}$	u_w/U_{ref}	L_w/c
x/c=10	2.235×10^{-4}	2.214×10^{-4}	2.410×10^{-4}	0.01653	0.1288
x/c=15	1.348×10^{-4}	1.166×10^{-4}	1.437×10^{-4}	0.01320	0.1531
x/c=22	8.400×10^{-5}	5.933×10^{-5}	8.716×10^{-5}	0.01024	0.1750
x/c=30	7.242×10^{-5}	5.592×10^{-5}	7.615×10^{-5}	0.009398	0.1938

Table 5. Flow conditions, vortex core parameters, and characteristics of wandering motions for quad hot-wire measurement cases of isolated vortex experiment of Devenport et al(1995). The core parameters are deduced from mean velocity profiles corrected for wandering using the method of Devenport et al(1995). The angle of principle axis of wandering is measured from the y axis toward the negative z axis.

Conditions			Vortex core parameters					Wandering			
x/c	Re_c	α	Trip	r_1/c	$V_{\theta 1}/U_{ref}$	U_D/U_{ref}	Γ_D/Γ_0	$U_D/V_{\theta 1}$	σ_y/c	σ_z/c	Angle
10	530000	5°	20-40%	0.037	0.286	0.152	0.275	0.531	0.007	0.005	68.5°
15	530000	5°	20-40%	0.036	0.277	0.141	0.261	0.511	0.008	0.006	59.9°
20	530000	5°	20-40%	0.039	0.278	0.153	0.287	0.55	0.009	0.007	56.9°
30	530000	5°	20-40%	0.036	0.263	0.16	0.248	0.609	0.013	0.012	54.6°

Table 6. Comparison between conclusions of isolated vortex study and the vortex pair studies.

	Isolated vortex	Counter-rotating vortex	Co-rotating vortex
$x/c=10$	core center spectra scale on wake parameters	core center spectra scale on wake parameters	core center spectra scale on wake parameters
	spectral and filtered results indicate core is laminar	spectral and filtered results indicate cores are laminar	spectral and filtered results indicate cores are not laminar, however they are not producing turbulence
	turbulence structure outside the cores is dominated by spiral wake	turbulence structure outside the cores is dominated by spiral wakes	turbulence structure outside the cores is dominated by portions of wakes immediately surrounding the cores
$x/c=15$	core center spectra scale on wake parameters		core center spectra do not scale on wake parameters
	spectral and filtered results indicate core is laminar		spectral and filtered results indicate cores are producing turbulence
	turbulence structure outside the cores is dominated by the spiral wake		turbulence structure outside the cores is dominated by the portions of the wakes immediately surrounding the cores
	turbulence decays from $x/c=10$ to 15 in spiral wake		turbulence decays from $x/c=10$ to 15 in the spiral wakes
	3% decrease in peak tangential velocity from $x/c=10$ indicating small core decay		4% decrease in peak tangential velocity from $x/c=10$ indicating small core decay
$x/c=20$ of	core center spectra scale on wake parameters		core center spectra do not scale on wake parameters
isolated vortex	spectral and filtered results indicate core is laminar		spectral and filtered results indicate core is producing turbulence and turbulence levels in the cores have increased from $x/c=15$
$x/c=22$ of co-rotating pair	turbulence outside the core is dominated by the spiral wake		turbulence outside the core is dominated by the portions of the wakes immediately surrounding the core.
	turbulence decays in the spiral wake from $x/c=15$ to		turbulence decays in the spiral wakes from $x/c=15$

	20		to 22
	8% increase in core size from $x/c=15$ indicating core growth		67% increase in core size and 15% decrease in peak tangential velocity from $x/c=15$ indicating core decay
$x/c=30$	core center spectra scale on wake parameters	core center spectra do not scale on wake parameters	core center spectra scale on wake parameters
	spectral and filtered results indicate core is laminar	spectral and filtered results indicate core is producing turbulence and turbulence levels in the wakes have increased from $x/c=10$	spectral and filtered results indicate core is not producing turbulence and turbulence levels in the core have decreased from $x/c=22$
	turbulence outside the core is dominated by the spiral wake	turbulence outside the cores is dominated by the wakes	turbulence outside the core is dominated by the portions of the wakes immediately surrounding the core.
	5% decrease in peak tangential velocity from $x/c=20$ indicating core decay	6% increase in core size and 16% decrease in peak tangential velocity indicate core decay	5% increase in core size and 3% decrease in peak tangential velocity indicate core decay

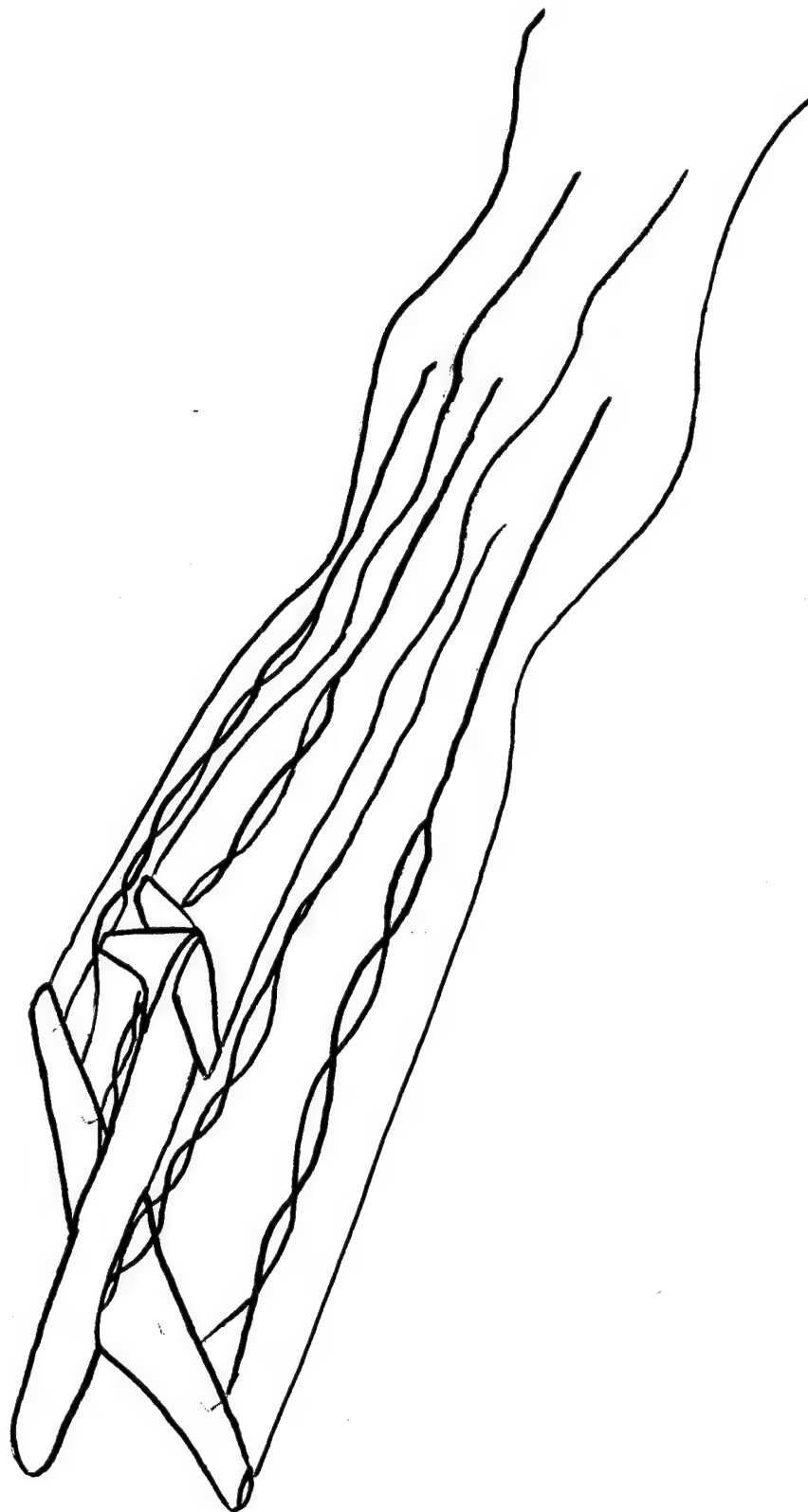


Figure 1. View of aircraft generating vortex pairs.

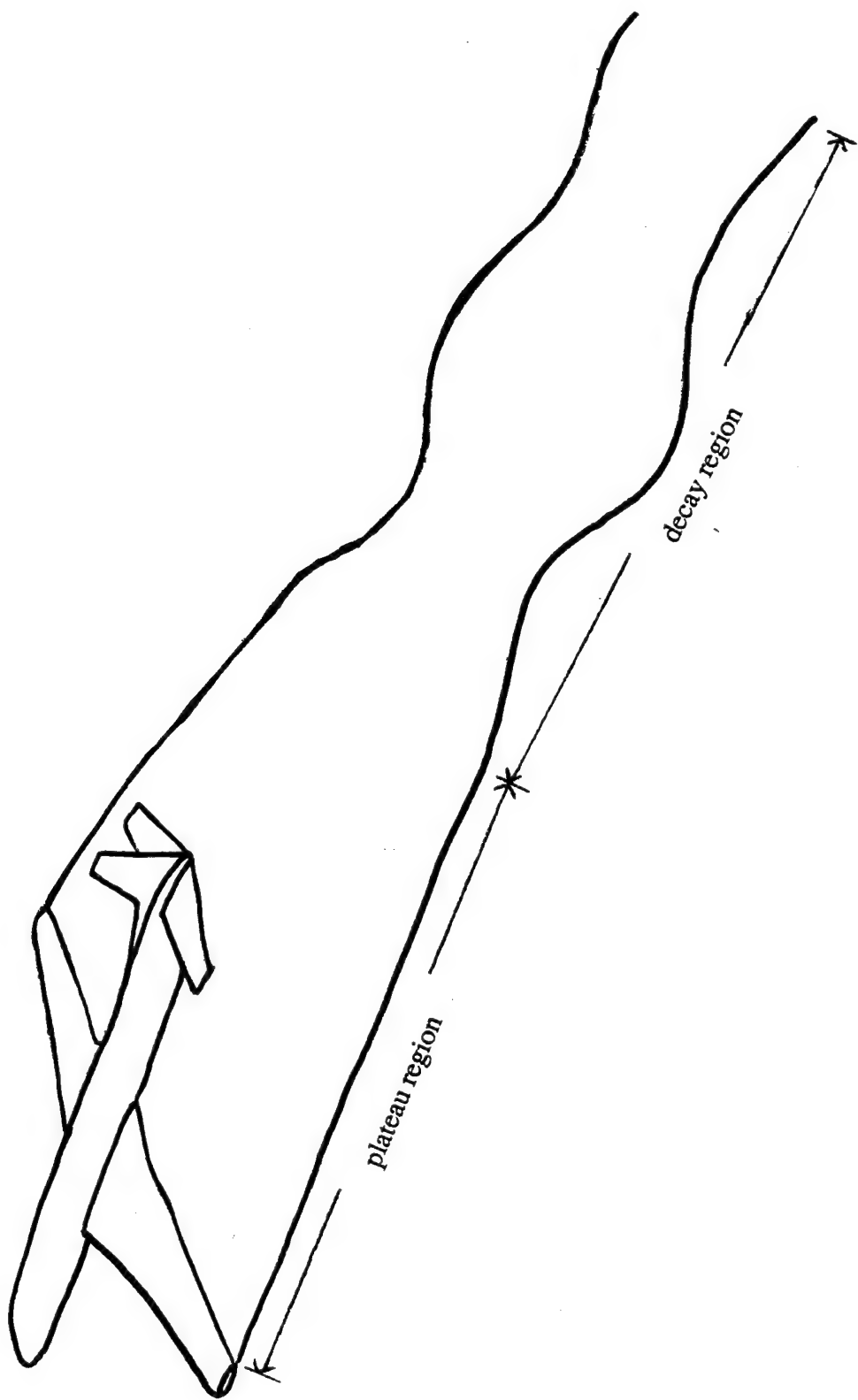


Figure 2(a) View of aircraft generating a counter-rotating vortex pair.

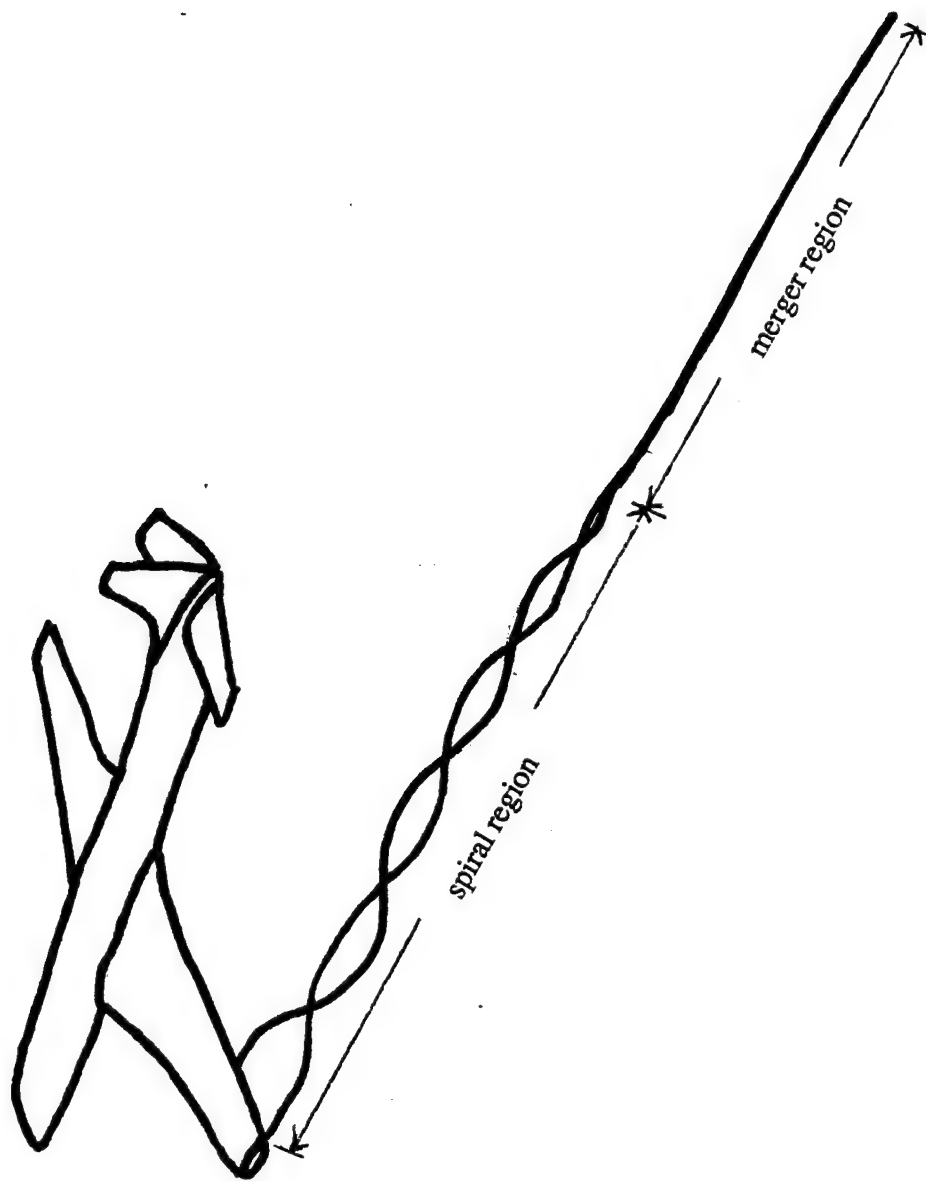


Figure 2(b). View of an aircraft generating a co-rotating vortex pair.

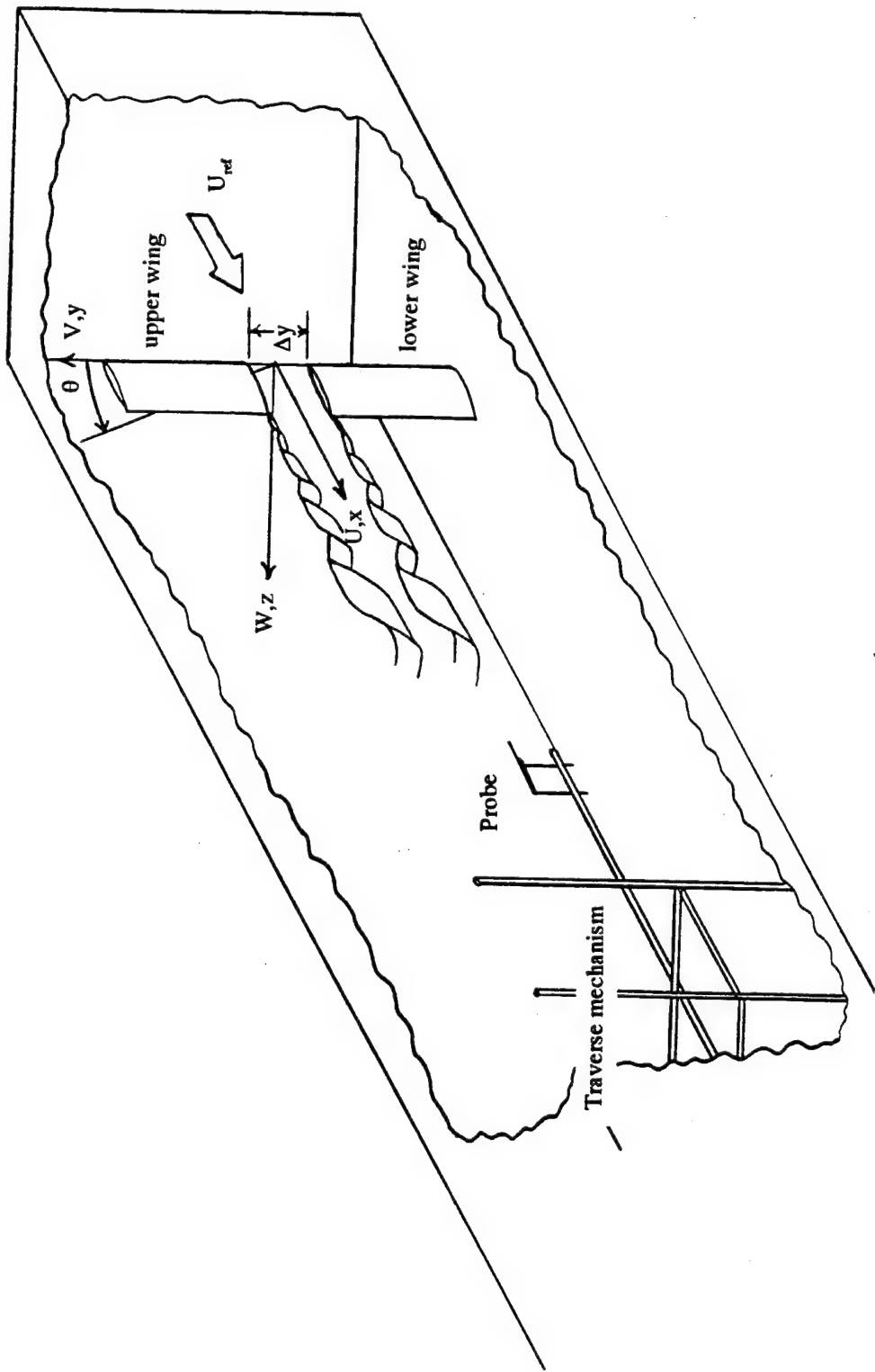


Figure 3(a). Schematic of the test section showing the coordinate system for the vortex pair study, the two NACA 0012 wings, and traverse mechanism from Zsoldos(1992).

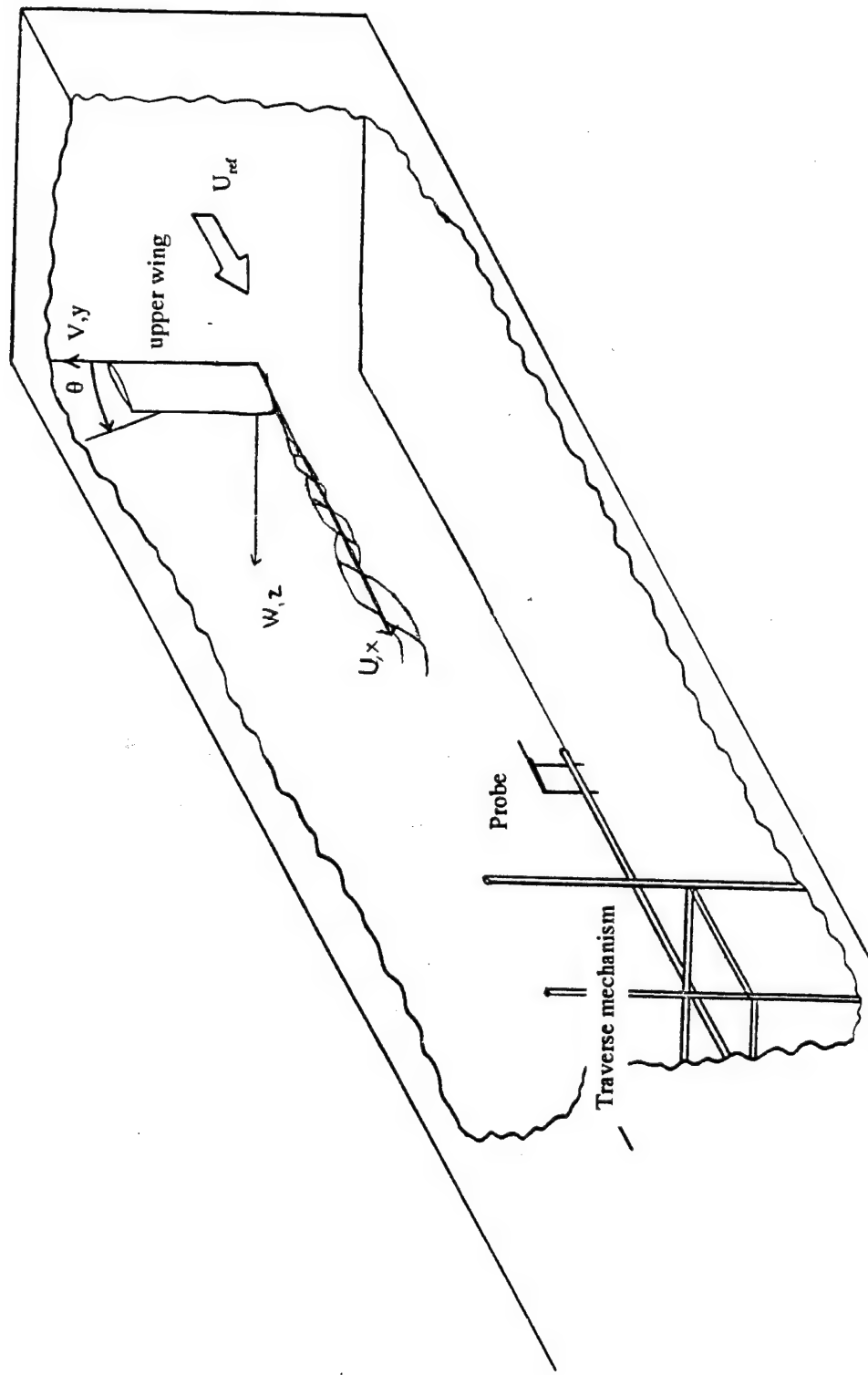


Figure 3(b). Schematic of test section showing the coordinate system for the isolated vortex study of Devenport et al(1995), the single NACA 0012 wing, and traverse mechanism.

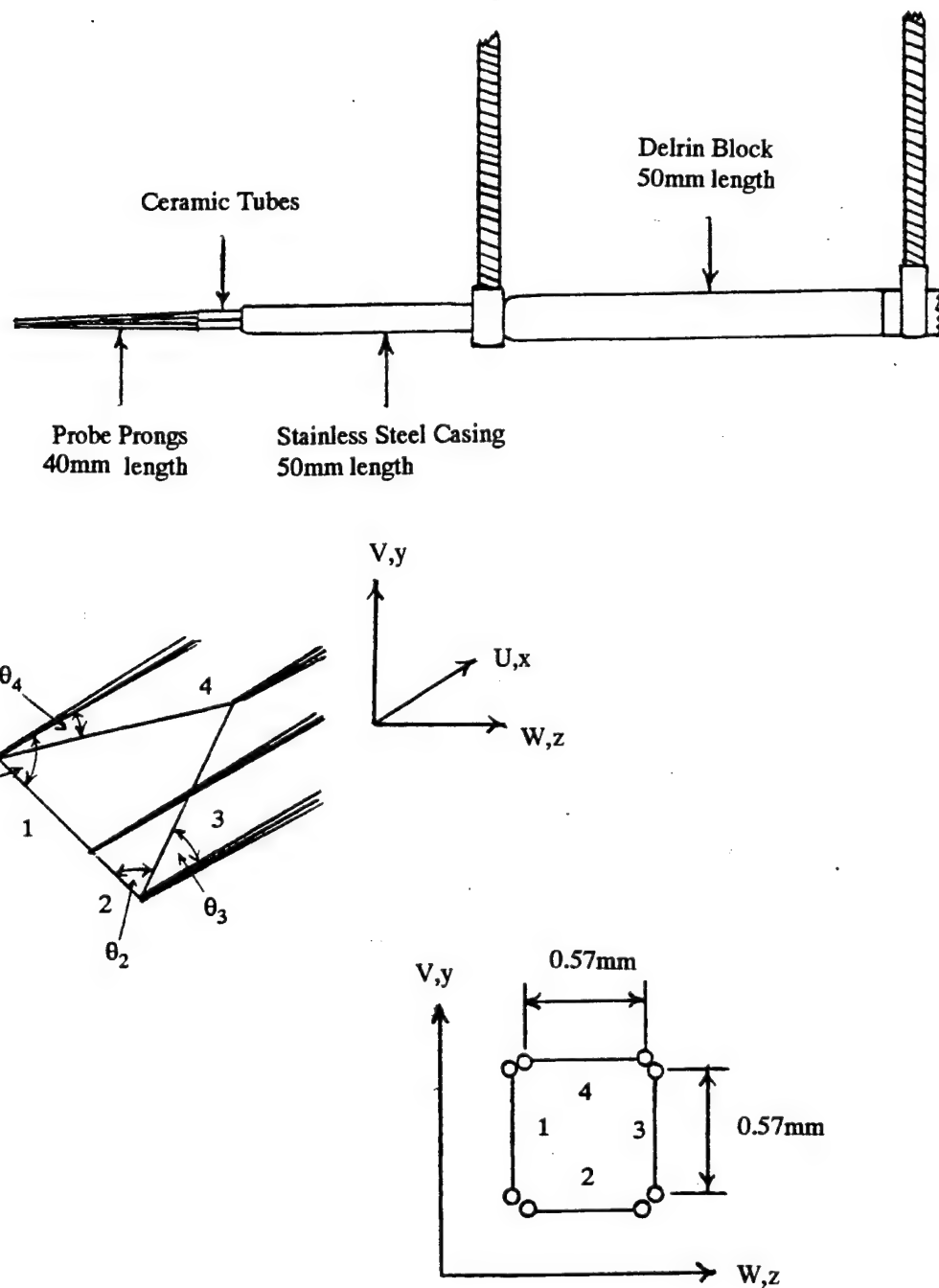


Figure 4. Schematic of the quad hot-wire probe showing dimensions and wire configuration in the measurement plane.

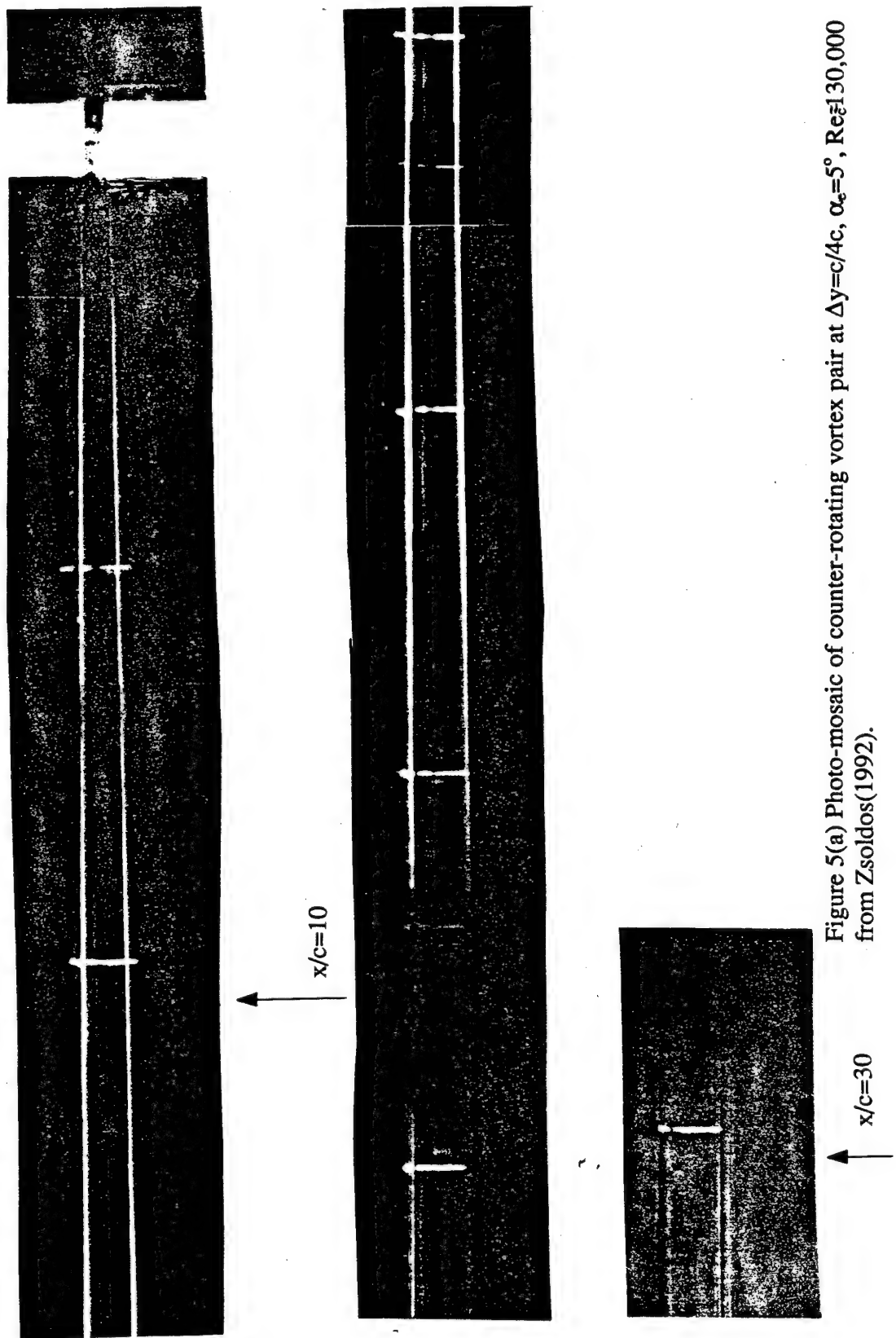


Figure 5(a) Photo-mosaic of counter-rotating vortex pair at $\Delta y = c/4c$, $\alpha_c = 5^\circ$, $Re = 130,000$ from Zsoldos(1992).

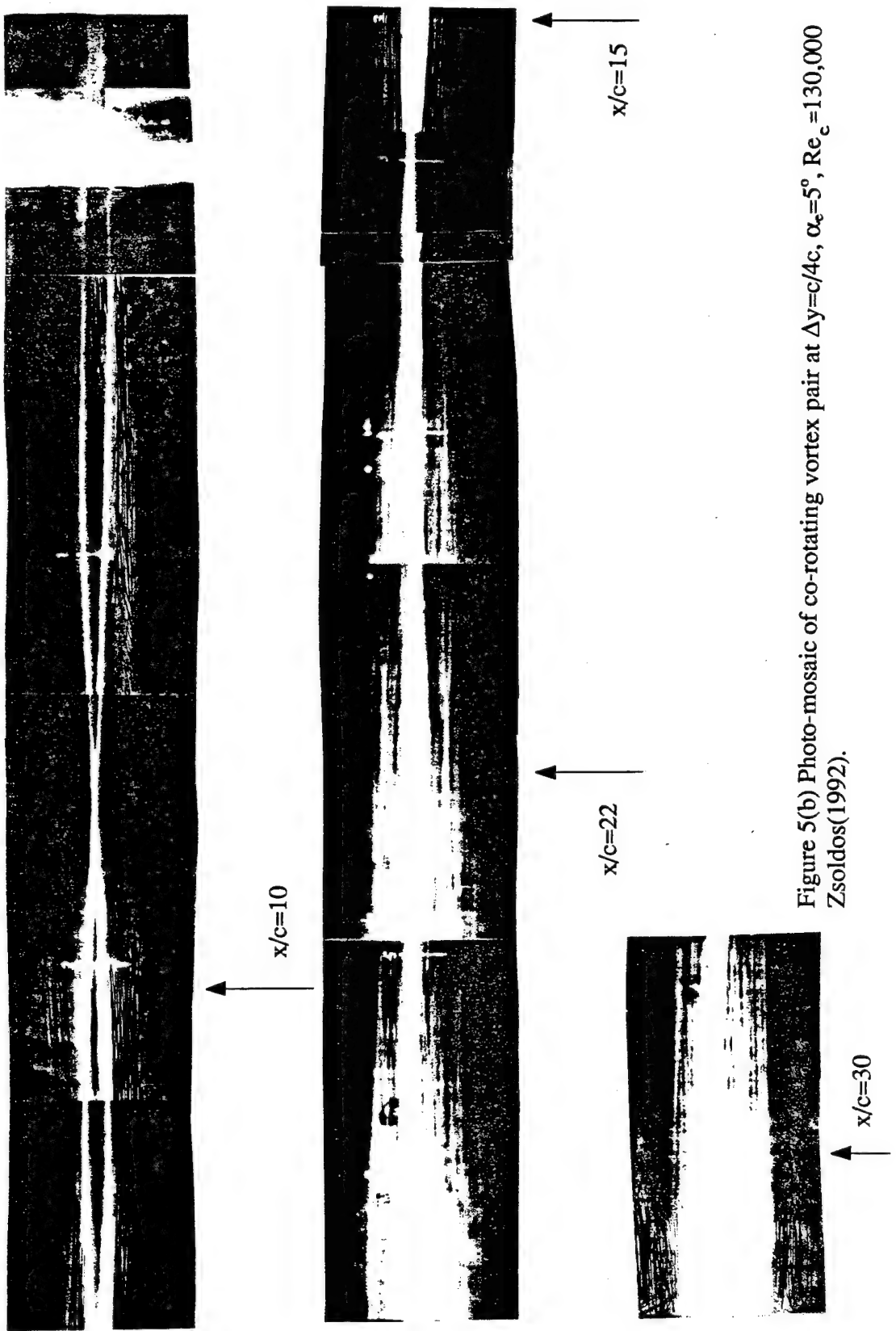


Figure 5(b) Photo-mosaic of co-rotating vortex pair at $\Delta y = c/4c$, $\alpha_c = 5^\circ$, $Re_c = 130,000$
Zsoldos(1992).

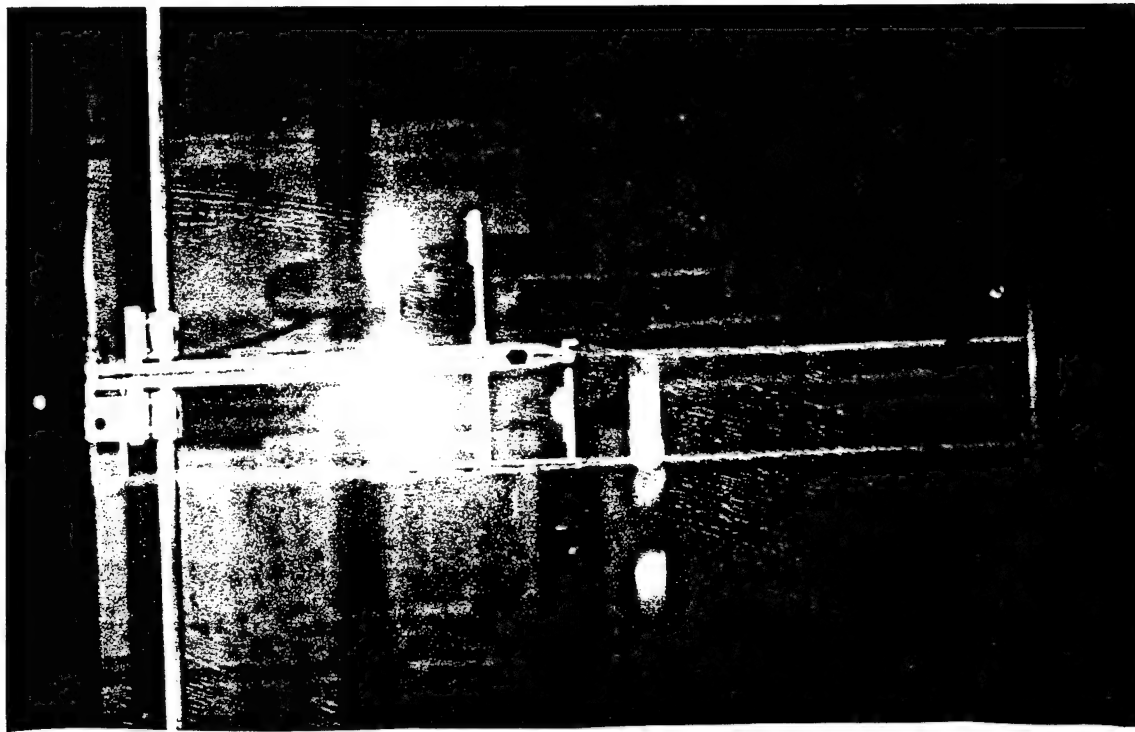


Figure 6(a) Flow visualization of dummy hot-wire probe in the lower core of the counter-rotating pair at $\Delta y = c/4c$, $\alpha_e = 5^\circ$, $Re_c = 400,000$ at streamwise location $x/c = 22$.

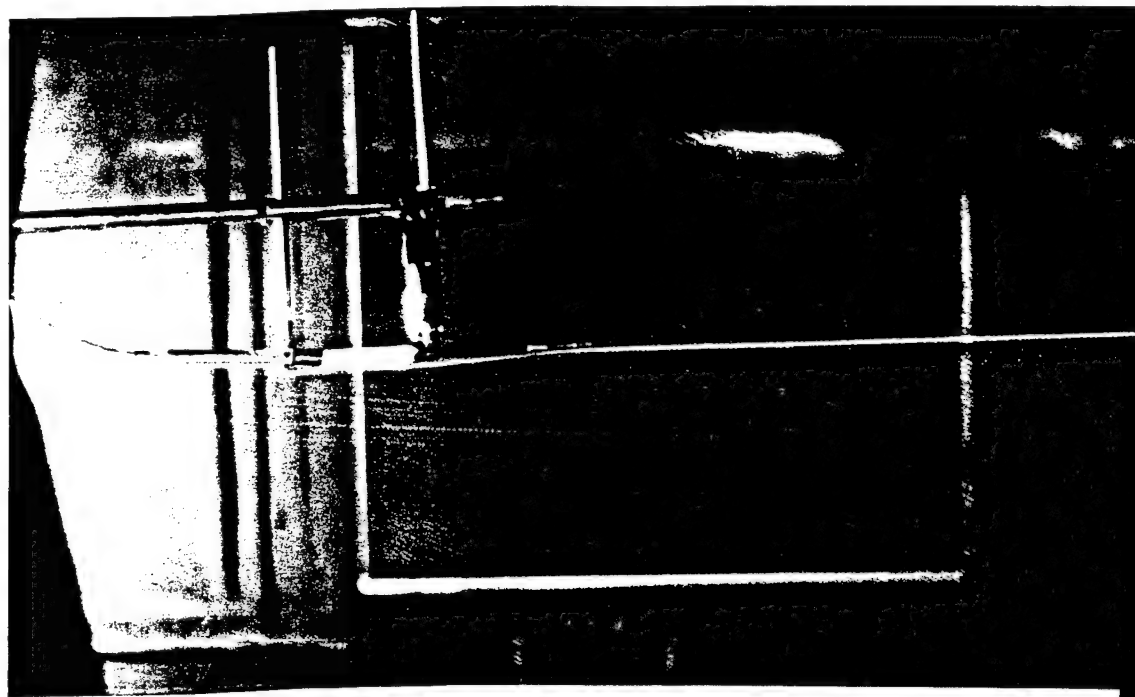


Figure 6(b) Flow visualization of quad hot-wire probe in isolated vortex core at $\alpha = 5^\circ$, $Re_c = 130,000$ from Engel(1995).

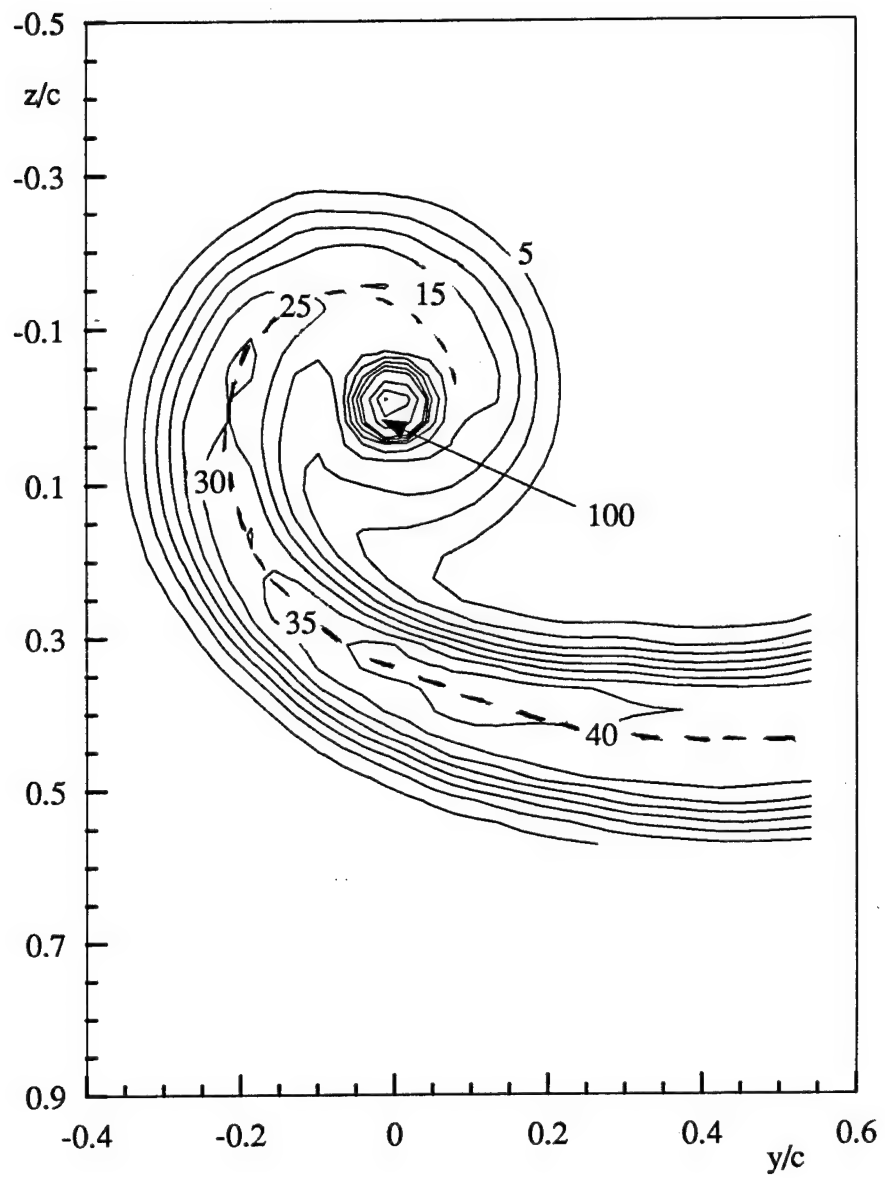


Figure 7(a) Contours of axial normal stress $\bar{u}^2/U_{ref}^2 \times 10^5$ at $x/c = 10$ of isolated vortex from Devenport et al (1995). Dashed line denotes spiral wake centerline.

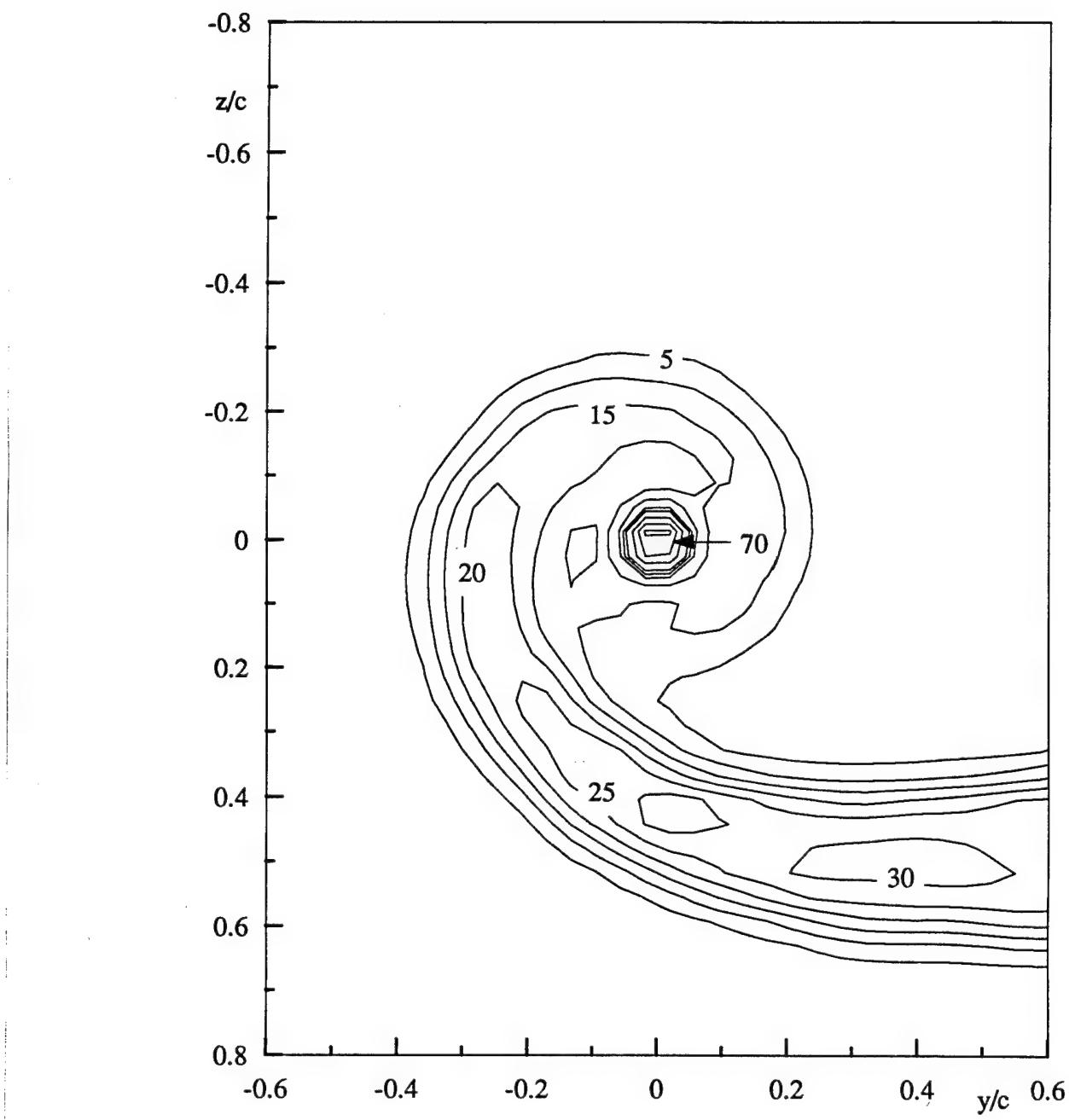


Figure 7(b) Contours of axial normal stress $\bar{u}^2/U_{ref}^2 \times 10^5$ at $x/c = 15$ of isolated vortex from Devenport et al(1995).

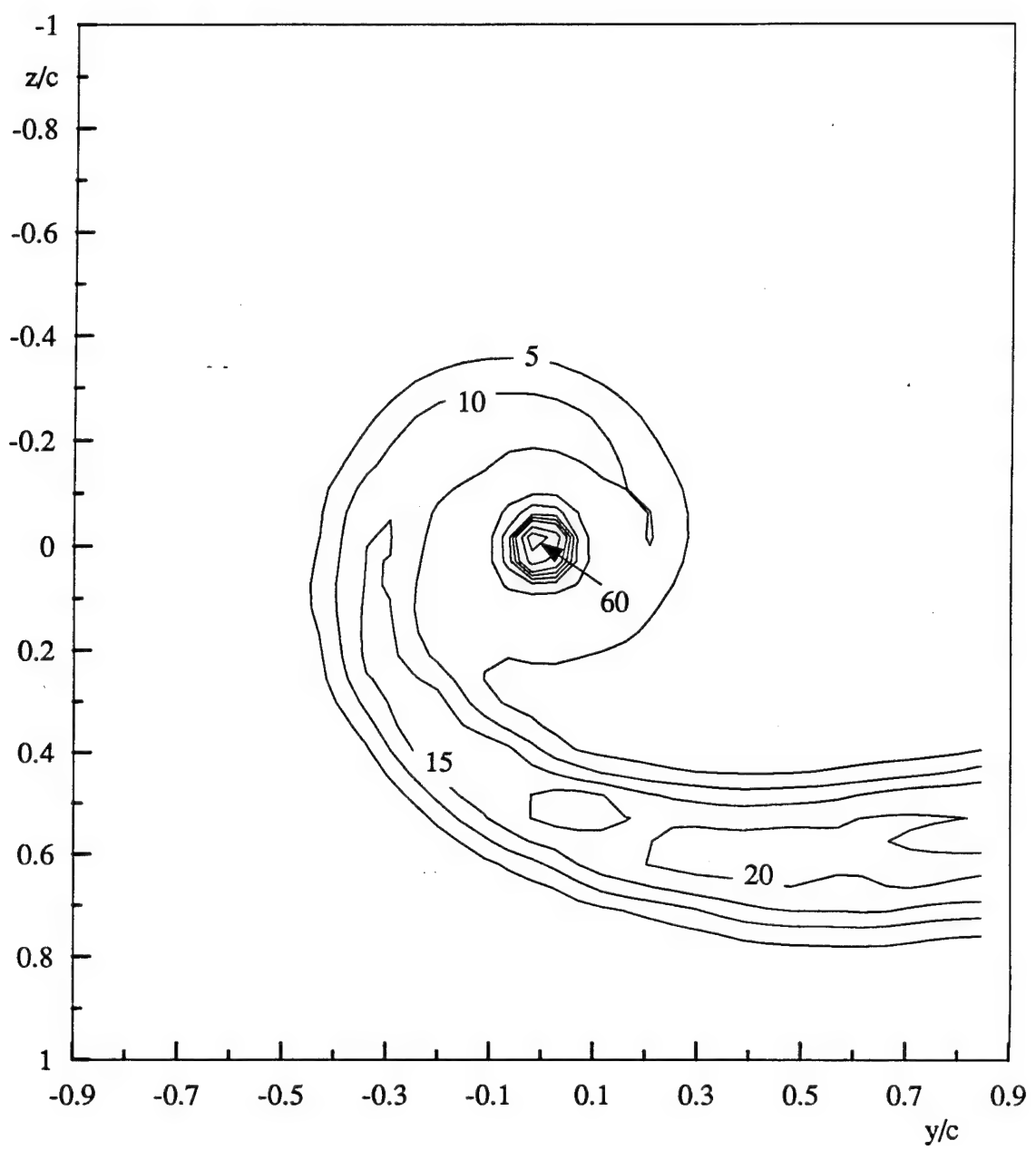


Figure 7(c) Contours of axial normal stress $\bar{u}^2/U_{ref}^2 \times 10^5$ at $x/c=20$ of isolated vortex from Devenport et al(1995).

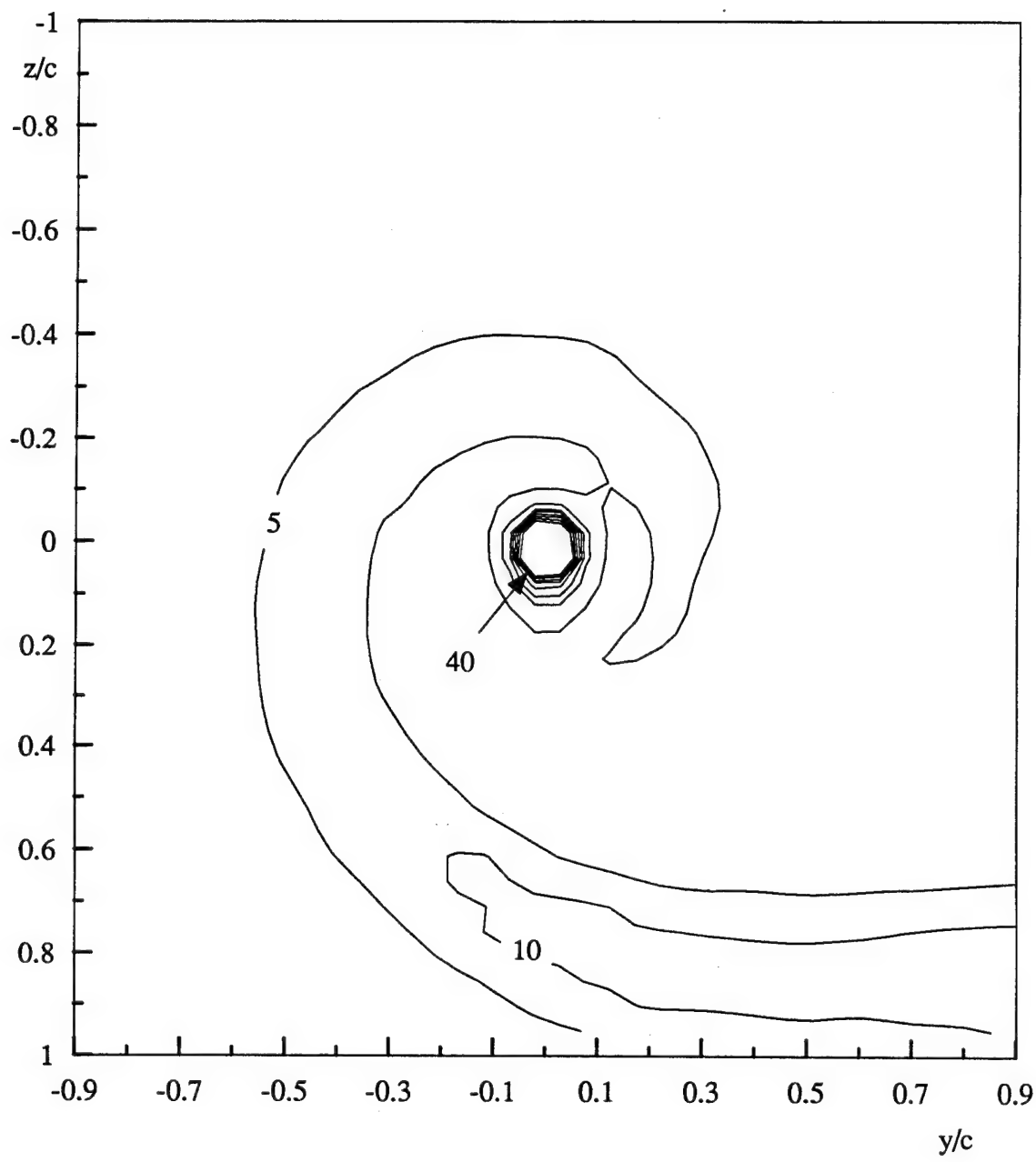


Figure 7(d) Contours of axial normal stress $u^2/U_{ref}^2 \times 10^5$ at $x/c=30$ of isolated vortex from Devenport et al(1995).

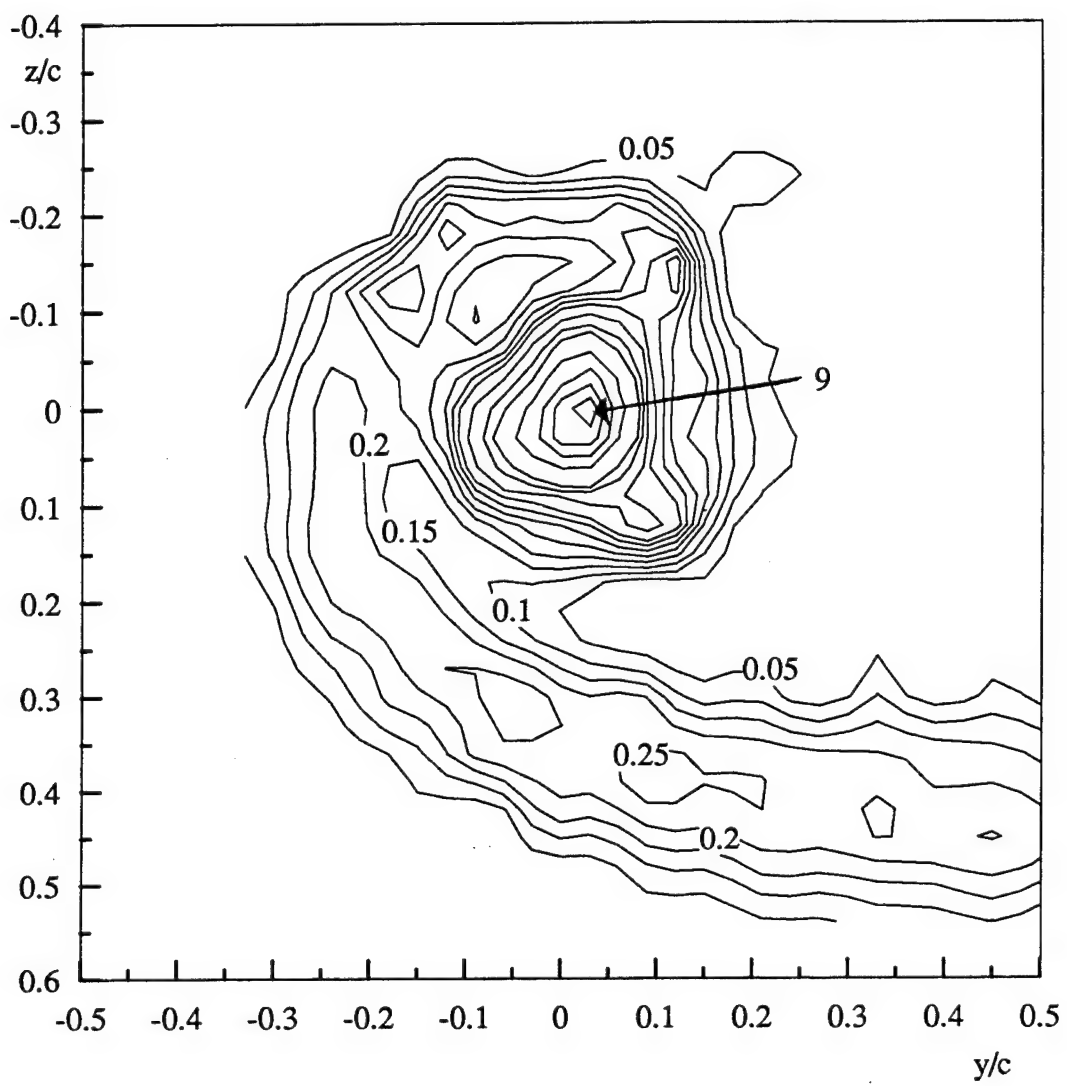


Figure 8. Contours of mean streamwise vorticity normalized on U_{ref} and c of the isolated vortex at $x/c=10$ from Devenport et al(1995).

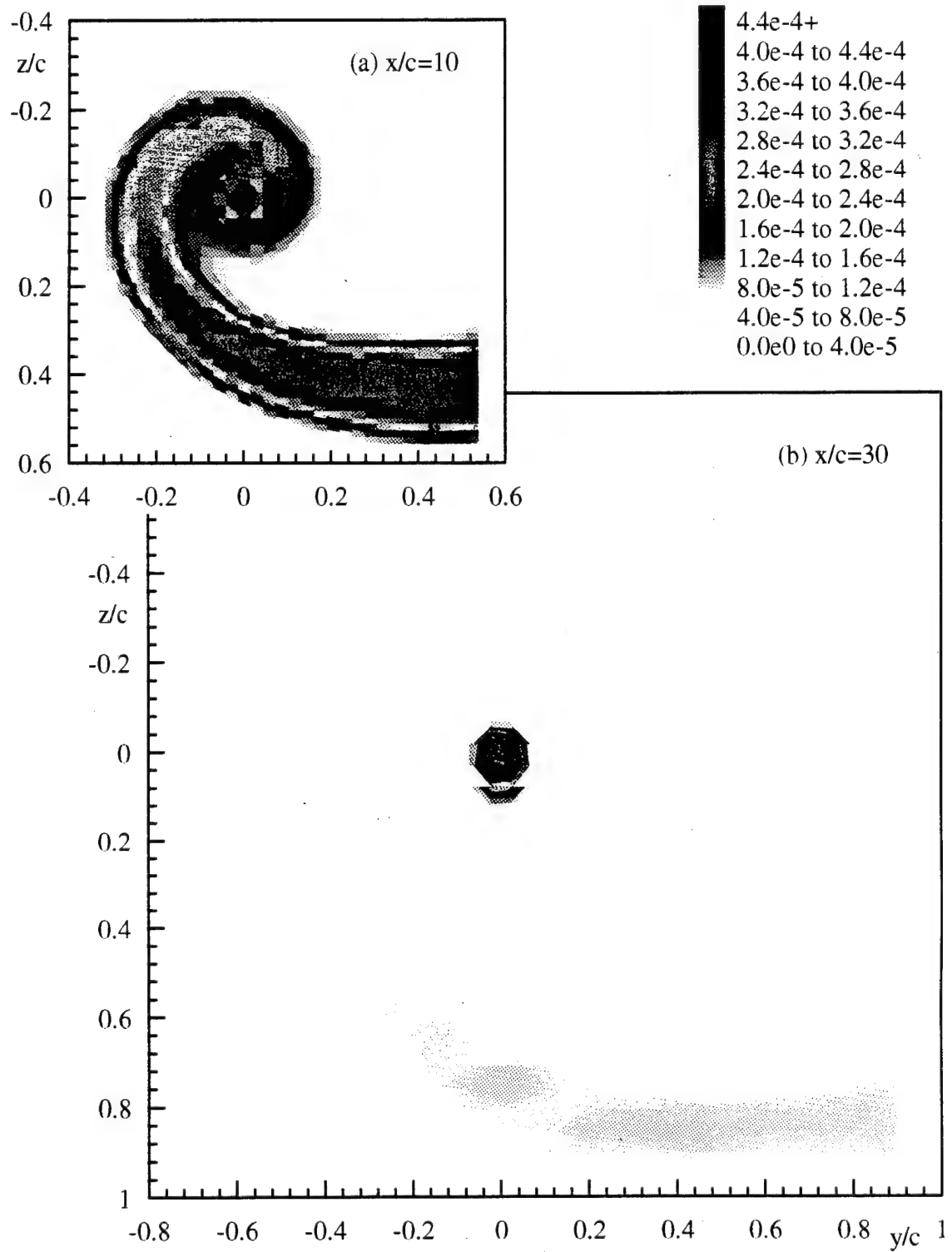


Figure 9. Contours of axial normal stress $\bar{U}^2/U_{\text{ref}}^2$ of isolated vortex at (a) $x/c=10$ and (b) $x/c=30$ from Devenport et al(1995).

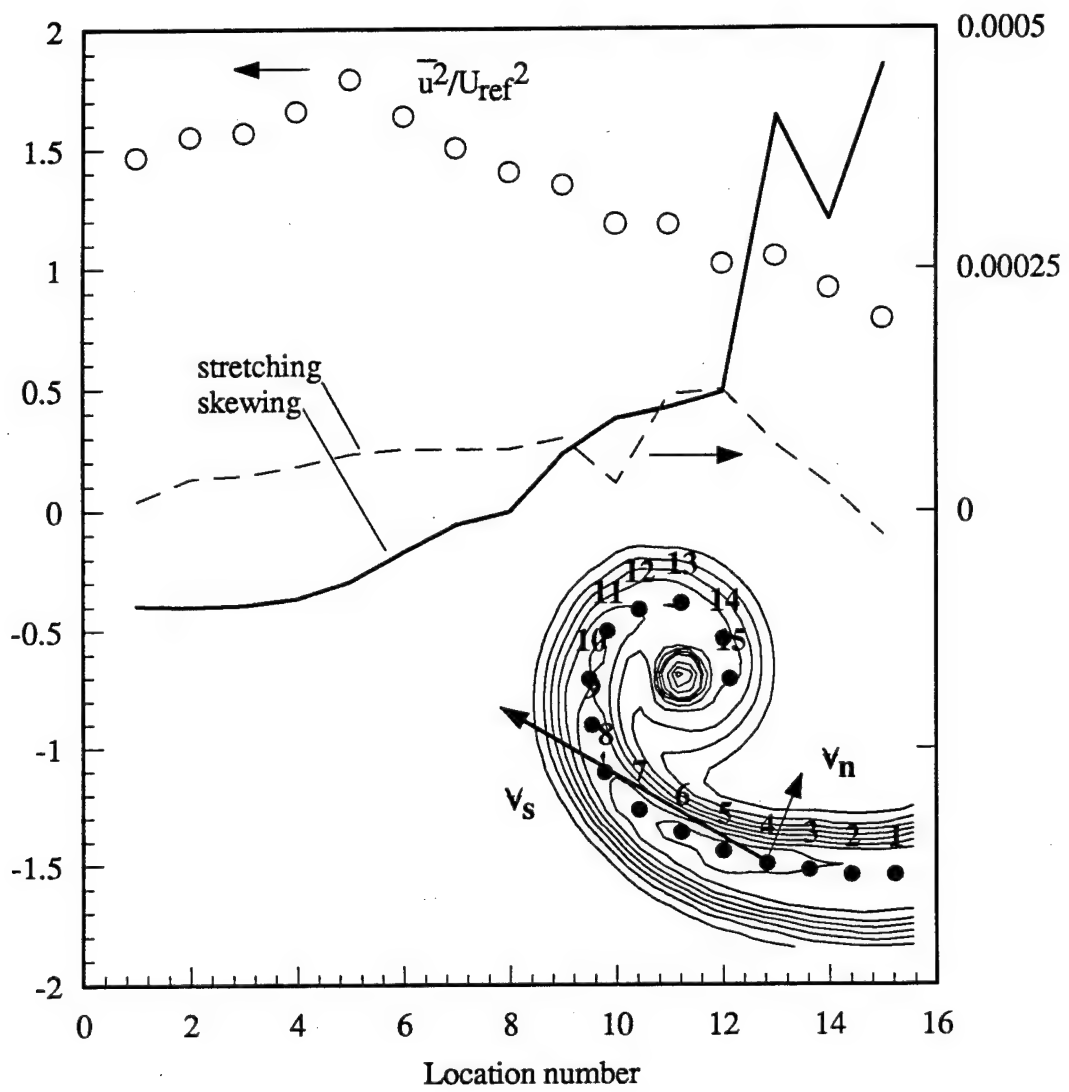


Figure 10. Rates of strain and turbulence stress on the spiral wake centerline at $x/c=10$ of isolated vortex. Strain rates normalized on the maximum axial velocity gradient in the two-dimensional portion of the wake (from Devenport et al(1995)).

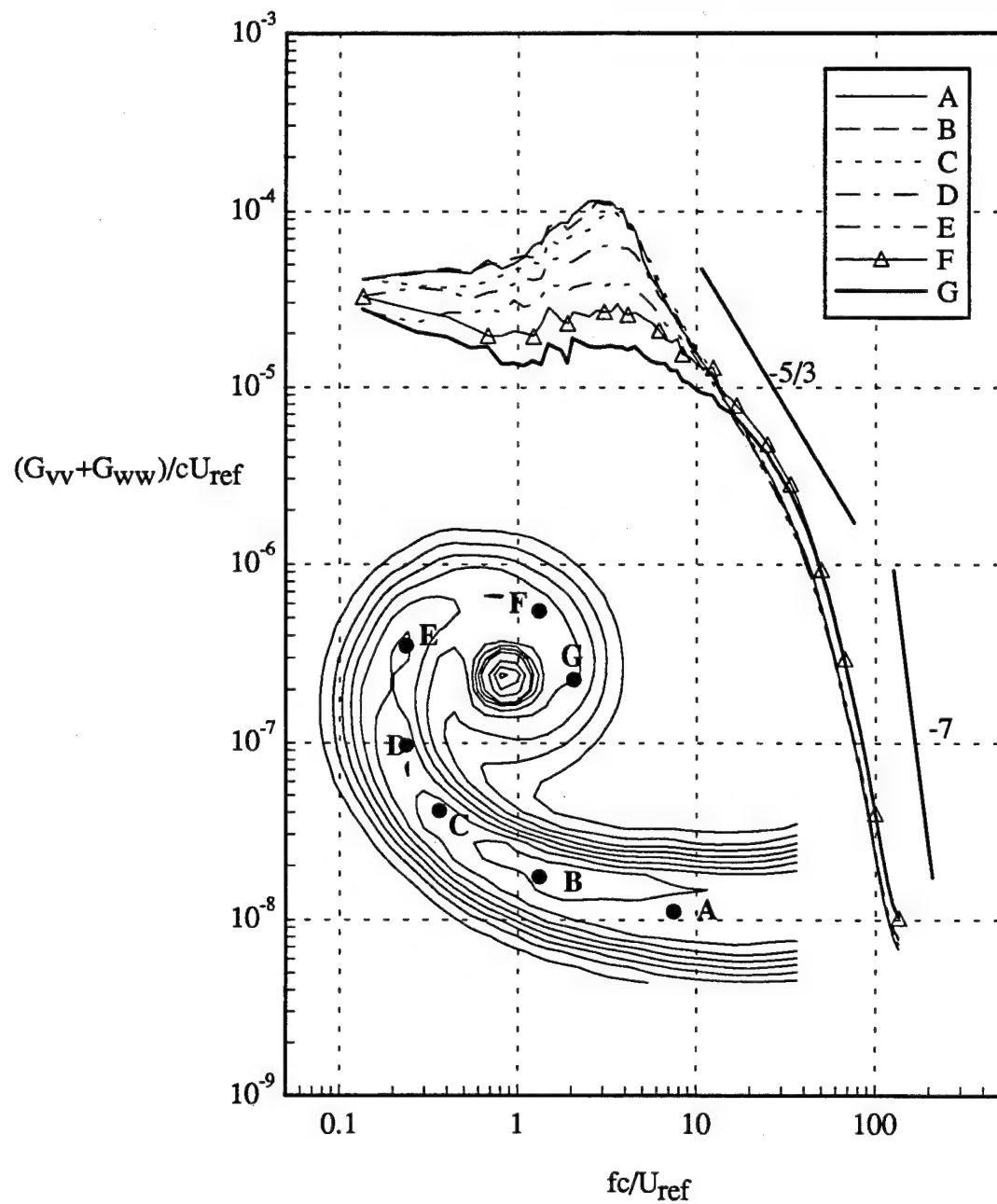


Figure 11. V +W velocity autospectra normalized on U_{ref} and c at selected locations along the spiral wake centerline at $x/c=10$ of isolated vortex from Devenport et al(1995).

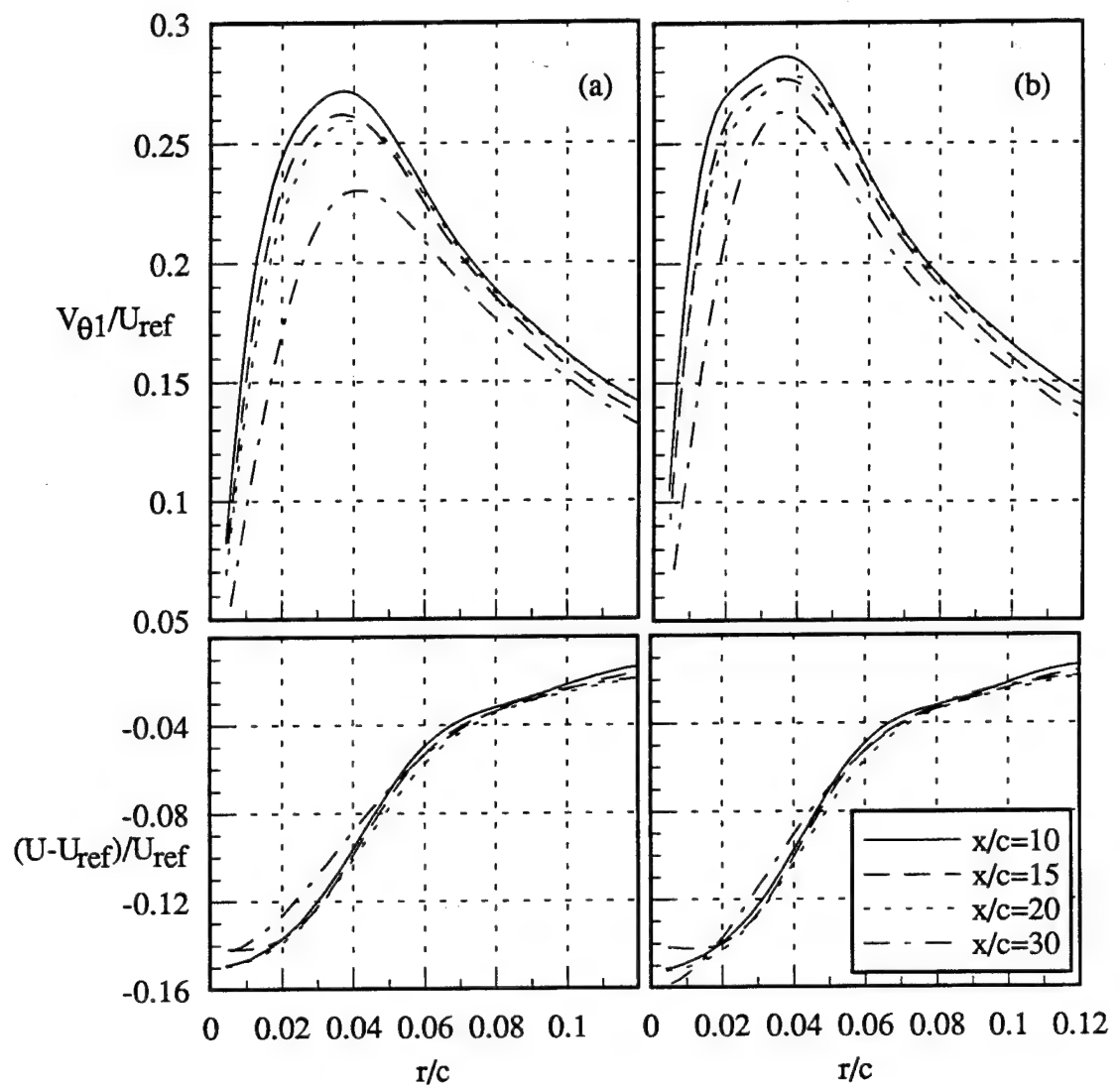


Figure 12. Vertical mean tangential and axial velocity profiles through the core of the isolated vortex (a) uncorrected and (b) corrected for the effects of wandering from Devenport et al(1995).

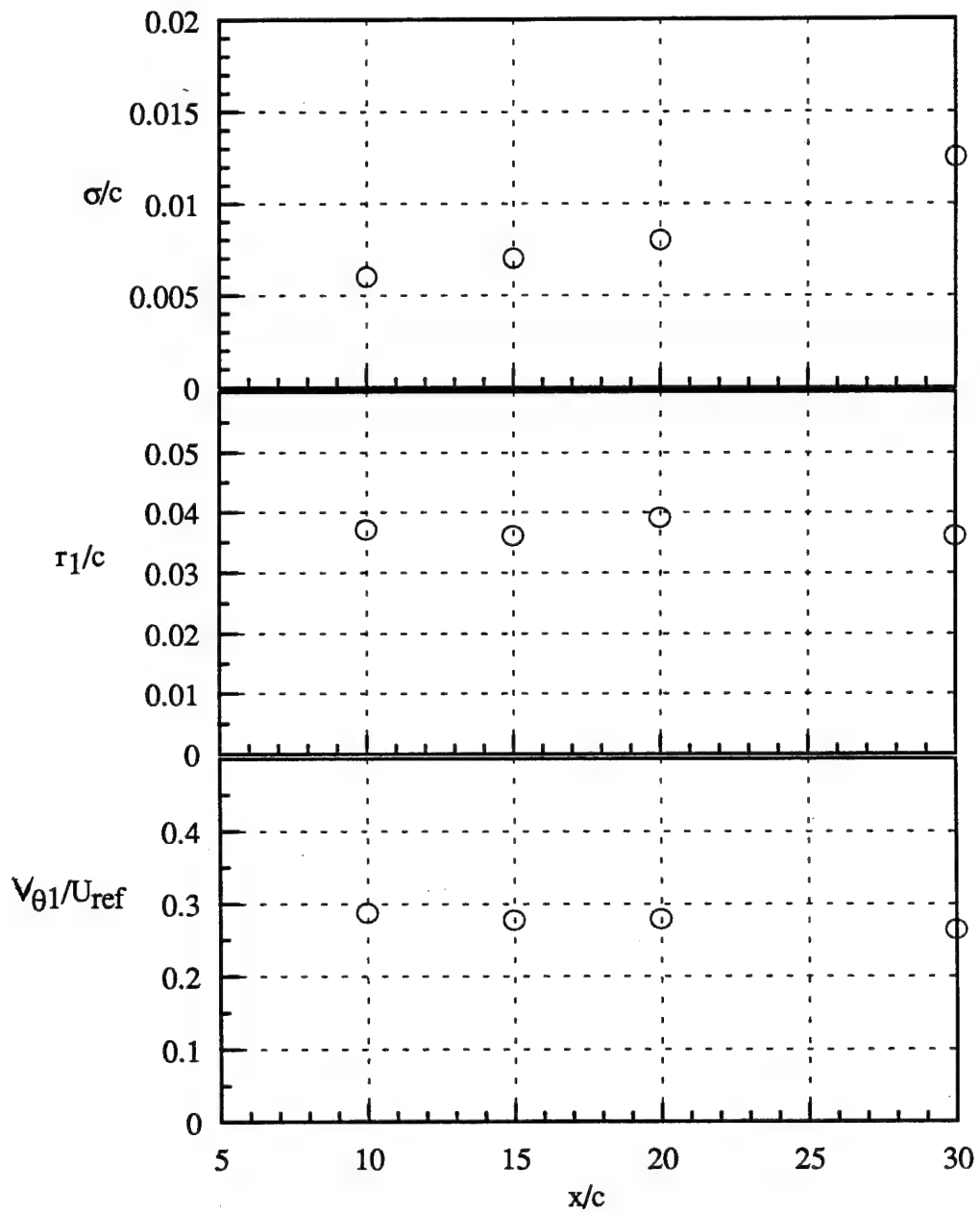


Figure 13. Variation in wandering amplitude, core radius, and peak tangential velocity with streamwise distance for isolated vortex from Devenport et al(1995)

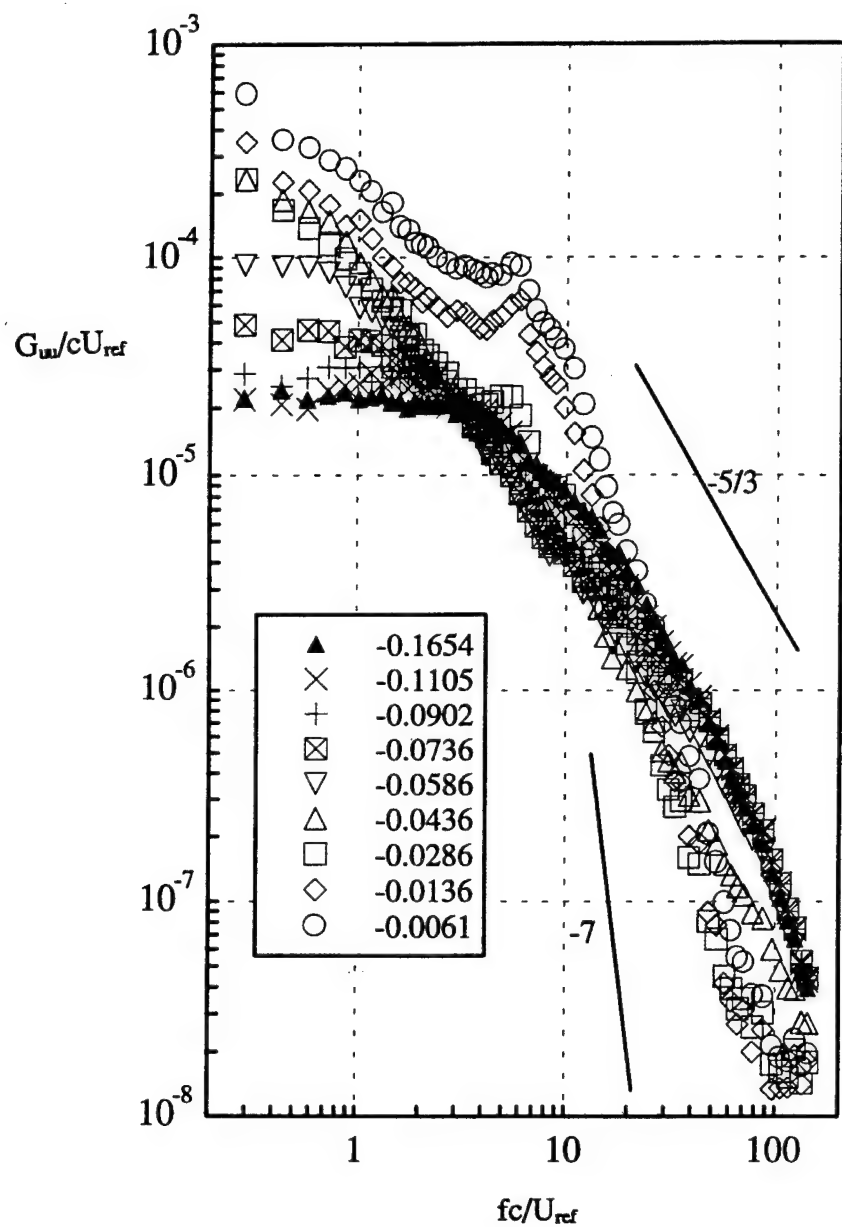


Figure 14. Axial velocity autospectra normalized on U_{ref} and c along a vertical profile from the spiral wake to the core center at $x/c=10$ of isolated vortex from Devenport et al(1995).

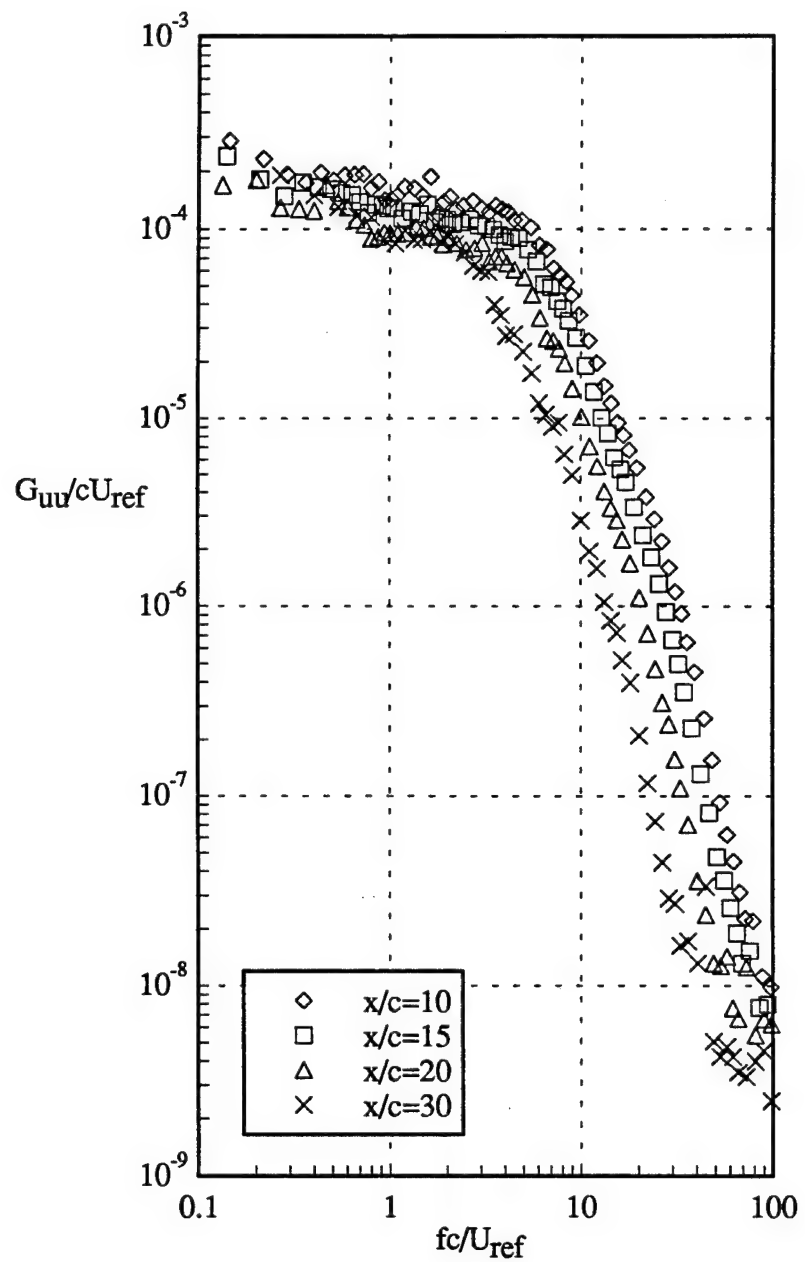


Figure 15. Variation of axial velocity autospectra at the core center normalized on U_{ref} and c with streamwise distance of isolated vortex from Devenport et al(1995)

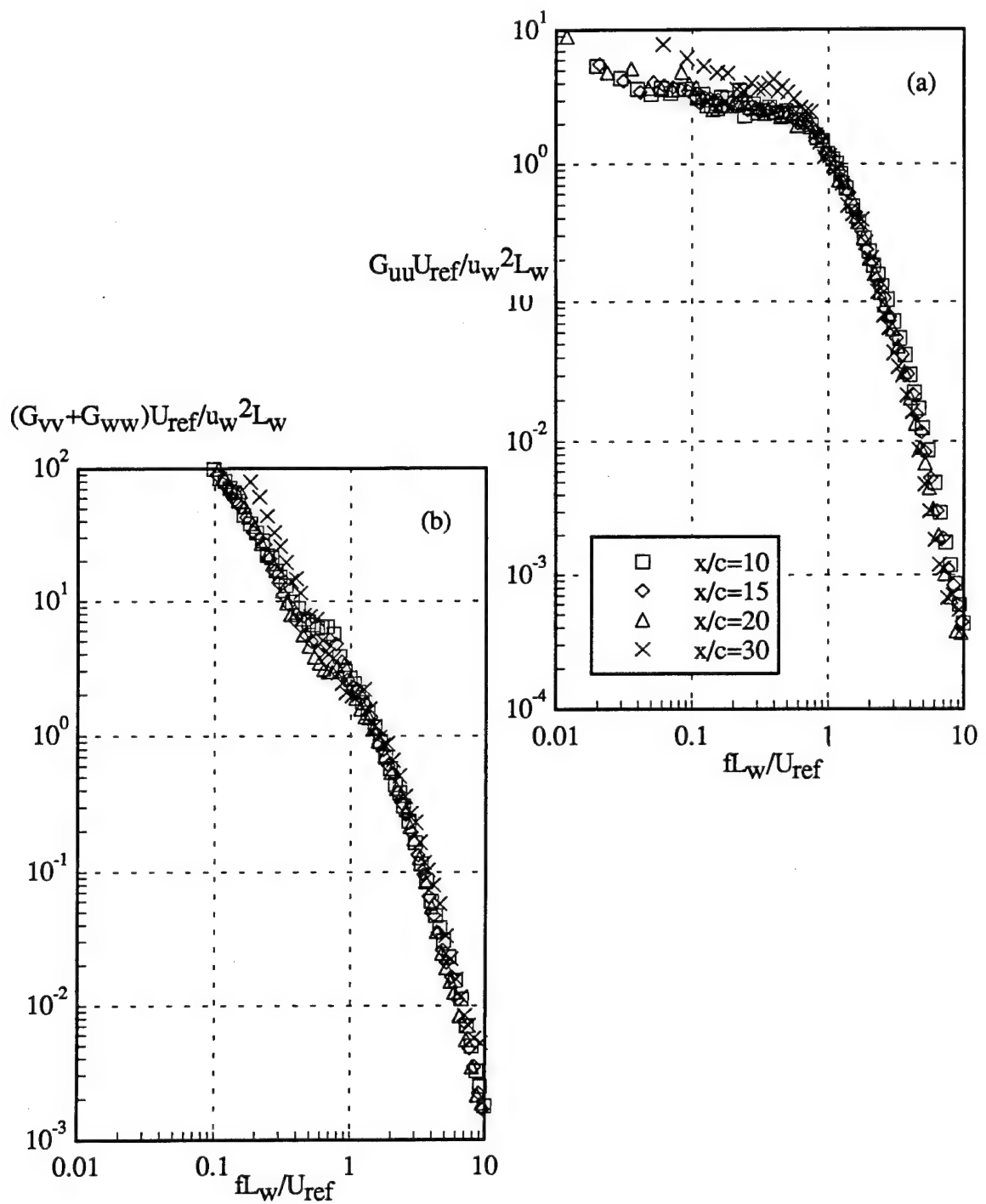


Figure 16. Velocity autospectra at the core center for all streamwise locations normalized on parameters of the two-dimensional wake of isolated vortex
 (a)U spectra, (b)V+W spectra (from Devenport et al(1995).)

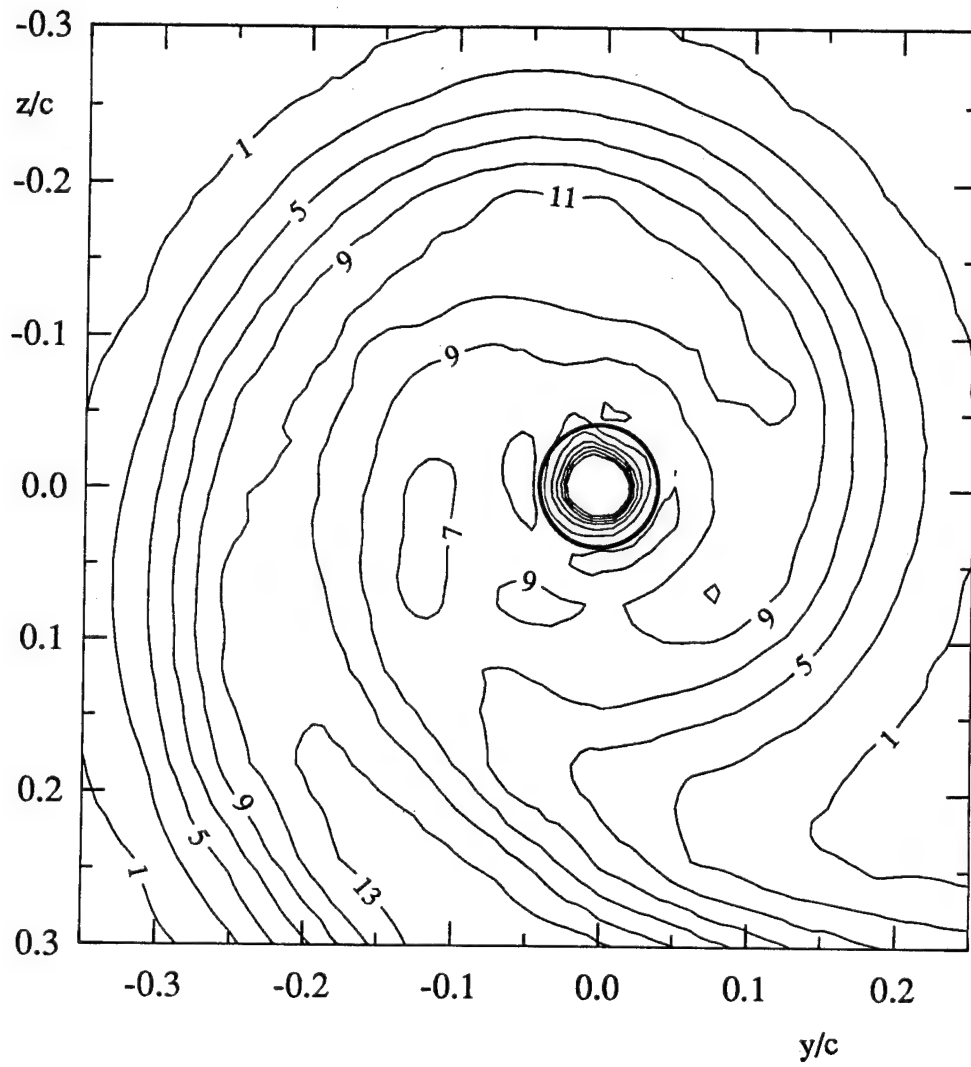


Figure 17. Contours of axial normal stress $\bar{u}^2/U_{ref}^2 \times 10^5$ filtered at $fc/U_{ref}=3$ at $x/c=10$ of isolated vortex from Devenport et al(1995).

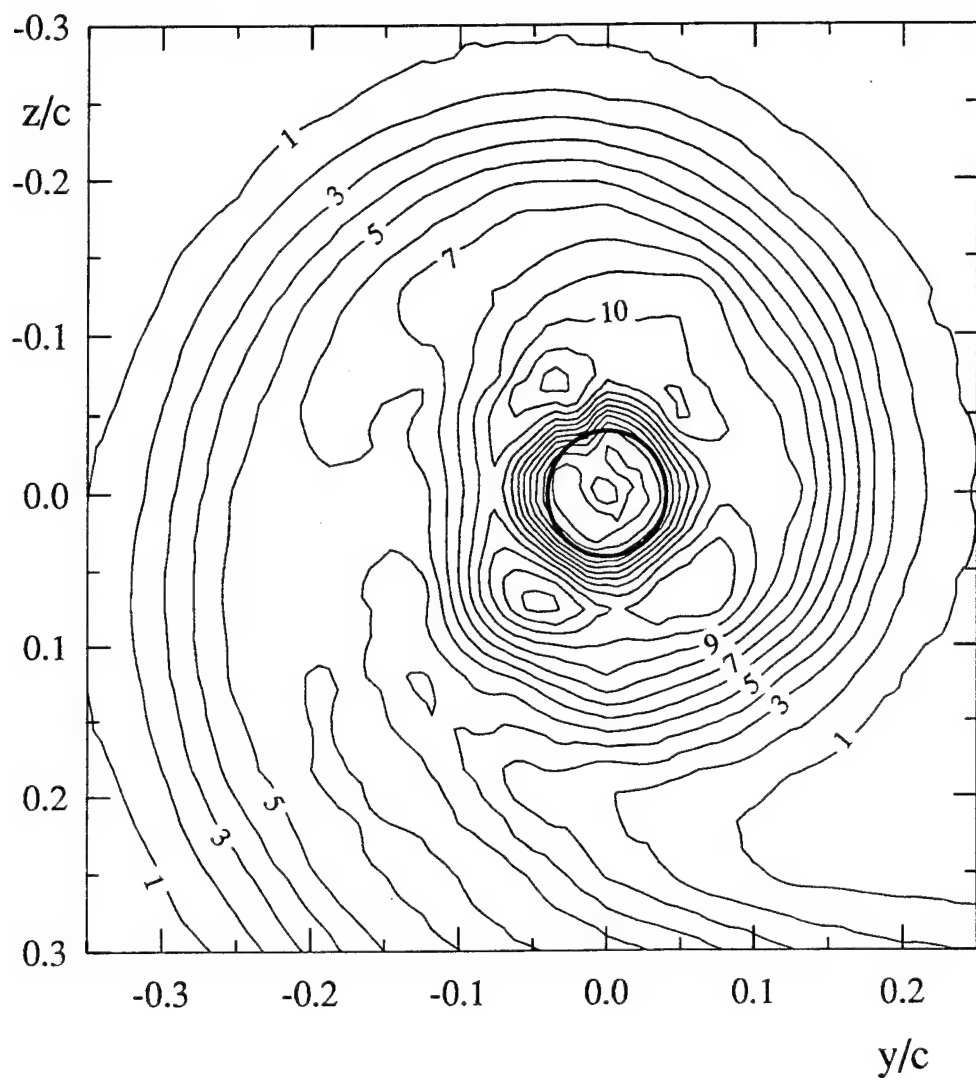


Figure 18. Contours of axial normal stress $\bar{u}^2/U_{ref}^2 \times 10^6$ filtered at $fc/U_{ref}=40$ at $x/c=10$ of isolated vortex from Devenport et al(1995).

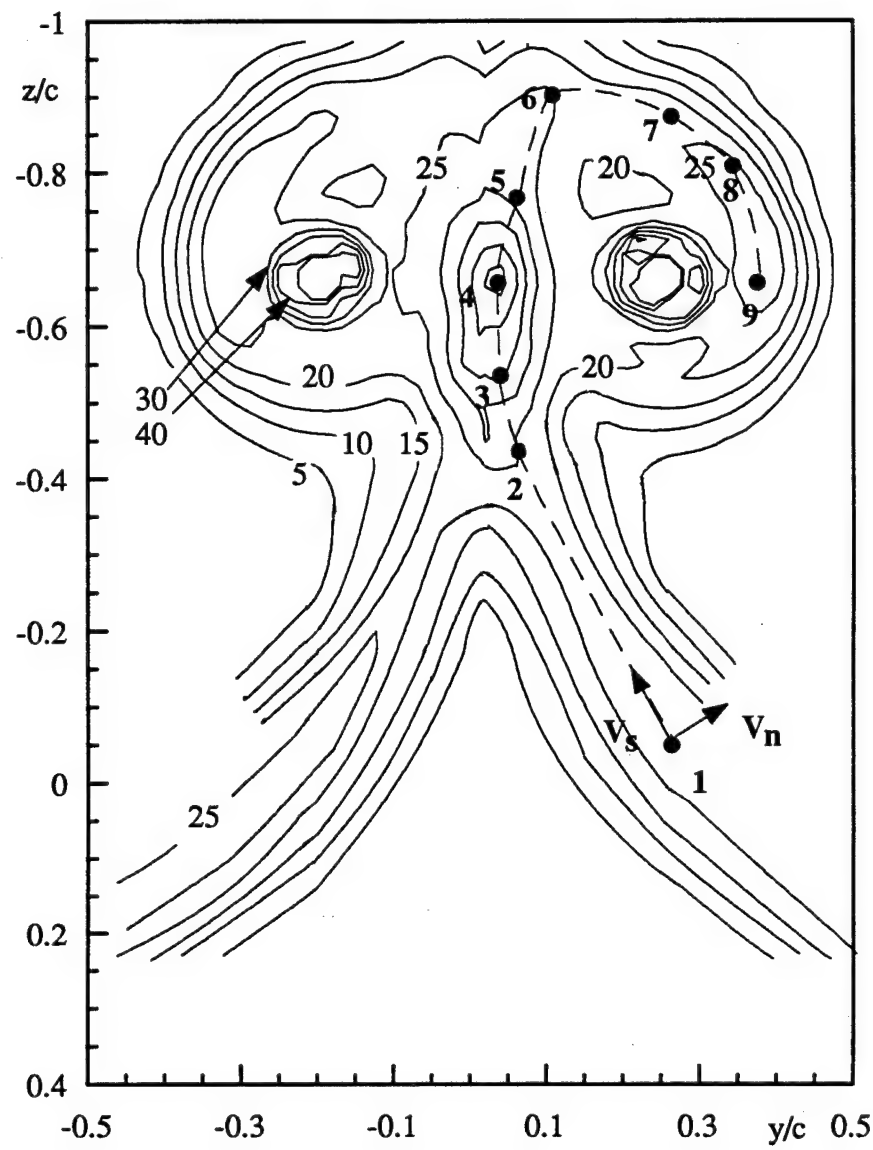


Figure 19. Contours of turbulence axial normal stress $\bar{u}^2/U_{\text{ref}}^2 \times 10^5$ at $x/c=10$ of counter-rotating pair. Dashed line denotes the spiral wake centerline. Dots indicate locations of profiles and autospectra of Figures 25 through 28.

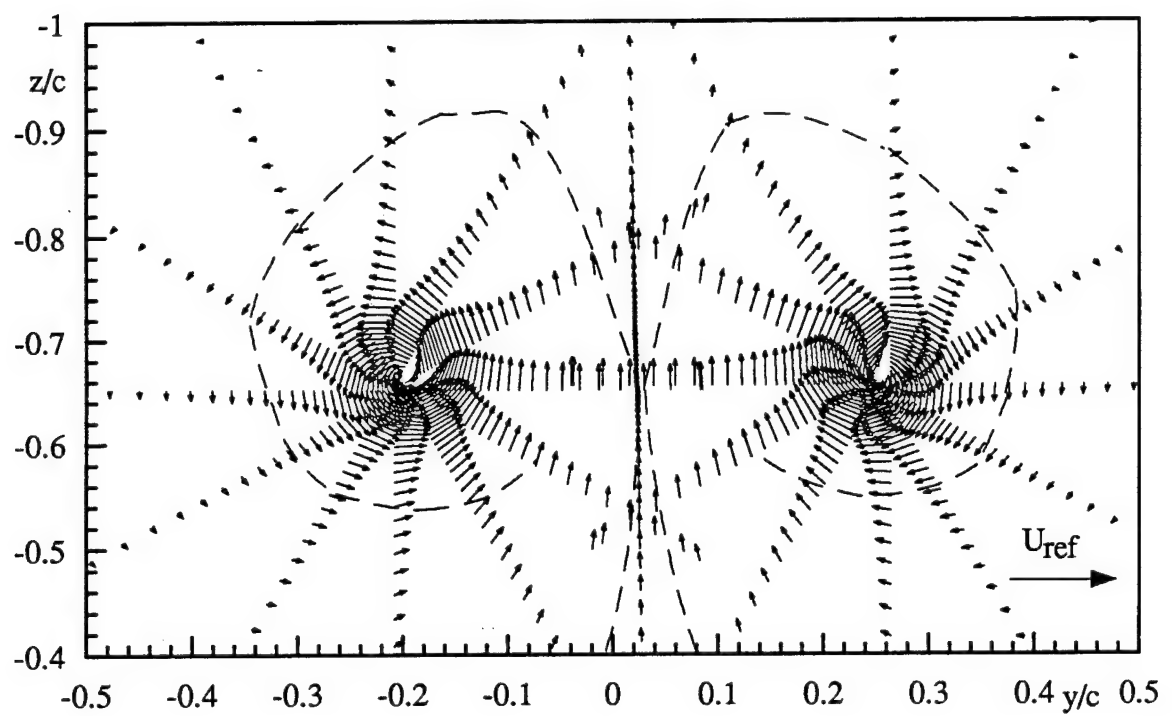


Figure 20. Mean cross-flow velocity vectors at $x/c=10$ of counter-rotating pair
Dashed lines denote spiral wake centerlines.

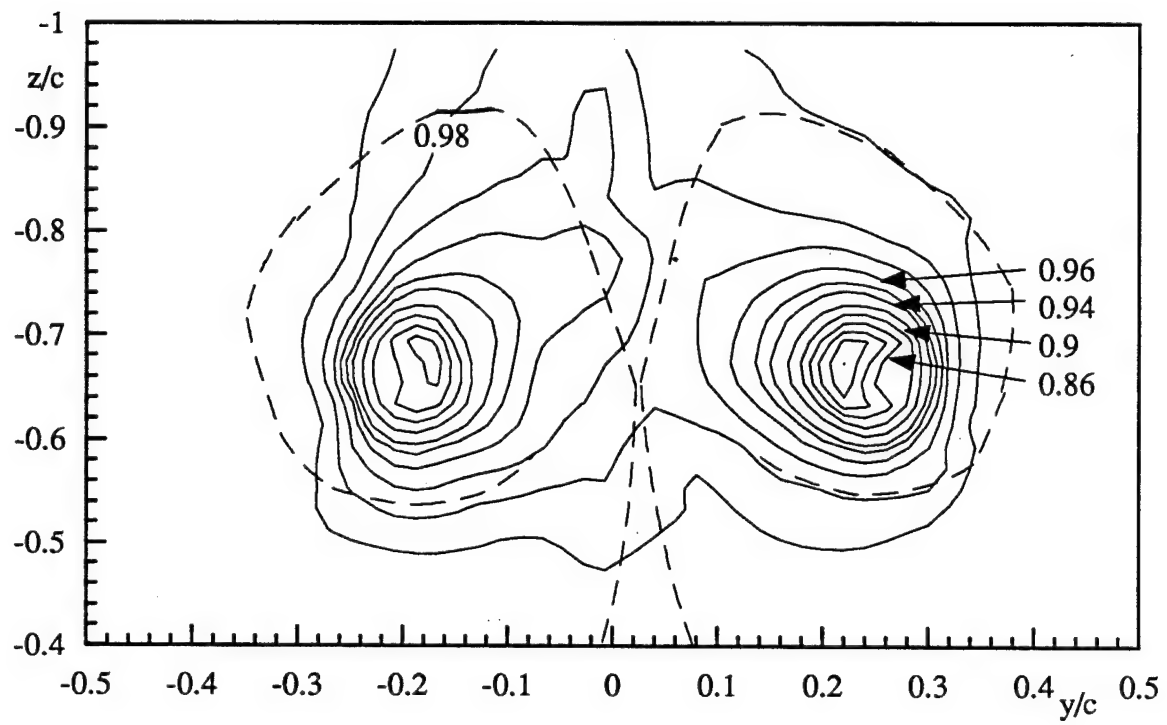


Figure 21. Contours of mean axial velocity U/U_{ref} at $x/c=10$ of counter-rotating pair
Dashed lines denotes spiral wake centerlines.

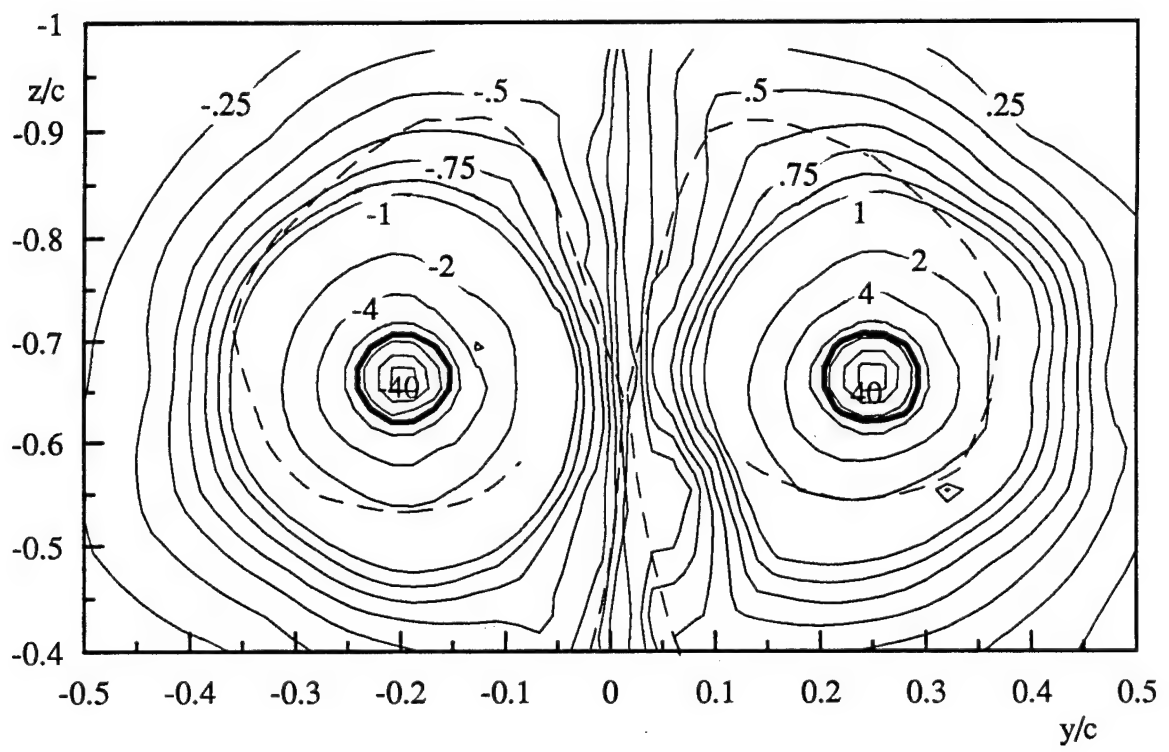


Figure 22. Contours of mean streamwise vorticity normalized on U_{ref} and c at $x/c=10$ of counter-rotating pair. Dashed lines denote spiral wake centerlines.

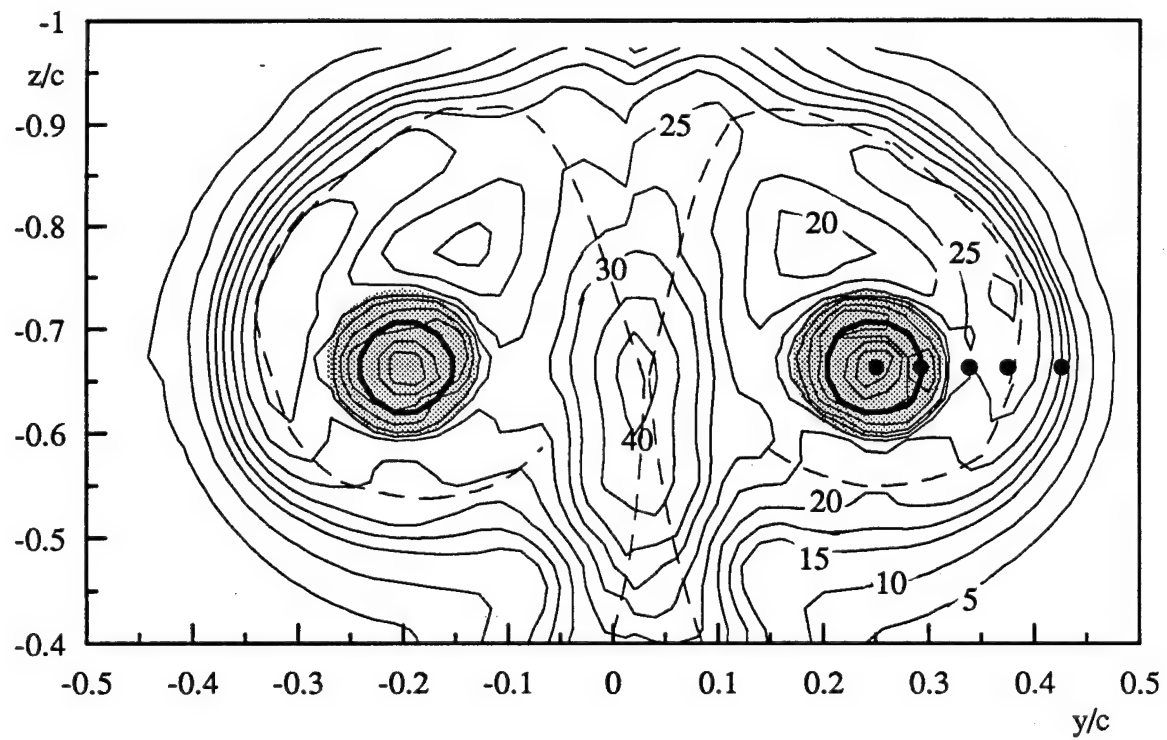


Figure 23. Contours of turbulence axial normal stress $\bar{u}^2/U_{ref}^2 \times 10^5$ at $x/c=10$ of counter-rotating pair. Dots show locations of autospectra in Figures 32-34. Shaded regions indicate where wandering has contributed more than 30% to normal stresses. Dashed lines denote spiral wake centerlines.

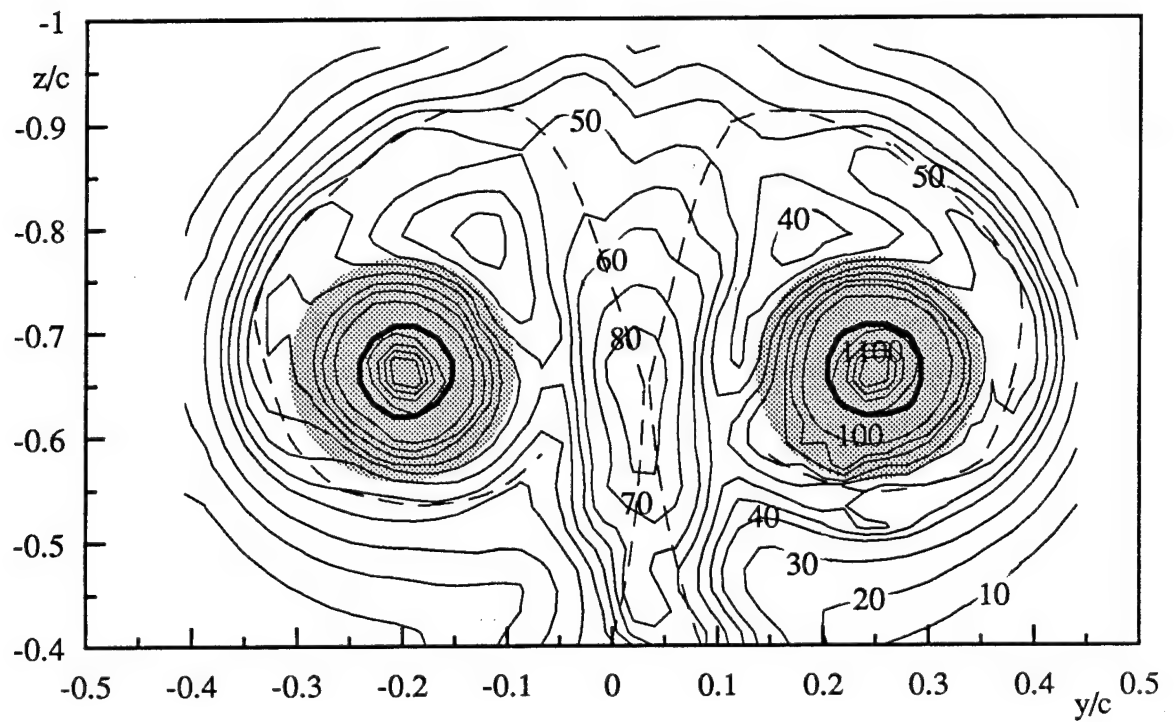


Figure 24. Contours of turbulence cross-flow normal stress sum $(\bar{v}^2 + \bar{w}^2)/U_{\text{ref}}^2 \times 10^5$ at $x/c = 10$ of counter-rotating pair. Shaded regions indicate where wandering has contributed more than 30% to the normal stresses. Dashed lines denote spiral wake centerlines.

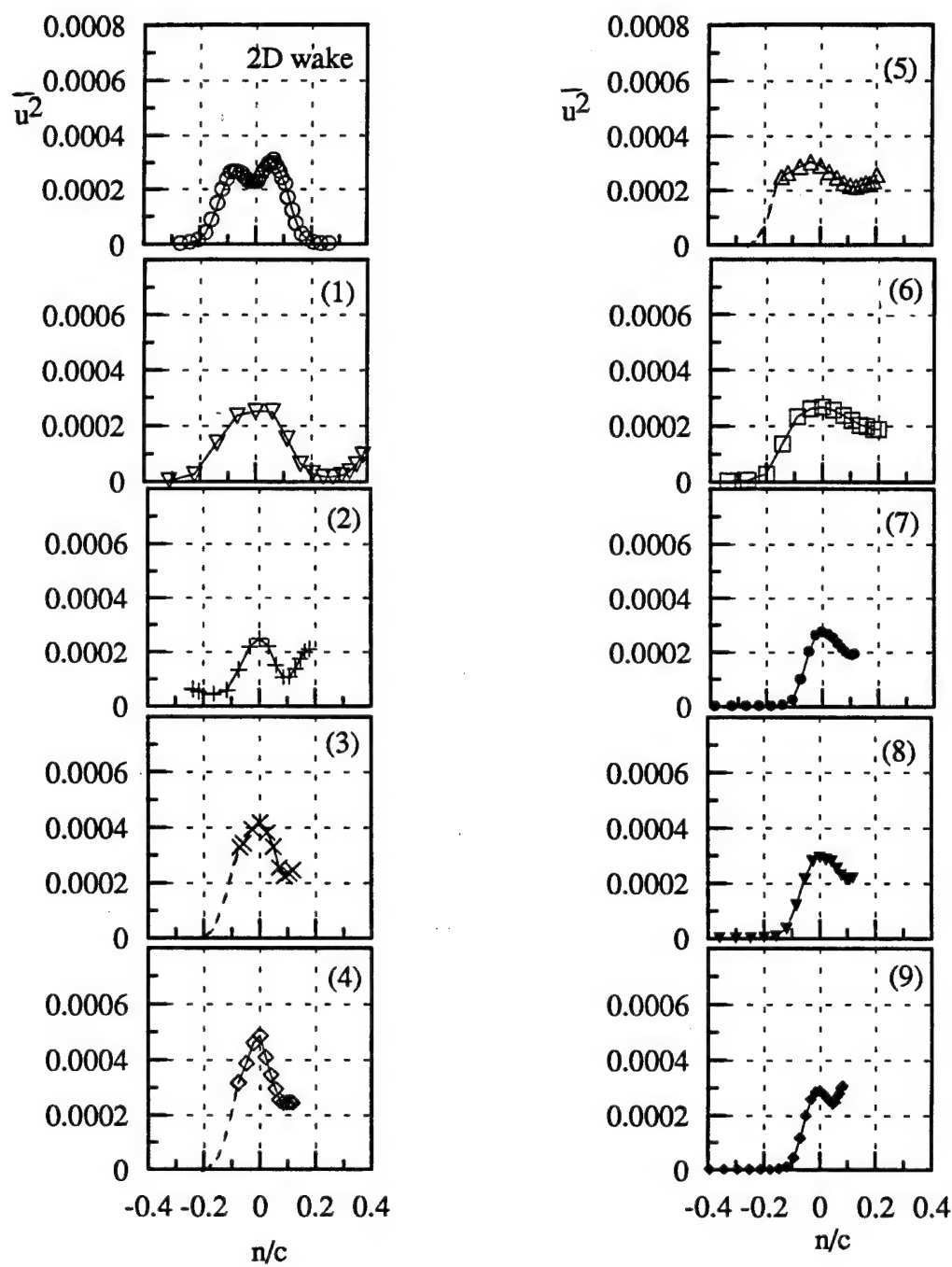


Figure 25. Profiles of axial normal stress $\bar{u}^2 / U_{\text{ref}}^2$ at selected locations along the spiral-wake centerline at $x/c=10$ of counter-rotating pair. Numbers indicate locations along wake centerline indicated by the dots in Figure 19.

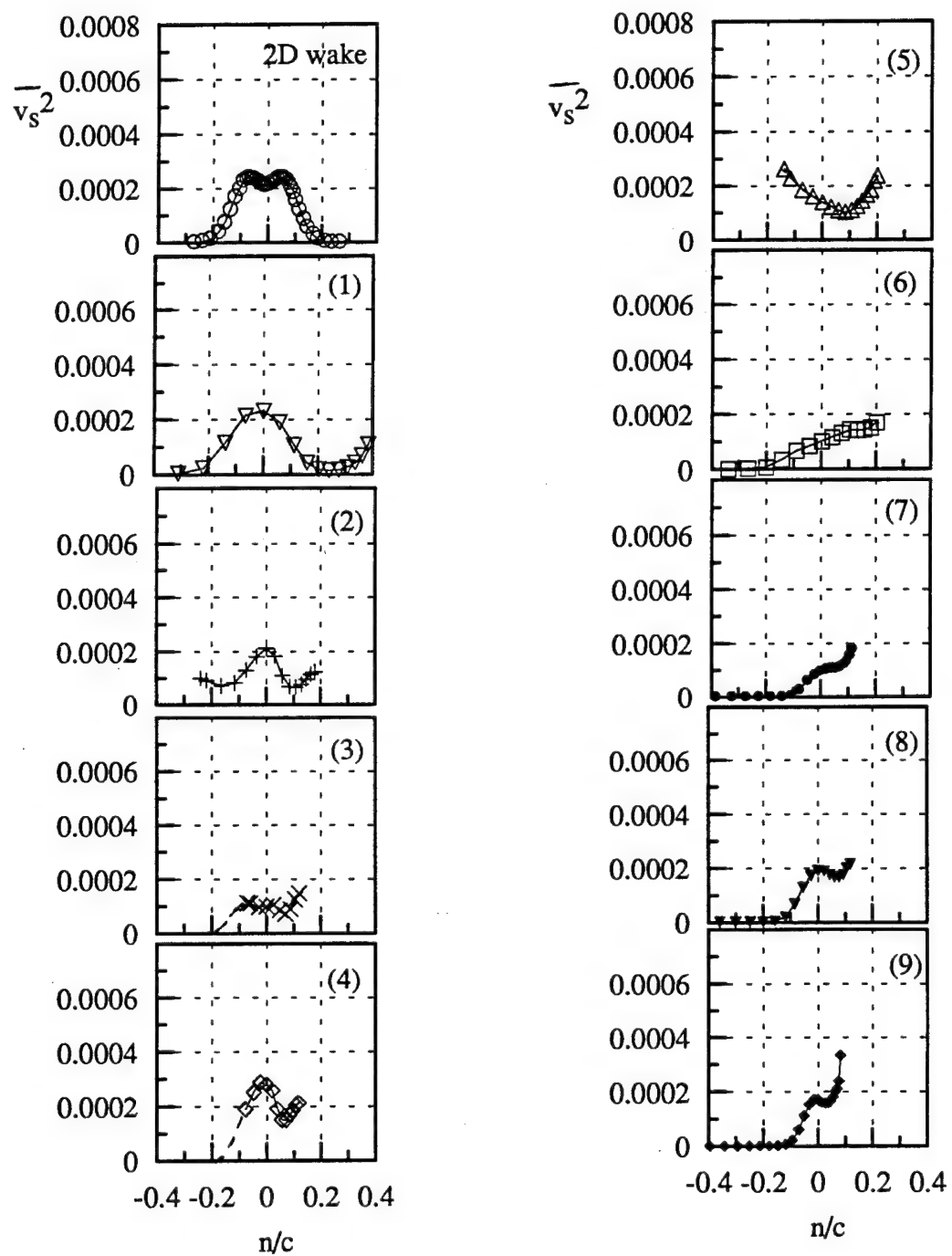


Figure 26. Profiles of normal stress \bar{v}_s^2/U_{ref}^2 parallel to wake centerline at selected locations along the spiral wake centerline at $x/c=10$ of counter-rotating pair. Numbers indicate locations along wake centerline indicated by the dots in Figure 19.

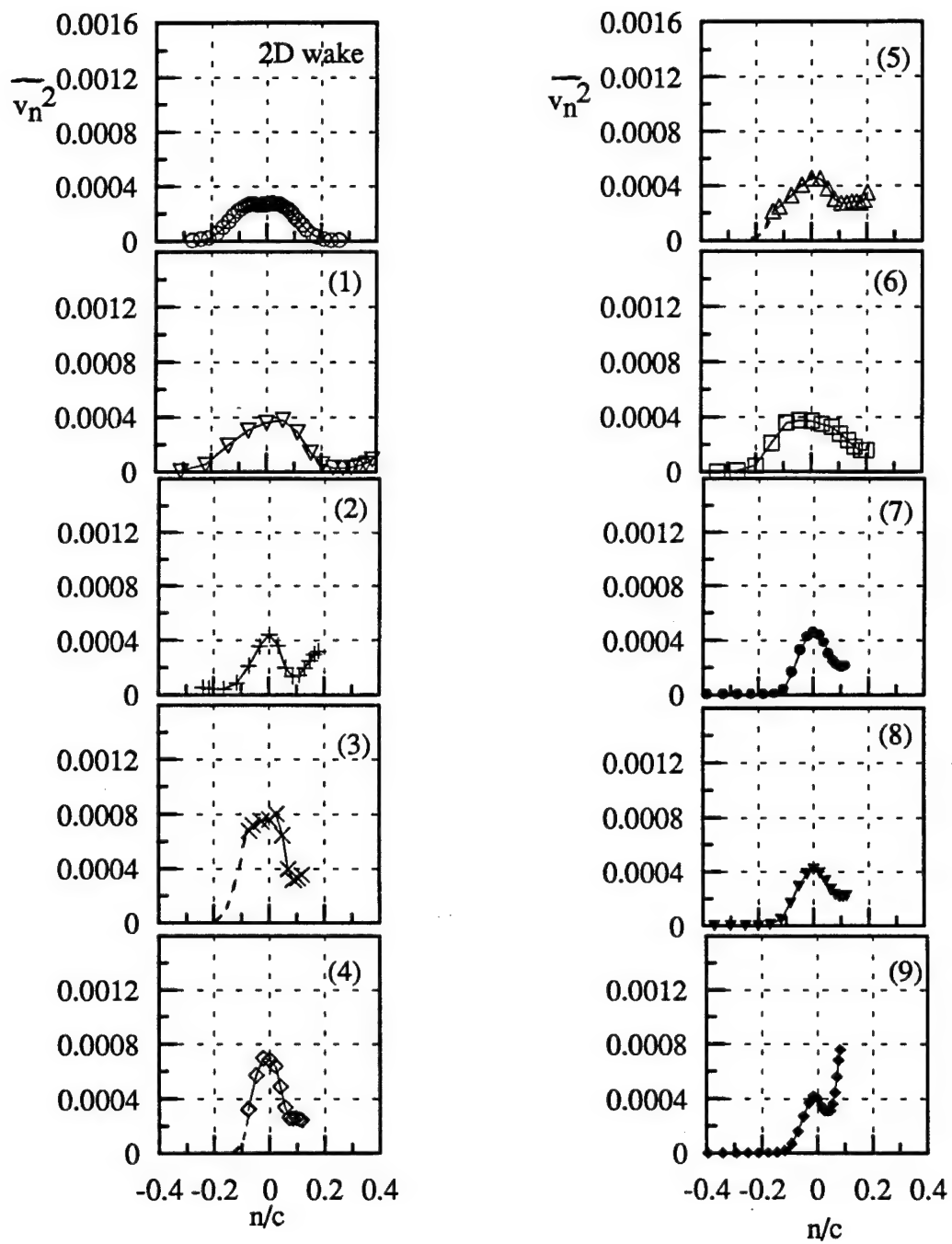


Figure 27. Profiles of normal stress \bar{v}_n^2/U_{ref}^2 normal to wake centerline at selected locations along the spiral wake centerline at $x/c=10$ of counter-rotating pair. Numbers indicate locations along wake centerline indicated by the dots in Figure 19.

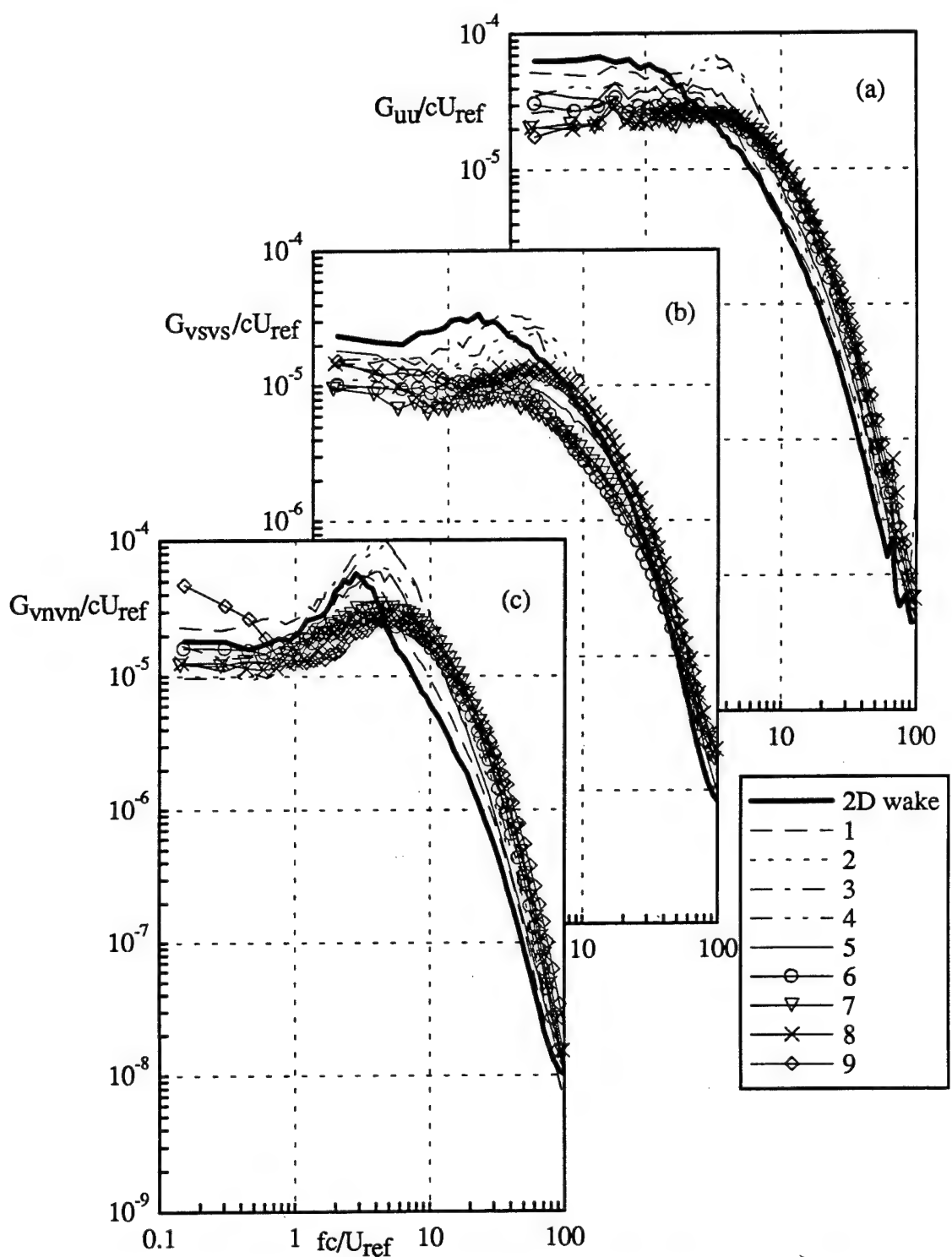


Figure 28 Velocity autospectra in coordinates aligned with the spiral-wake centerline at $x/c=10$ of counter-rotating pair (a) U spectra, (b) V_s spectra, (c) V_n spectra. Locations indicated by dots in Figure 19.

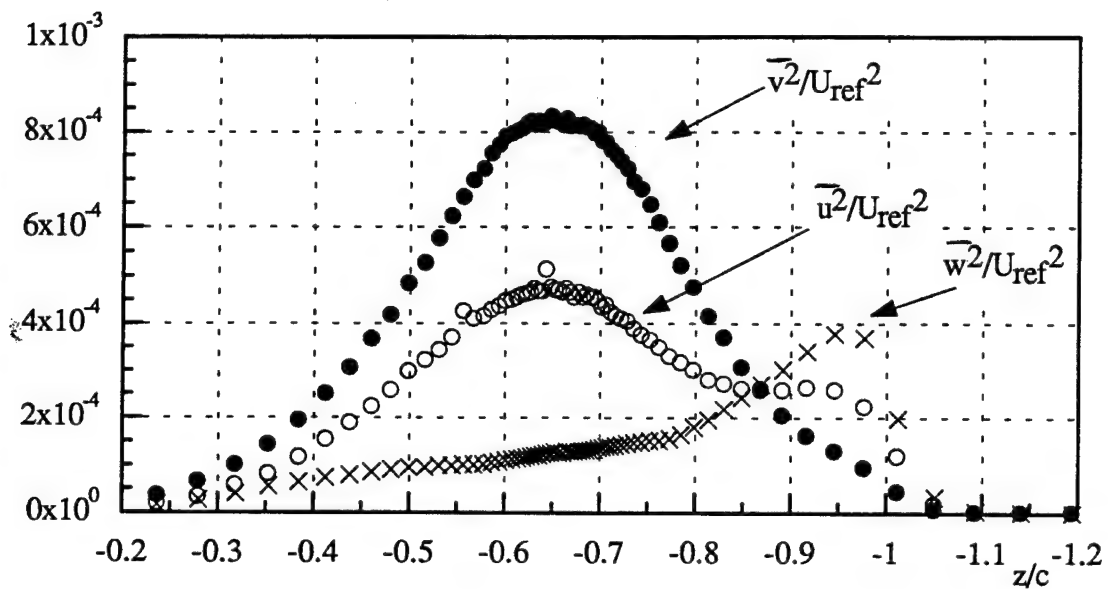


Figure 29. Normal stress profiles along the plane of symmetry between the vortices at $x/c=10$ of counter-rotating pair

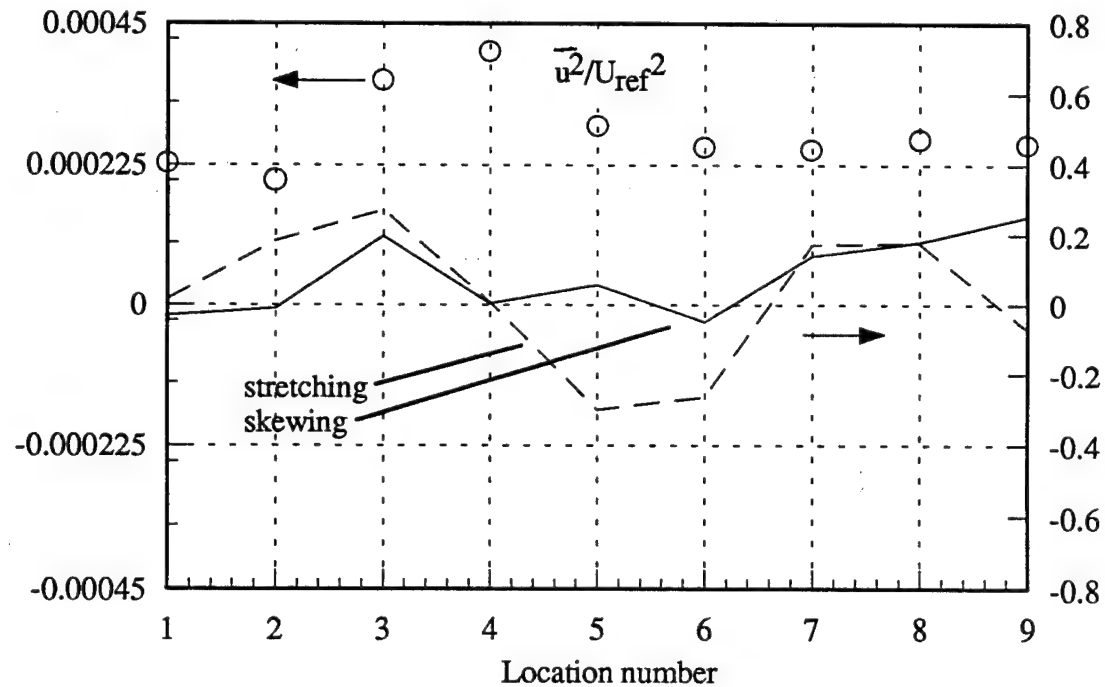


Figure 30. Rates of strain and turbulence stress at the spiral wake centerline at $x/c=10$ of counter-rotating pair. Strain rates normalized on maximum axial velocity gradient in the two-dimensional portion of the wake. Locations indicated by the dots in Figure 19.

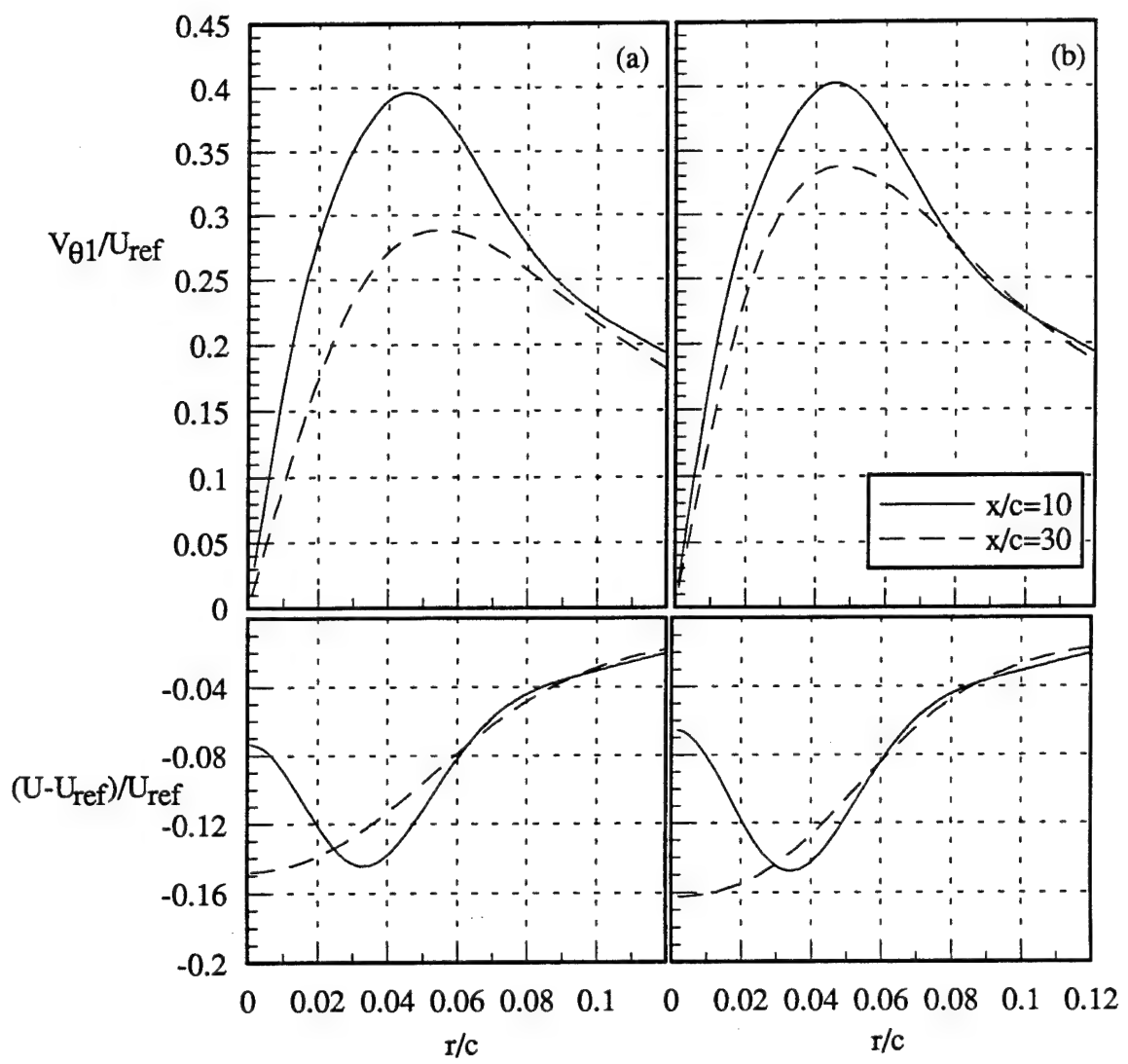


Figure 31. Mean tangential and axial velocity profiles through the right-hand core of counter-rotating pair (a) uncorrected and (b) corrected for the effects of wandering.

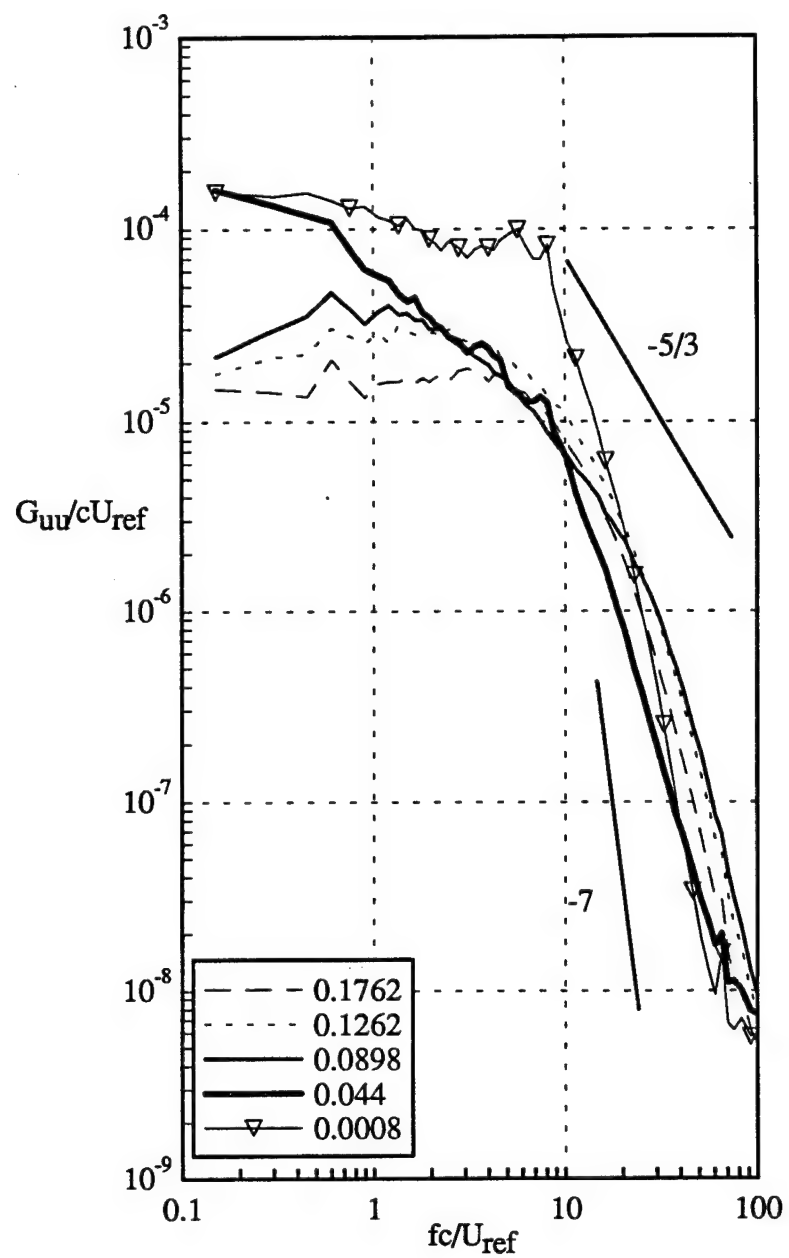


Figure 32. Autospectra of U velocity fluctuations at various spanwise locations along a horizontal profile through the right-hand core center indicated by the dots in Figure 23 at $x/c=10$ of counter-rotating pair. Locations relative to the core center at $y/c=0.25$.

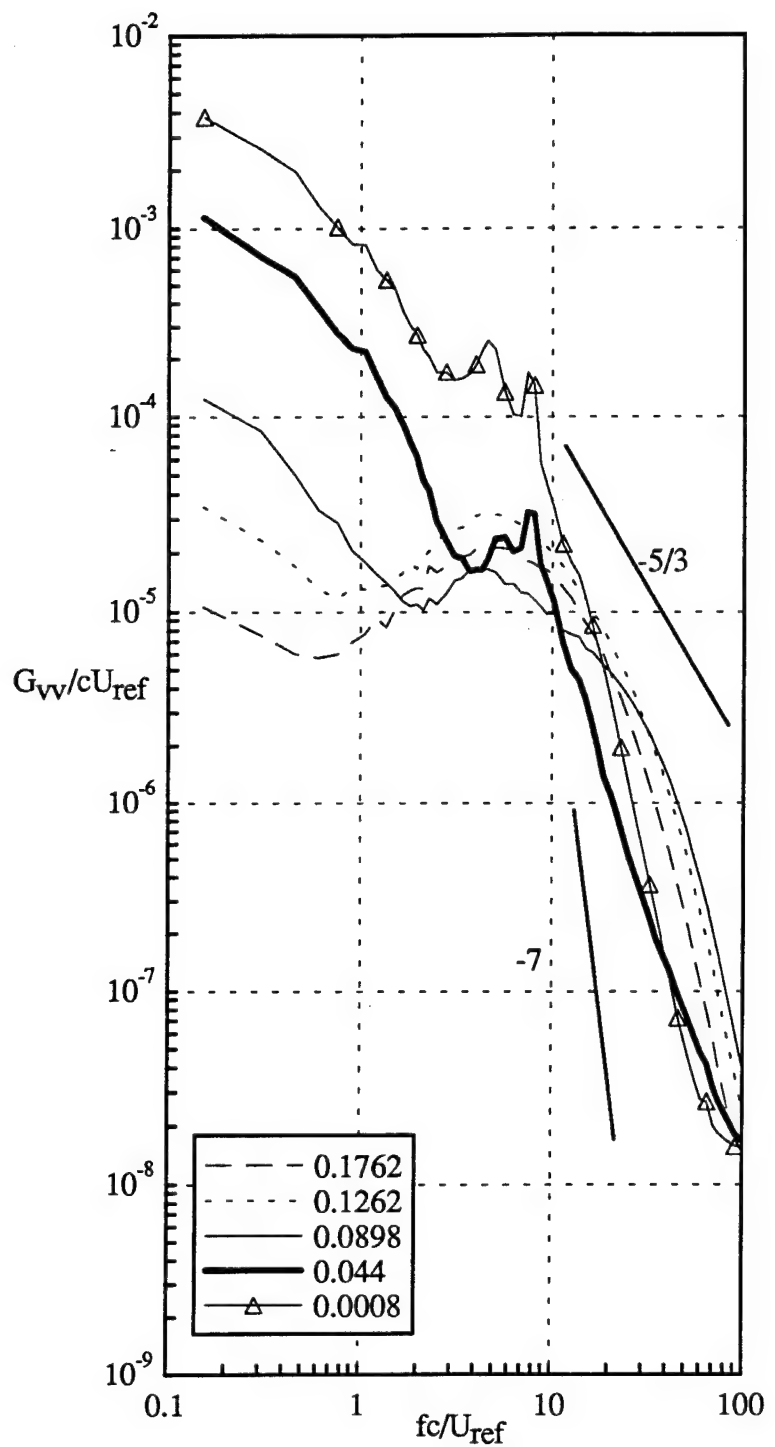


Figure 33. Autospectra of V velocity fluctuations at various spanwise locations along a horizontal profile through the right-hand core center indicated by the dots in Figure 23 at $x/c=10$ of counter-rotating pair. Locations relative to the core center at $y/c=0.25$.

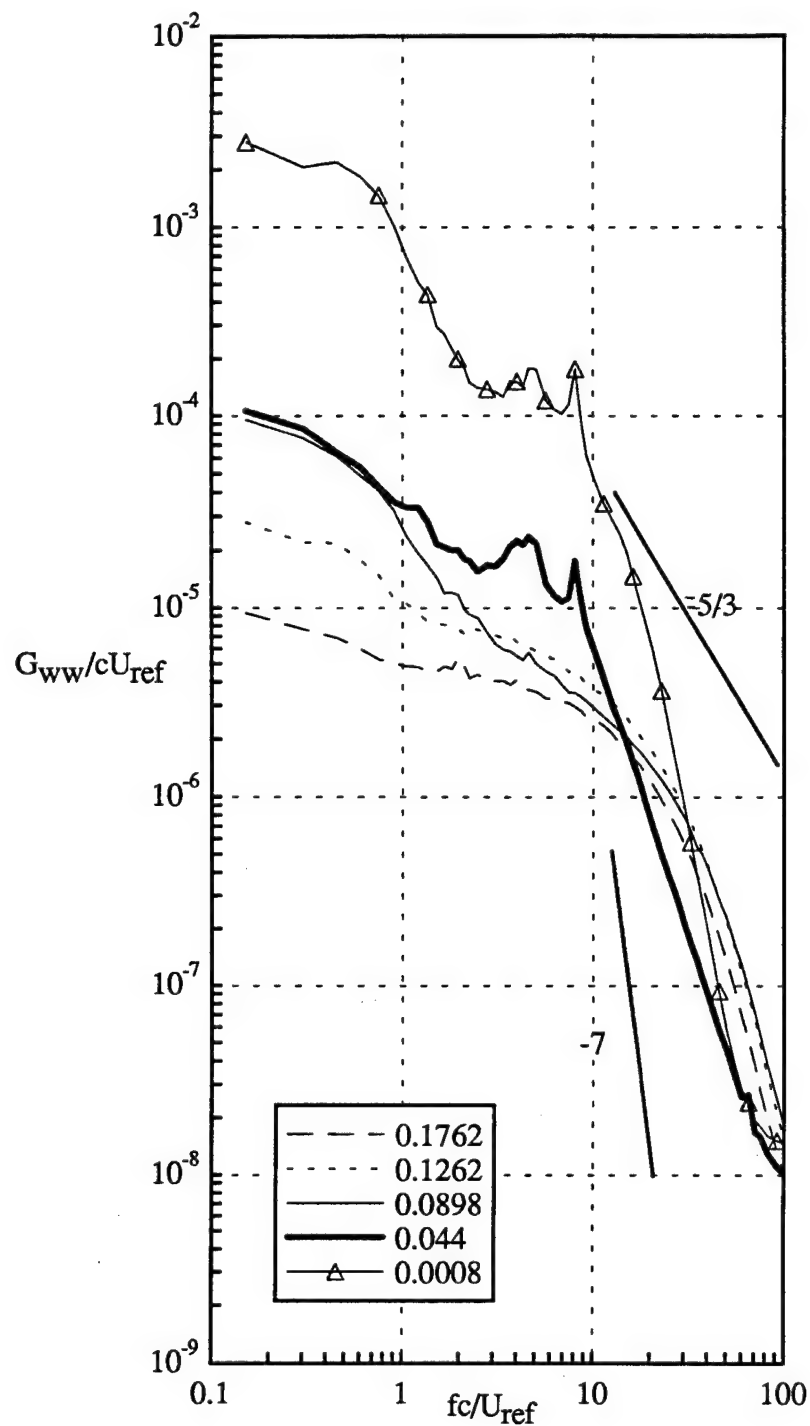


Figure 34. Autospectra of W velocity fluctuations at various spanwise locations along a horizontal profile through the right-hand core center indicated by the dots in Figure 23 at $x/c=10$ of counter-rotating pair. Locations relative to the core center at $y/c=0.25$.

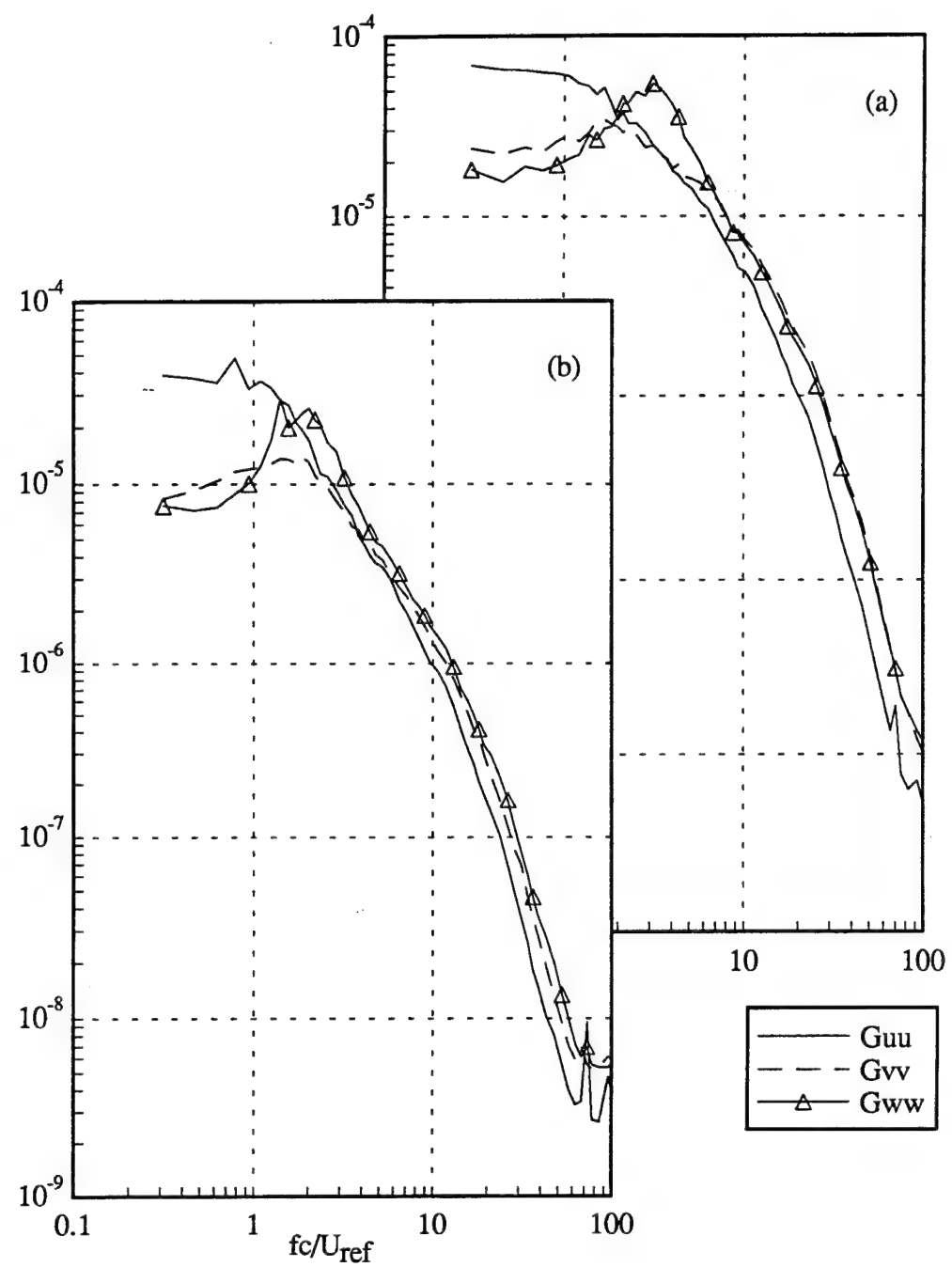


Figure 35. Autospectra at the centerline of the two-dimensional portion of the spiral wake of the counter-rotating pair at (a) $x/c=10$, (b) $x/c=30$ normalized on U_{ref} and c .

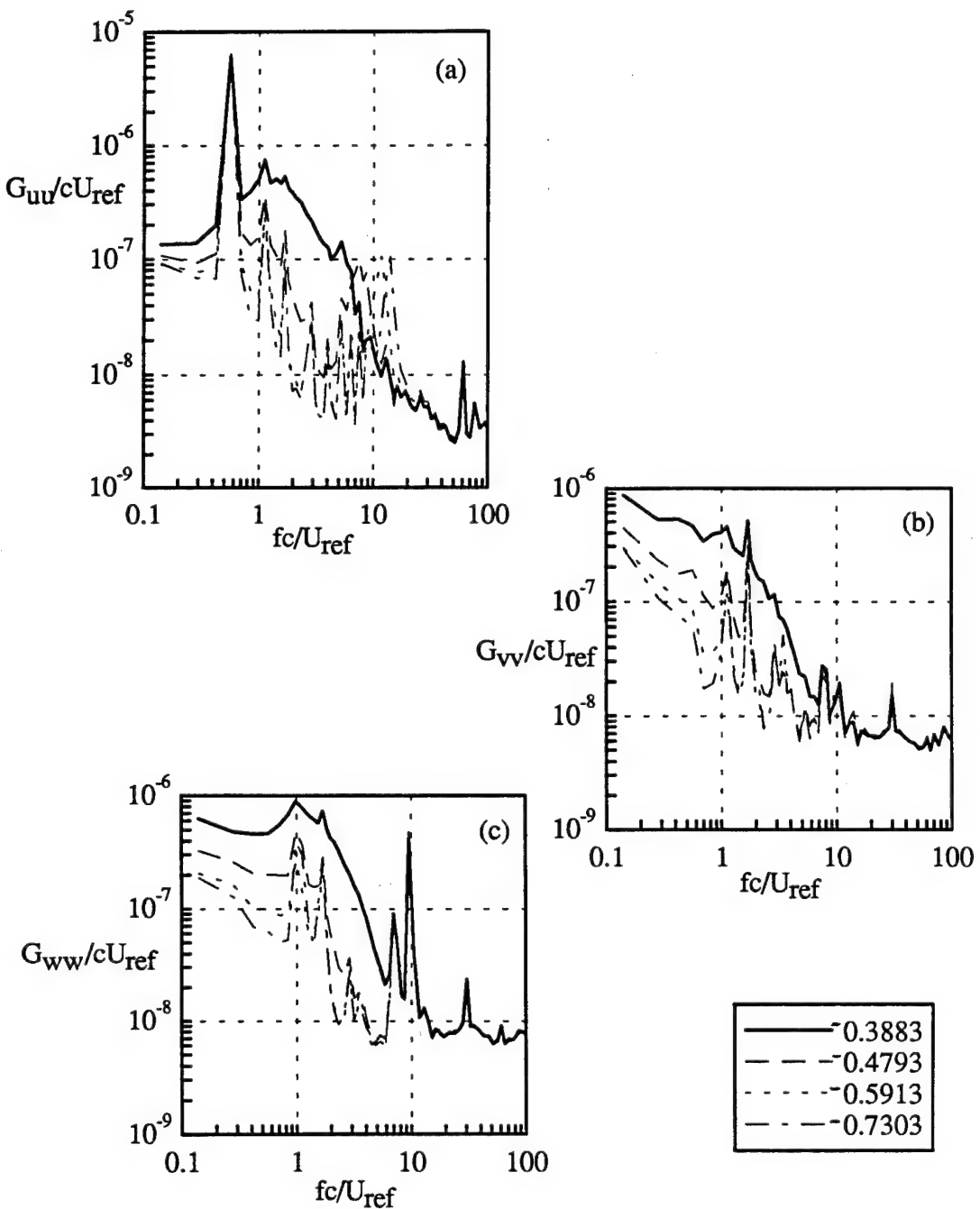


Figure 36. Autospectra at locations moving from the edge of the turbulent region into the free-stream along a vertical profile through the right-hand core center at $x/c=10$ of counter-rotating pair (a)U spectra, (b)V spectra, (c) W spectra. Locations relative to core center at $z/c=-0.66$.

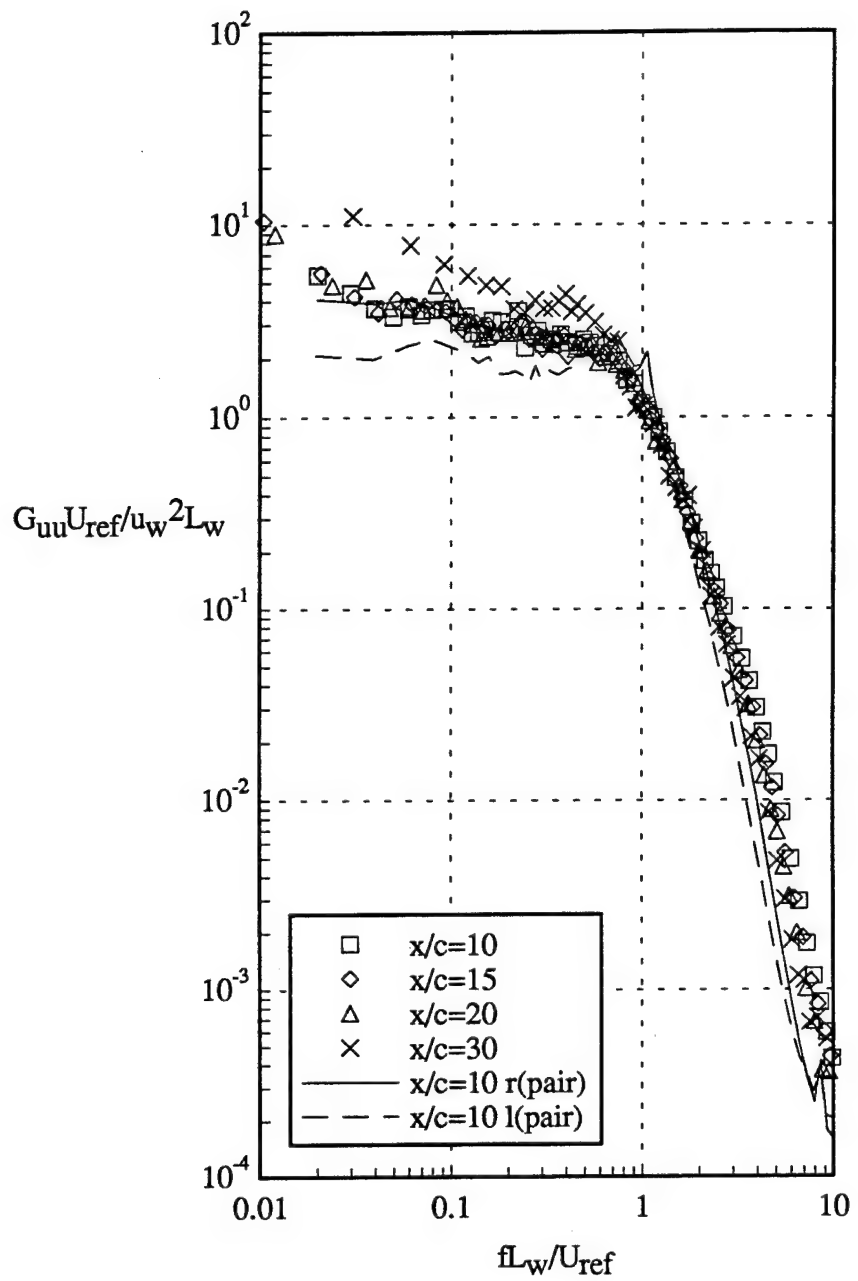


Figure 37. Autospectra of U velocity fluctuations at core center normalized on parameters of the two-dimensional portion of the wake for isolated vortex cases and counter-rotating pair at $x/c=10$. Solid line is the right-hand core and dashed line is the left-hand core.

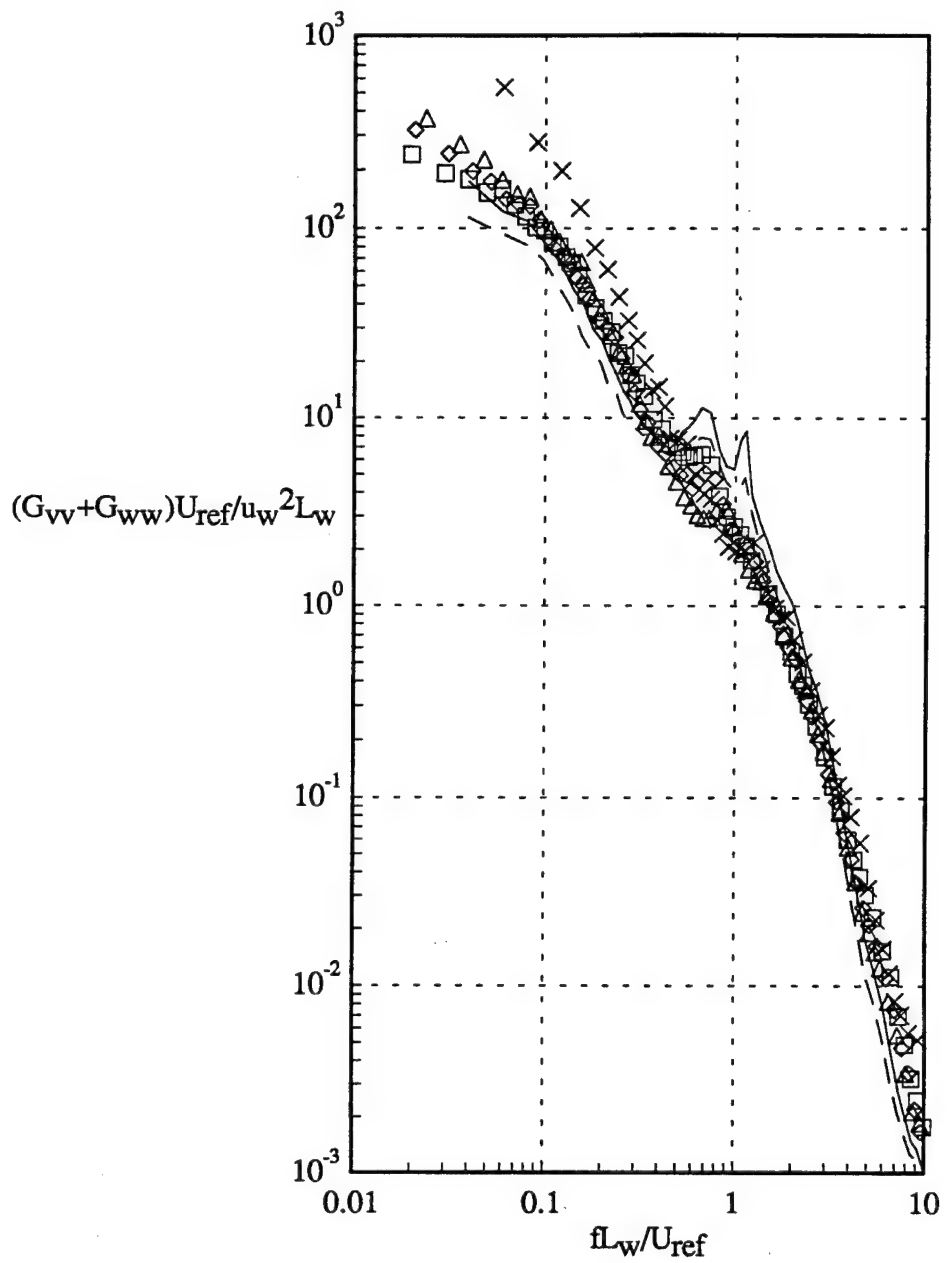


Figure 38. Autospectra of V+W velocity fluctuations at core center normalized on two-dimensional wake parameters for isolated vortex cases and counter-rotating pair at $x/c=10$. Solid line is right-hand core and dashed line is left-hand core.

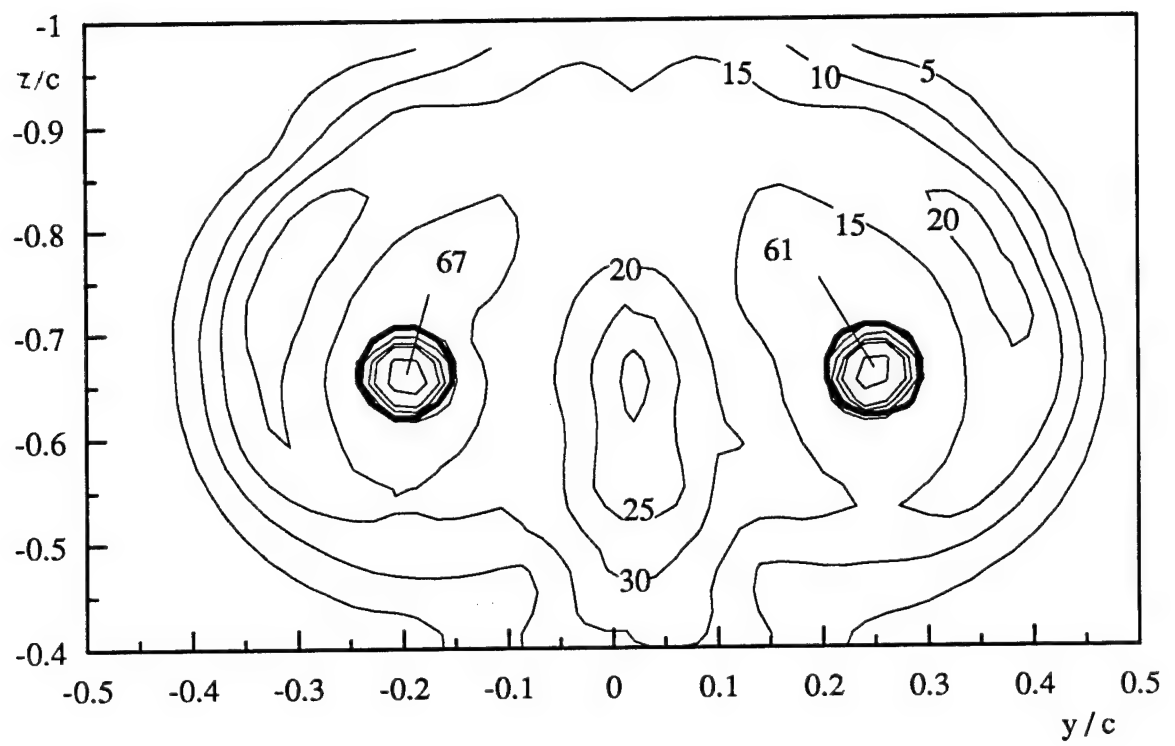


Figure 39. Contours of axial normal stress $\bar{u}^2/U_{ref}^2 \times 10^5$ filtered at $fc/U_{ref}=3$ at $x/c=10$ of counter-rotating pair

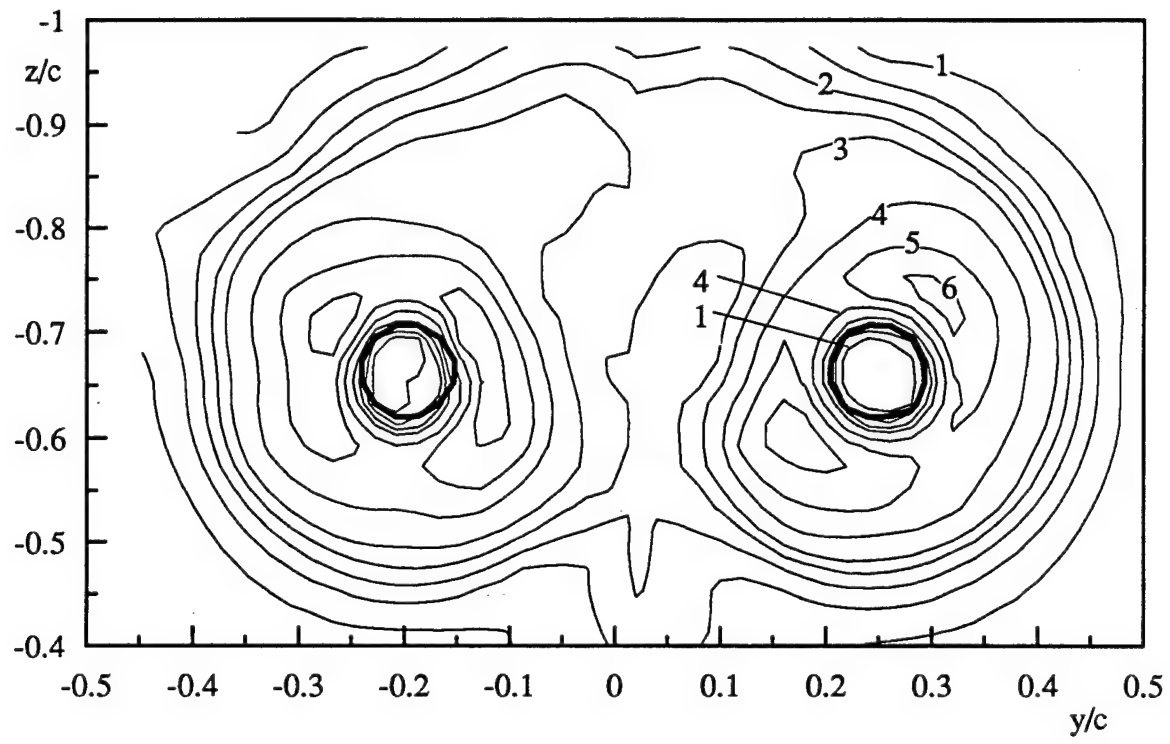


Figure 40. Contours of axial normal stress $\bar{u}^2/U_{ref}^2 \times 10^6$ filtered at $fc/U_{ref}=40$ at $x/c=10$ of counter-rotating pair

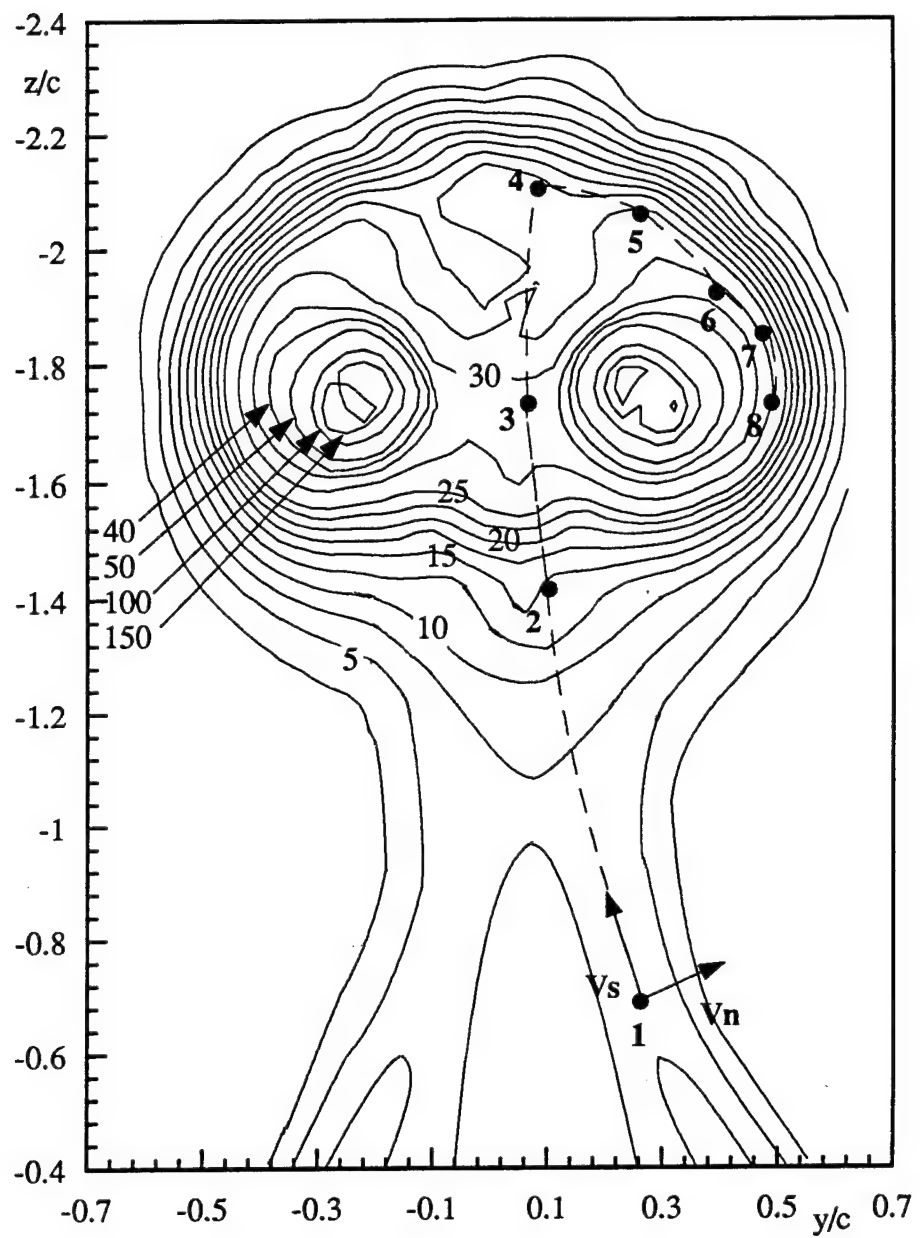


Figure 41. Contours of turbulence axial normal stress $\bar{u}^2/U_{ref}^2 \times 10^5$ at $x/c=30$ of counter-rotating pair. Dots indicate locations of profiles and autospectra in Figures 48-51.

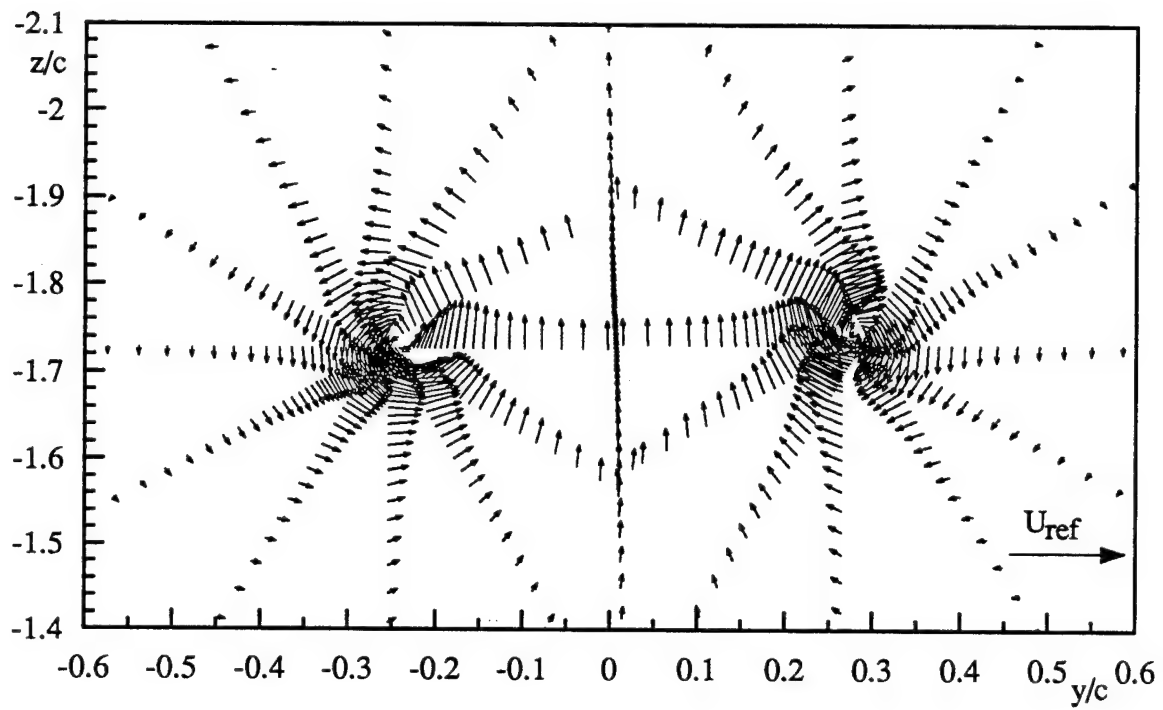


Figure 42. Mean cross-flow velocity vectors at $x/c=30$ of counter-rotating pair

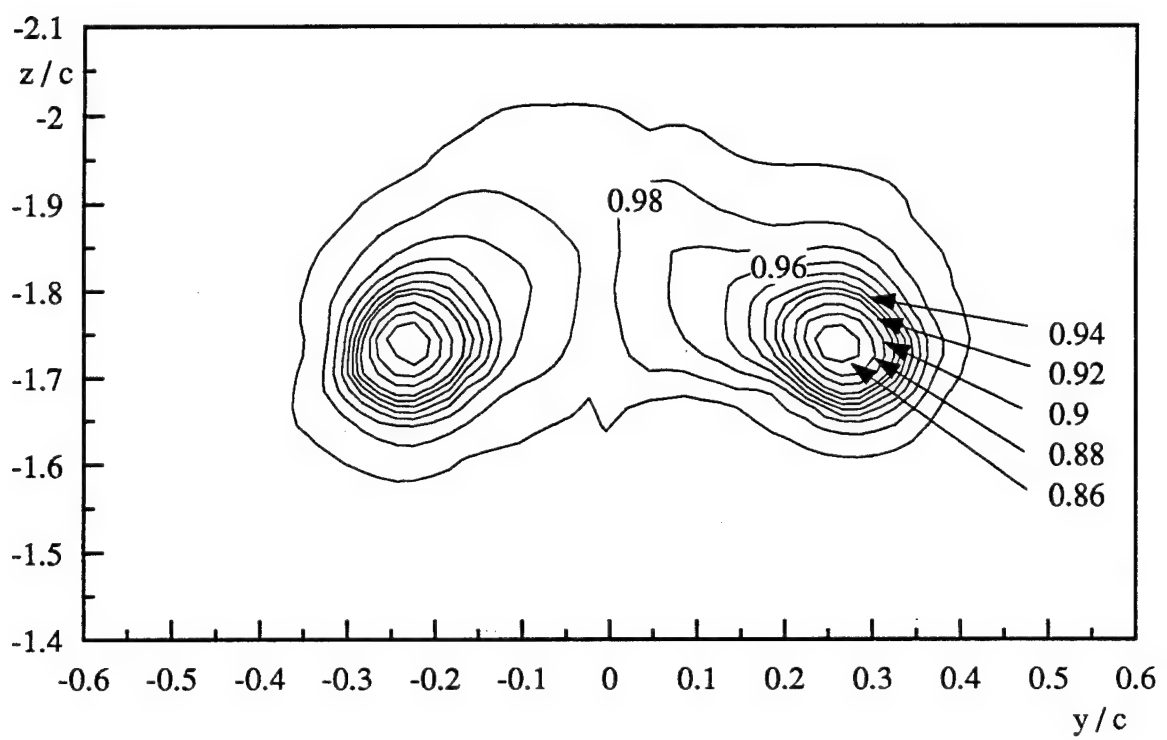


Figure 43. Contours of mean axial velocity U/U_{ref} at $x/c=30$ of counter-rotating pair

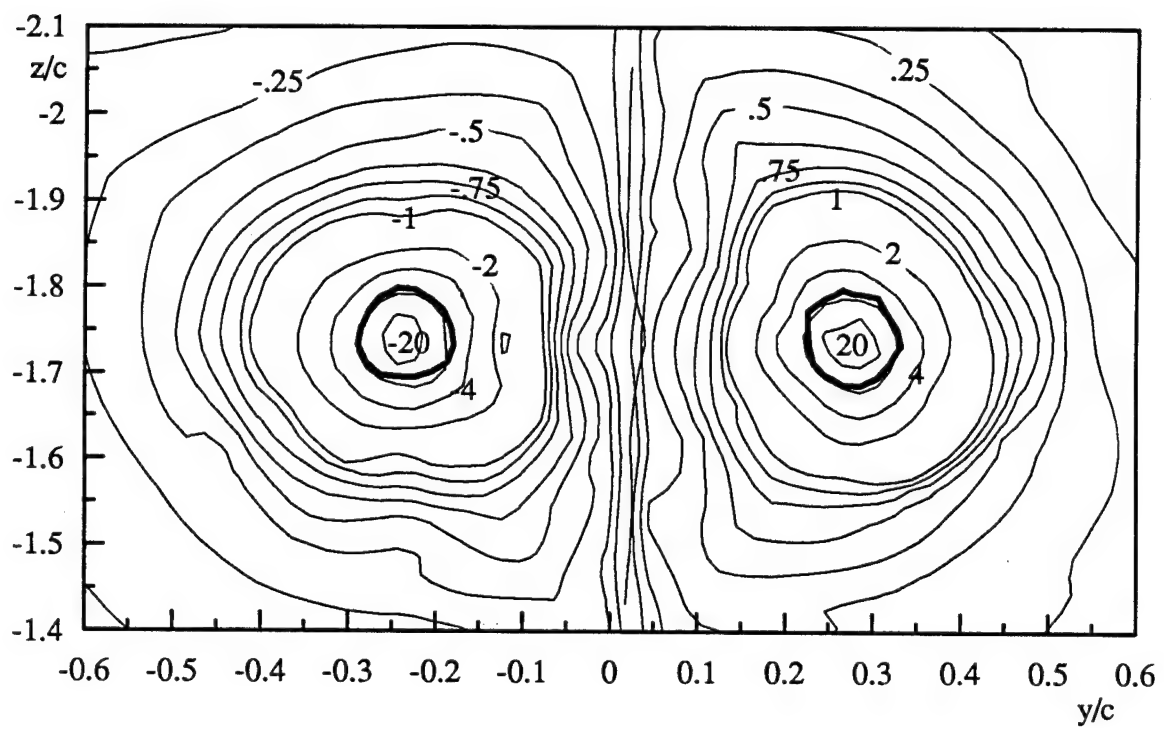


Figure 44. Contours of mean streamwise vorticity normalized on U_{ef} and c at $x/c=30$ of counter-rotating pair

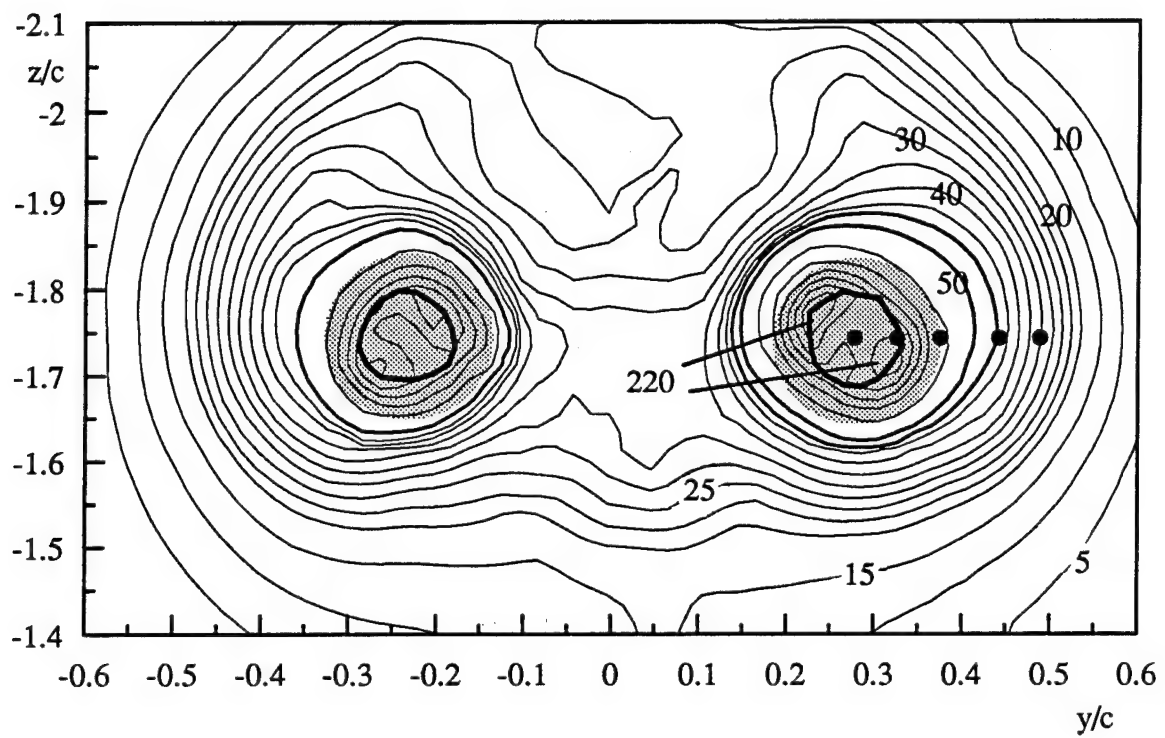


Figure 45. Contours of turbulence axial normal stress $\bar{u}^2/U_{ref}^2 \times 10^5$ at $x/c=30$ of counter-rotating pair. Dots show locations of autospectra in Figures 54-56. Shaded regions indicate where wandering has contributed more than 30% to the normal stresses.

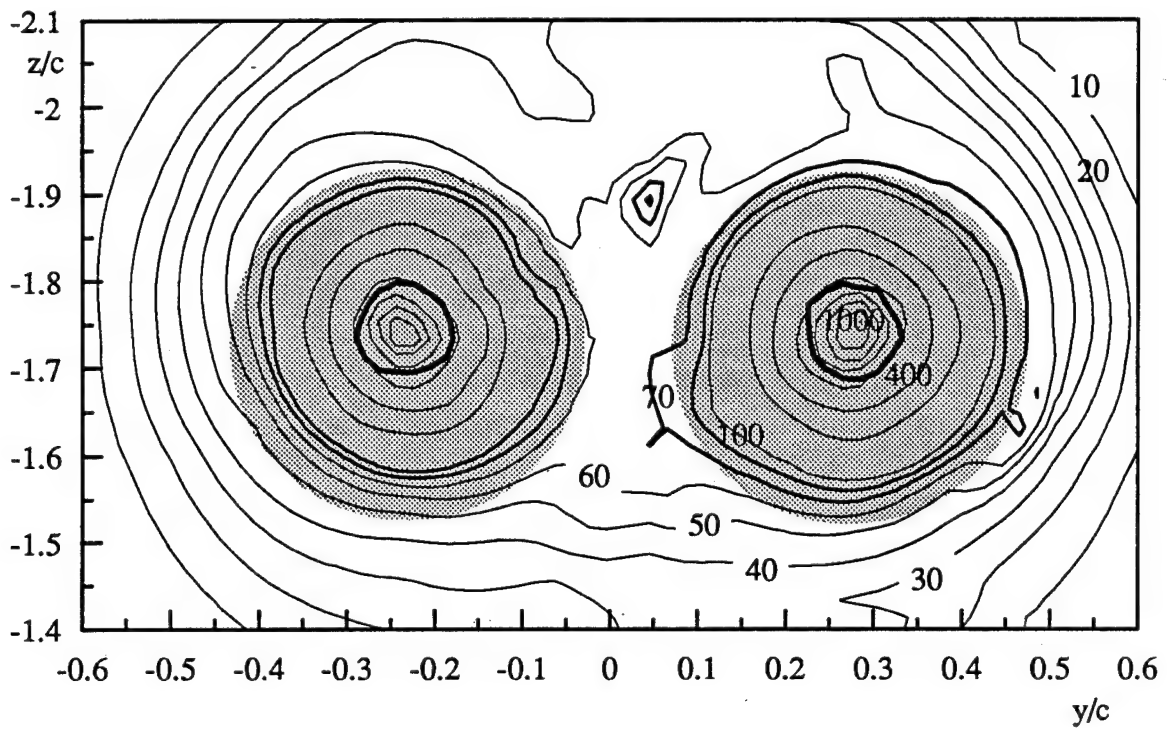


Figure 46. Contours of turbulence cross-flow normal stress sum $(\bar{v}^2 + \bar{w}^2)/U_{ref}^2 \times 10^5$ at $x/c = 30$ of counter-rotating pair. Shaded regions indicate where wandering has contributed more than 30% to the normal stresses.

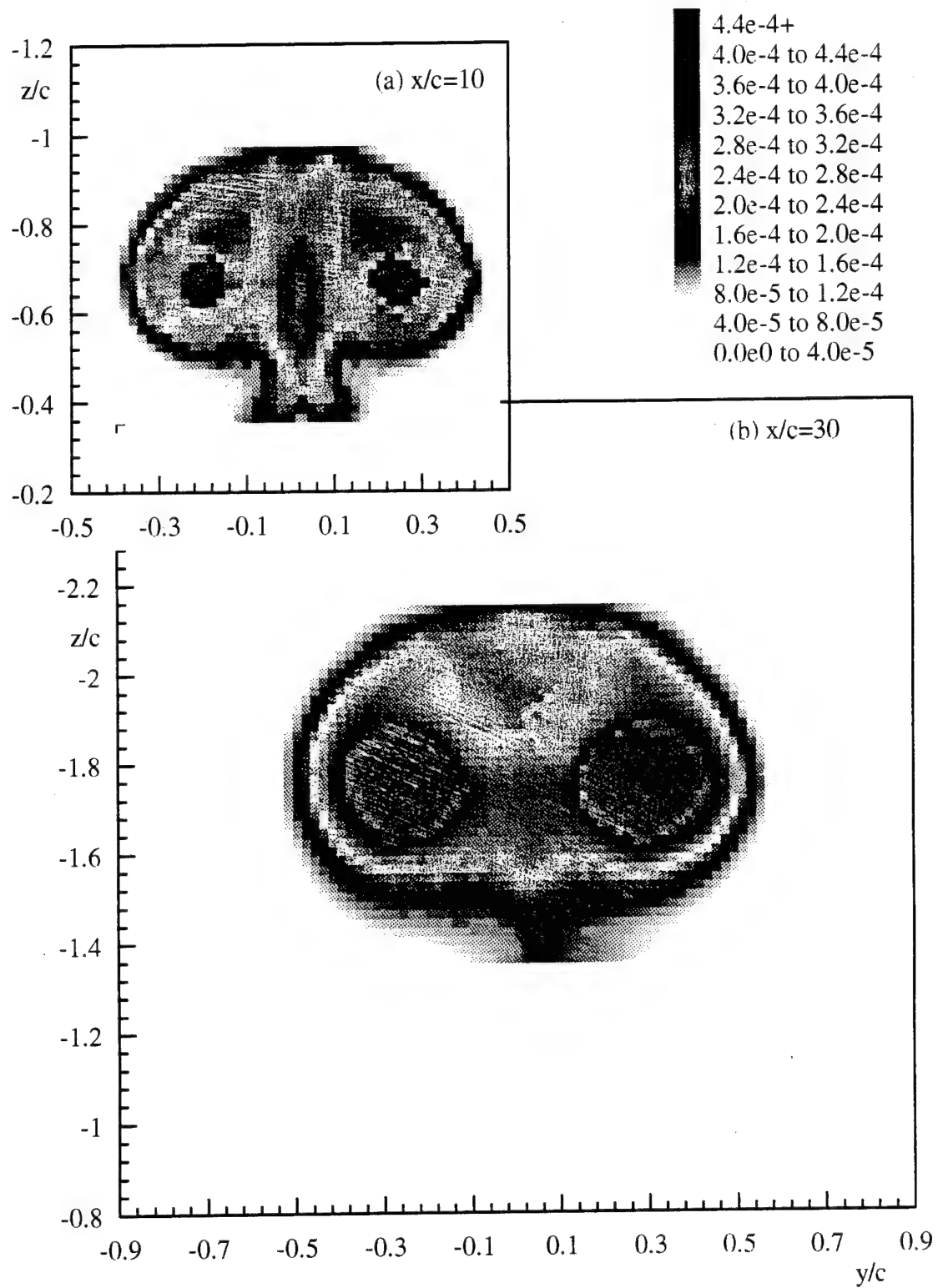


Figure 47. Contours of axial normal stress \bar{u}^2/U_{ref}^2 of counter-rotating pair at (a) $x/c=10$ and (b) $x/c=30$.

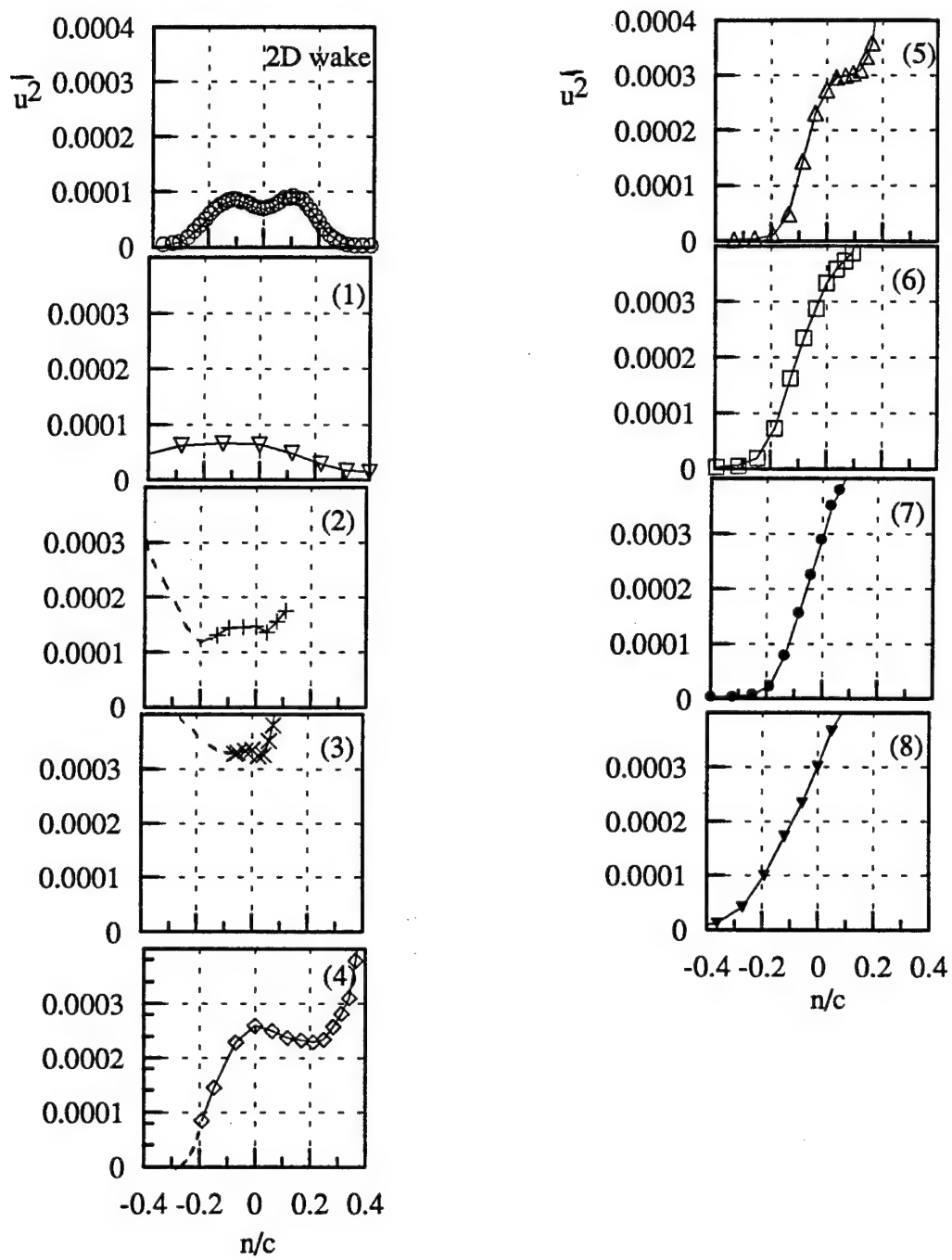


Figure 48. Profiles of axial normal stress \bar{u}^2/U_{ref}^2 at selected locations along the curve about the right-hand core at $x/c=30$ of counter-rotating pair. Numbers indicate locations along the dashed line in Figure 41.

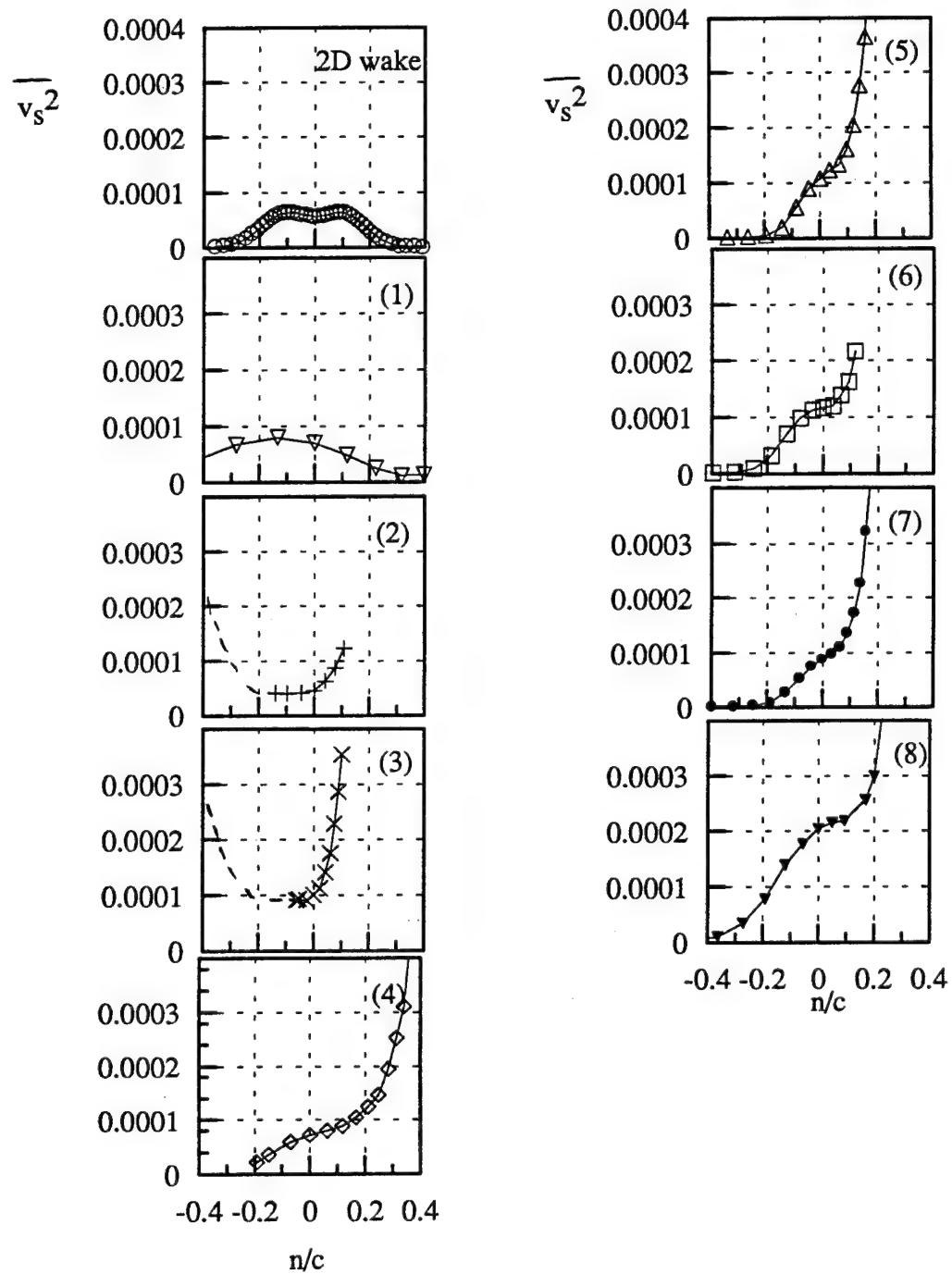


Figure 49. Profiles of normal stress v_s^2/U_{ref}^2 parallel to curve about right-hand core at selected locations along this line at $x/c=30$ of counter-rotating pair. Numbers indicate locations along the dashed line in Figure 41.

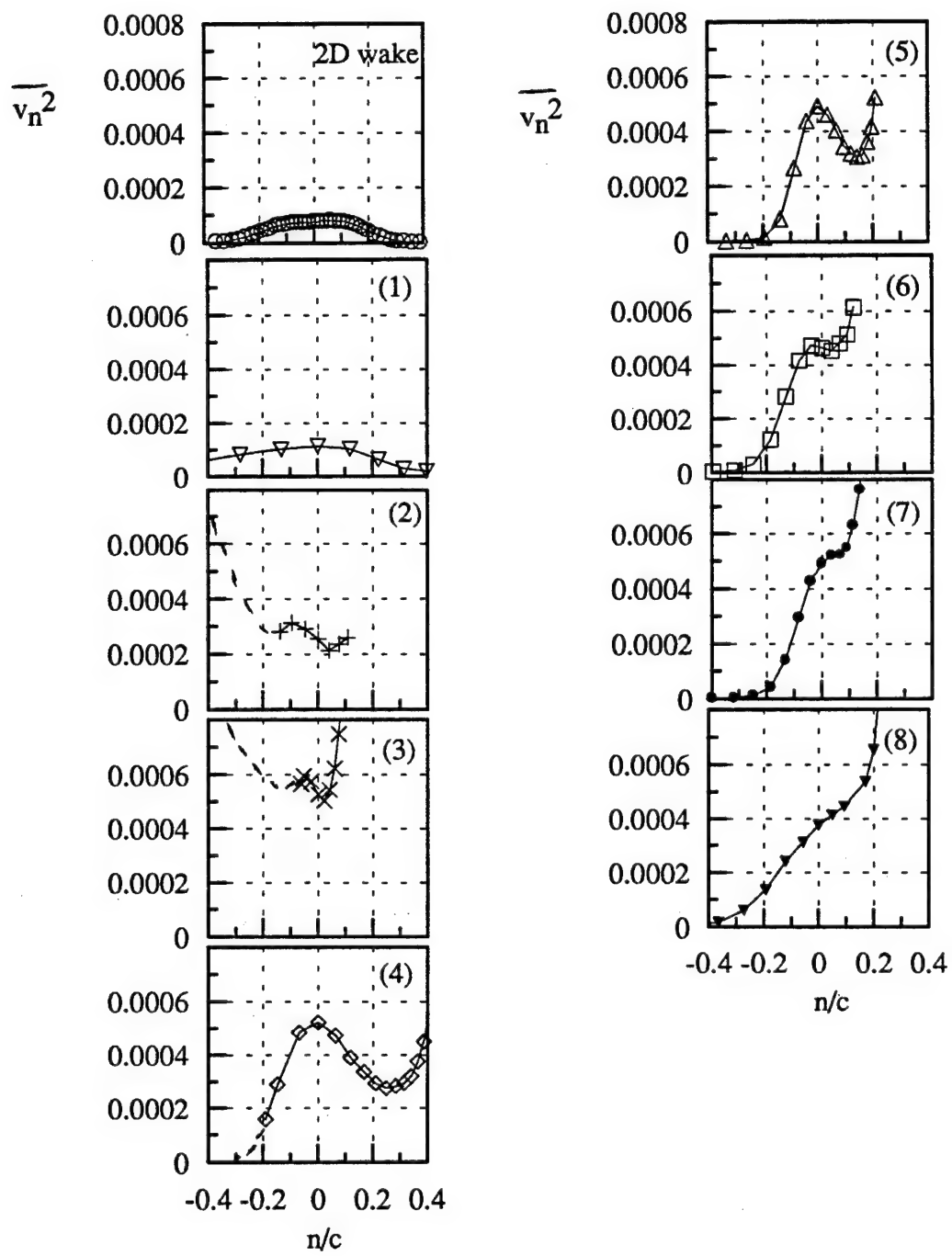


Figure 50. Profiles of normal stress $\overline{v_n^2}/U_{ref}^2$ normal to curve about right-hand core at selected locations along this line at $x/c=30$ of counter-rotating pair. Numbers indicate locations along dashed line in Figure 41.

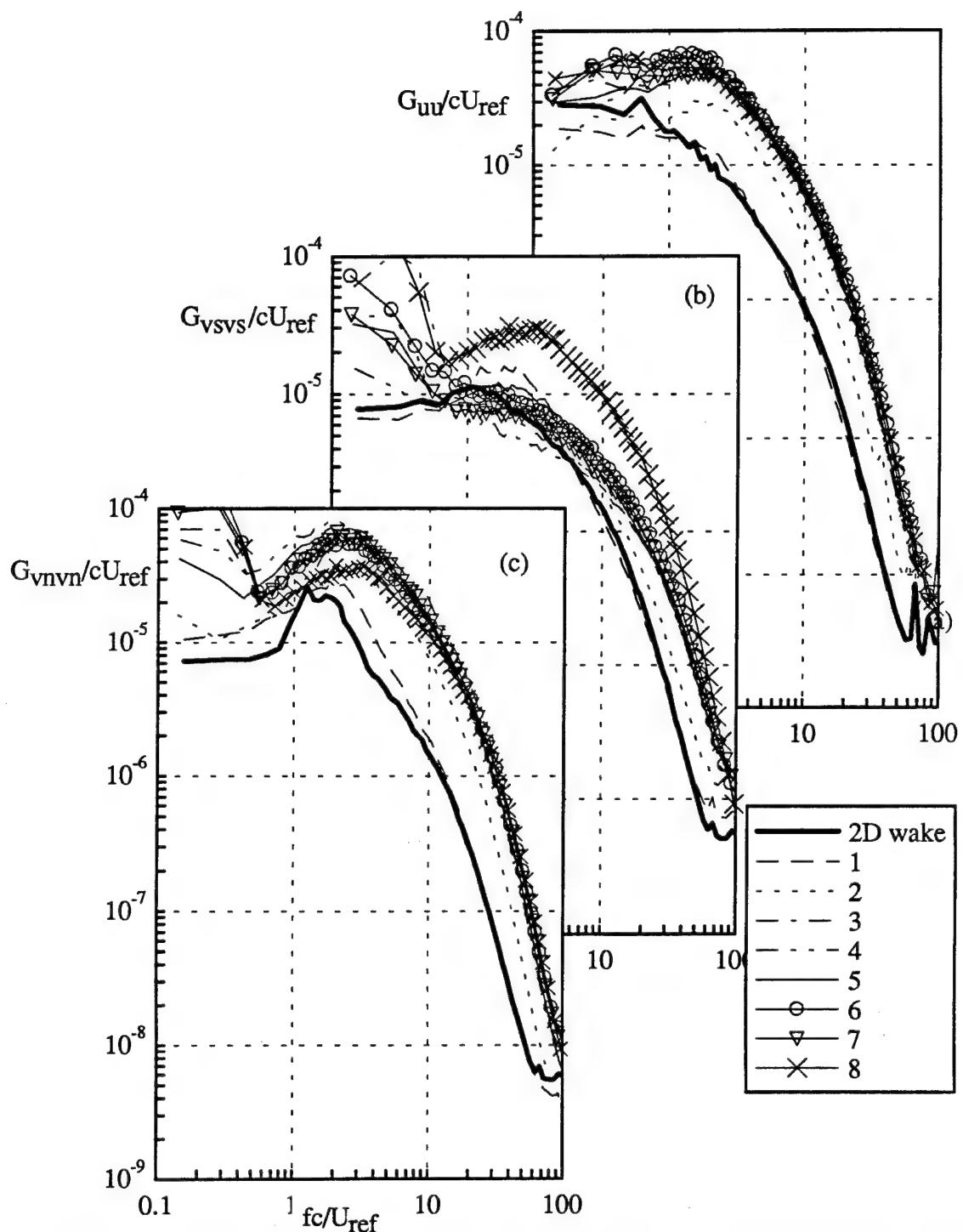


Figure 51 Velocity autospectra in coordinates aligned with the curve about right-hand core in Figure 41 at $x/c=30$ of counter-rotating pair (a) U spectra, (b) V spectra, (c) V_n spectra. Locations indicated by dots in Figure 41.

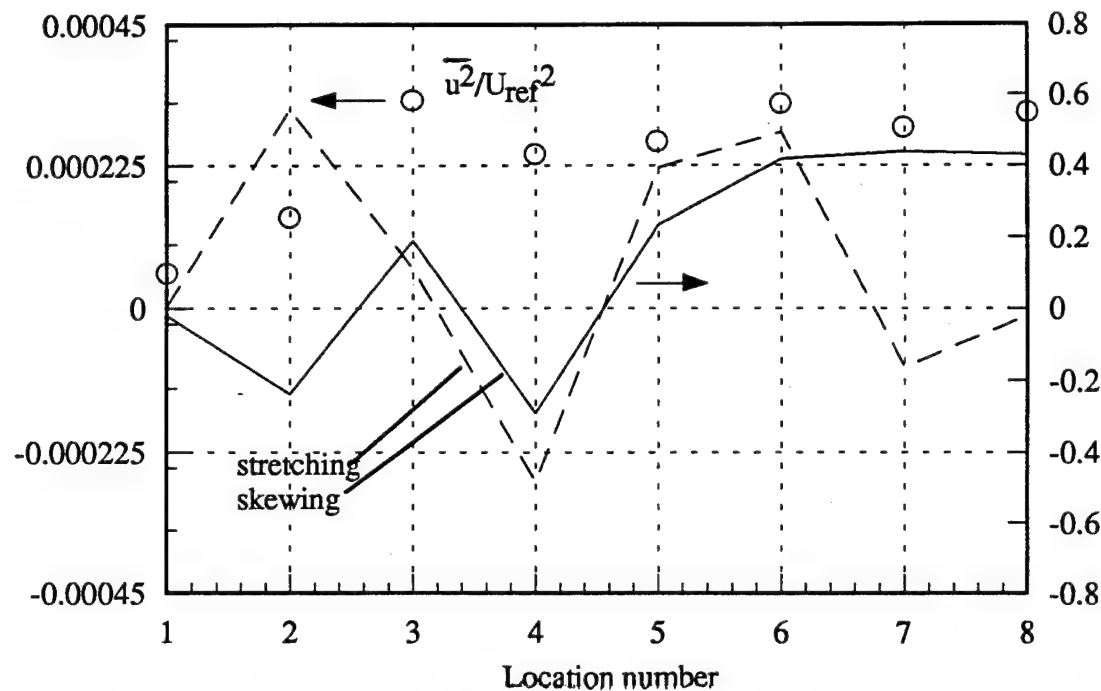


Figure 52. Rates of strain and turbulence stress on the curve about the right-hand core at $x/c=30$ of counter-rotating pair. Strain rates normalized on maximum axial velocity gradient in the two-dimensional portion of the wake.

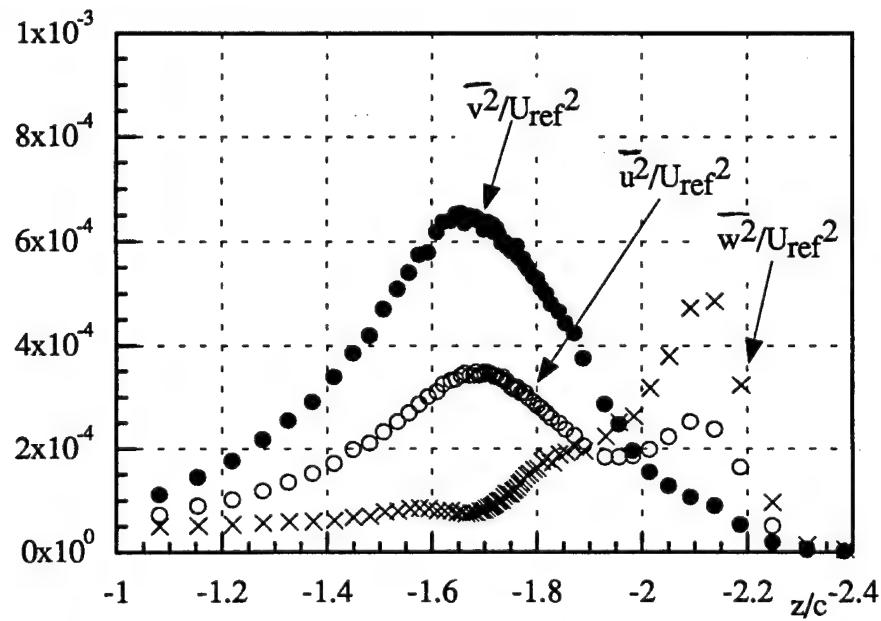


Figure 53. Normal stress profiles along the plane of symmetry between the vortices at $x/c=30$ of counter-rotating pair

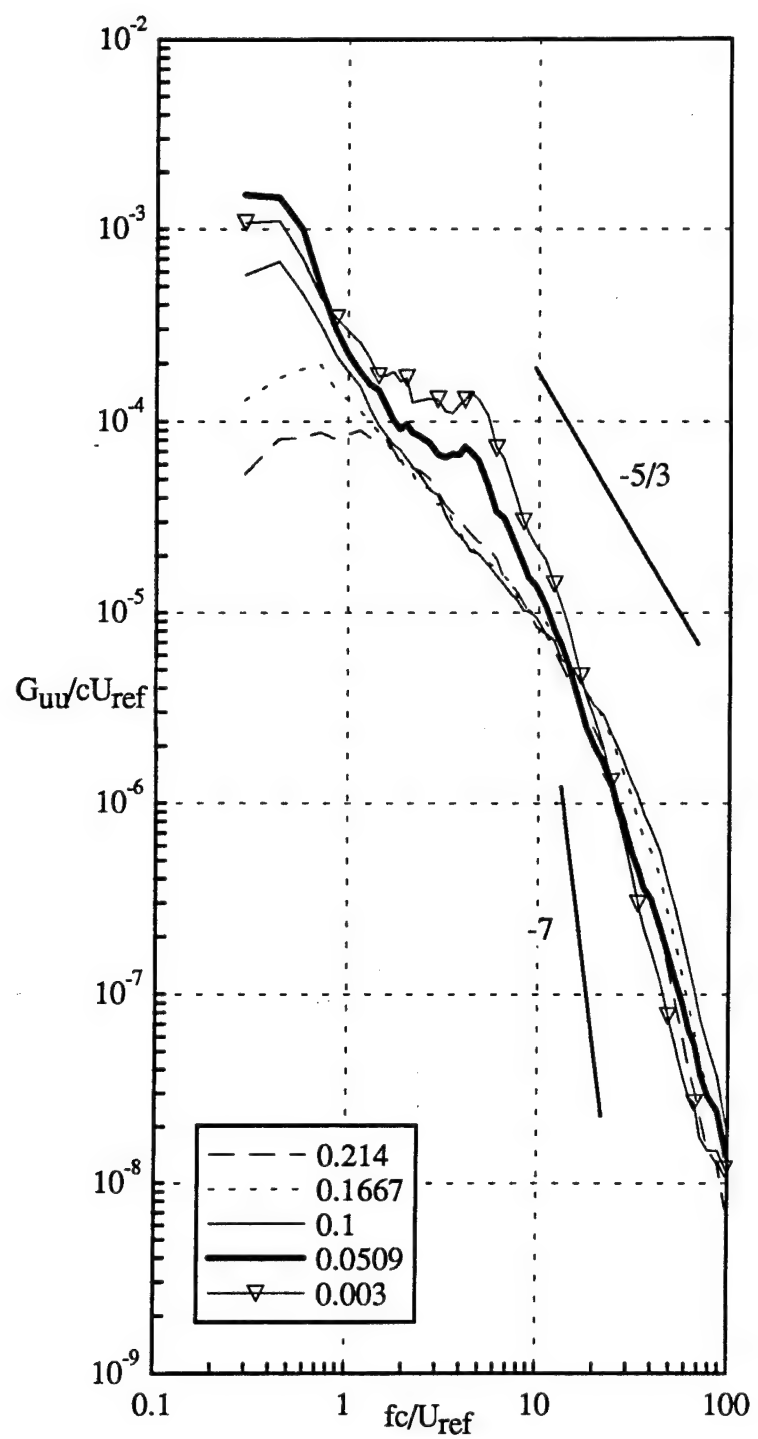


Figure 54. Autospectra of U velocity fluctuations at various spanwise locations along a horizontal profile through the right-hand core center indicated by dots in Figure 45 at $x/c=30$ of counter-rotating pair. Locations relative to the core center at $y/c=0.275$.

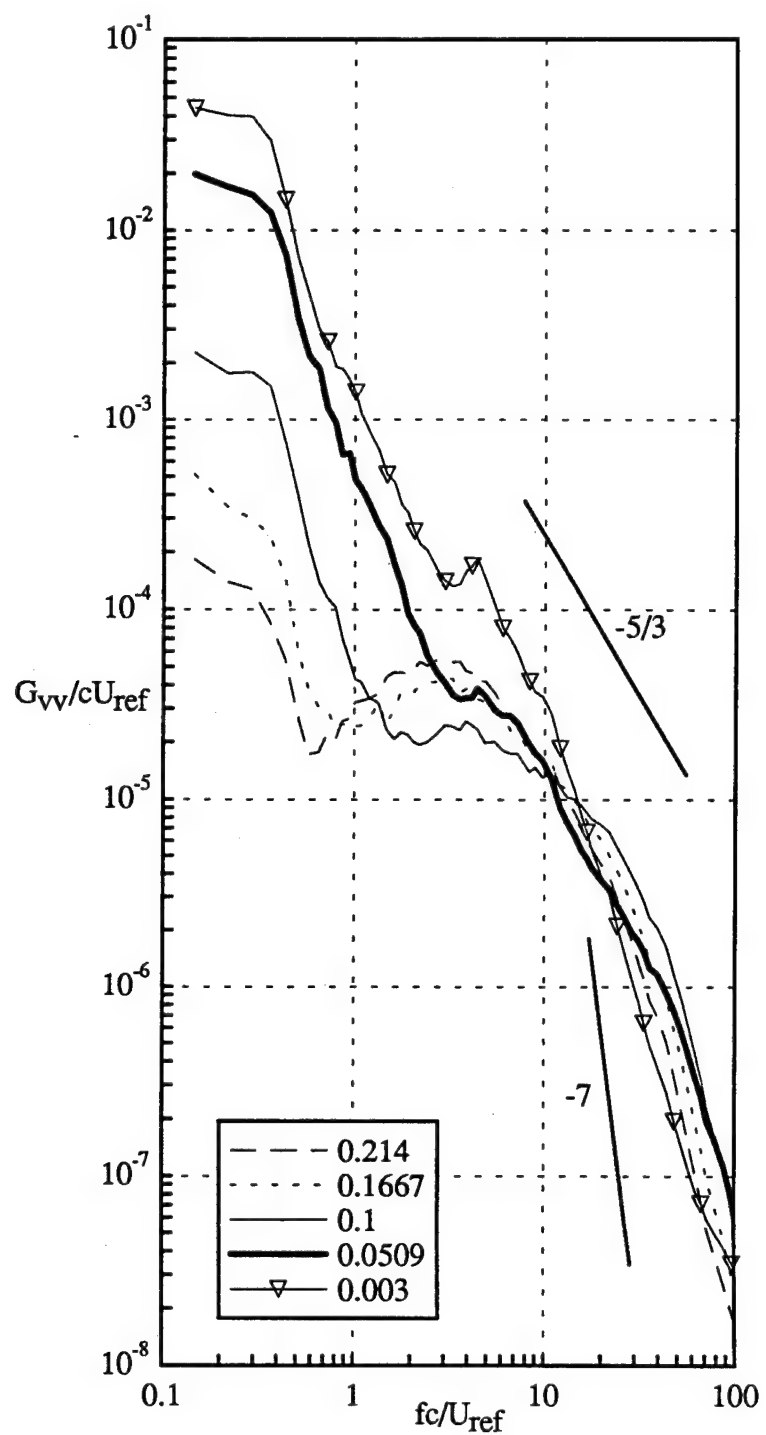


Figure 55. Autospectra of V velocity fluctuations at various spanwise locations along a horizontal profile through the right-hand core center indicated by dots in Figure 45 at $x/c=30$ of counter-rotating pair. Locations relative to the core center at $y/c=0.275$.

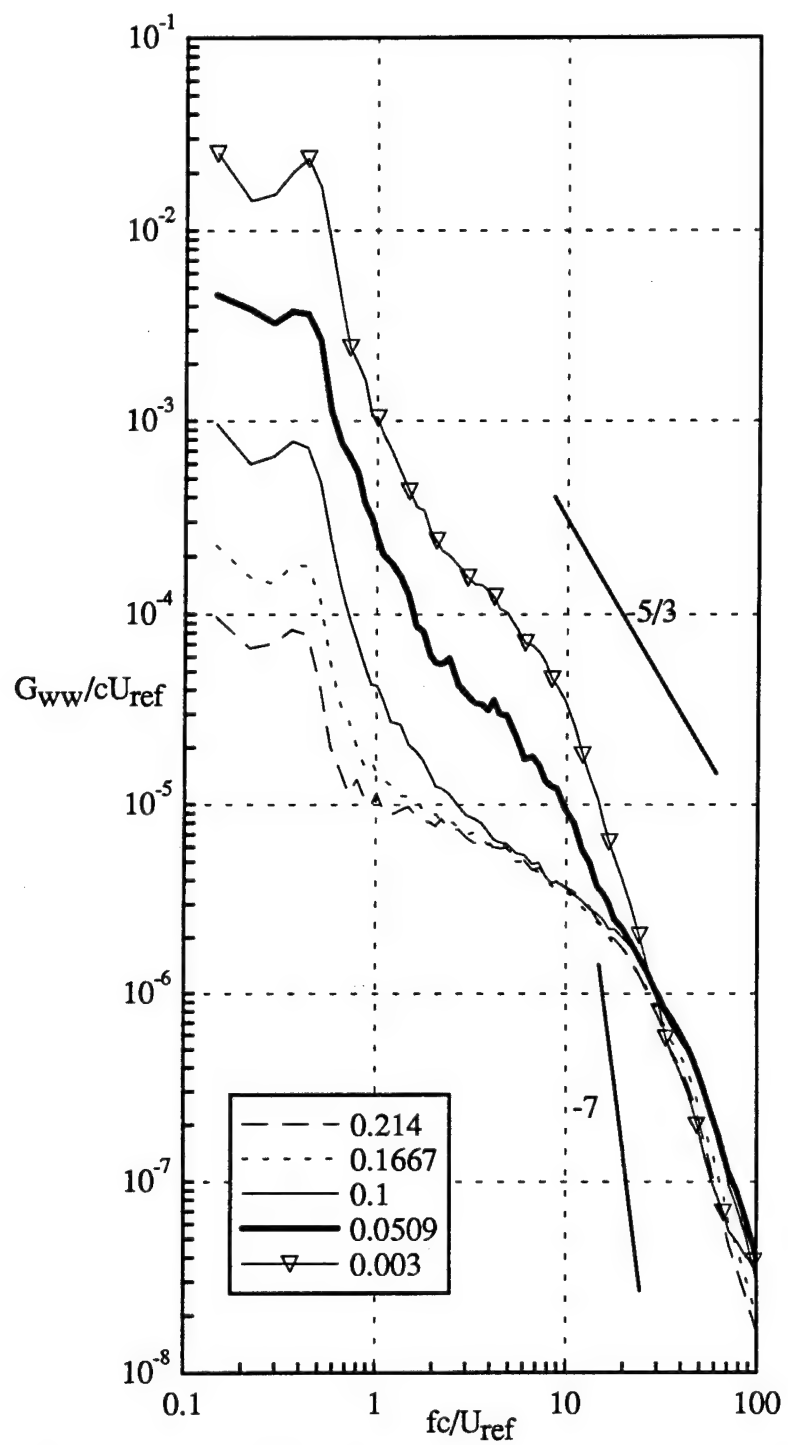


Figure 56. Autospectra of W velocity fluctuations at various spanwise locations along a horizontal profile through the right-hand core center indicated by dots in Figure 45 at $x/c=30$ of counter-rotating pair. Locations relative to the core center at $y/c=0.275$.

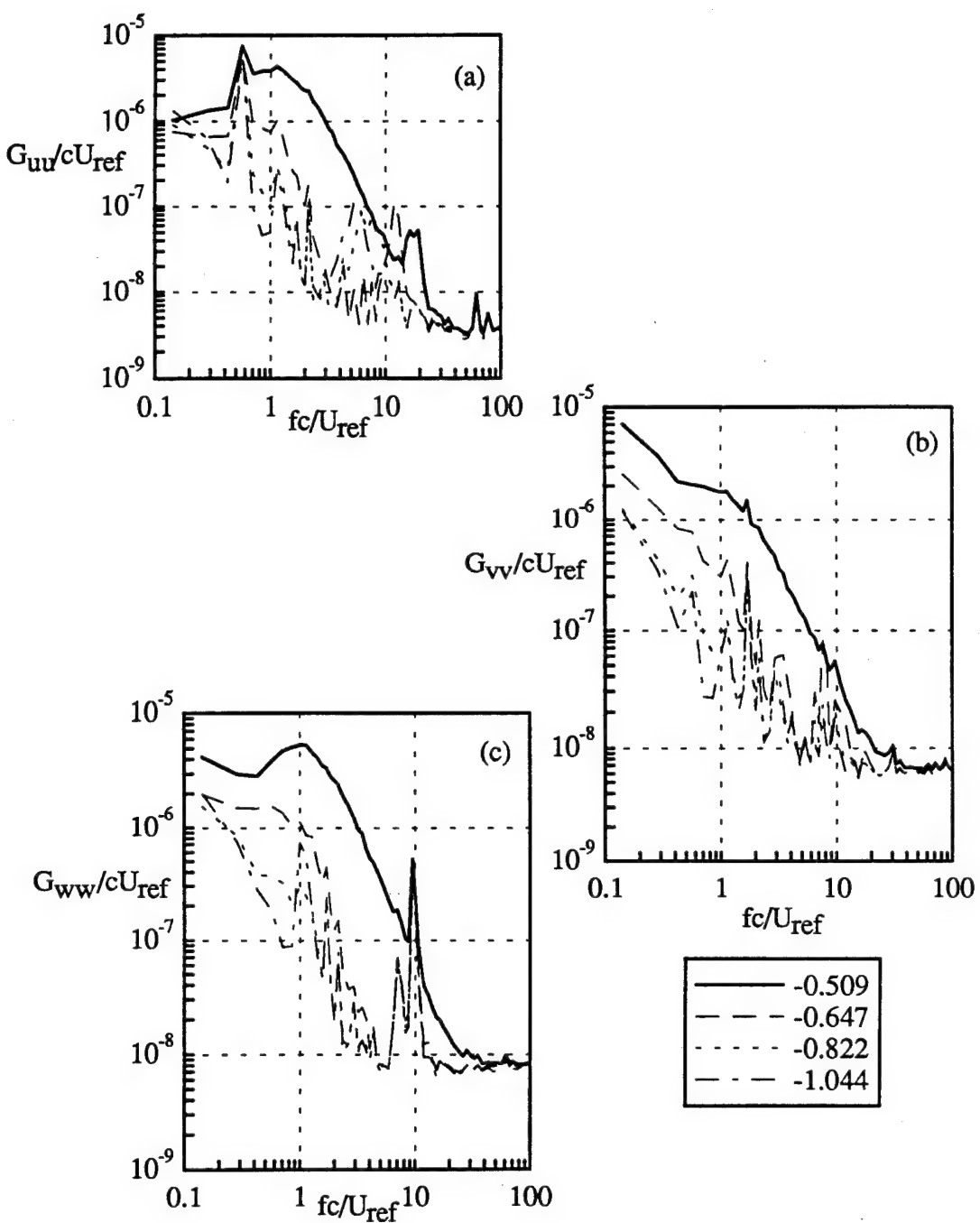


Figure 57. Autospectra at locations moving from the edge of the turbulent region into the free-stream along a vertical profile through the right-hand core center at $x/c=30$ of counter-rotating pair (a)U spectra, (b)V spectra, (c) W spectra. Locations relative to the core center at $z/c=-1.74$.

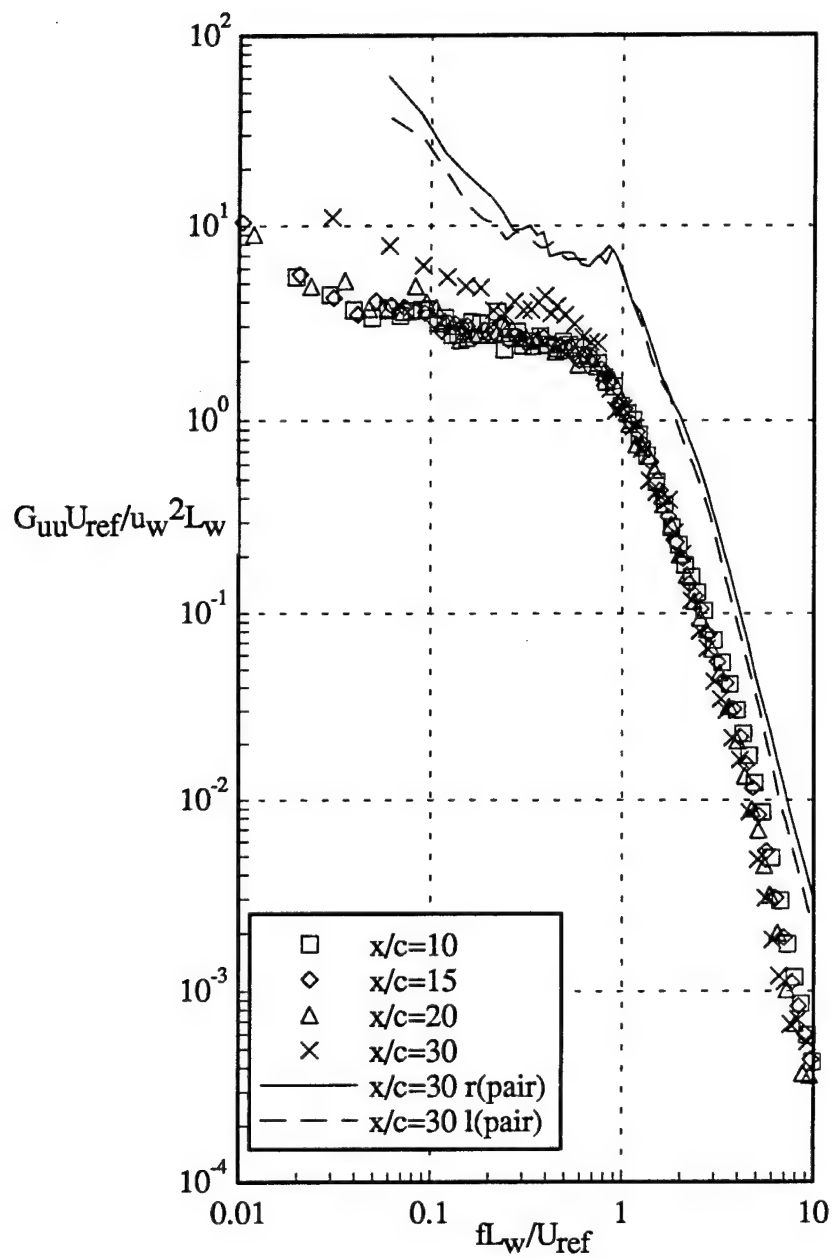


Figure 58. Autospectra of U velocity fluctuations at core center normalized on two-dimensional wake parameters for isolated vortex cases and counter-rotating pair at $x/c=30$. Solid line is the right-hand core and dashed line is the left-hand core.

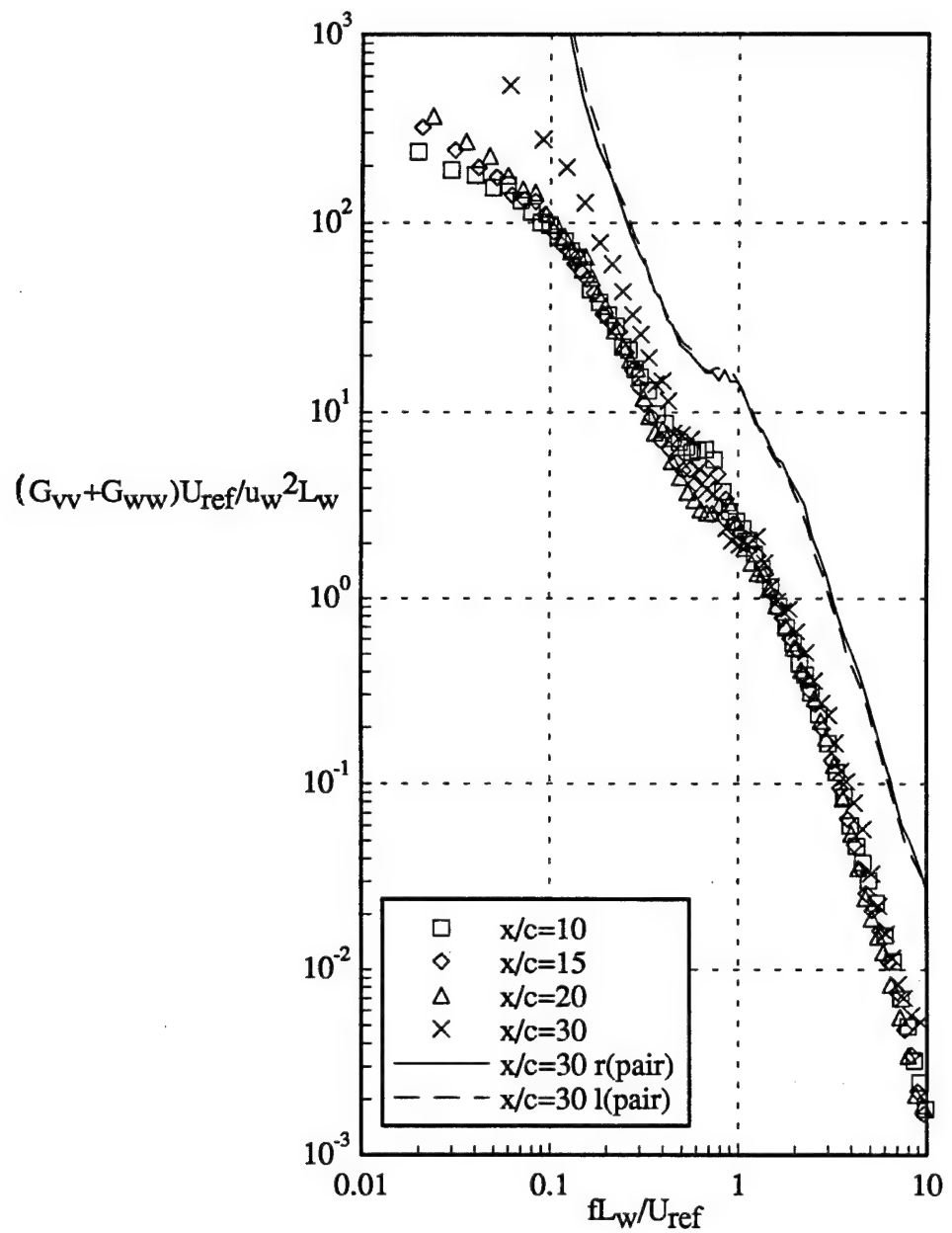


Figure 59. Autospectra of V+W velocity fluctuations at core center normalized on parameters of the two-dimensional wake for isolated vortex and counter-rotating pair at $x/c=30$. Solid line is right-hand vortex and dashed line is left-hand vortex.

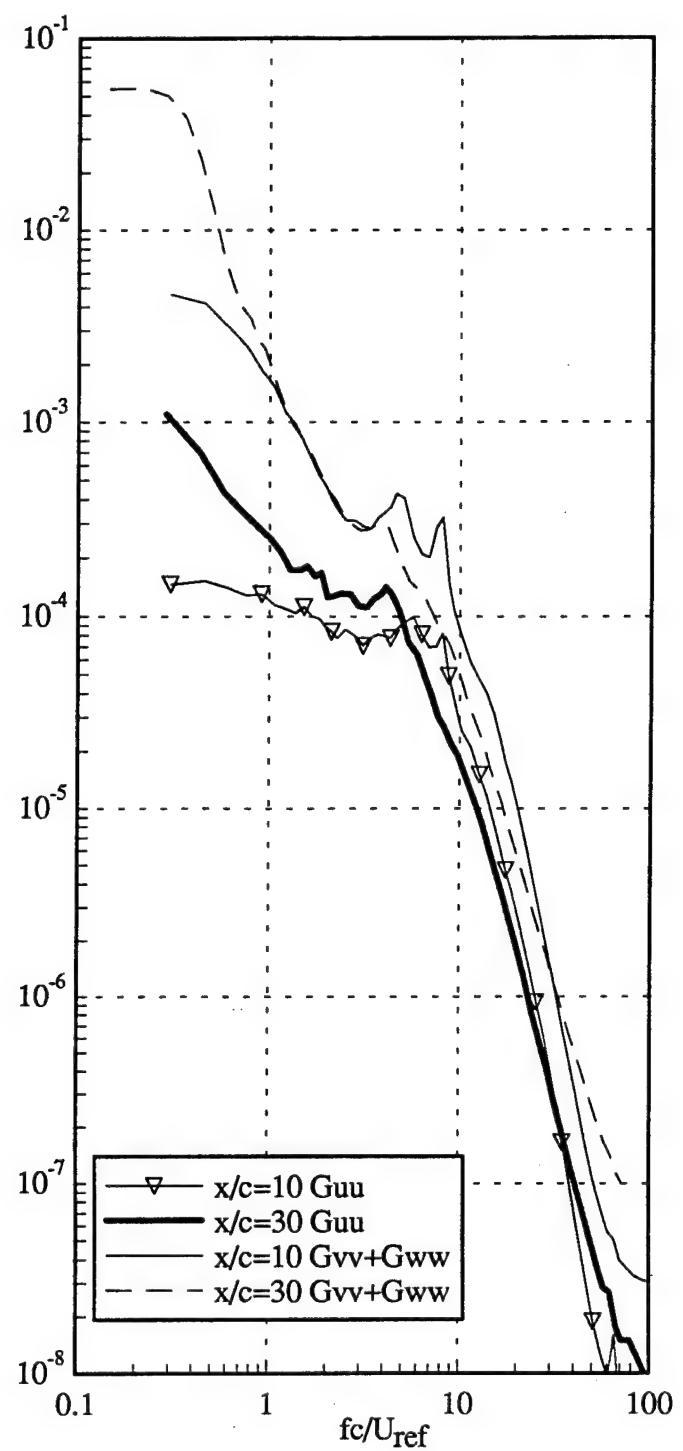


Figure 60. Variation of velocity autospectra at core center with streamwise distance of counter-rotating pair. Autospectra normalized on U_{ref} and c

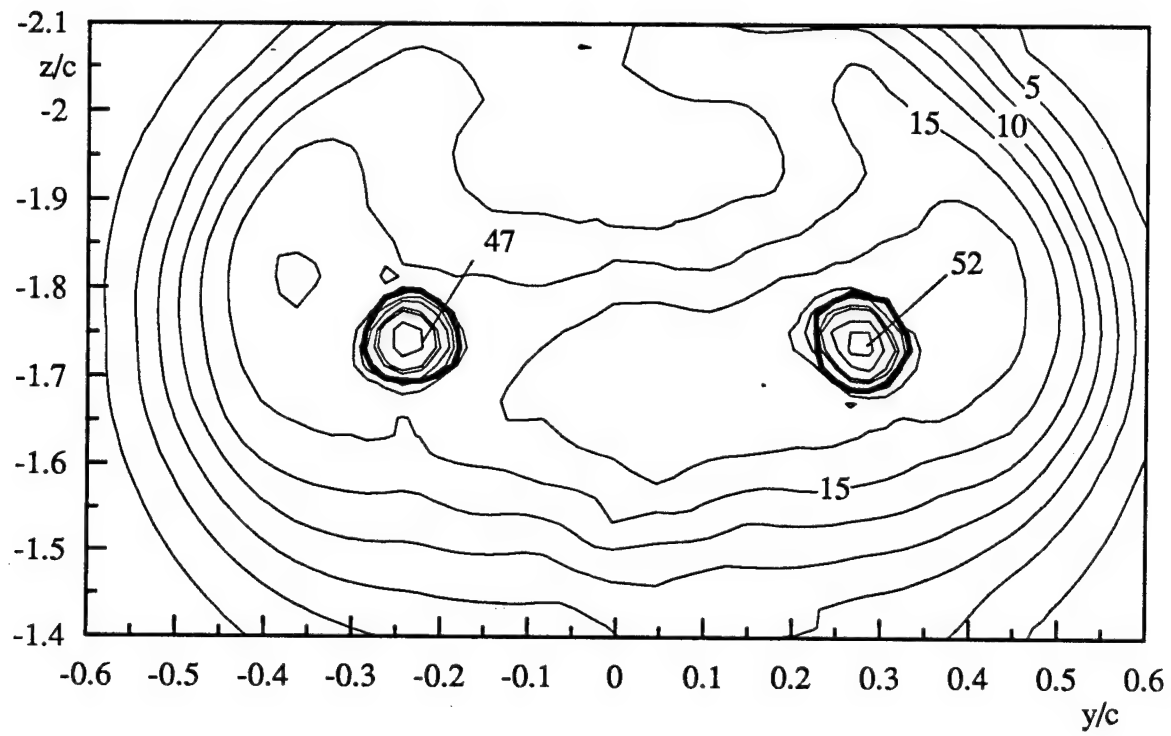


Figure 61. Contours of axial normal stress $\bar{u}^2/U_{ref}^2 \times 10^5$ filtered at $fc/U_{ref}=3$ at $x/c=30$ of counter-rotating pair

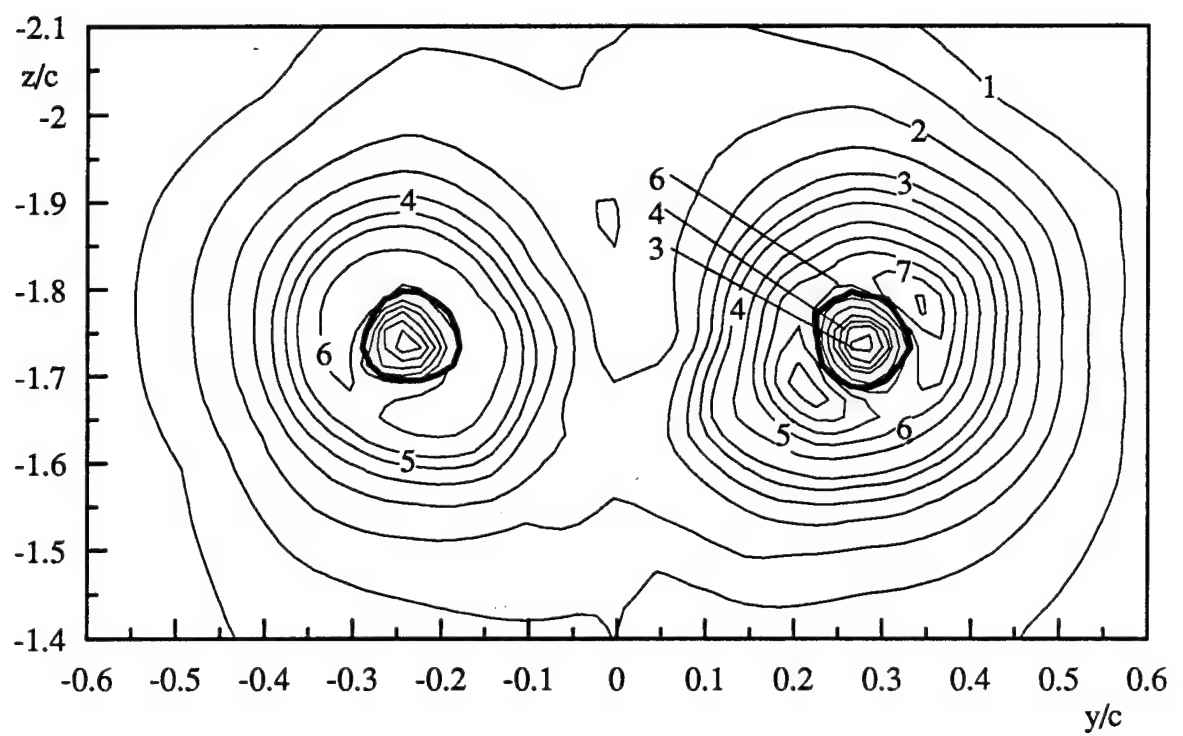


Figure 62. Contours of axial normal stress $\bar{\tau}/U_{\text{ref}}^2 \times 10^6$ filtered at $fc/U_{\text{ref}}=40$ at $x/c=30$ of counter-rotating pair

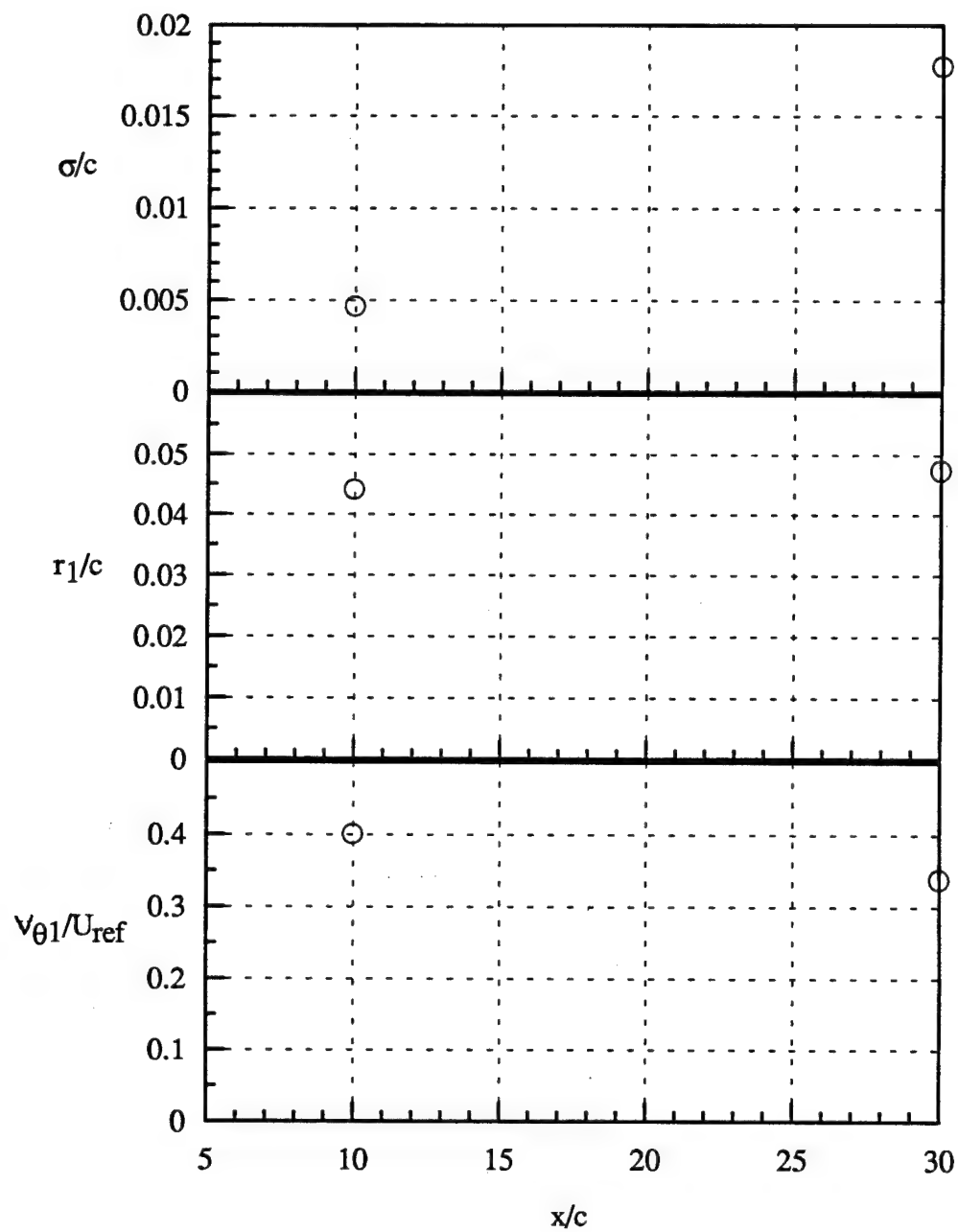


Figure 63. Variation in wandering amplitude, core radius, and peak tangential velocity with streamwise distance for counter-rotating pair.

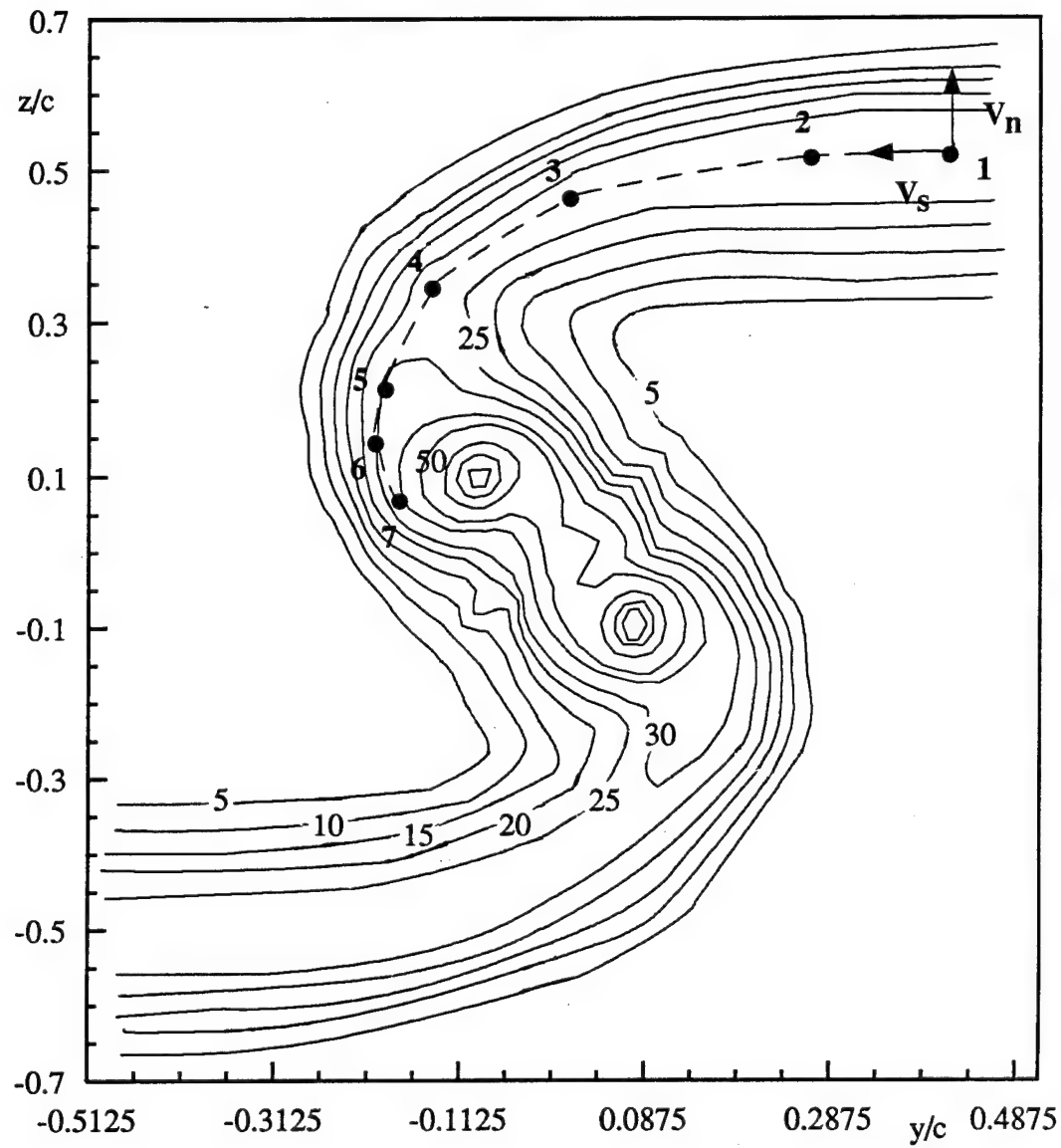


Figure 64. Contours of turbulence axial normal stress $\bar{u}^2/U_{\text{ref}}^2 \times 10^5$ at $x/c=10$ of co-rotating pair. Dashed line denotes spiral wake centerline in the spiral wake tail. Dots indicate locations of profiles and autospectra in Figures 70-73.

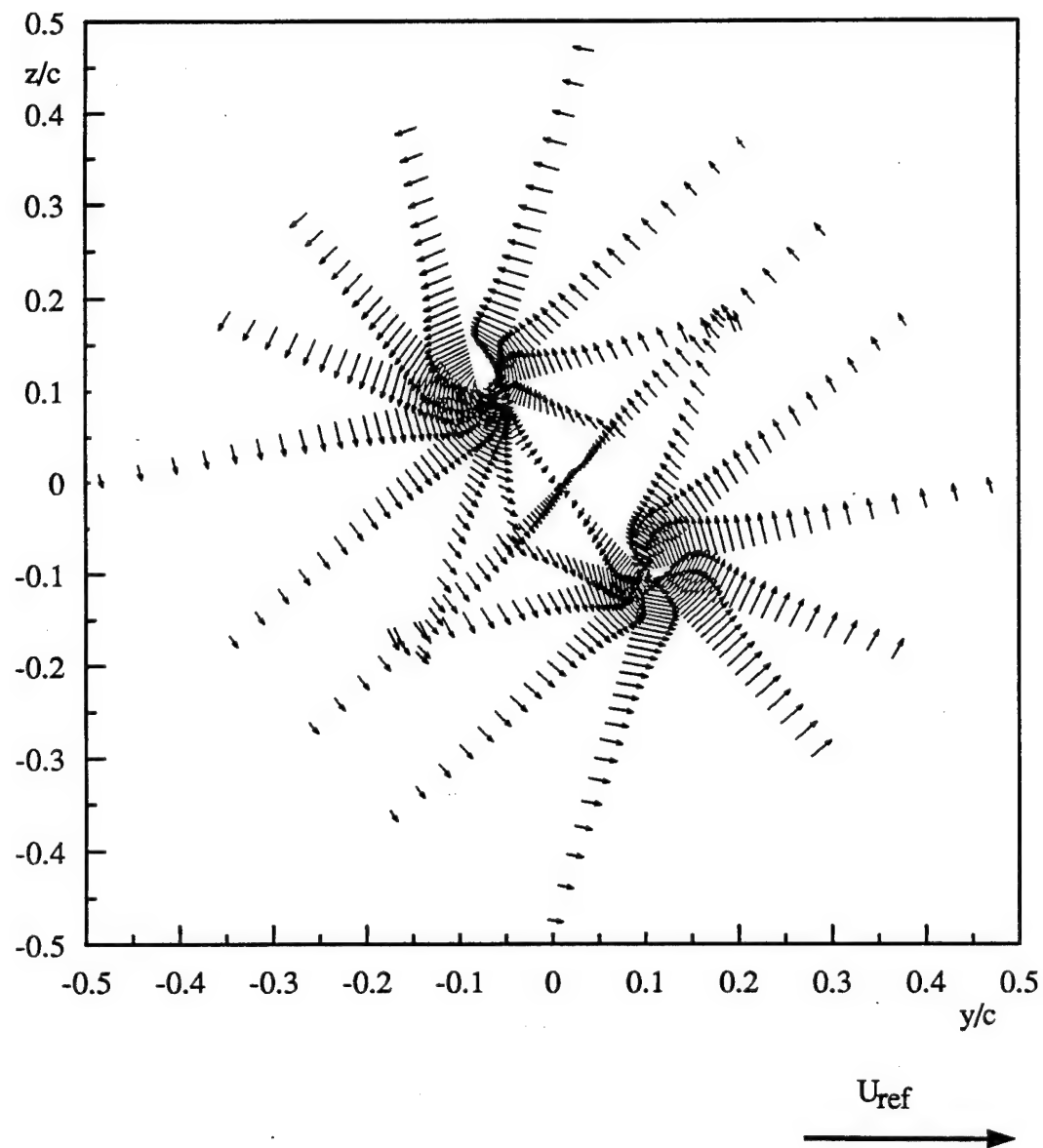


Figure 65. Mean cross-flow velocity vectors at $x/c=10$ of co-rotating pair

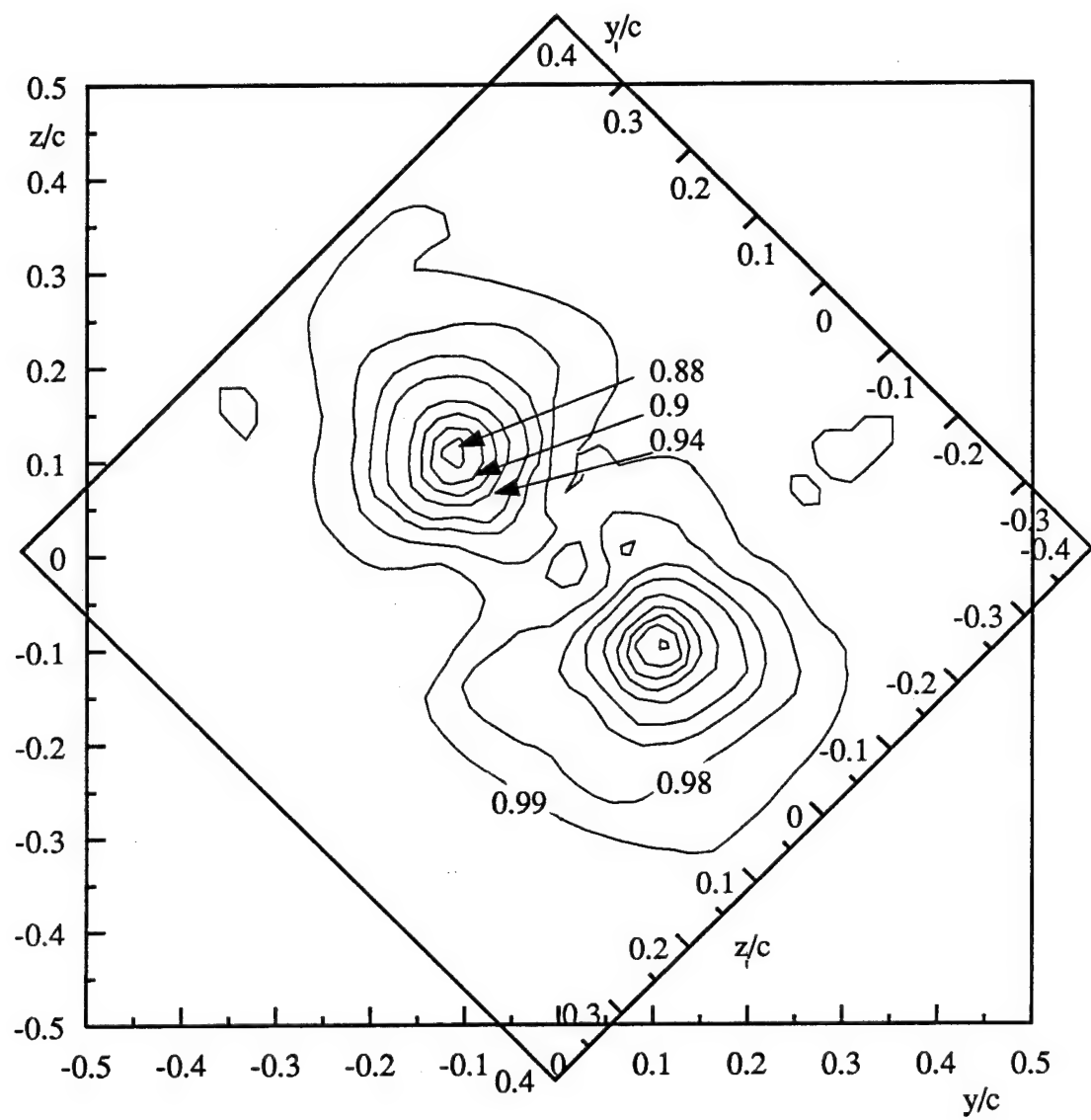


Figure 66. Contours of mean axial velocity U/U_{ref} at $x/c=10$ of co-rotating pair. Additional axes define rotated coordinate system (y_1, z_1) .

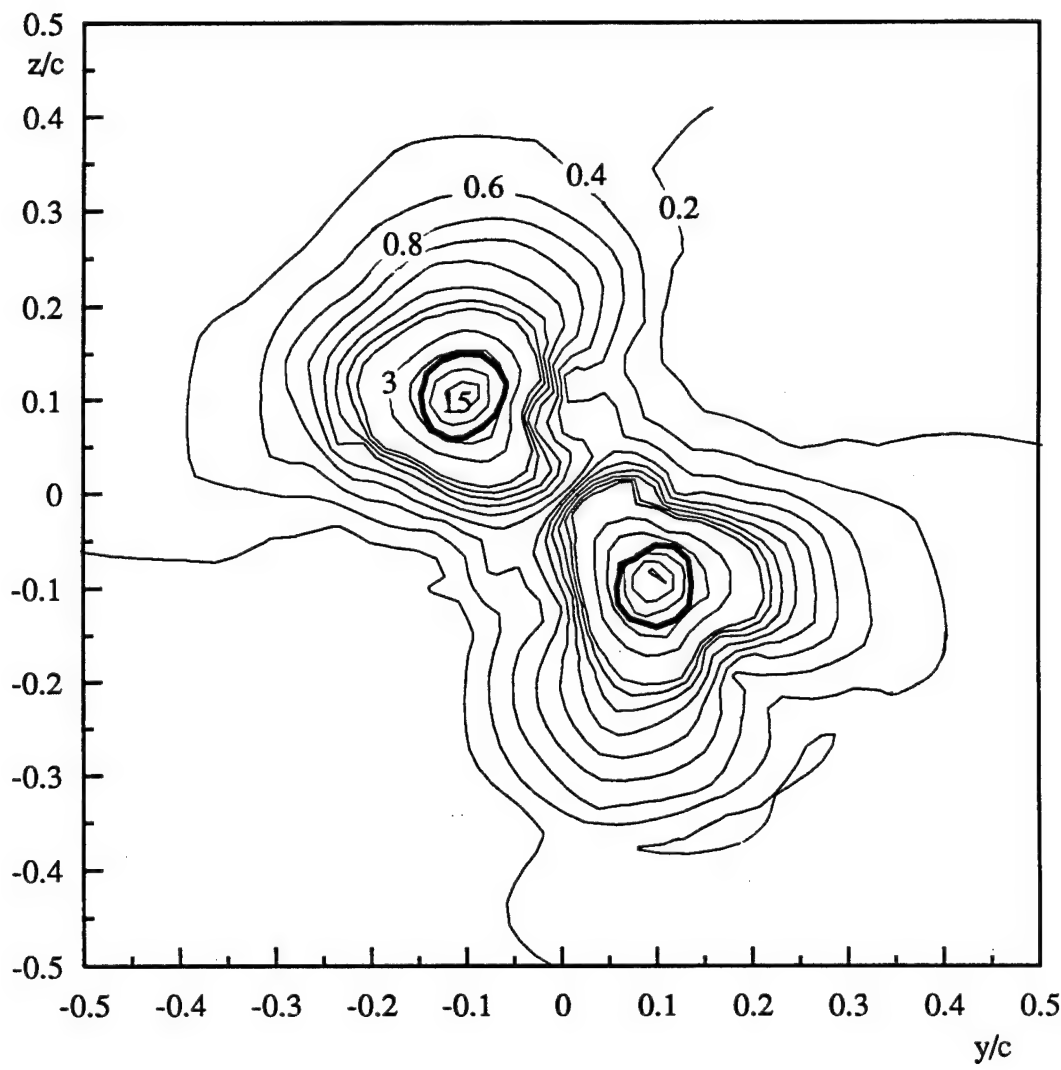


Figure 67. Contours of mean streamwise vorticity normalized on U_{ref} and c at $x/c=10$ of co-rotating pair

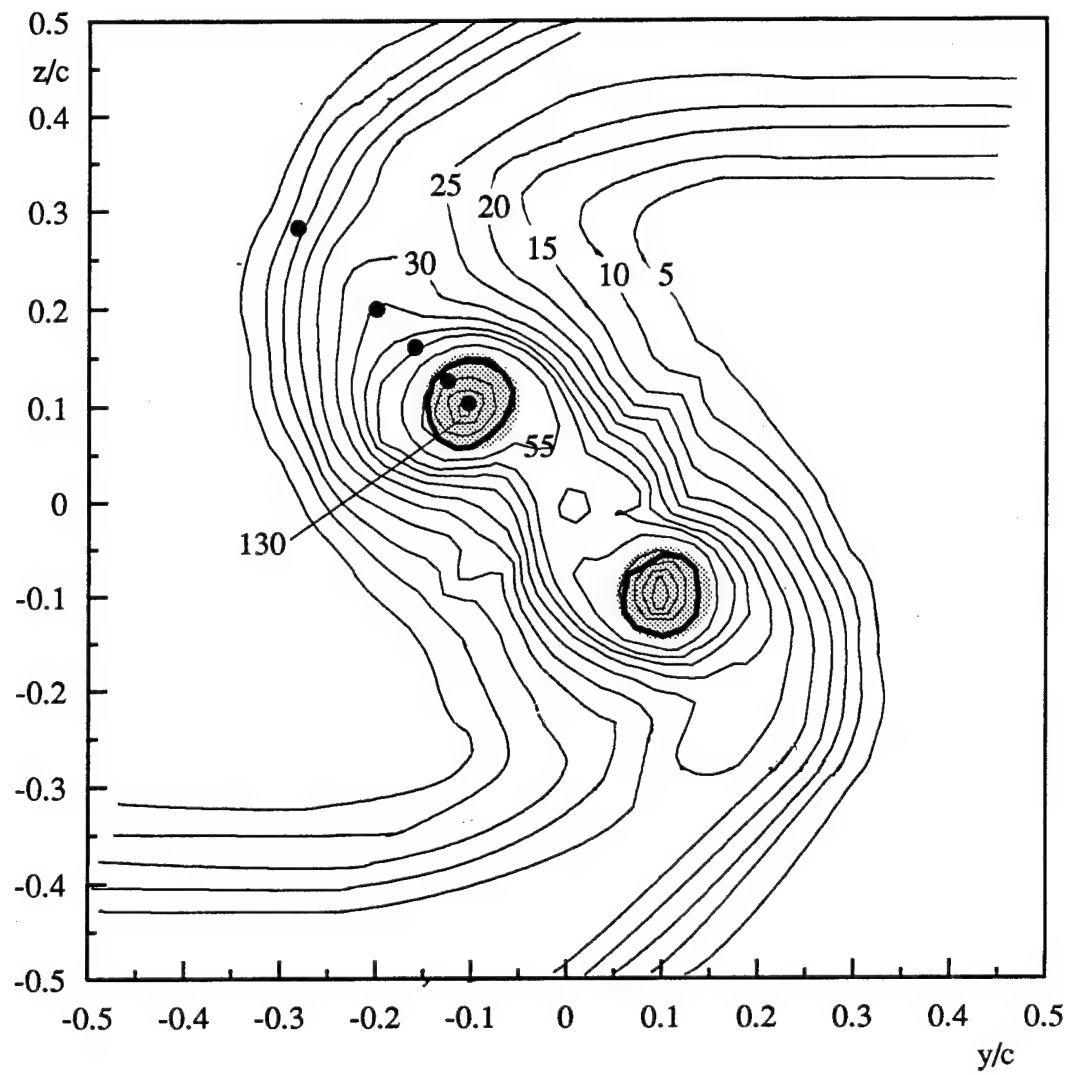


Figure 68. Contours of turbulence axial normal stress $\bar{u}^2/U_{ref}^2 \times 10^5$ at $x/c=10$ of co-rotating pair. Shaded regions indicate where wandering contributes more than 30% to the normal stresses.

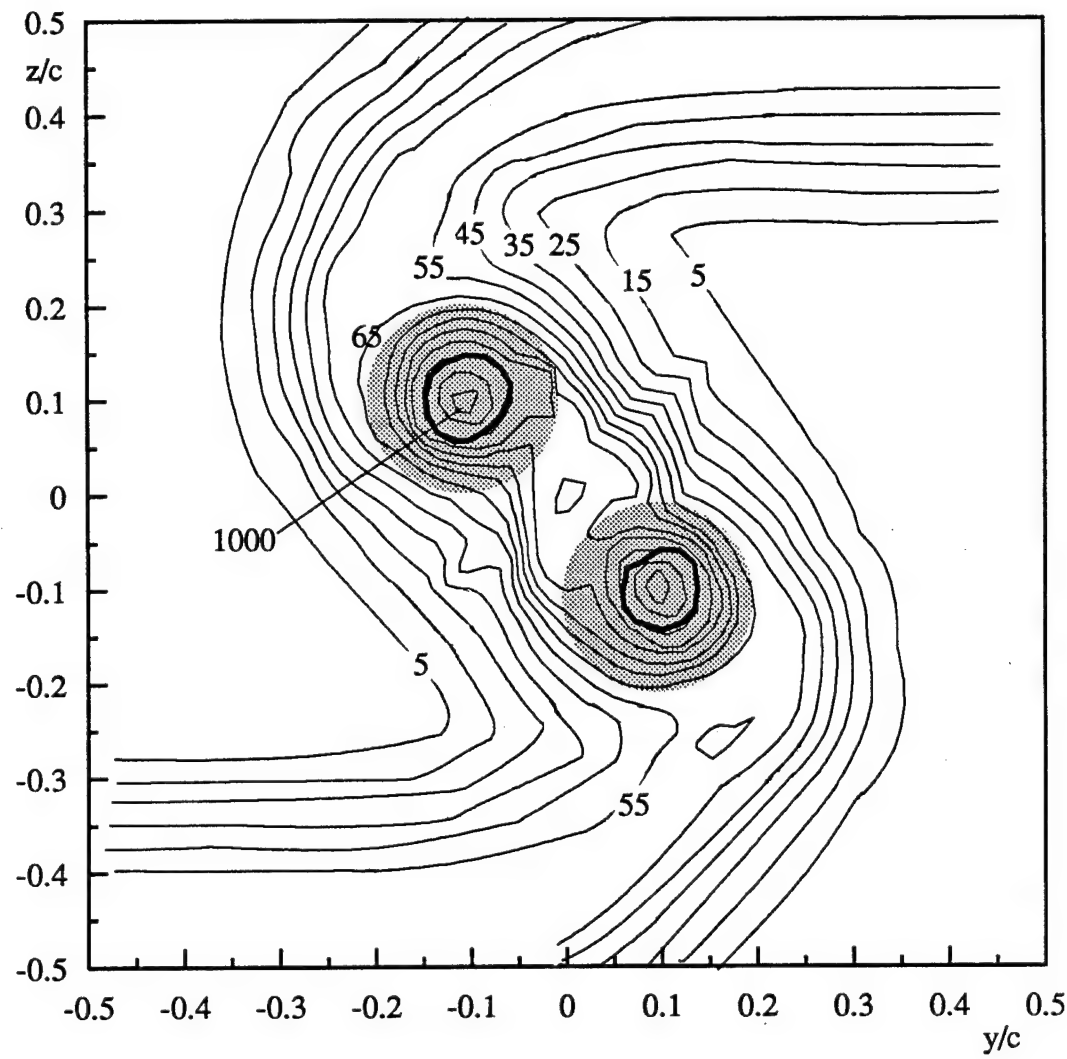


Figure 69. Contours of turbulence cross-flow normal stress sum $(\bar{v}^2 + \bar{w}^2)/U_{ref}^2 \times 10^5$ at $x/c=10$ of co-rotating pair. Shaded regions indicate where wandering contributes more than 30% to normal stresses.

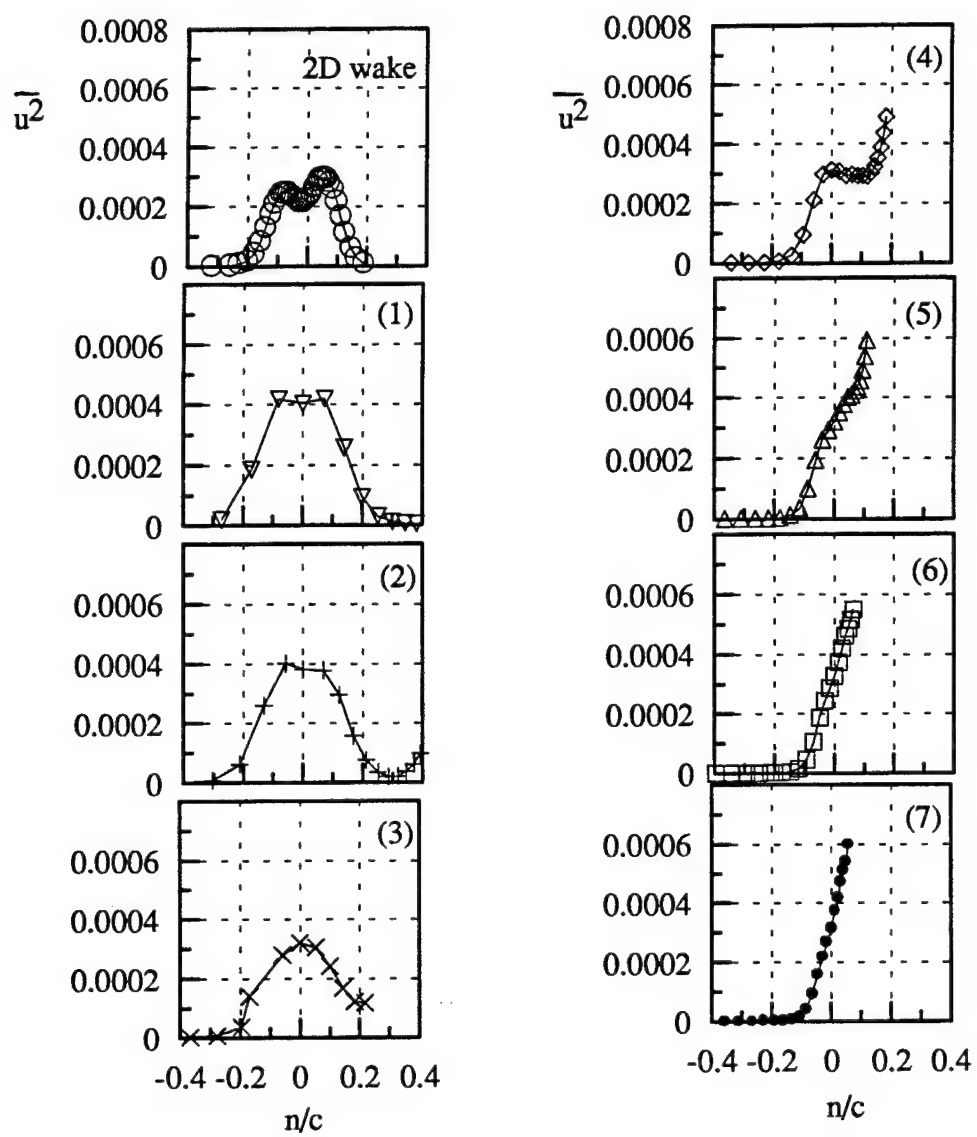


Figure 70. Profiles of axial normal stress $\bar{u}^2/U_{\text{ref}}^2$ at selected locations along the dashed line in Figure 64 at $x/c=10$ of co-rotating pair. Numbers indicate locations along this line.

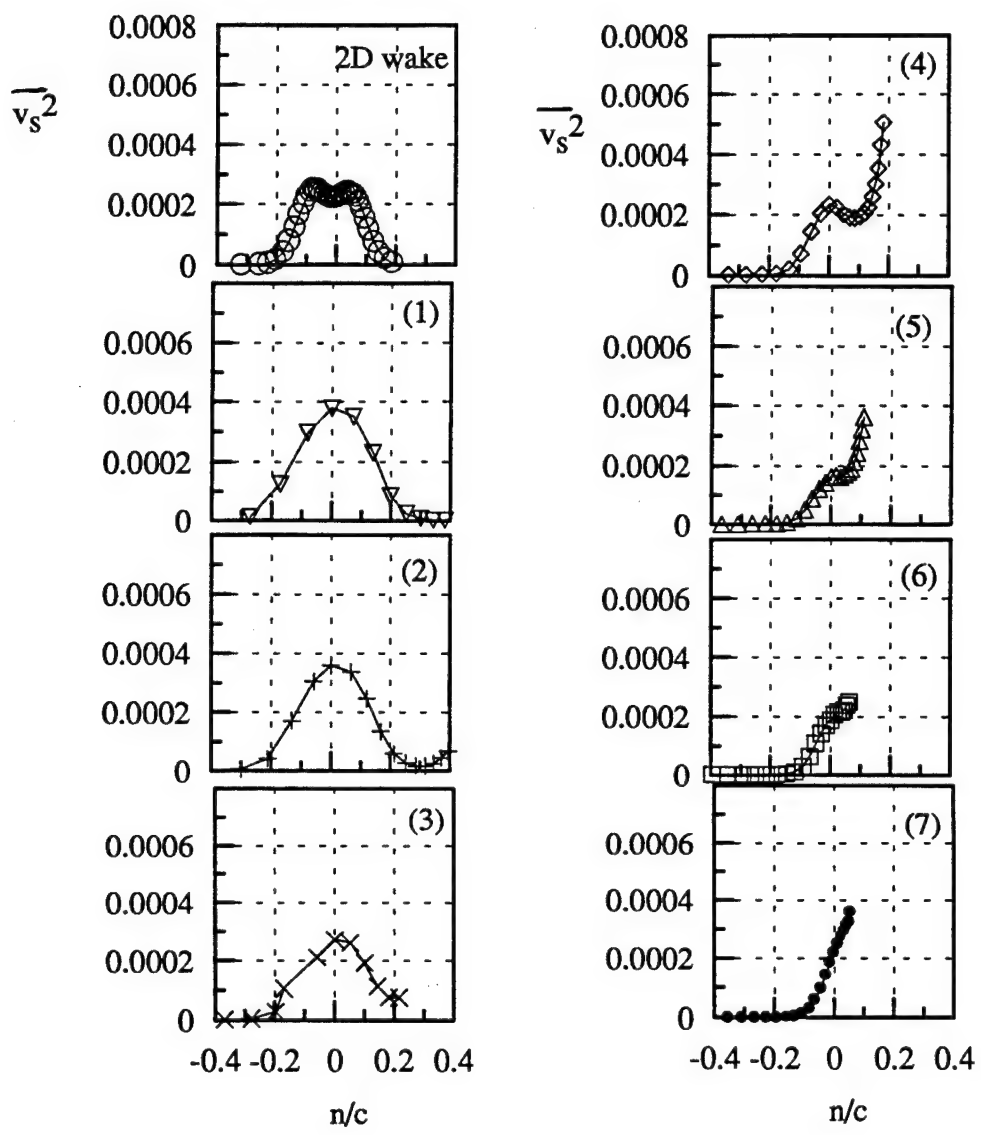


Figure 71. Profiles of normal stress $\bar{v_s}^2/U_{ref}^2$ parallel to spiral wake centerline in the spiral wake tail at selected locations along the dashed line in Figure 64 at $x/c=10$ of co-rotating pair. Numbers indicate locations along this line.

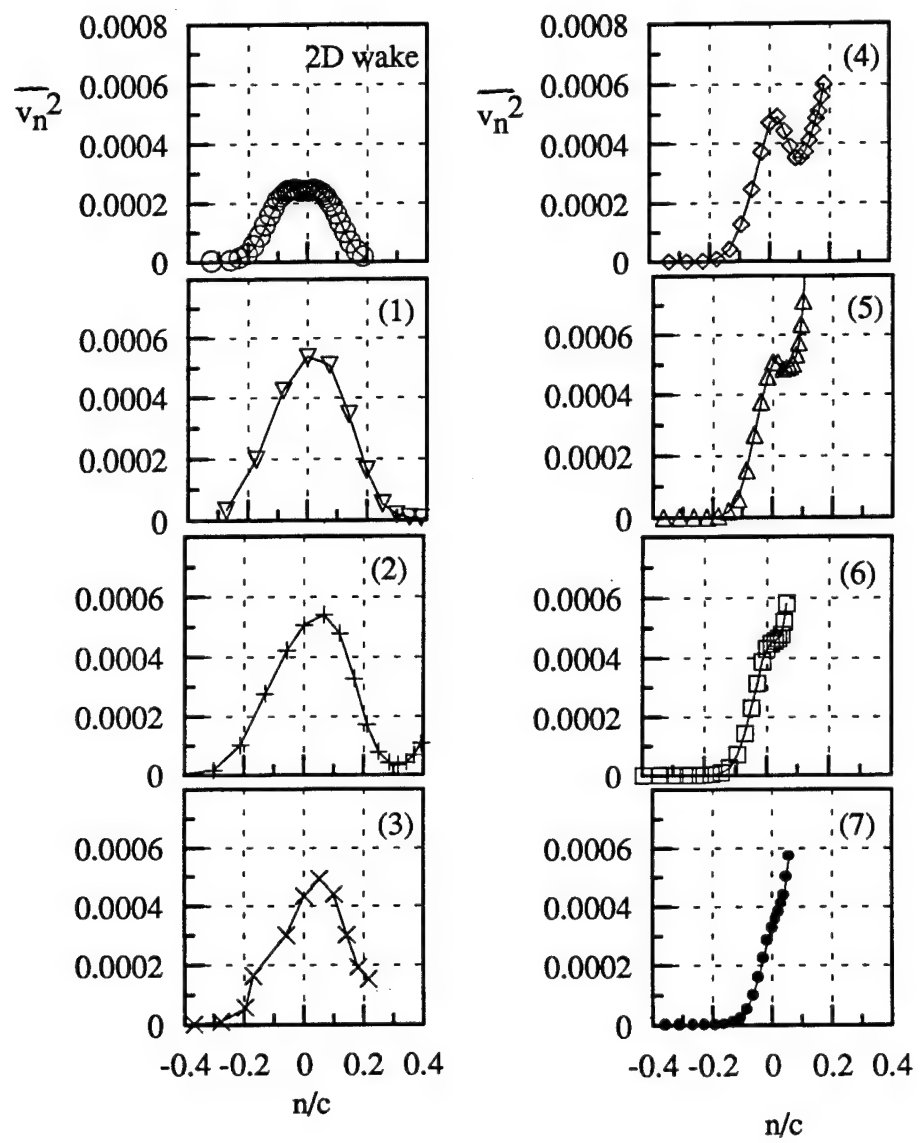


Figure 72. Profiles of normal stress $\overline{v_n^2}/U_{ref}^2$ normal to spiral wake centerline in the spiral wake tail at selected locations along the dashed line in Figure 64 at $x/c=10$ of co-rotating pair. Numbers indicate locations along this line.

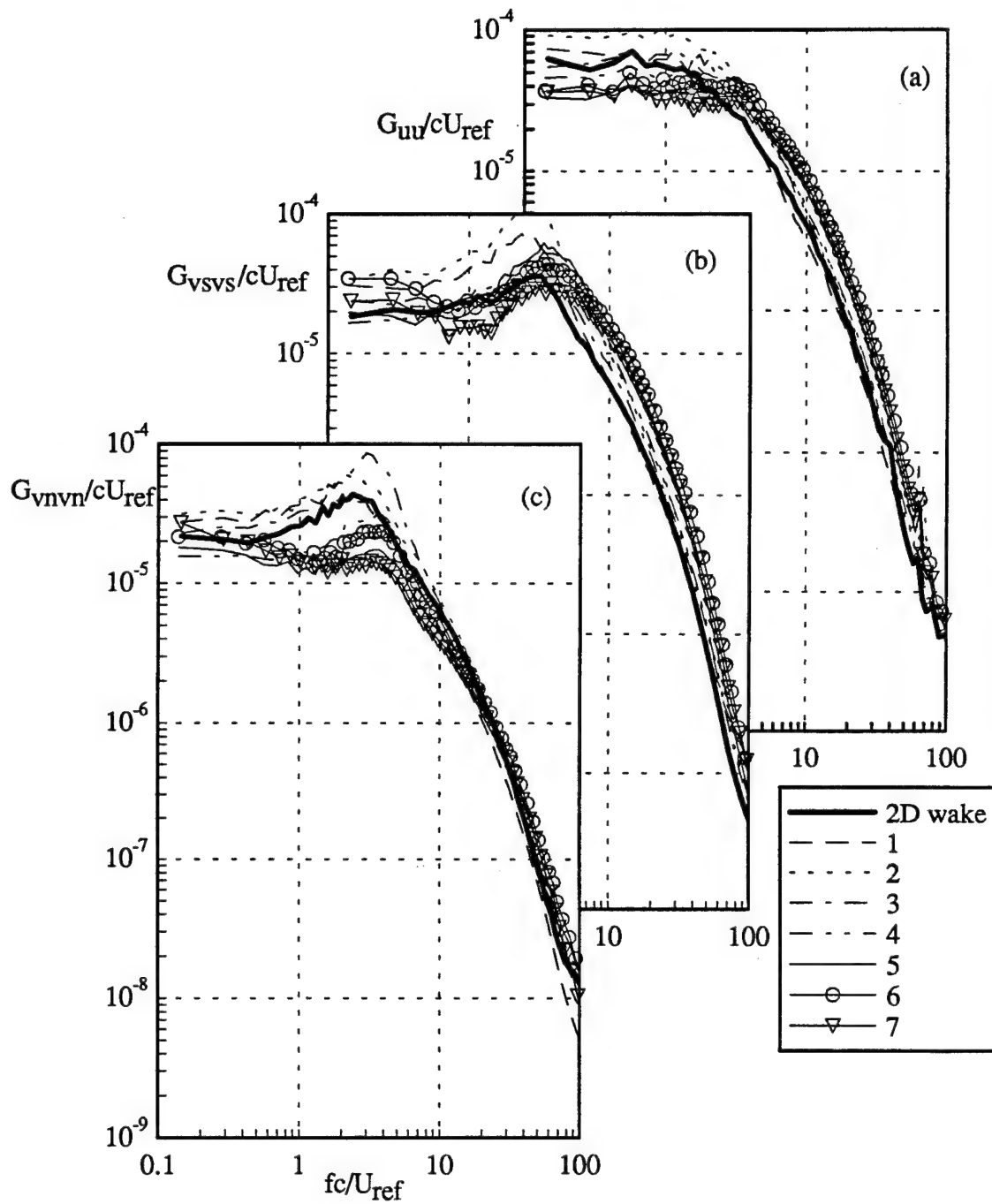


Figure 73 Velocity autospectra in coordinates aligned with the spiral-wake centerline in the spiral wake tail at $x/c=10$ of co-rotating pair (a) U spectra, (b) V_s spectra, (c) V_n spectra. Locations indicated by dots in Figure 64.

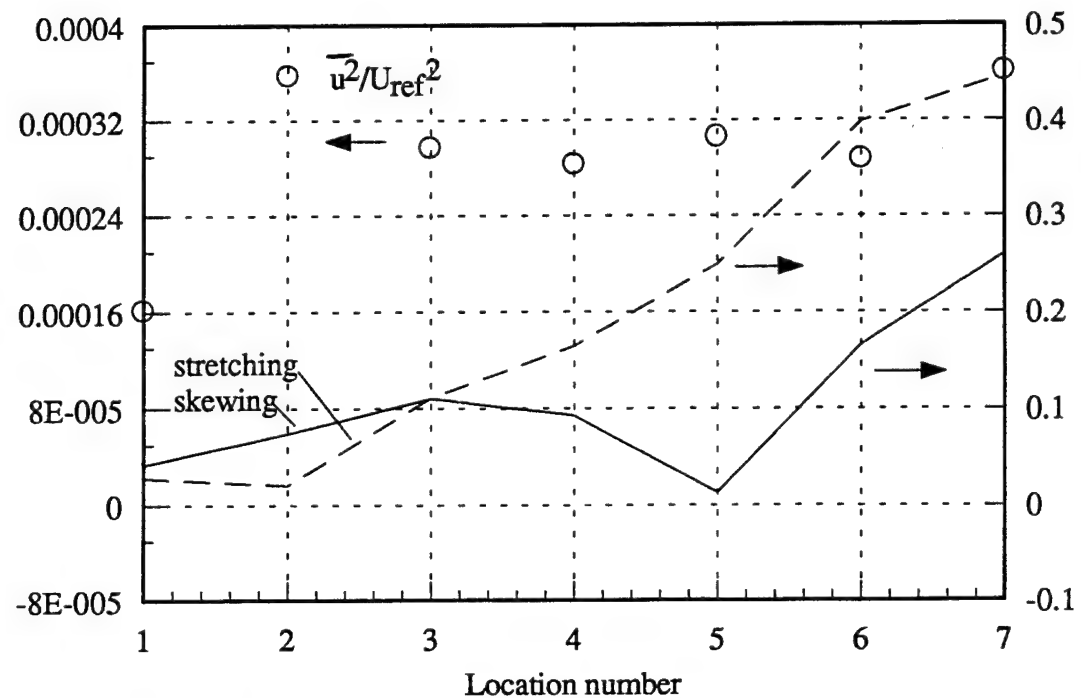


Figure 74. Rates of strain and turbulence stress on the curve about the upper core in Figure 64 at $x/c=10$ of co-rotating pair. Strain rates normalized on maximum axial velocity gradient in the two-dimensional portion of the wake.

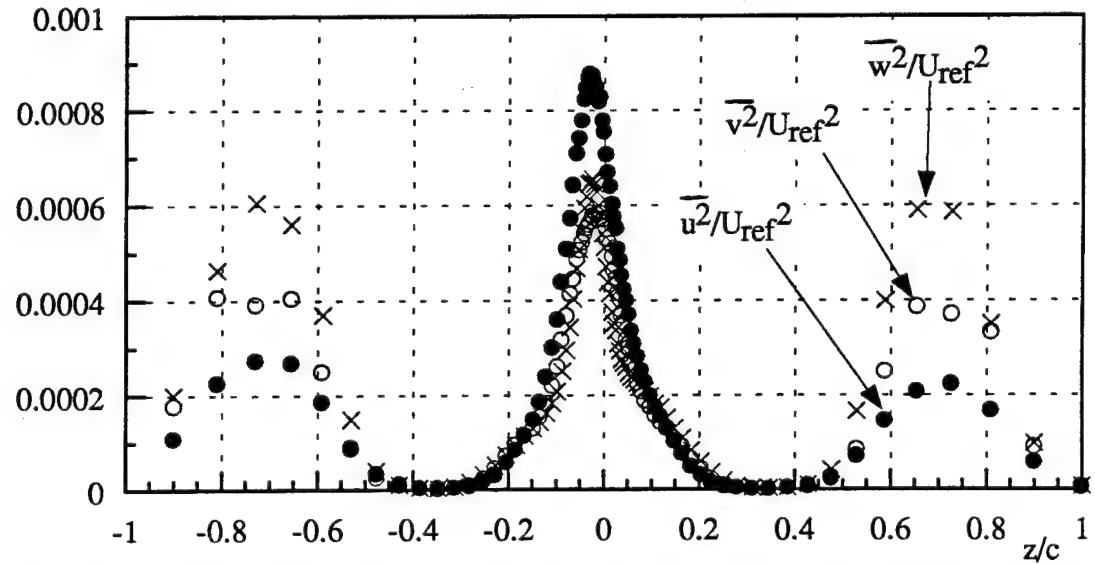


Figure 75. Normal stress profiles along the plane of antisymmetry between the vortex cores at $x/c=10$ of co-rotating pair

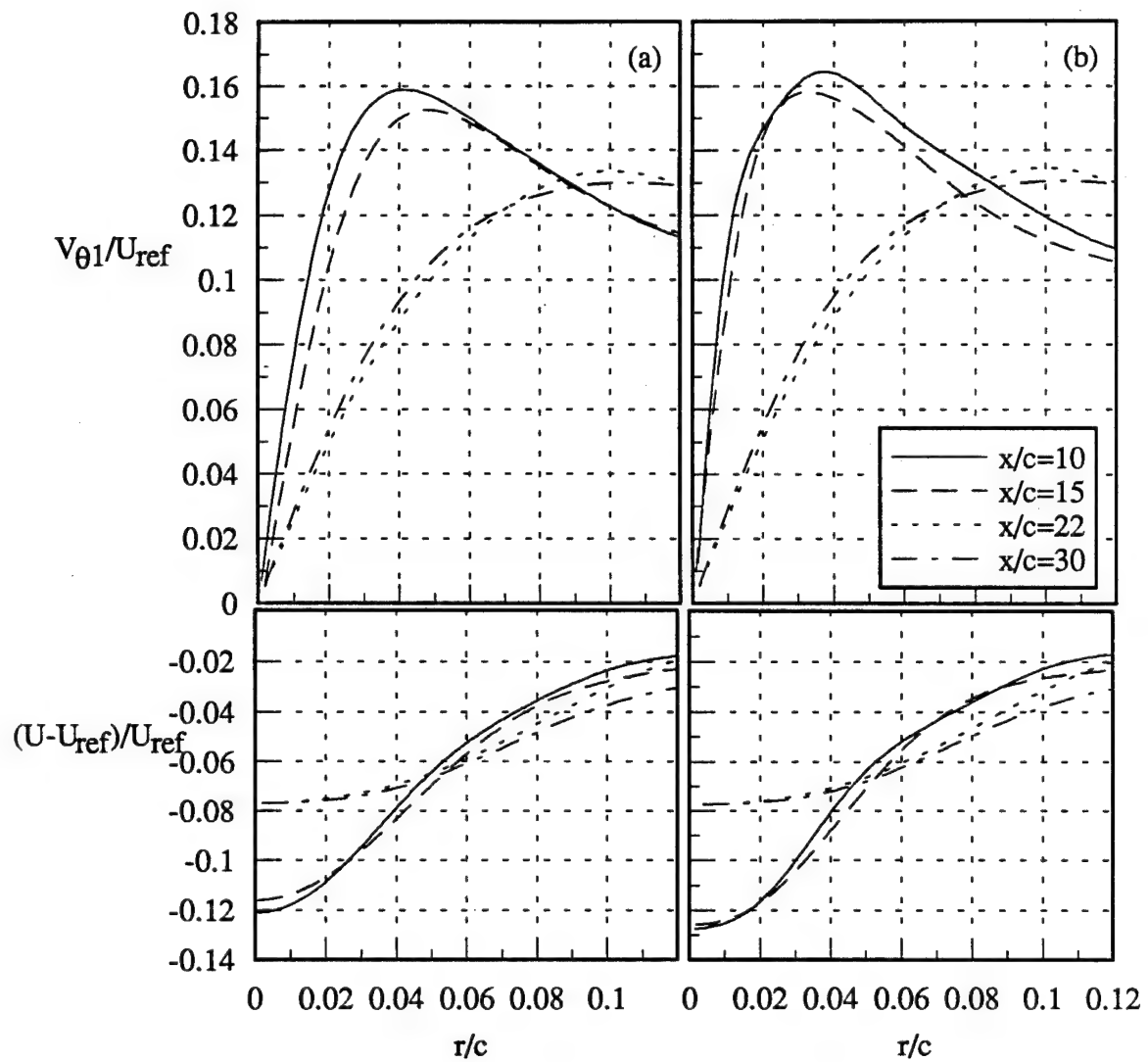


Figure 76. Mean tangential and axial velocity profiles through the upper core of co-rotating pair at $x/c=10$ and lower core at $x/c=15$ and through the single core at $x/c=22$ and 30 (a) uncorrected and (b) corrected for the effects of wandering

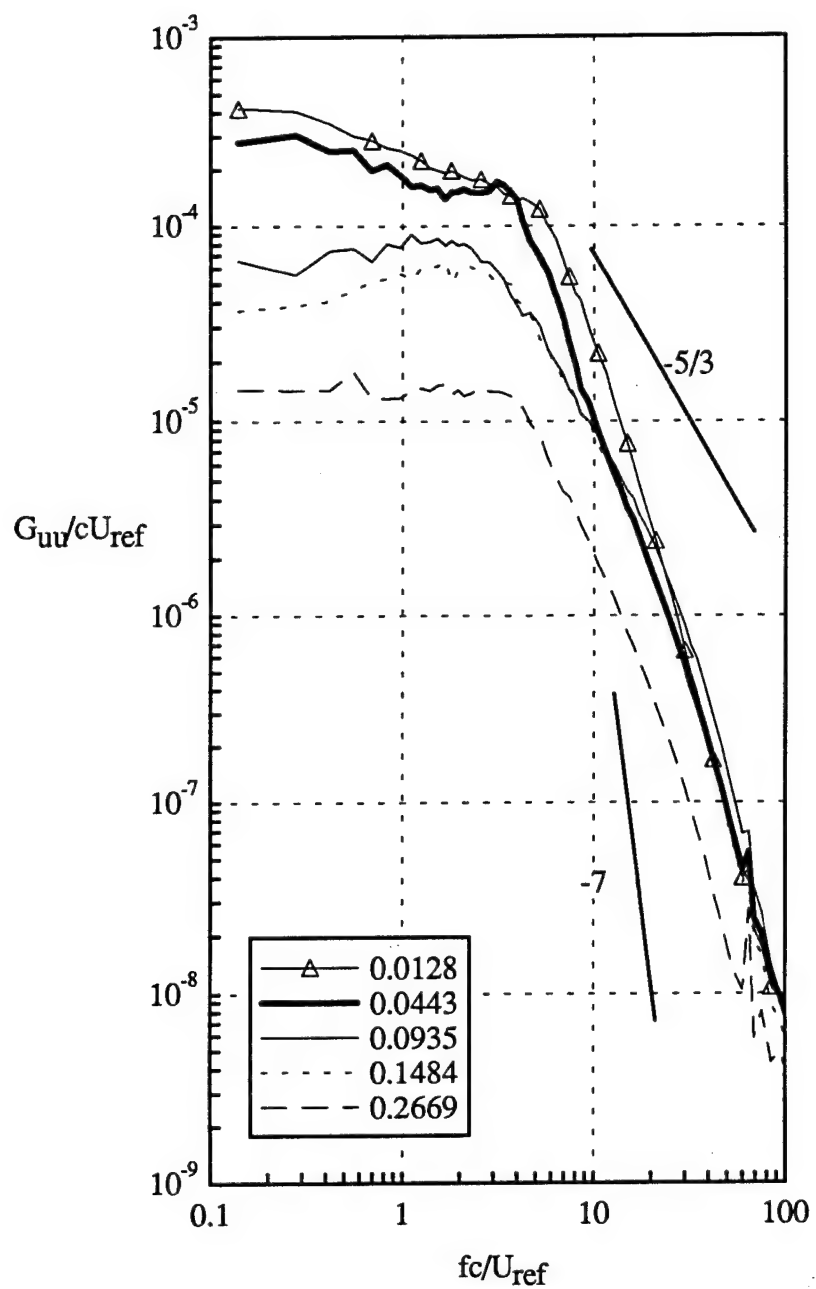


Figure 77 Autospectra of U velocity fluctuations at various spanwise locations along a horizontal profile through the upper core center indicated by dots in Figure 68 at $x/c=10$ of co-rotating pair. Locations relative to the core center at $y/c=0.129$.

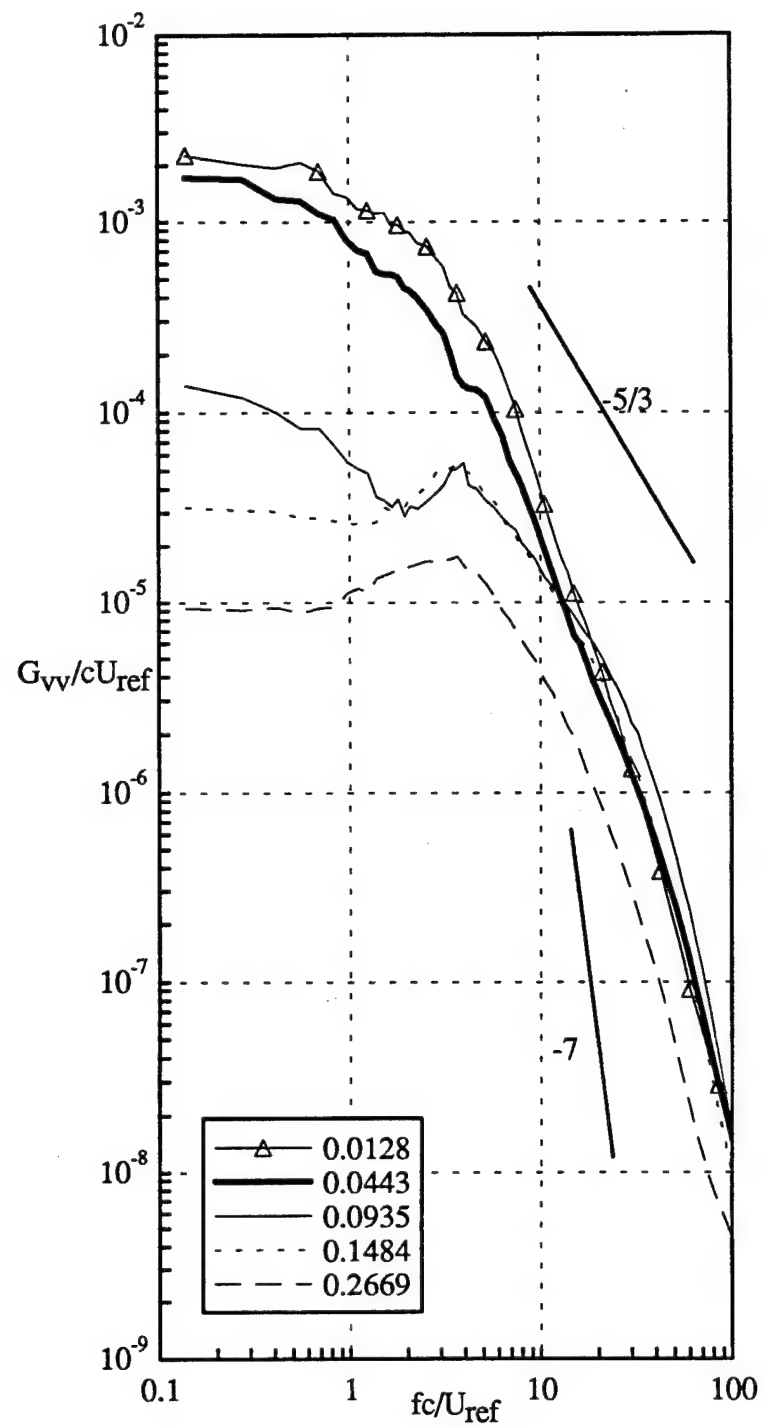


Figure 78 Autospectra of V velocity fluctuations at various spanwise locations along a horizontal profile through the upper core center indicated by dots in Figure 68 at $x/c=10$ of co-rotating pair. Locations relative to the core center at $y/c=0.129$.

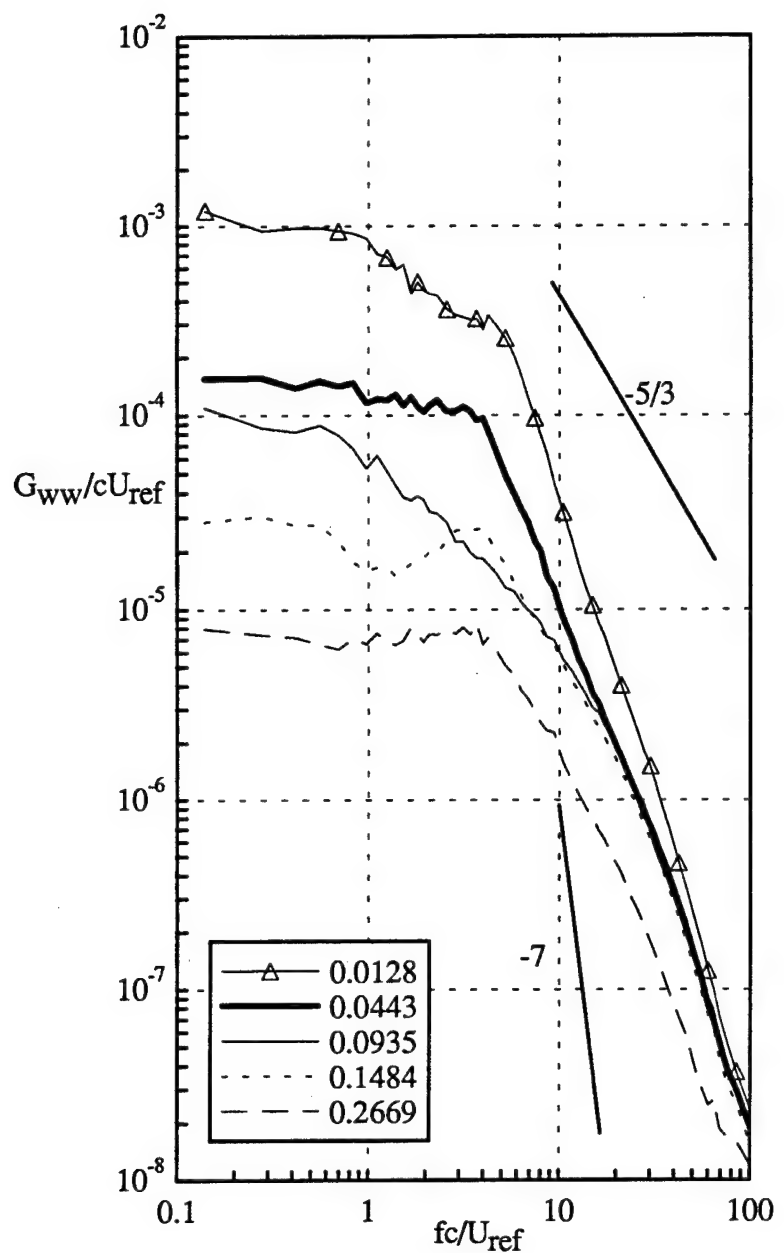


Figure 79. Autospectra of W velocity fluctuations at various spanwise locations along a horizontal profile through the upper core center indicated by dots in Figure 68 at $x/c=10$ of co-rotating pair. Locations relative to the core center at $y/c=0.129$.

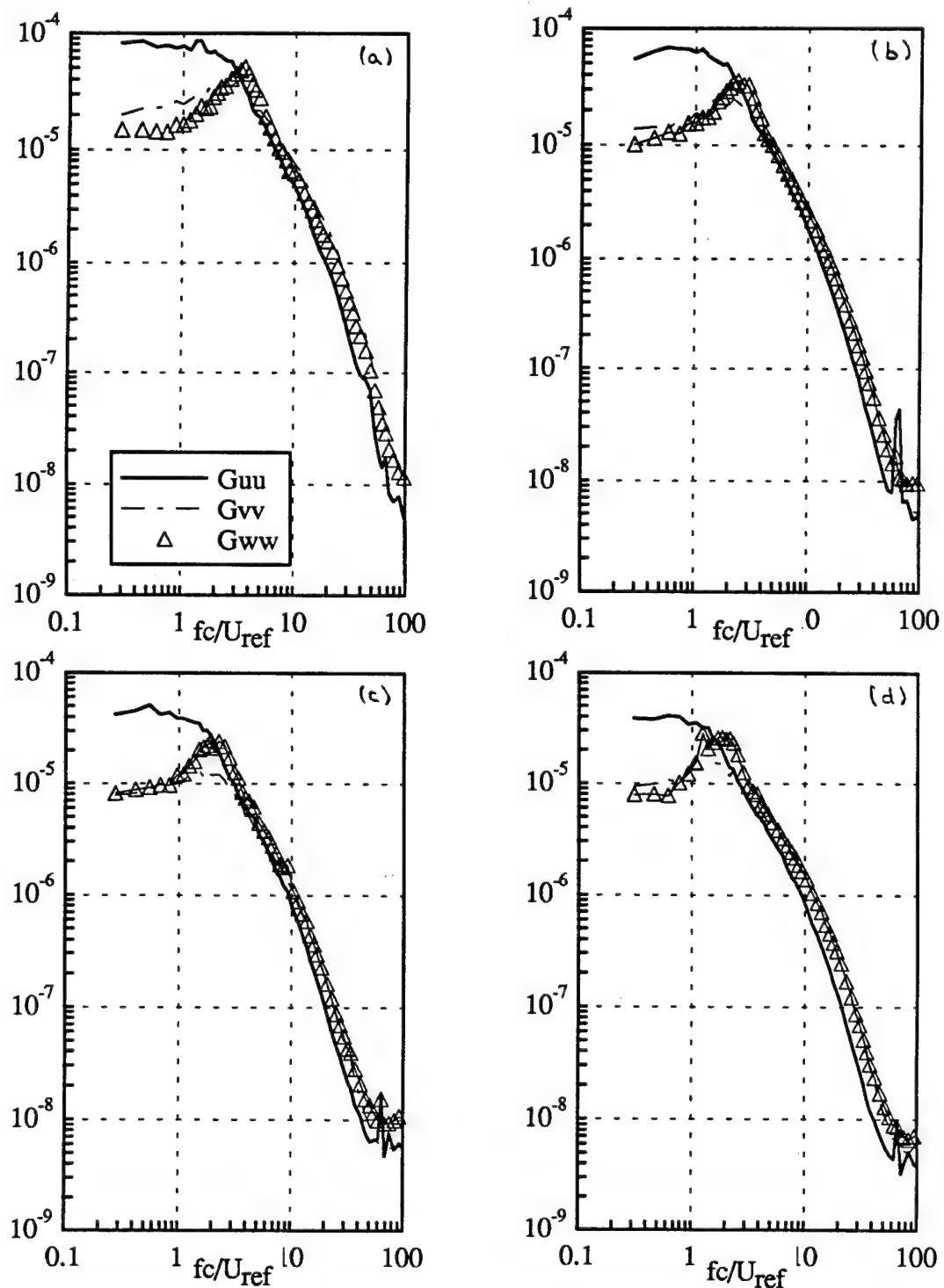


Figure 80 Autospectra at centerline of two-dimensional portion of the wake of the co-rotating pair at (a) $x/c=10$, (b) $x/c=15$, (c) $x/c=22$, (d) $x/c=30$ normalized on U_{ref} and c

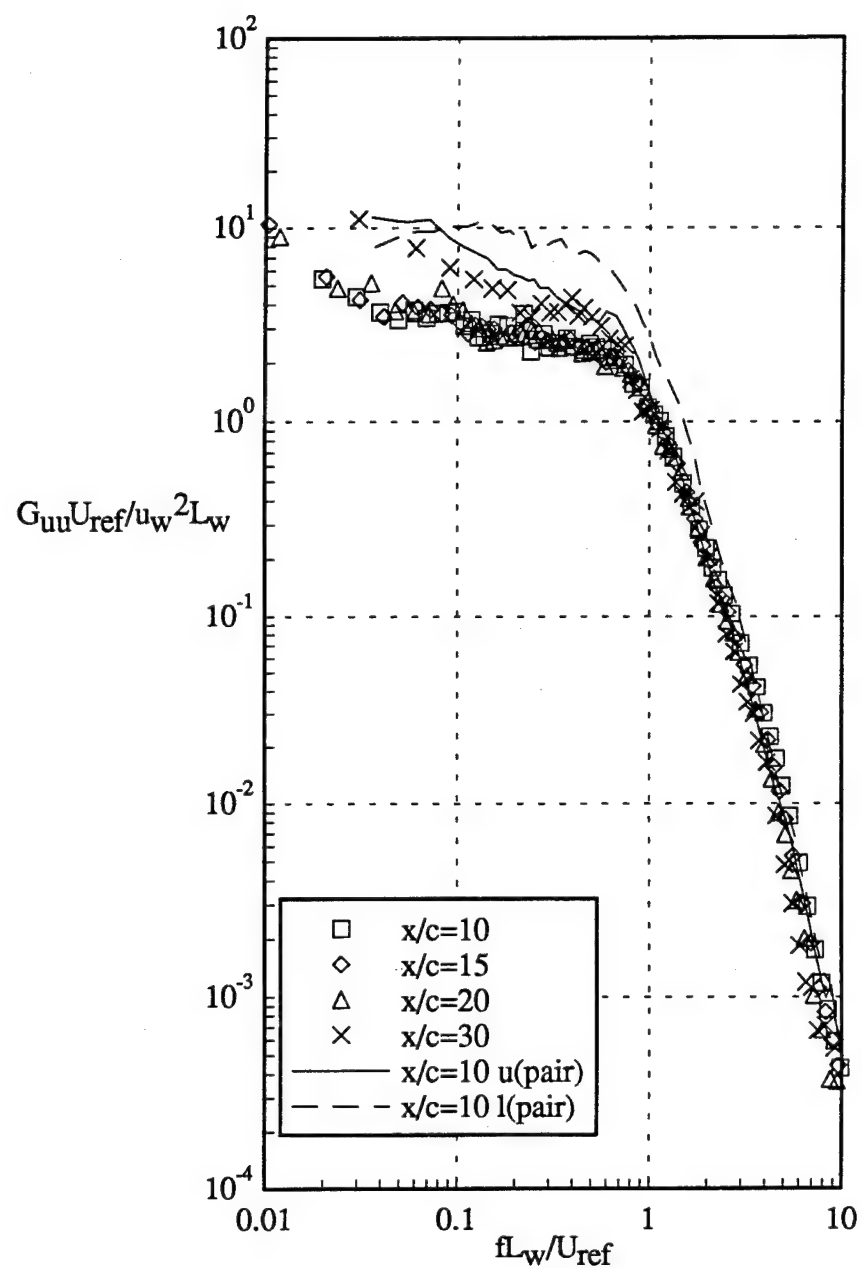


Figure 81. Autospectra of U velocity fluctuations at core center normalized on two-dimensional wake parameters for isolated vortex cases and co-rotating pair at $x/c=10$. Solid line is the upper core and dashed line is the lower core.

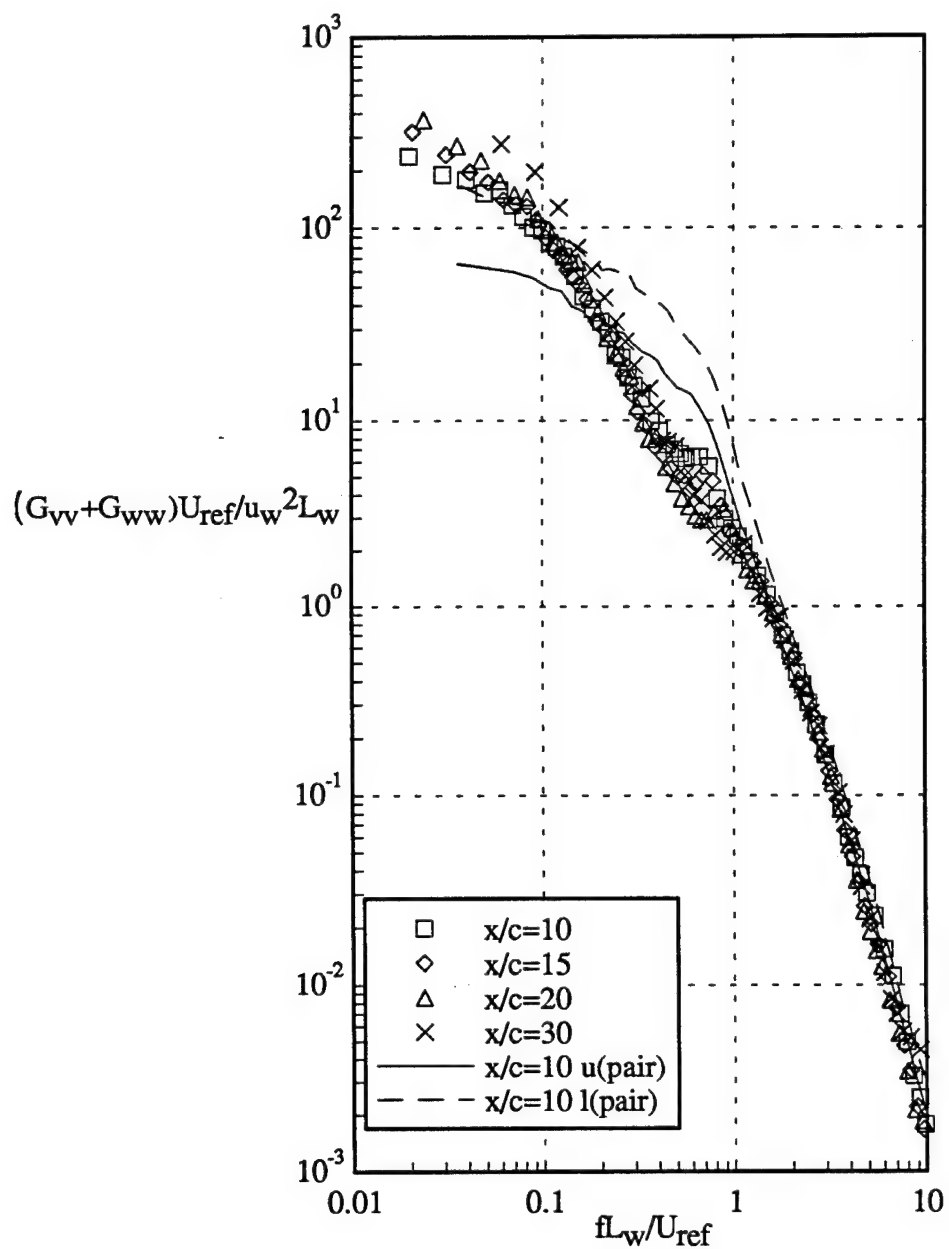


Figure 82 Autospectra of V+W velocity fluctuations at core center normalized on parameters of the two-dimensional wake for isolated vortex and co-rotating pair at $x/c=10$. Solid line is upper vortex and dashed line is lower vortex.

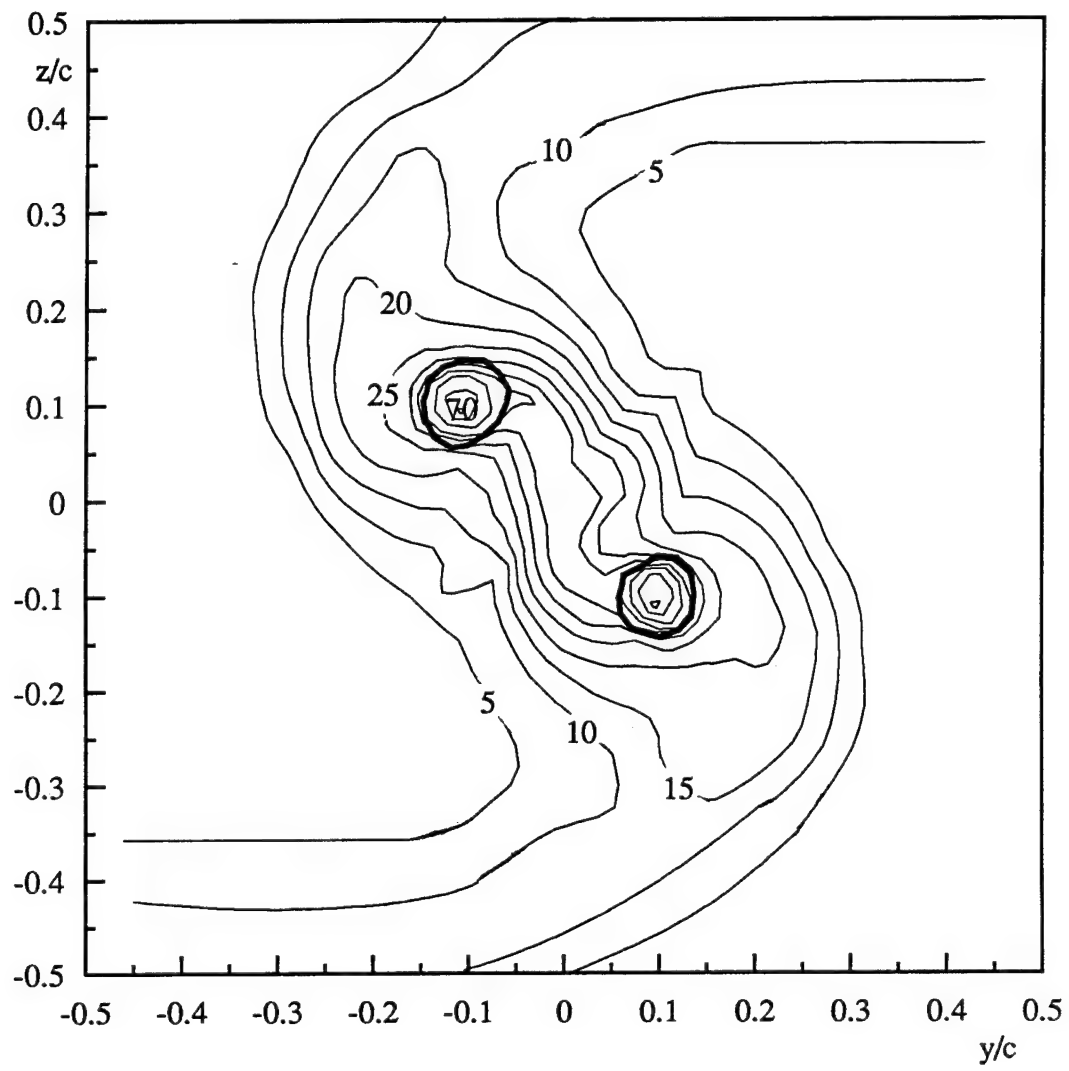


Figure 83 Contours of axial normal stress $\bar{u}^2/U_{ref}^2 \times 10^5$ filtered at $fc/U_{ref} = 3$ at $x/c = 10$ of co-rotating pair.

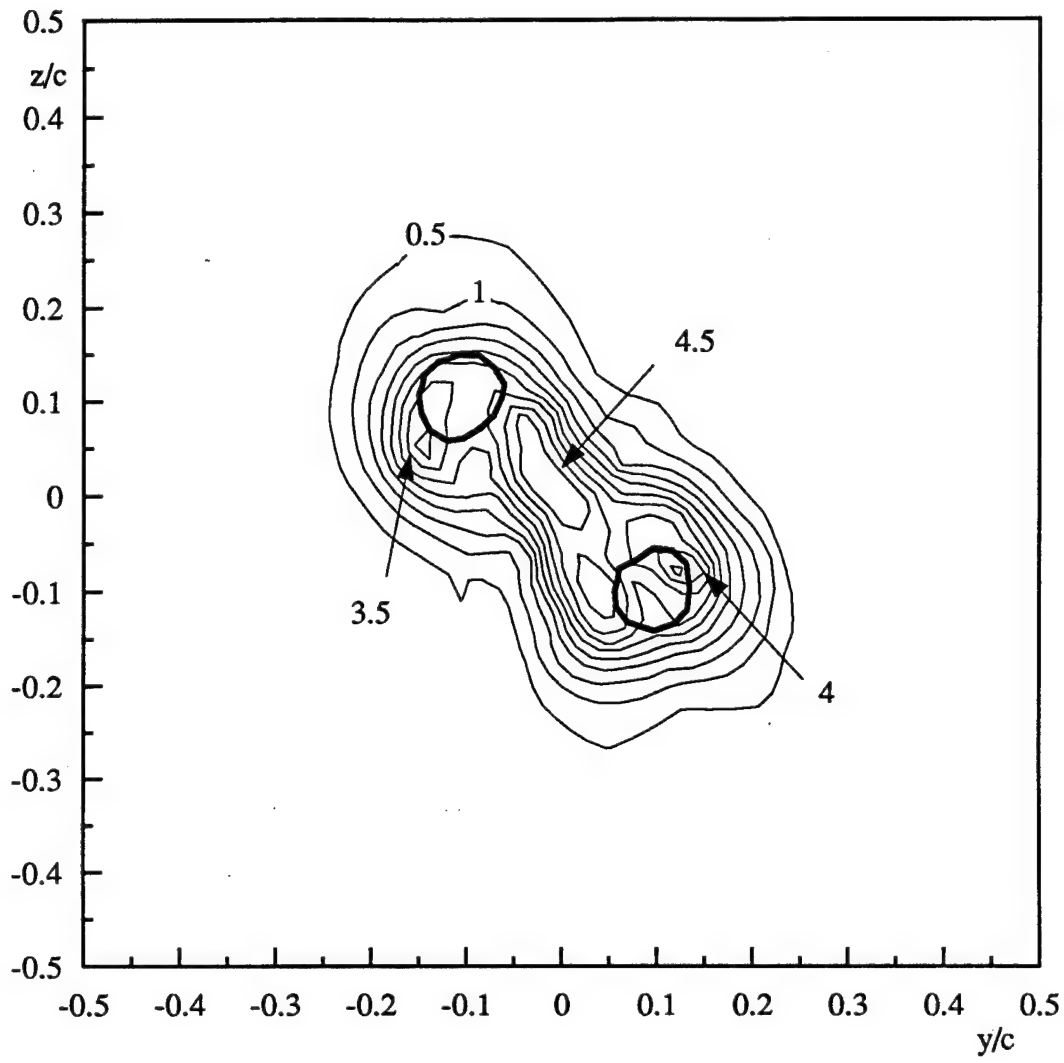


Figure 84 Contours of axial normal stress $\bar{u}^2/U_{ref}^2 \times 10^6$ filtered at $fc/U_{ref}=40$ at $x/c=10$ of co-rotating pair.

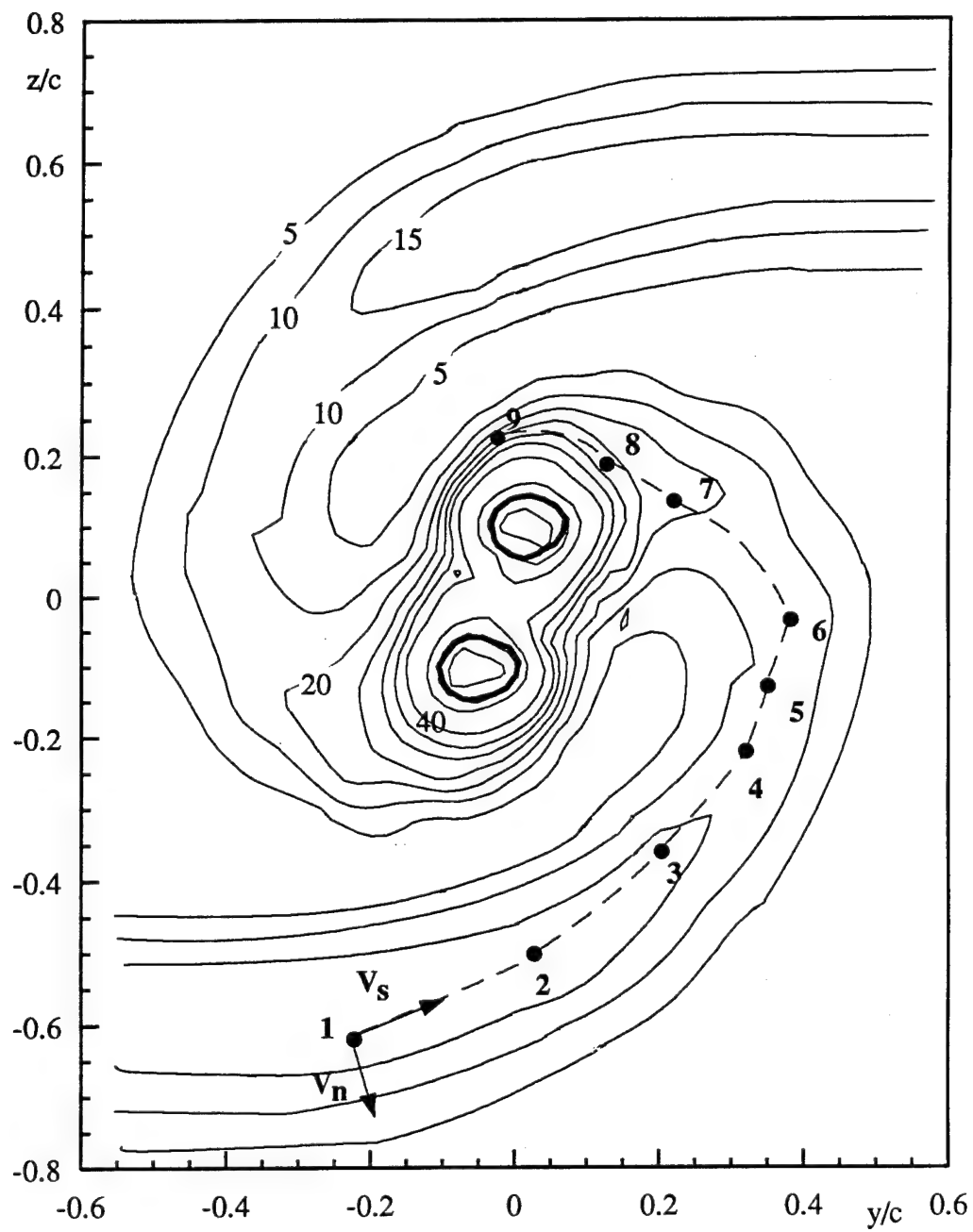


Figure 85. Contours of turbulence axial normal stress $\bar{u}^2/U_{ref}^2 \times 10^5$ at $x/c = 15$ of co-rotating pair. Dashed line denotes spiral wake centerline in the spiral wake tail. Dots indicate locations for profiles and autospectra in Figures 91-94.

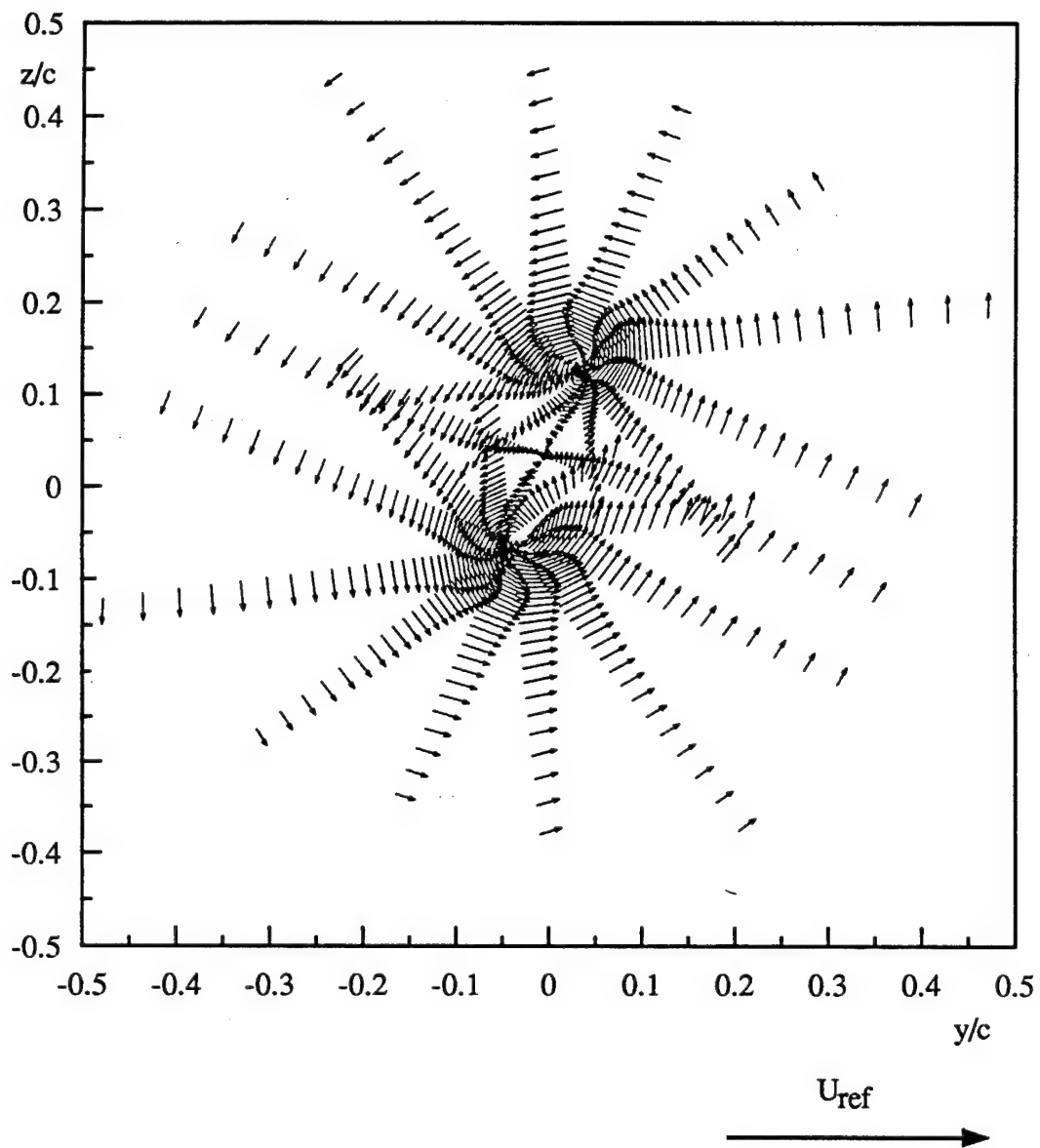


Figure 86 Mean cross-flow velocity vectors at $x/c=15$ of co-rotating pair

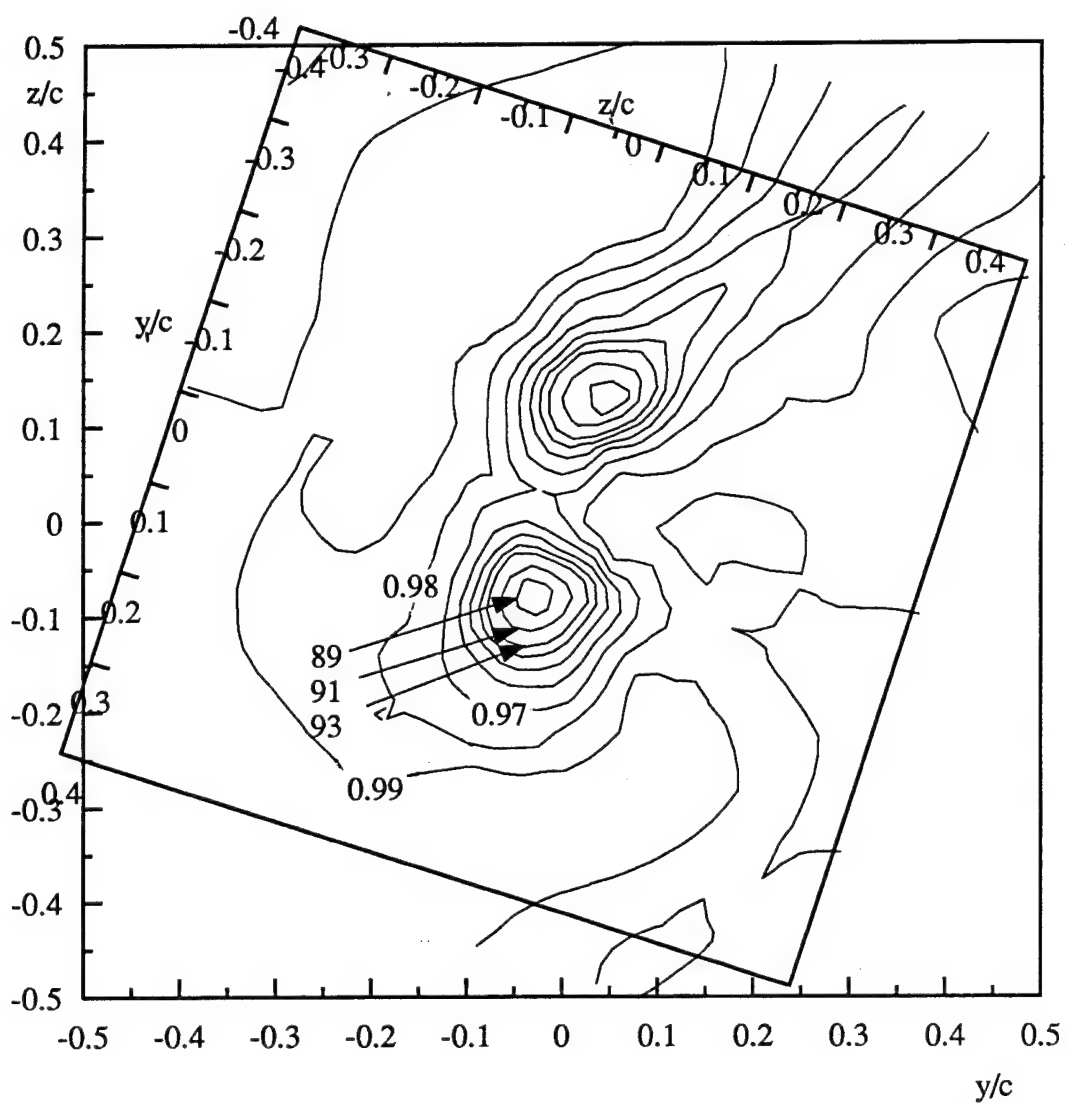


Figure 87. Contours of mean axial velocity U/U_{ref} at $x/c=15$ of co-rotating pair.
Additional axes define rotated coordinate system (y_1, z_1).

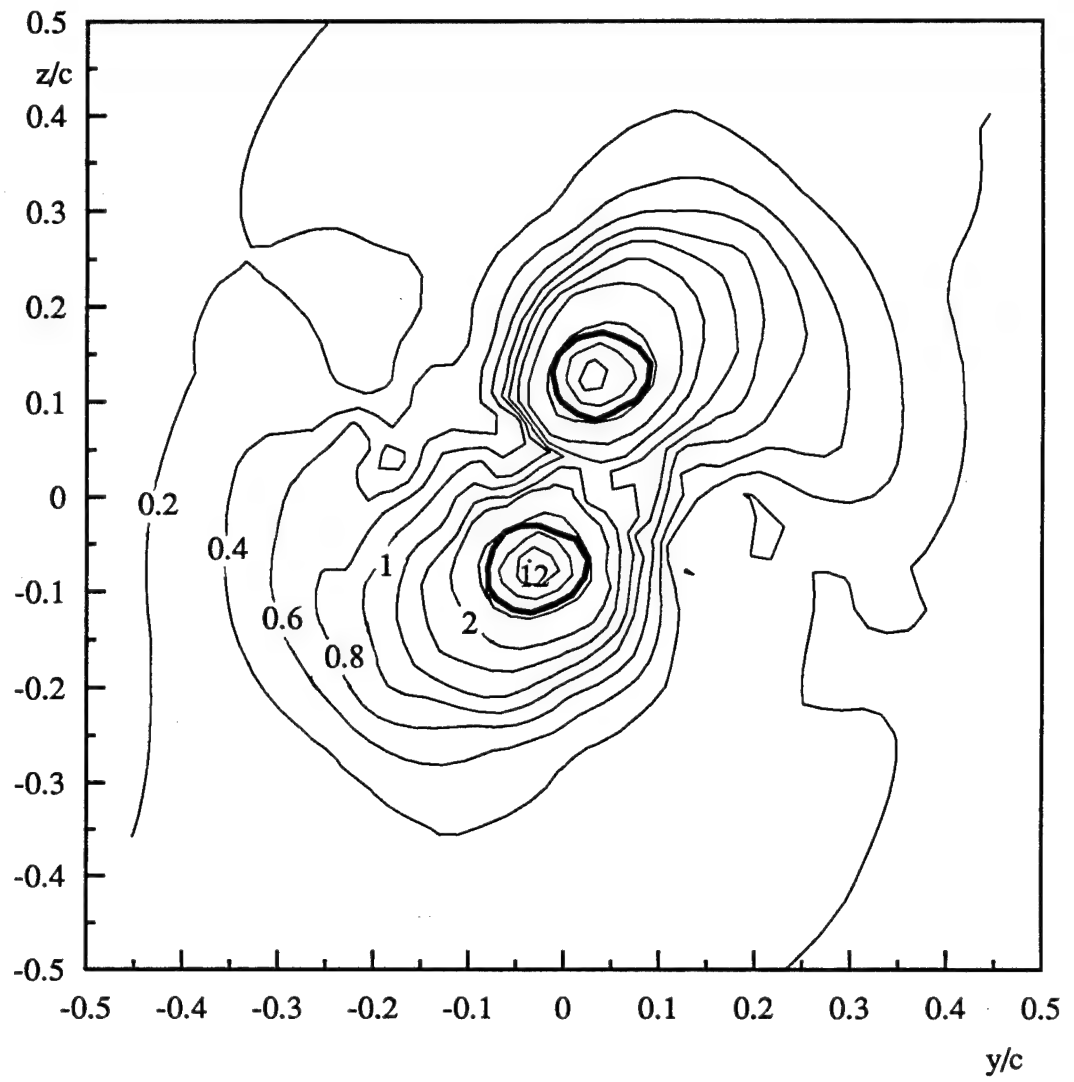


Figure 88 Contours of mean streamwise vorticity normalized on U_{ref} and c at $x/c=15$ of co-rotating pair

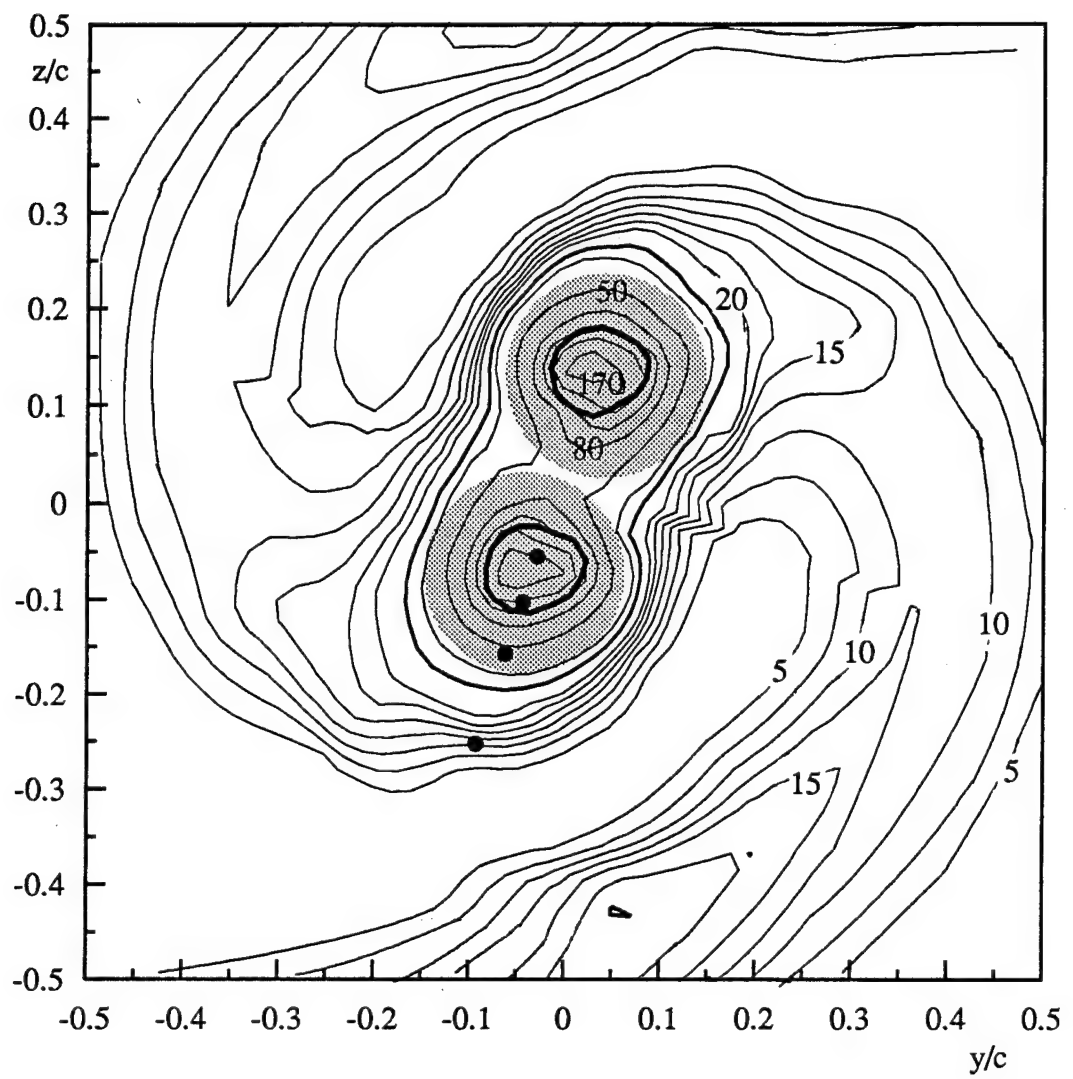


Figure 89. Contours of turbulence axial normal stress $\bar{u}^2/U_{ref}^2 \times 10^5$ at $x/c=15$ of co-rotating pair. Dots show locations of autospectra in Figure 97-99. Shaded regions indicate where wandering contributes more than 30% to turbulence stresses

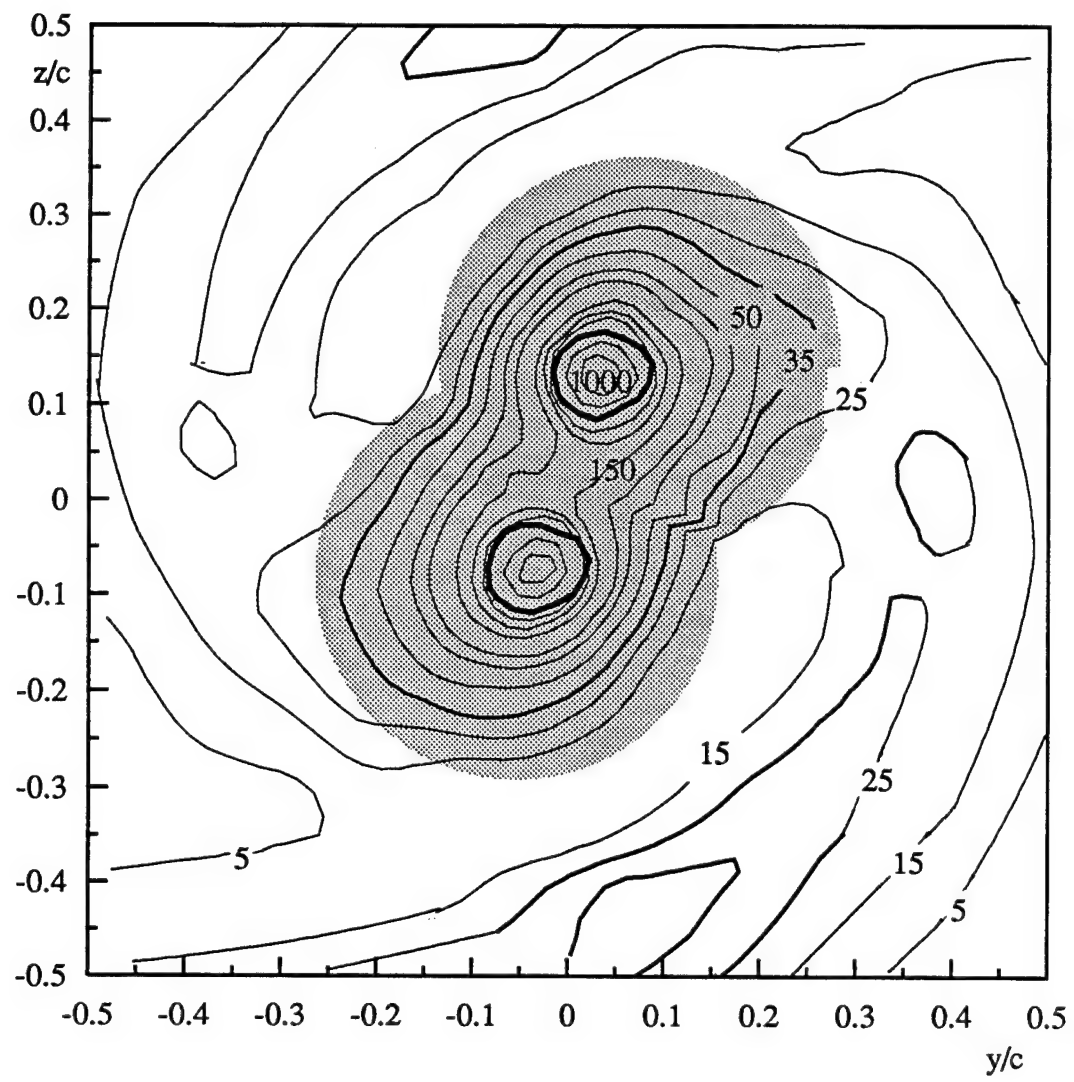


Figure 90 Contours of turbulence cross-flow normal stress sum $(\bar{v}^2 + \bar{w}^2)/U_{\text{ref}}^2 \times 10^5$ at $x/c = 15$ of co-rotating pair. Shaded regions indicate where wandering contributes more than 30% to turbulence normal stresses.

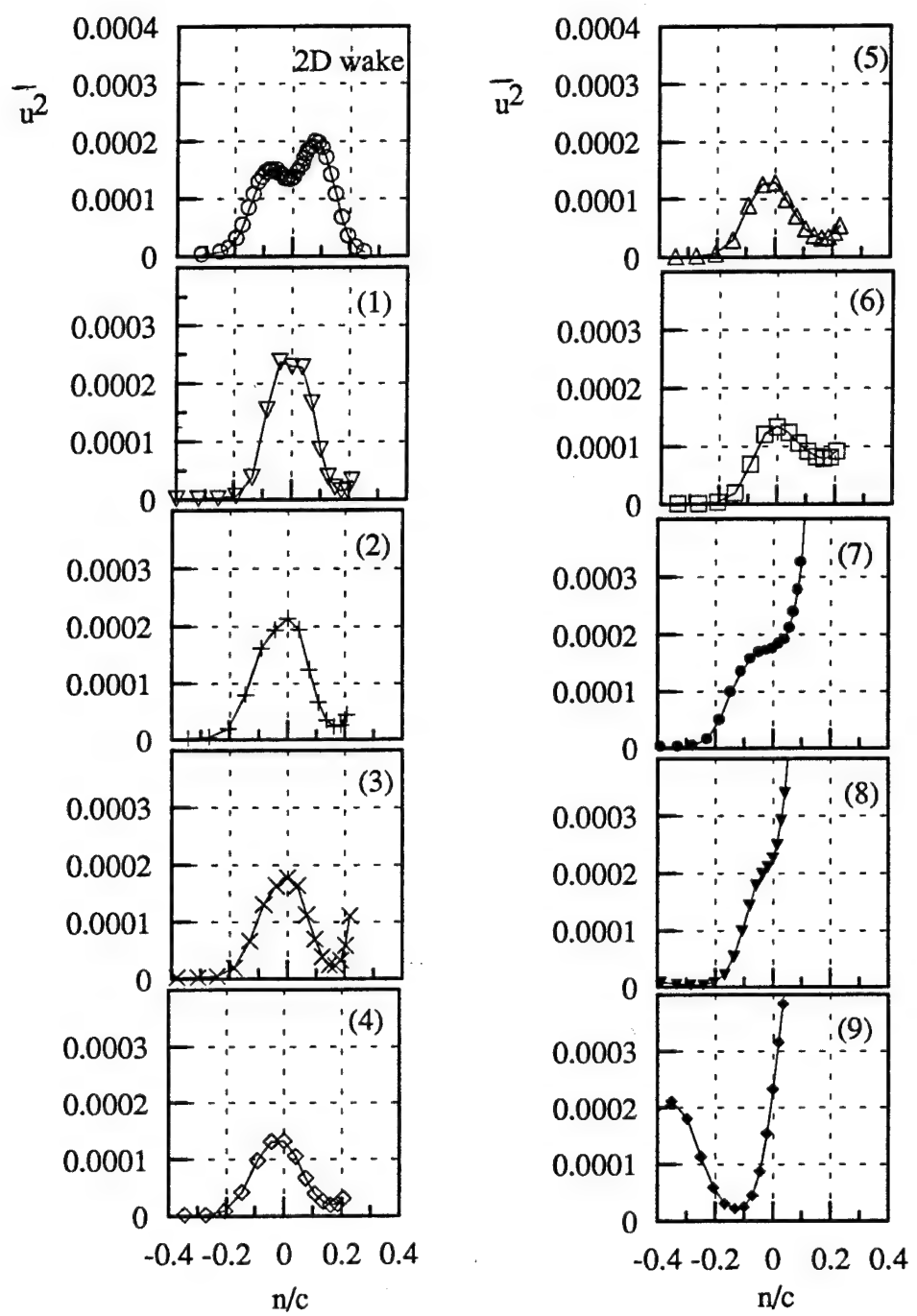


Figure 91. Profiles of axial normal stress $\bar{u}^2/U_{\text{ref}}^2$ at selected locations along the dashed line in Figure 85 at $x/c=15$ of co-rotating pair. Numbers indicate locations along this line.

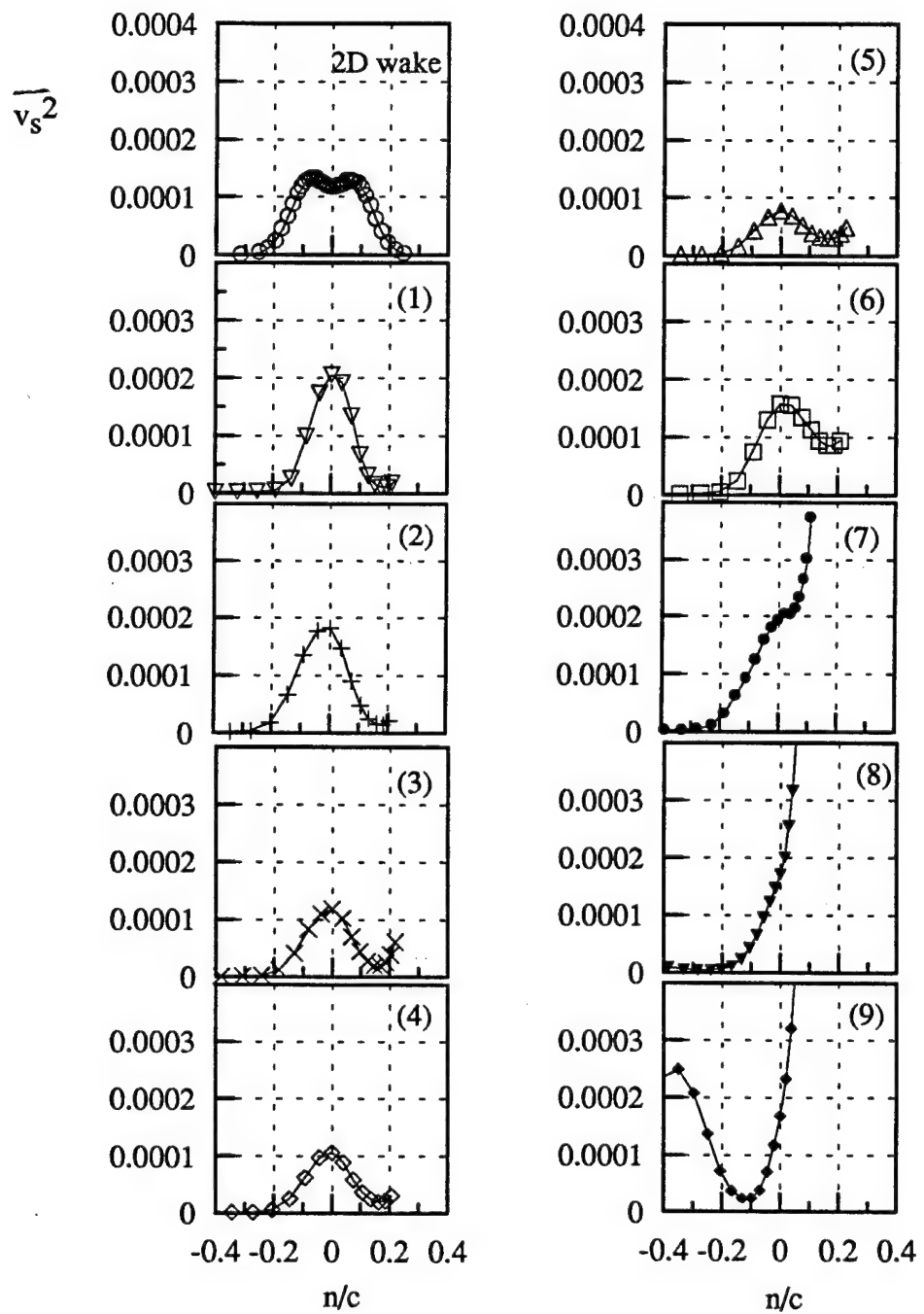


Figure 92. Profiles of normal stress $\bar{v_s}^2/U_{ref}^2$ parallel to spiral wake centerline in the spiral wake tail at selected locations along the dashed line in Figure 85 at $x/c=15$ of co-rotating pair. Numbers indicate locations along this line.

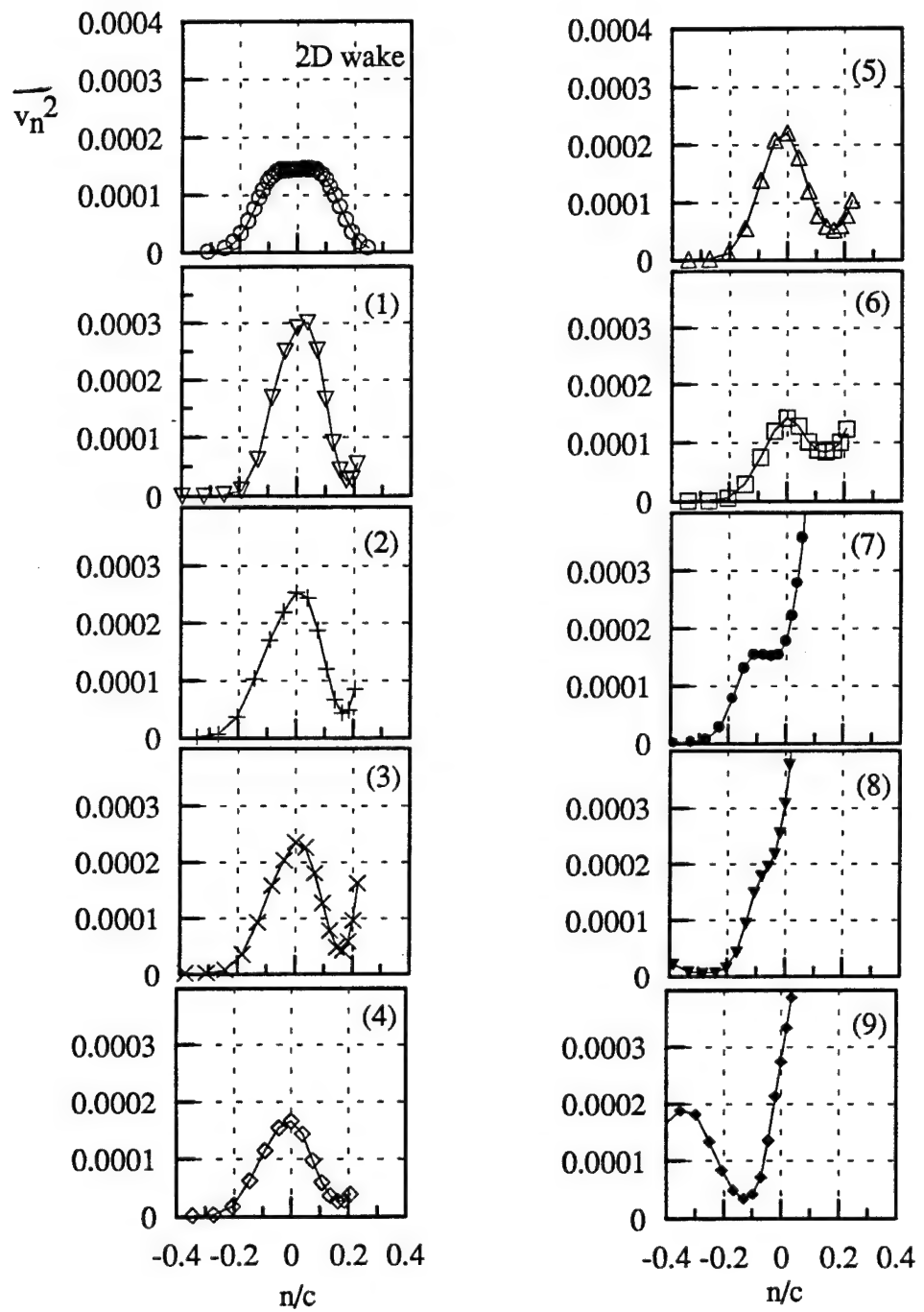


Figure 93. Profiles of normal stress \bar{v}_n^2/U_{ref}^2 normal to spiral wake centerline in the spiral wake tail at selected locations along the dashed line in Figure 85 at $x/c=15$ of co-rotating pair. Numbers indicate locations along this line.

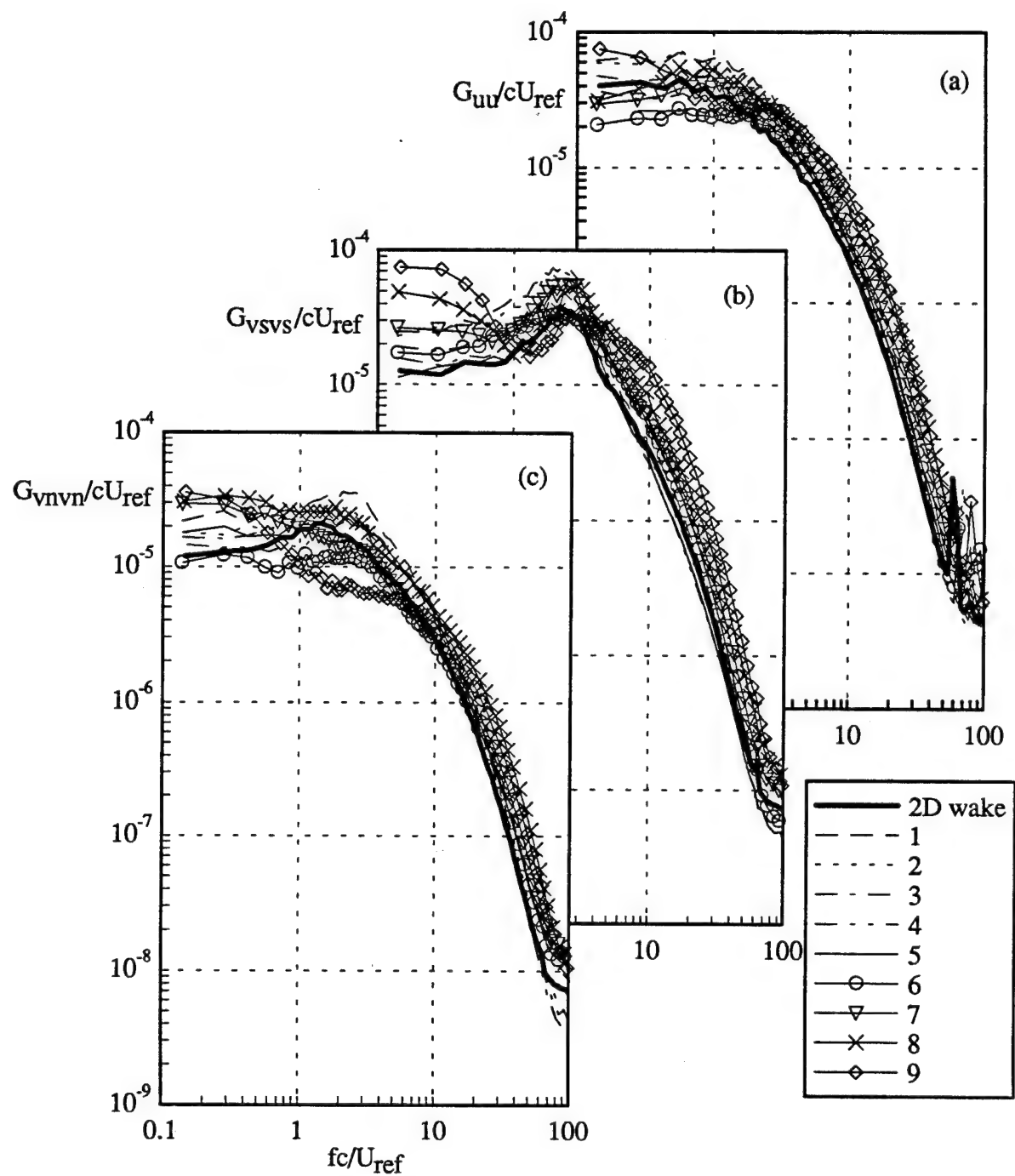


Figure 94 Velocity autospectra in coordinates aligned with the spiral-wake centerline in the spiral wake tail at $x/c=15$ of co-rotating pair (a) U spectra, (b) V_s spectra, (c) V_n spectra. Locations indicated by dots in Figure 85.

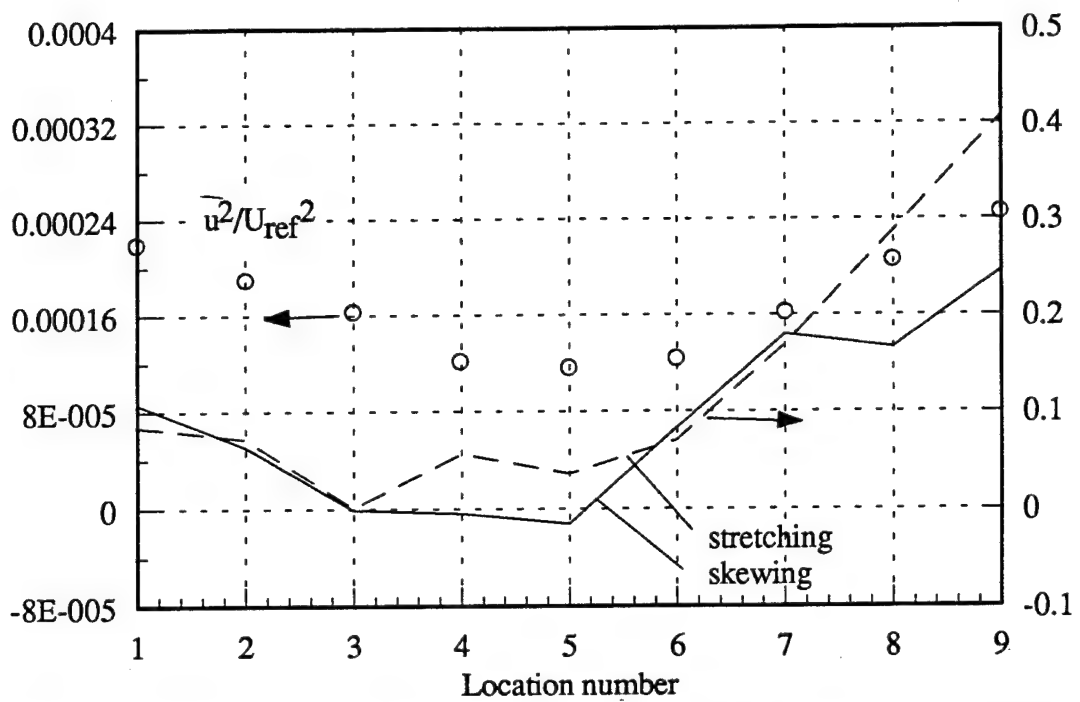


Figure 95. Rates of strain and turbulence stress on the dashed line in Figure 85 at $x/c=15$ of co-rotating pair. Strain rates normalized on maximum axial velocity gradient in the two-dimensional portion of the wake.

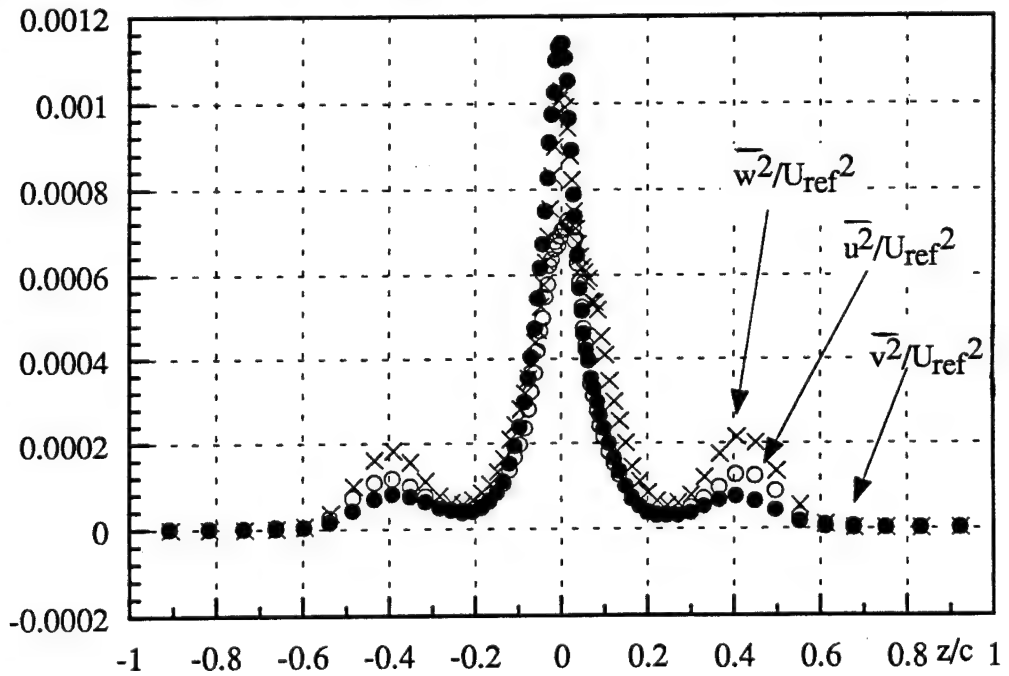


Figure 96 Normal stress profiles along the plane of antisymmetry between the vortex cores at $x/c=15$ of co-rotating pair

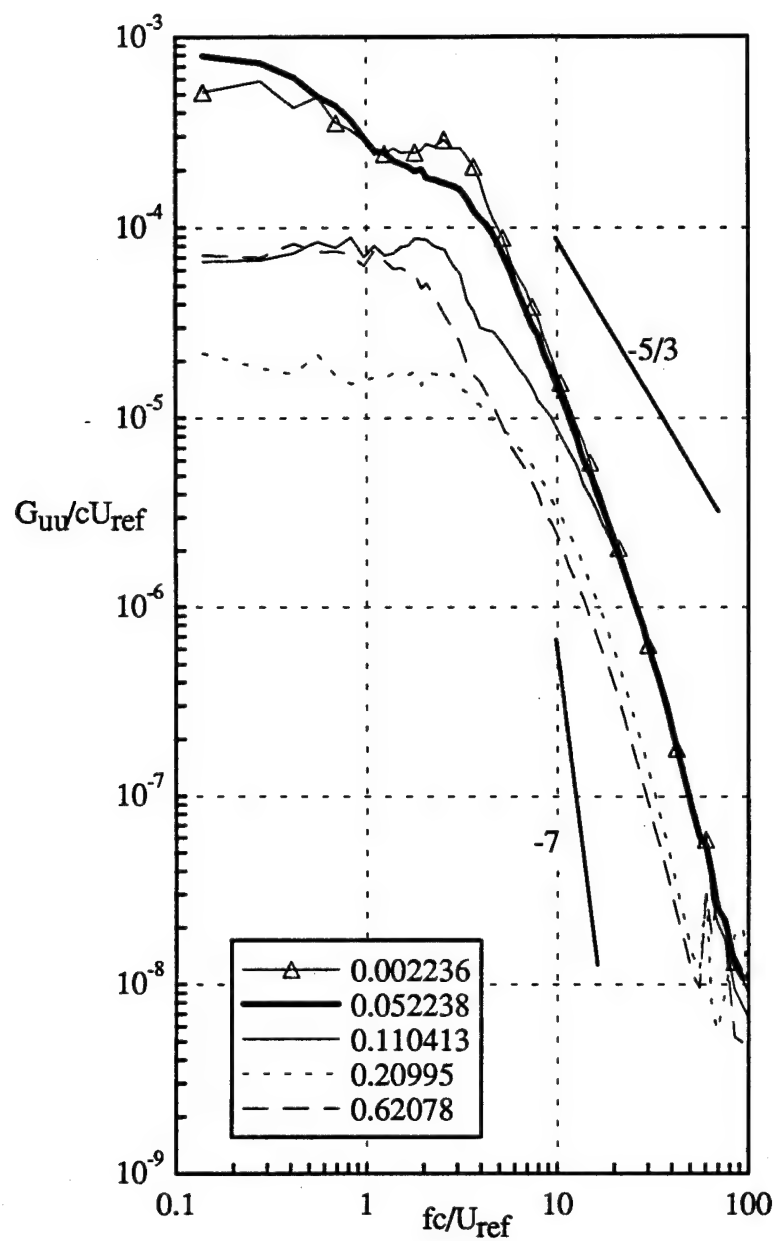


Figure 97. Autospectra of U velocity fluctuations at various spanwise locations along a horizontal profile through the lower core center indicated by the dots in Figure 89 at $x/c=15$ of co-rotating pair. Locations relative to the core center at $y/c=0.0847$.

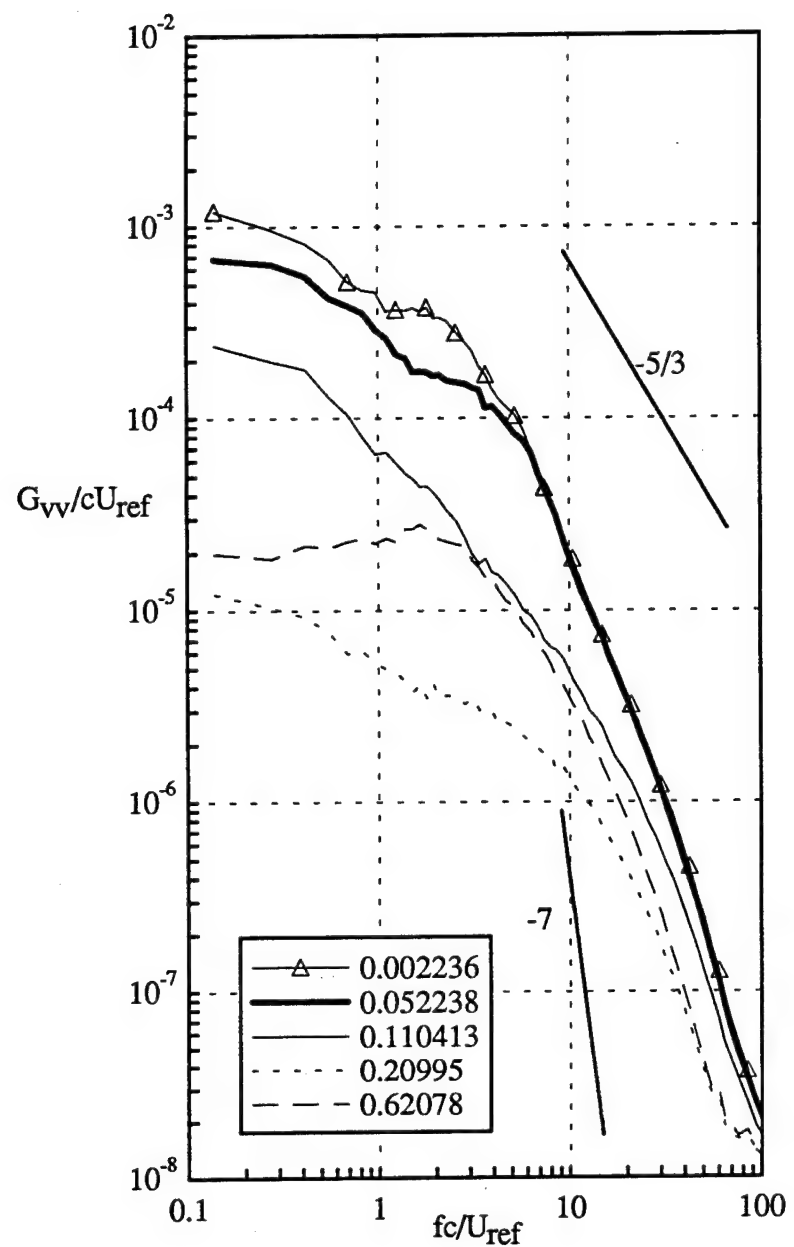


Figure 98. Autospectra of V velocity fluctuations at various spanwise locations along a horizontal profile through the lower core center indicated by dots Figure 89 at $x/c=15$ of co-rotating pair. Locations relative to the core center at $y/c=0.0847$.

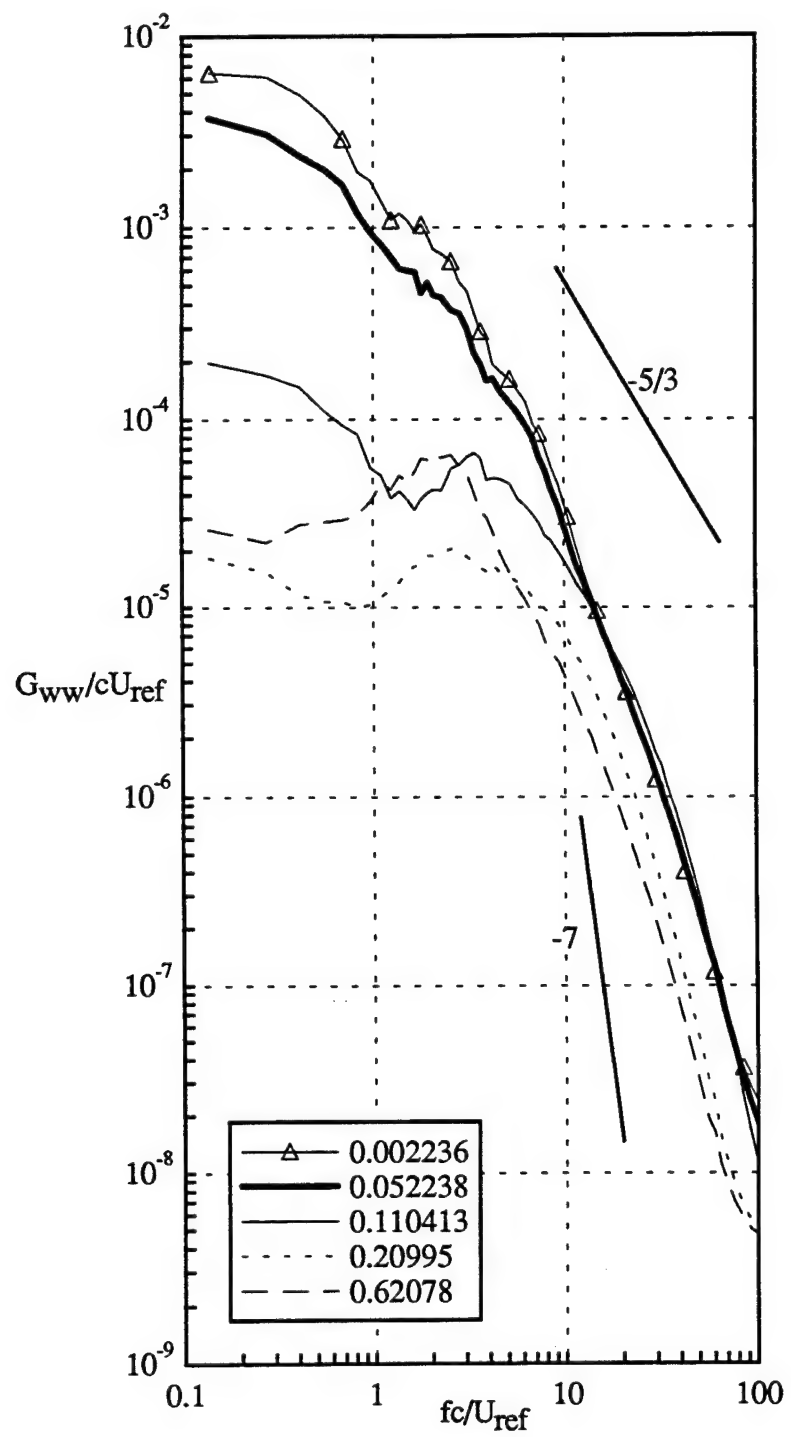


Figure 99. Autospectra of W velocity fluctuations at various spanwise locations along a horizontal profile through the lower core center indicated by dots in Figure 89 at $x/c=15$ of co-rotating pair. Locations relative to the core center at $y/c=0.0847$.

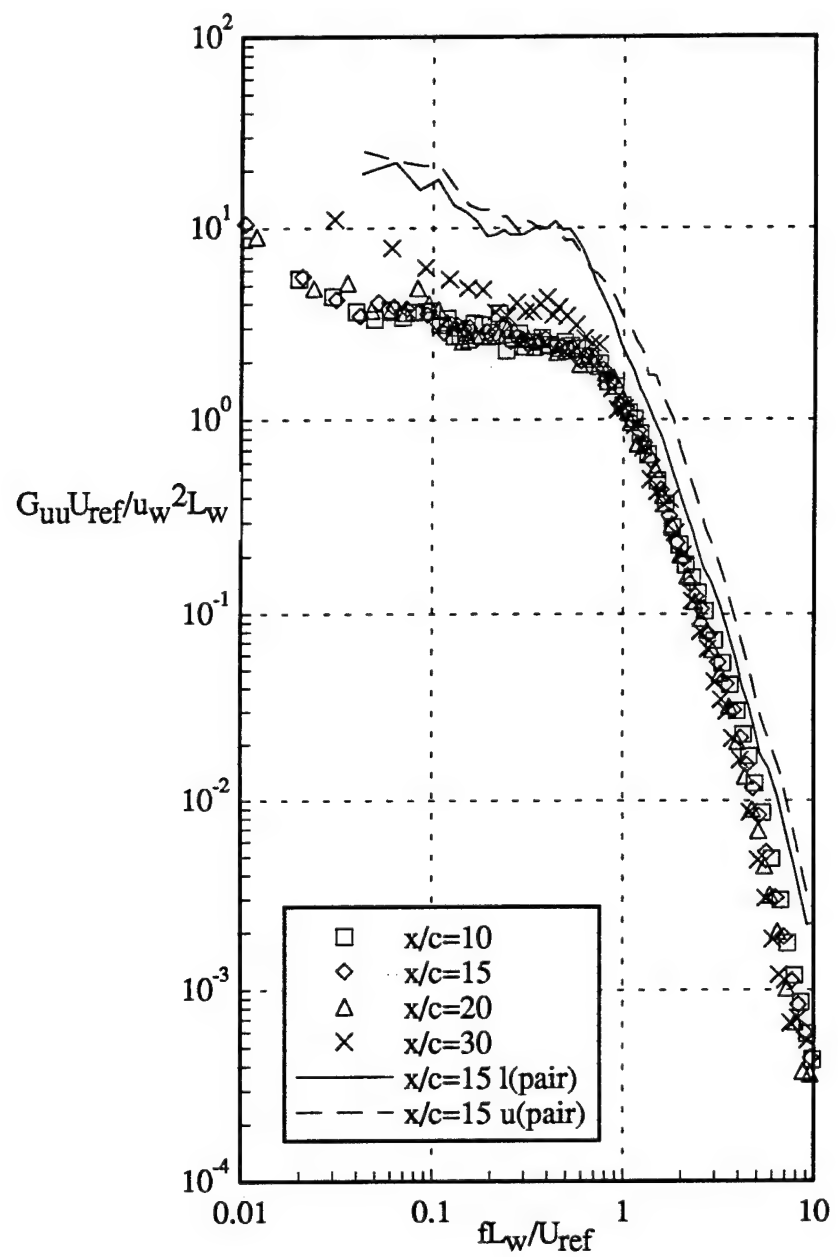


Figure 100 Autospectra of U velocity fluctuations at core center normalized on two-dimensional wake parameters for isolated vortex cases and co-rotating pair at $x/c=15$. Solid line is the lower core and dashed line is the upper core.

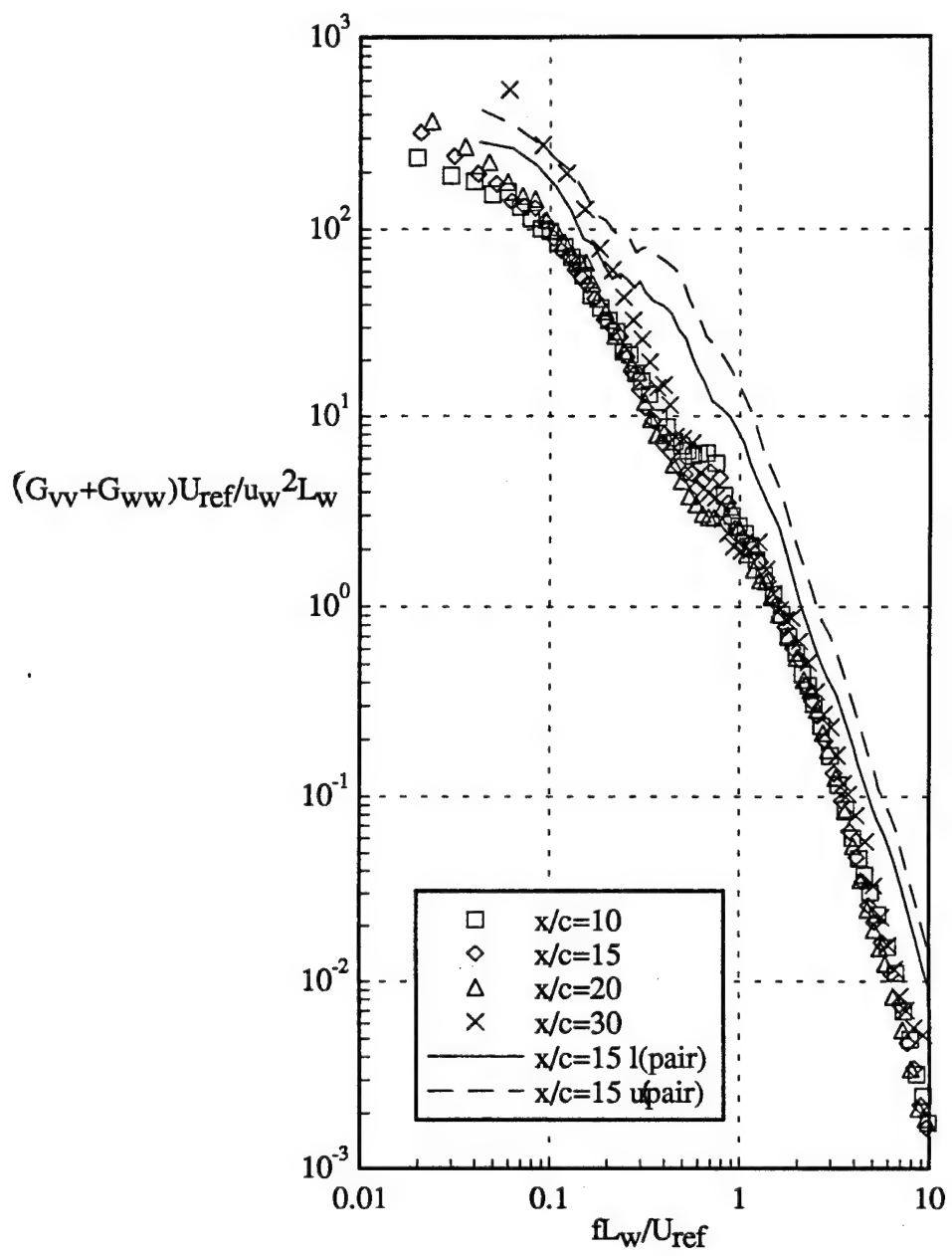


Figure 101 Autospectra of V+W velocity fluctuations of core center normalized on parameters of the two-dimensional wake for isolated vortex and co-rotating pair at $x/c=15$. Solid line is lower core and dashed line is upper core.

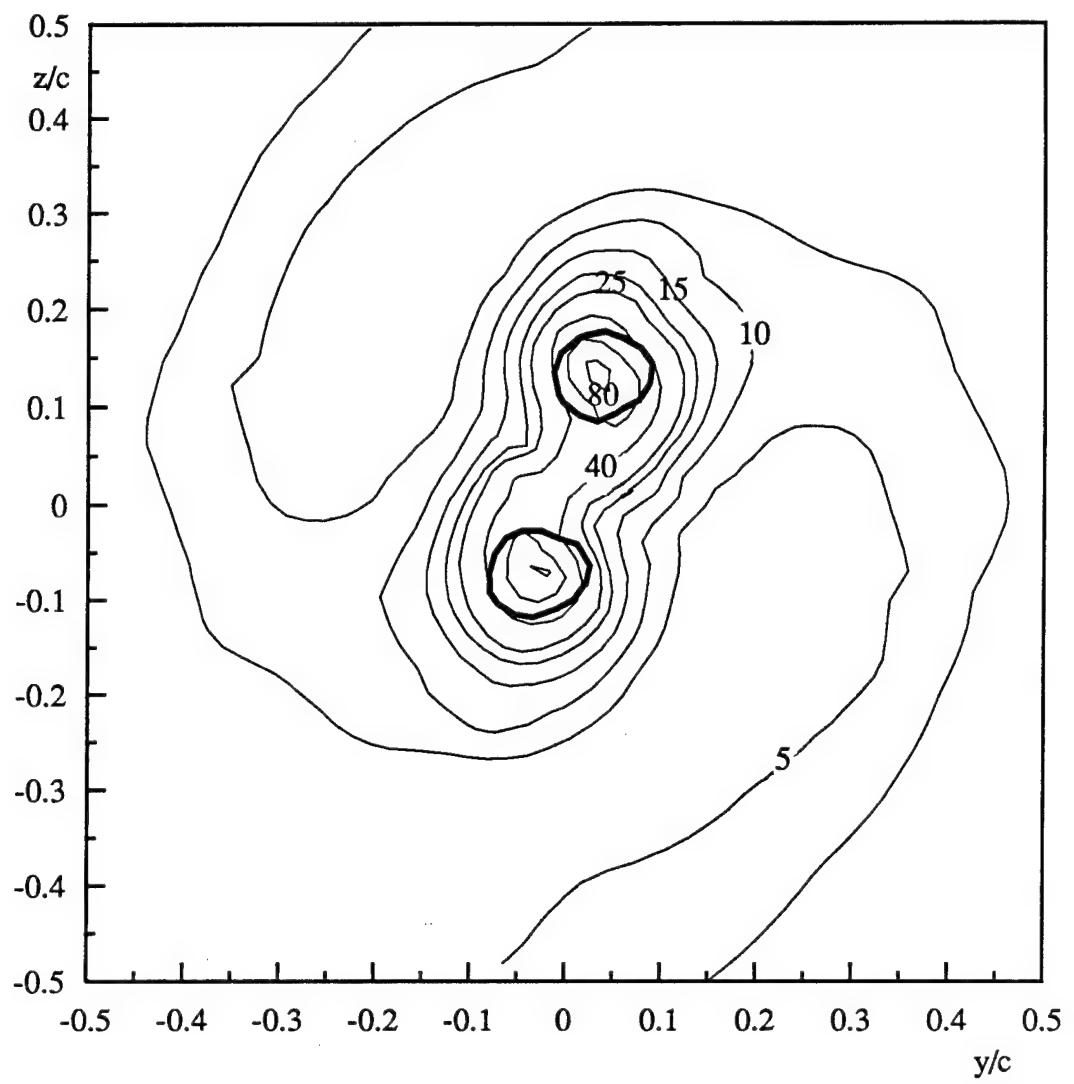


Figure 102 Contours of axial normal stress $\bar{u}^2/U_{ref}^2 \times 10^5$ filtered at $fc/U_{ref}=3$ at $x/c=15$ of co-rotating pair

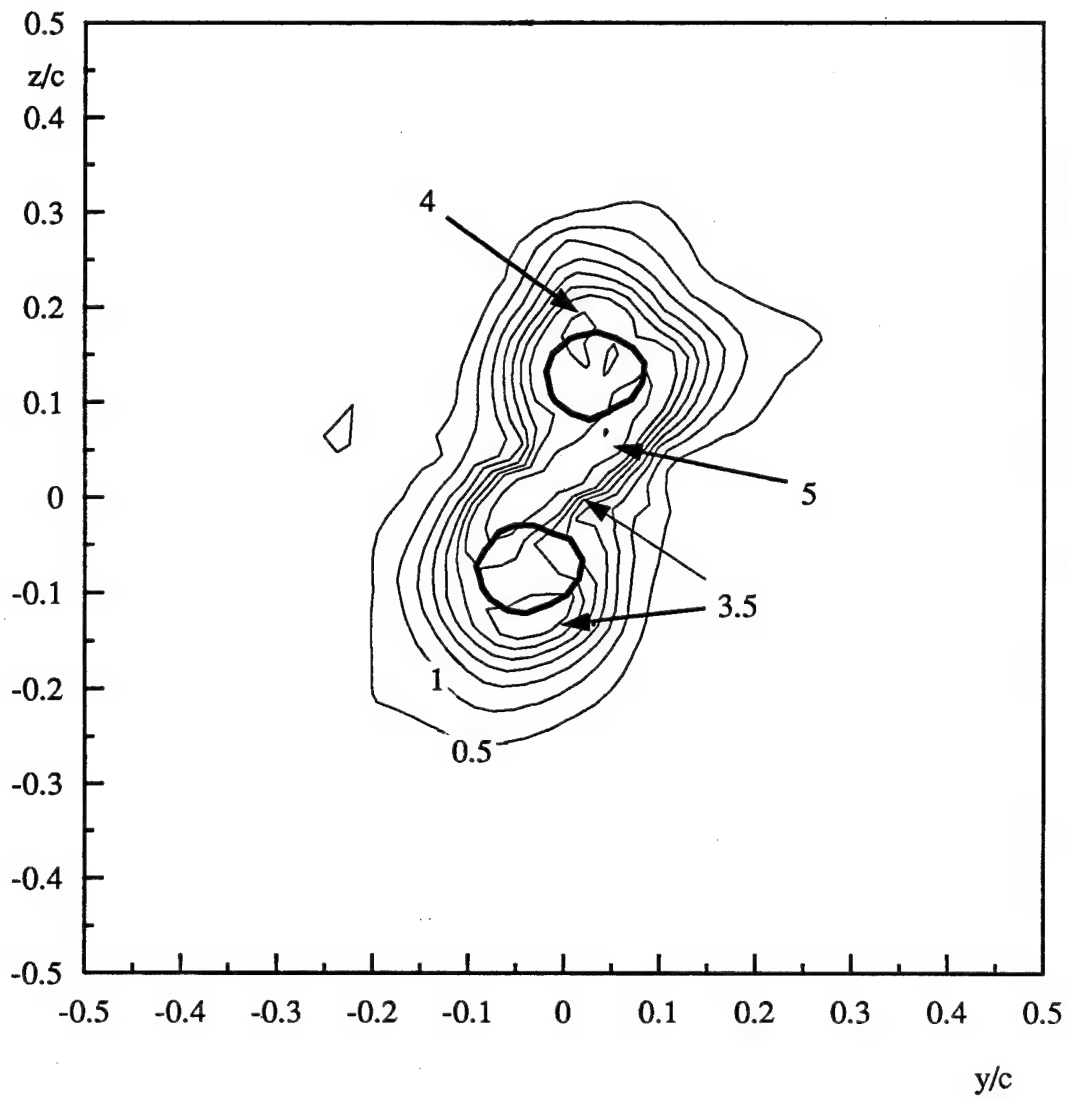


Figure 103 Contours of axial normal stress $\bar{u}^2/U_{ref}^2 \times 10^6$ filtered at $fc/U_{ref} = 40$ at $x/c = 15$ of co-rotating pair

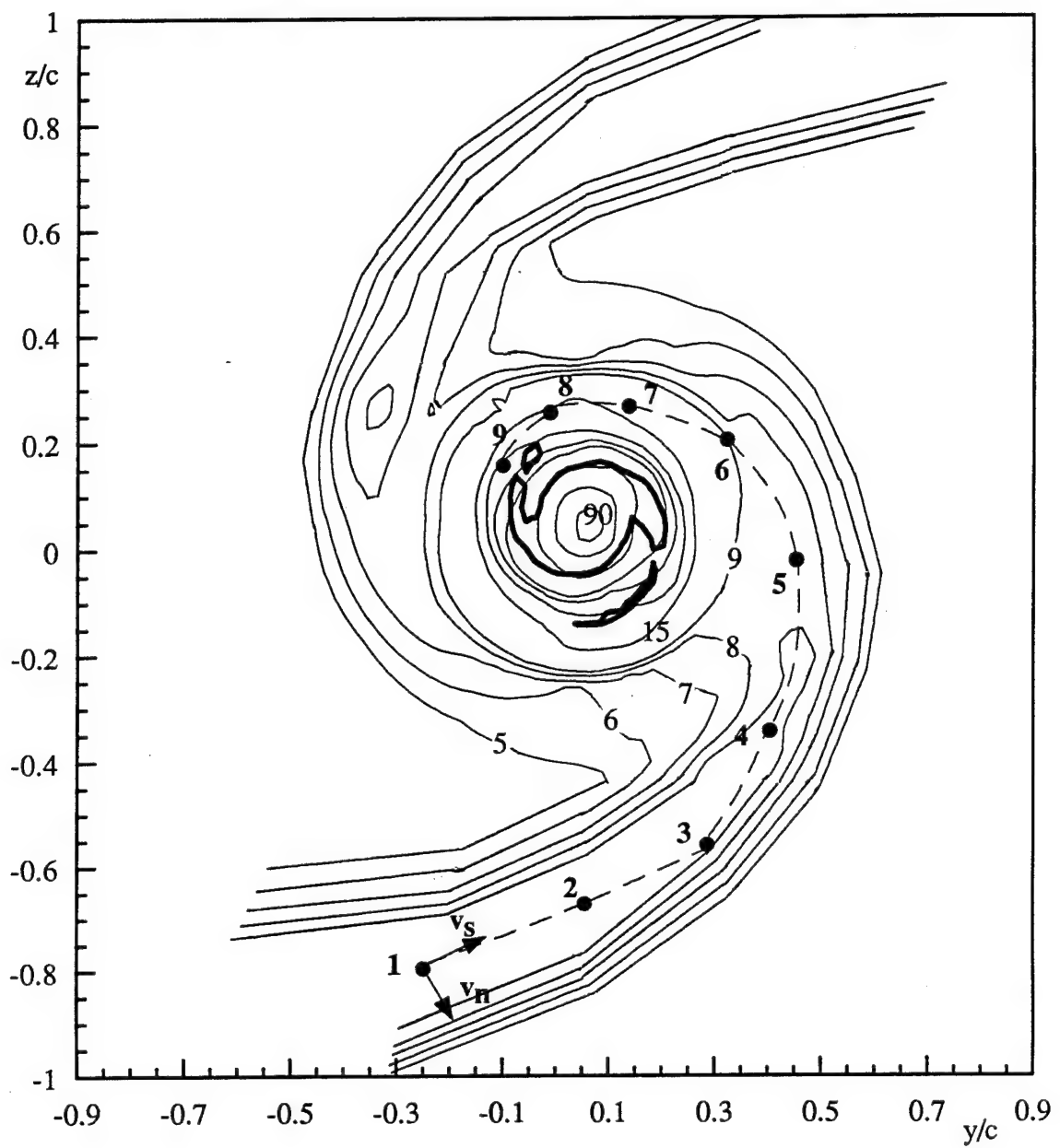


Figure 104. Contours of turbulence axial normal stress $\bar{u}'^2/U_{ref}^2 \times 10^5$ at $x/c=22$ of co-rotating pair. Dashed line denotes spiral wake centerline in spiral wake tail. Dots indicate locations of profiles and autospectra in Figures 110-113.

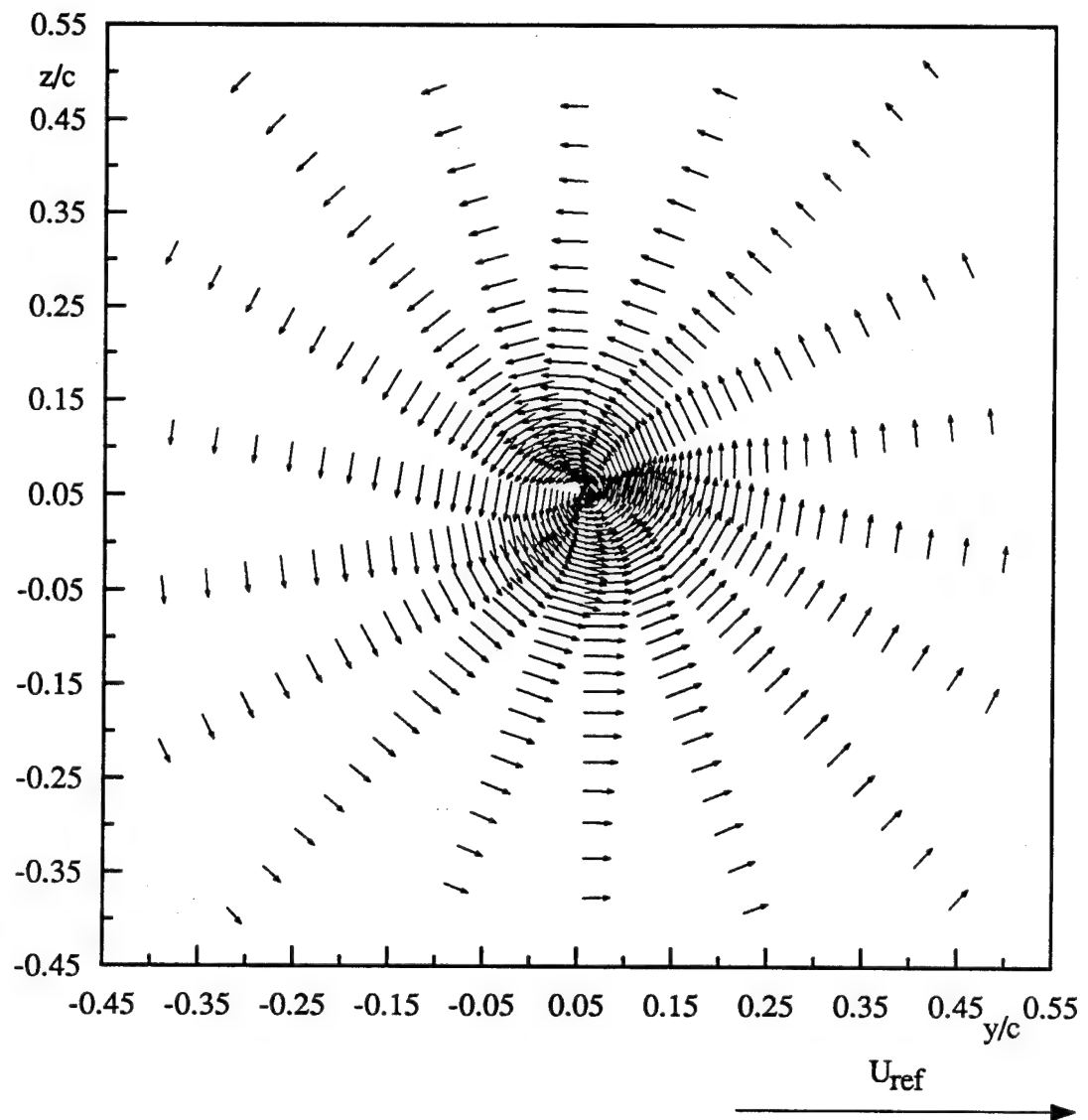


Figure 105. Mean cross-flow velocity vectors at $x/c=22$ of co-rotating pair

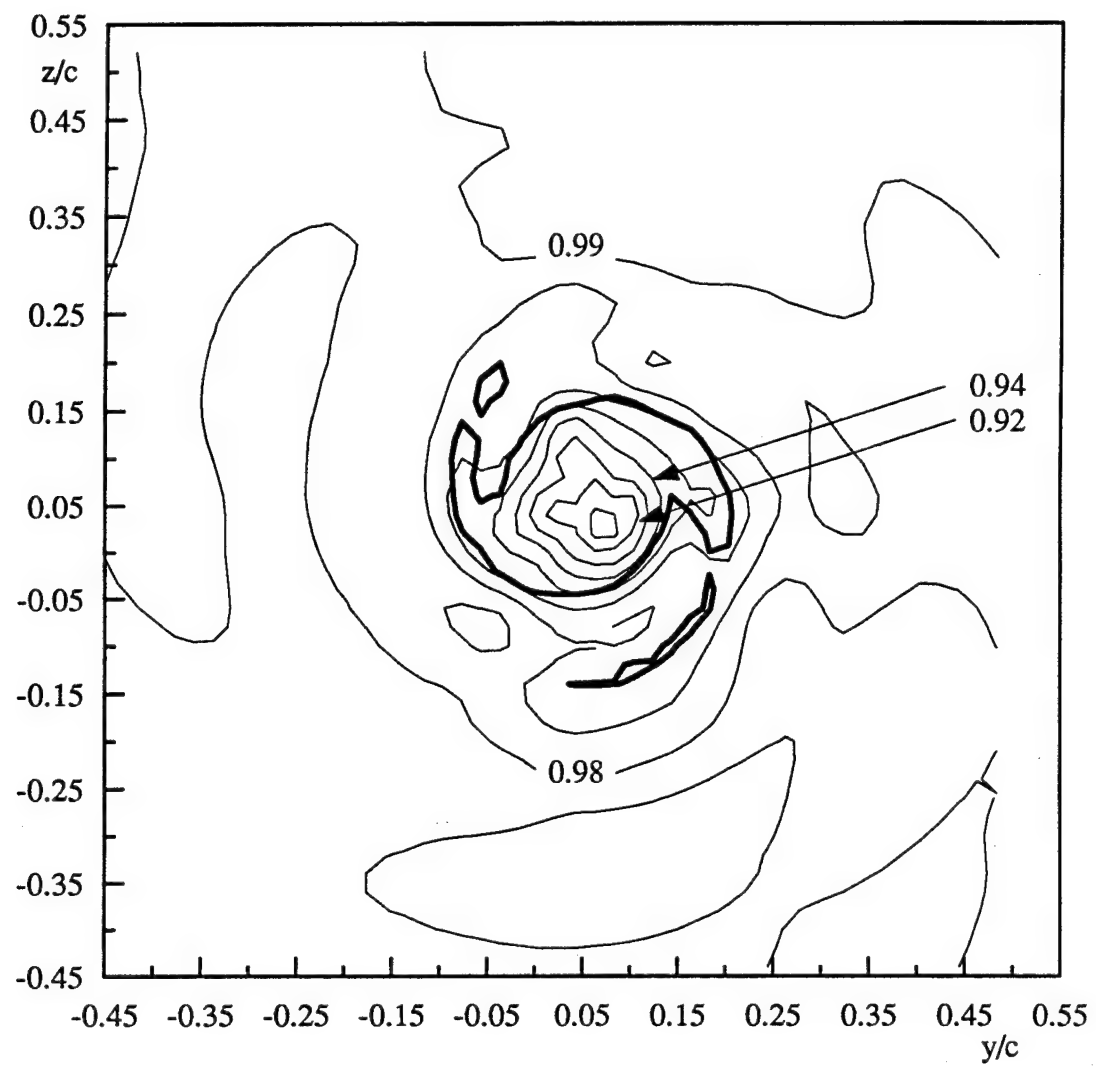


Figure 106. Contours of mean axial velocity U/U_{ref} at $x/c=22$ of co-rotating pair

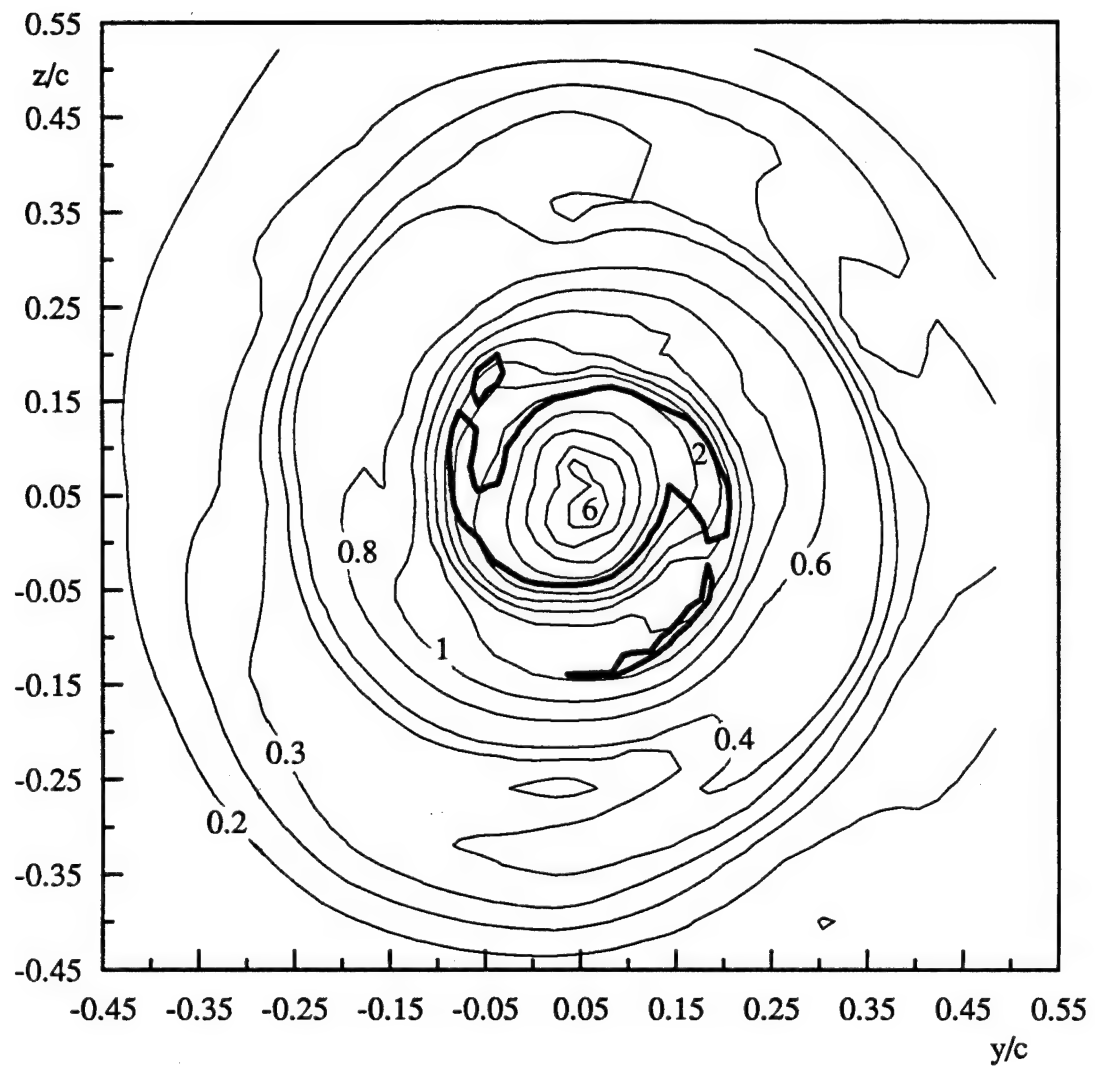


Figure 107. Contours of mean streamwise vorticity normalized on U_{ref} and c at $x/c=22$ of co-rotating pair

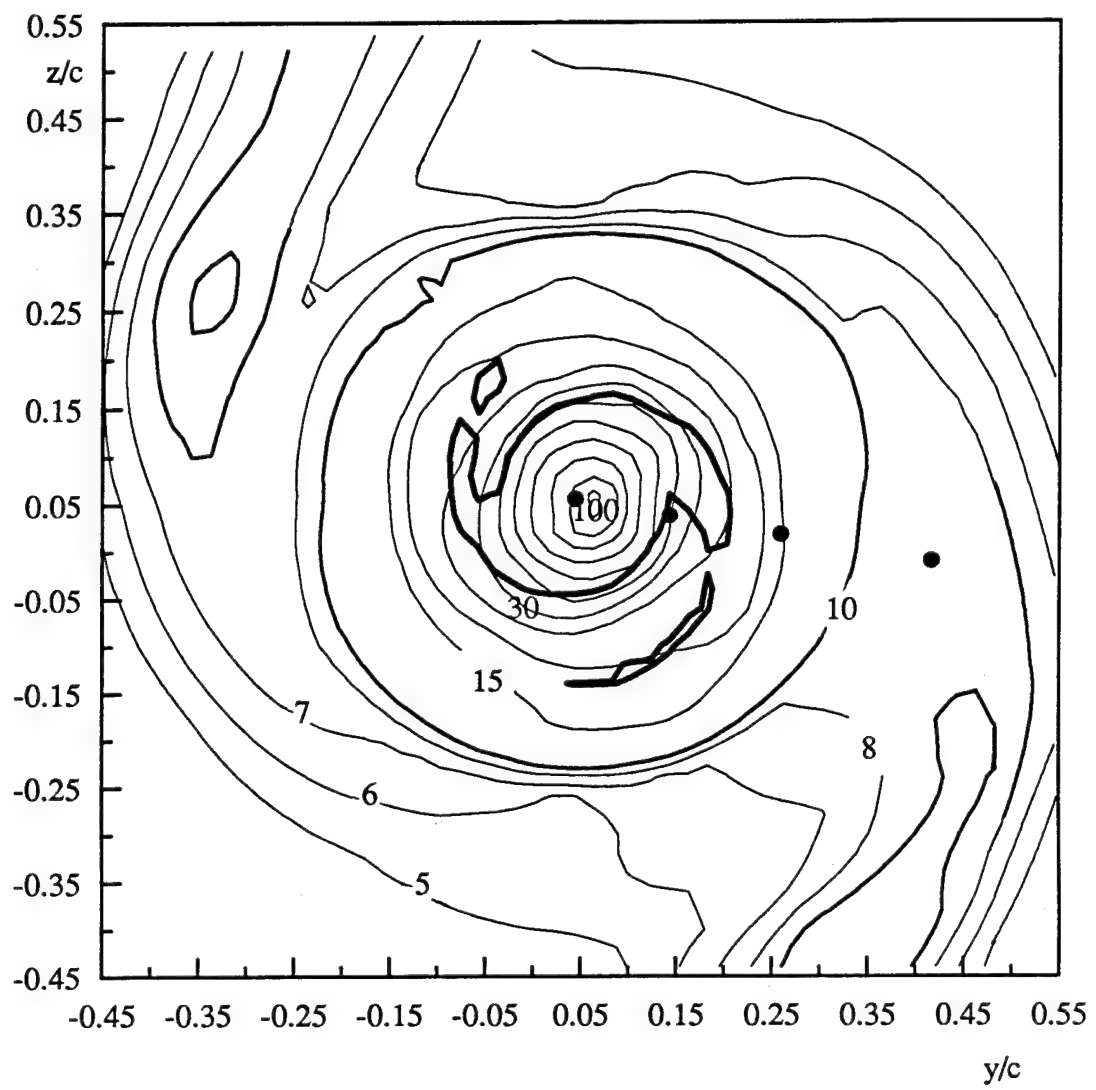


Figure 108. Contours of axial normal stress u^2/U_{ref}^2 at $x/c=22$ of co-rotating pair. Dots show locations of autospectra in Figures 115-117.

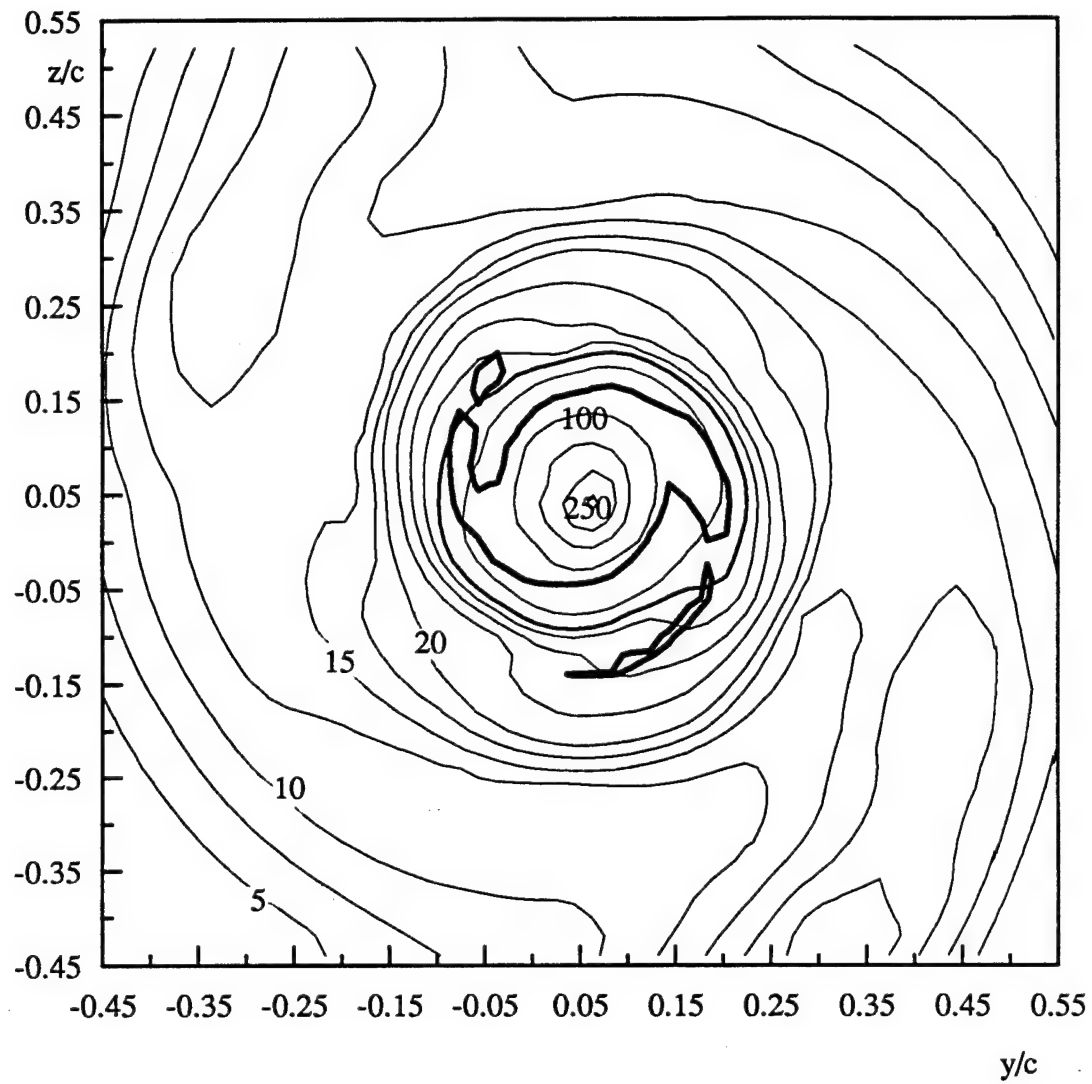


Figure 109. Contours of turbulence cross-flow normal stress sum $(v^2 + w^2)/U_{ref}^2 \times 10^5$ at $x/c = 22$ of co-rotating pair.

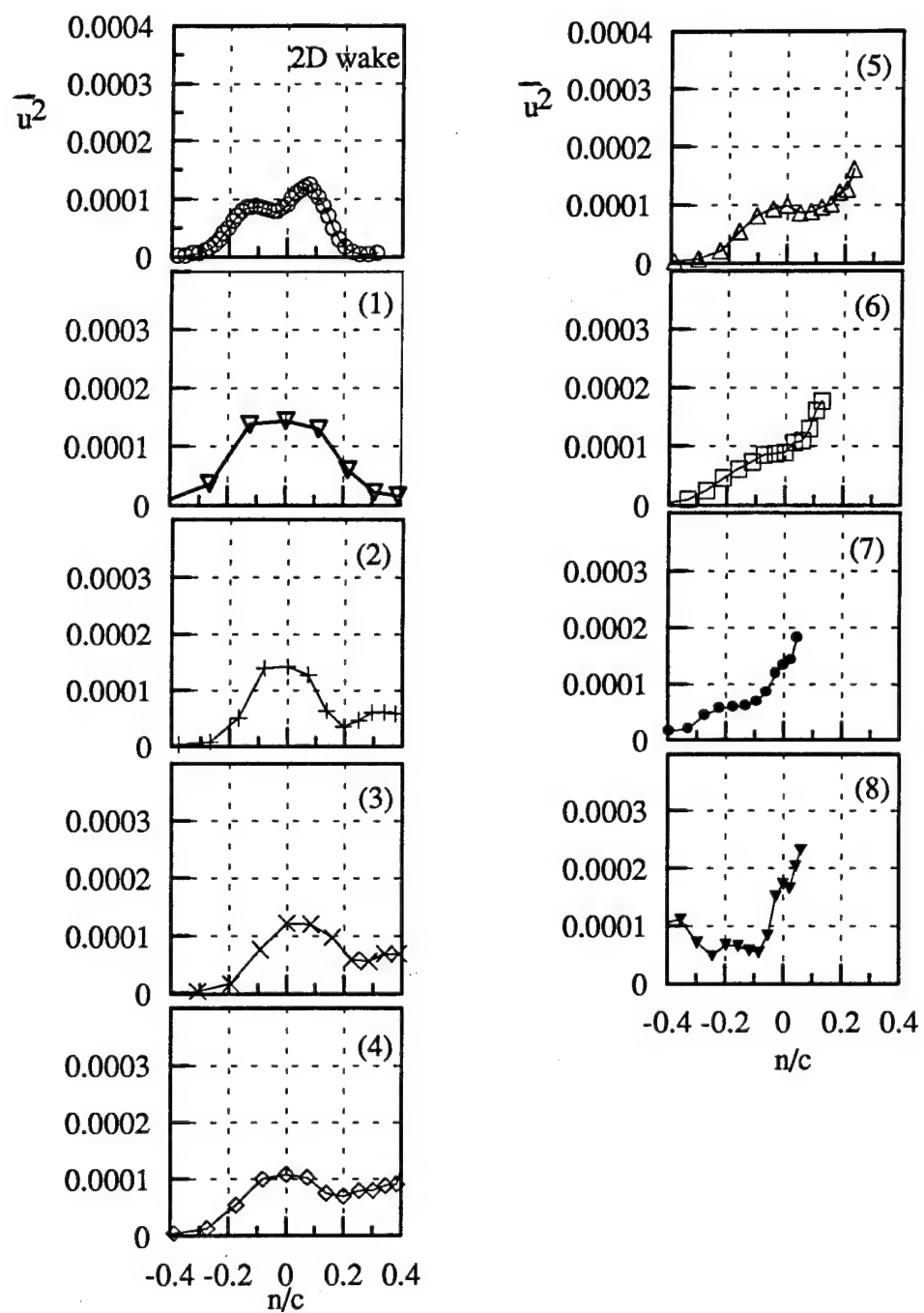


Figure 110. Profiles of axial normal stress $\bar{u}^2/U_{\text{ref}}^2$ at selected locations along the dashed line in Figure 104 at $x/c=22$ of co-rotating pair. Numbers indicate locations along this line.

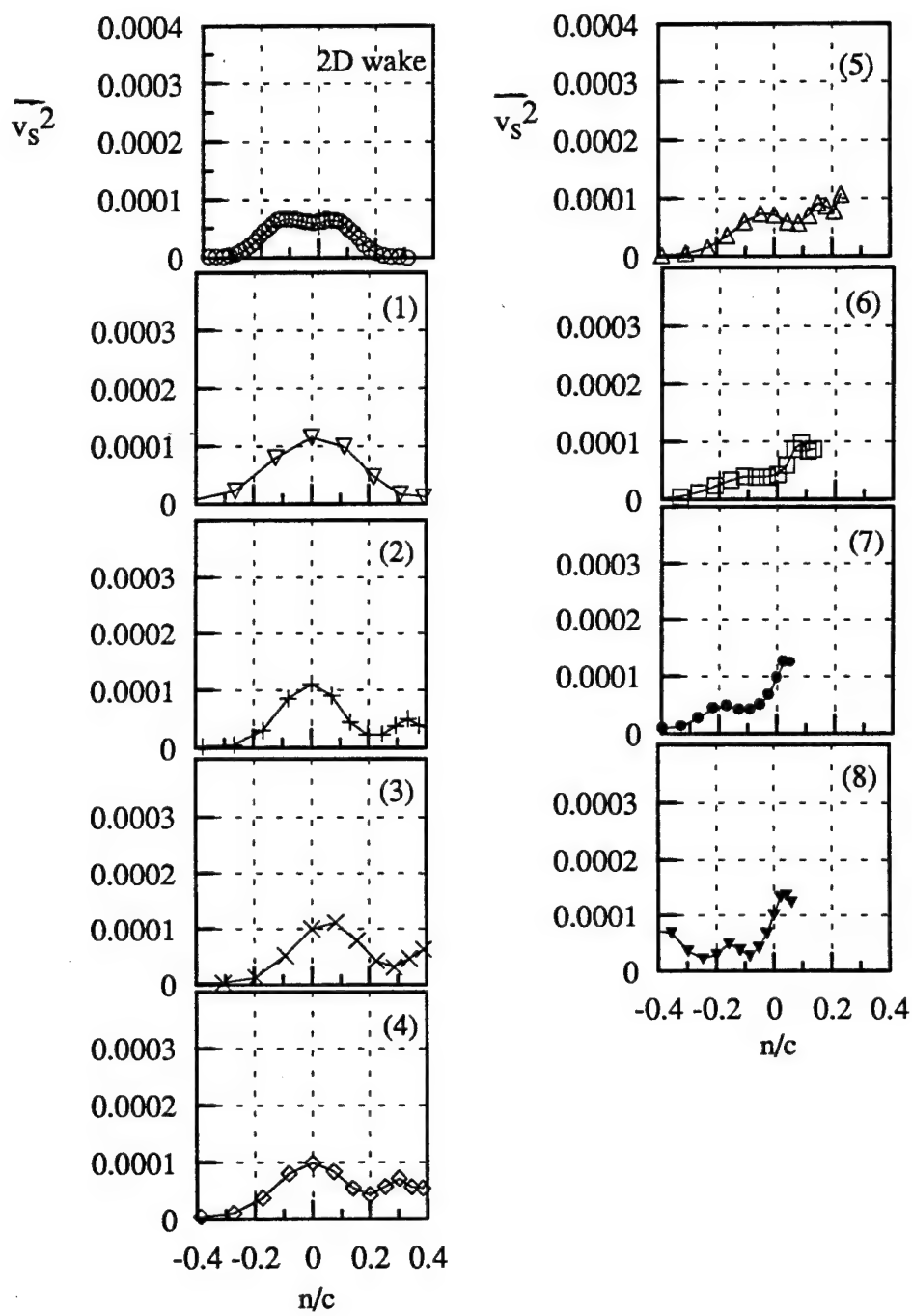


Figure 111. Profiles of normal stress \bar{v}_s^2/U_{ref}^2 parallel to spiral wake centerline in the spiral wake tail at selected locations along the dashed line in Figure 104 at $x/c=22$ of co-rotating pair. Numbers indicate locations along this line.

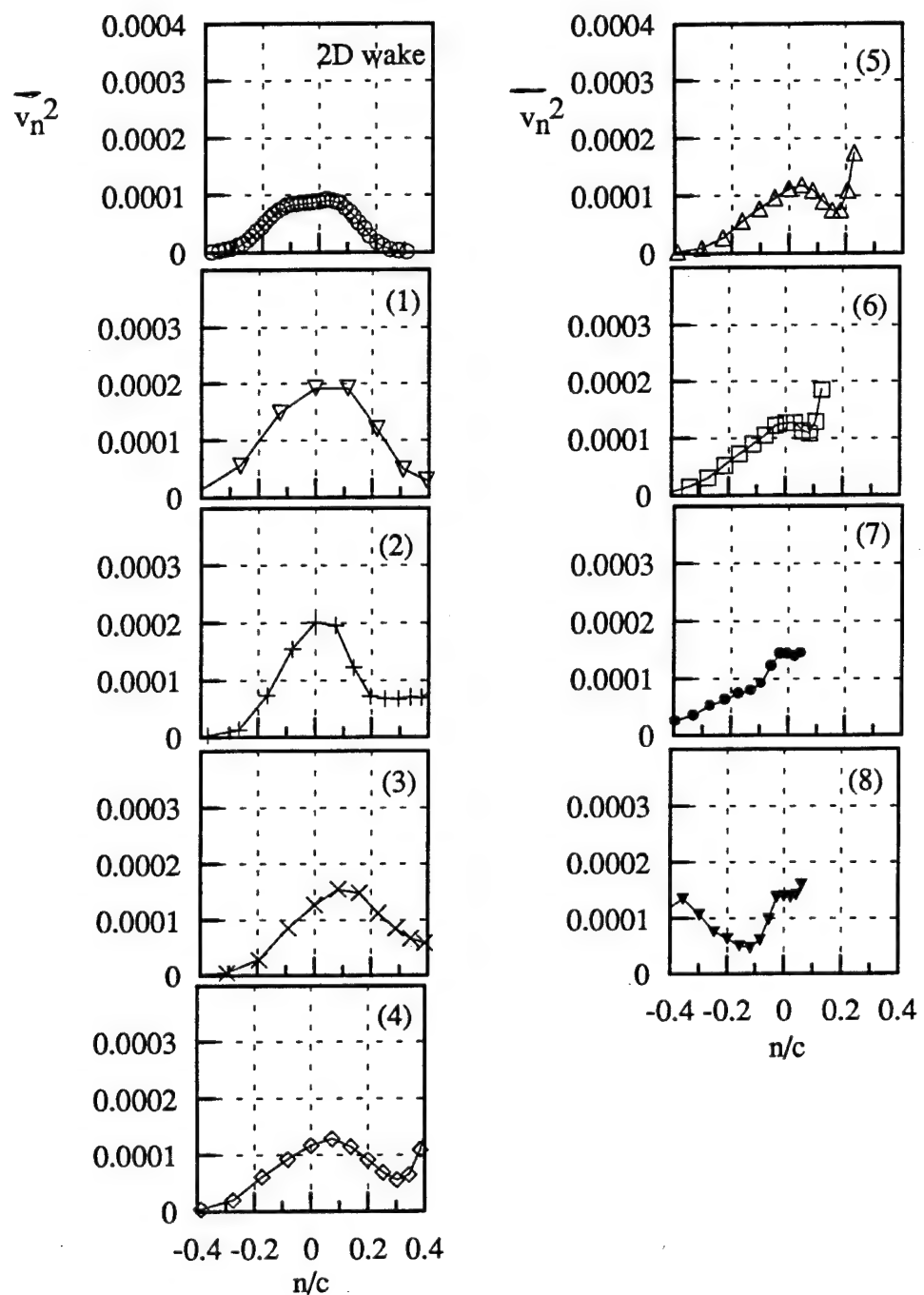


Figure 112. Profiles of normal stress \bar{v}_n^2/U_{ref}^2 normal to spiral wake centerline in the spiral wake tail at selected locations along the dashed line at $x/c=22$ of co-rotating pair. Numbers indicate locations along this line.

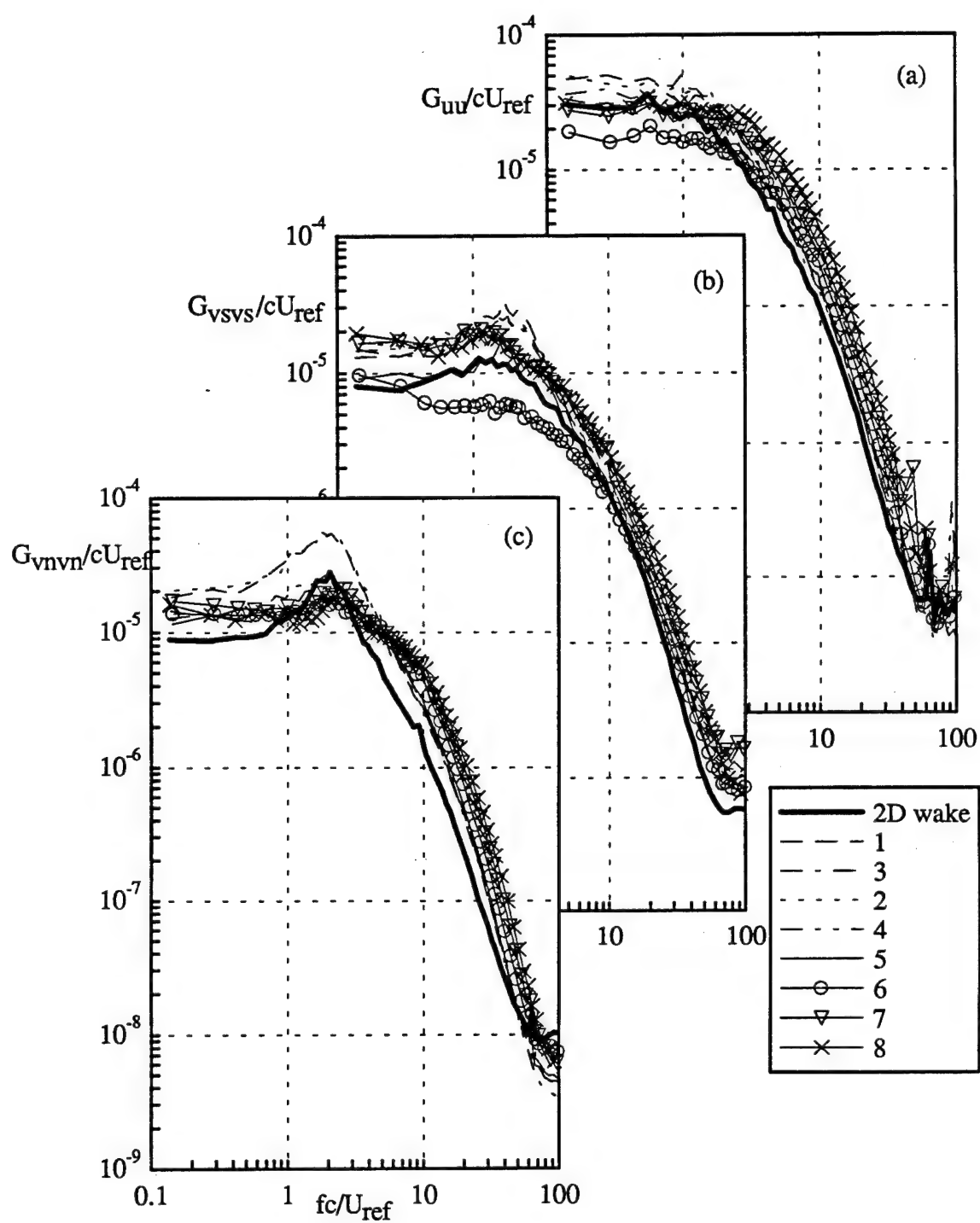


Figure 113 Velocity autospectra in coordinates aligned with the spiral wake centerline in the spiral wake tail at $x/c=22$ of co-rotating pair (a) U spectra, (b) V_s spectra, (c) V_n spectra. Locations indicated by dots in Figure 104.

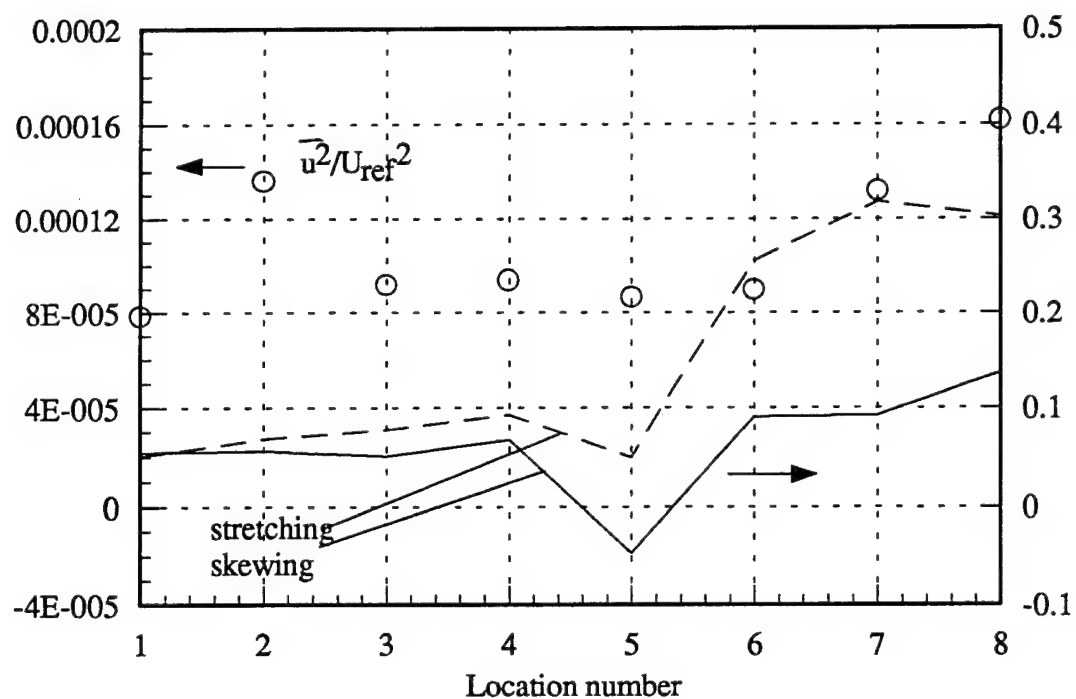


Figure 114. Rates of strain and turbulence stress on the dashed curve in Figure 104 at $x/c=22$ of co-rotating pair. Strain rates normalized on maximum axial velocity gradient in the two-dimensional portion of the wake.

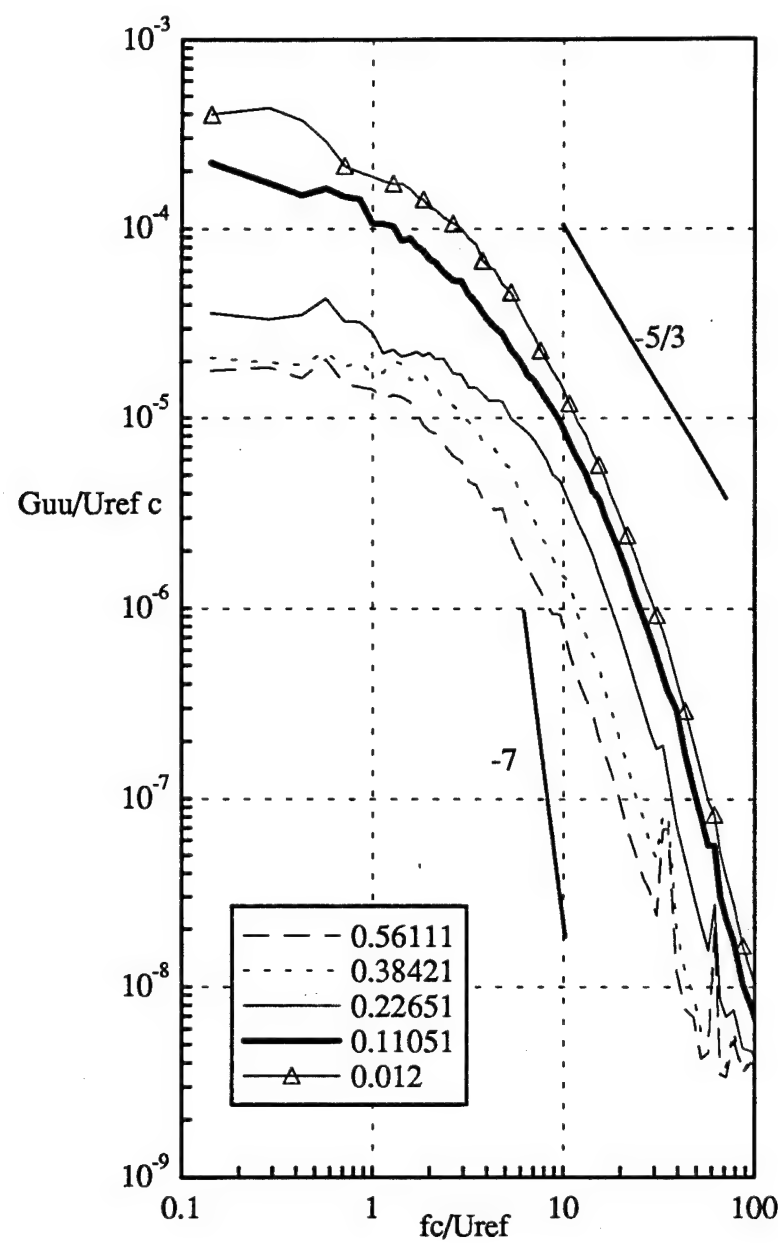


Figure 115. Autospectra of U velocity fluctuations at various spanwise locations along a horizontal profile through the center indicated by dots in Figure 108 at $x/c=22$ of co-rotating pair. Locations relative to the core center at $y/c=0.033$.

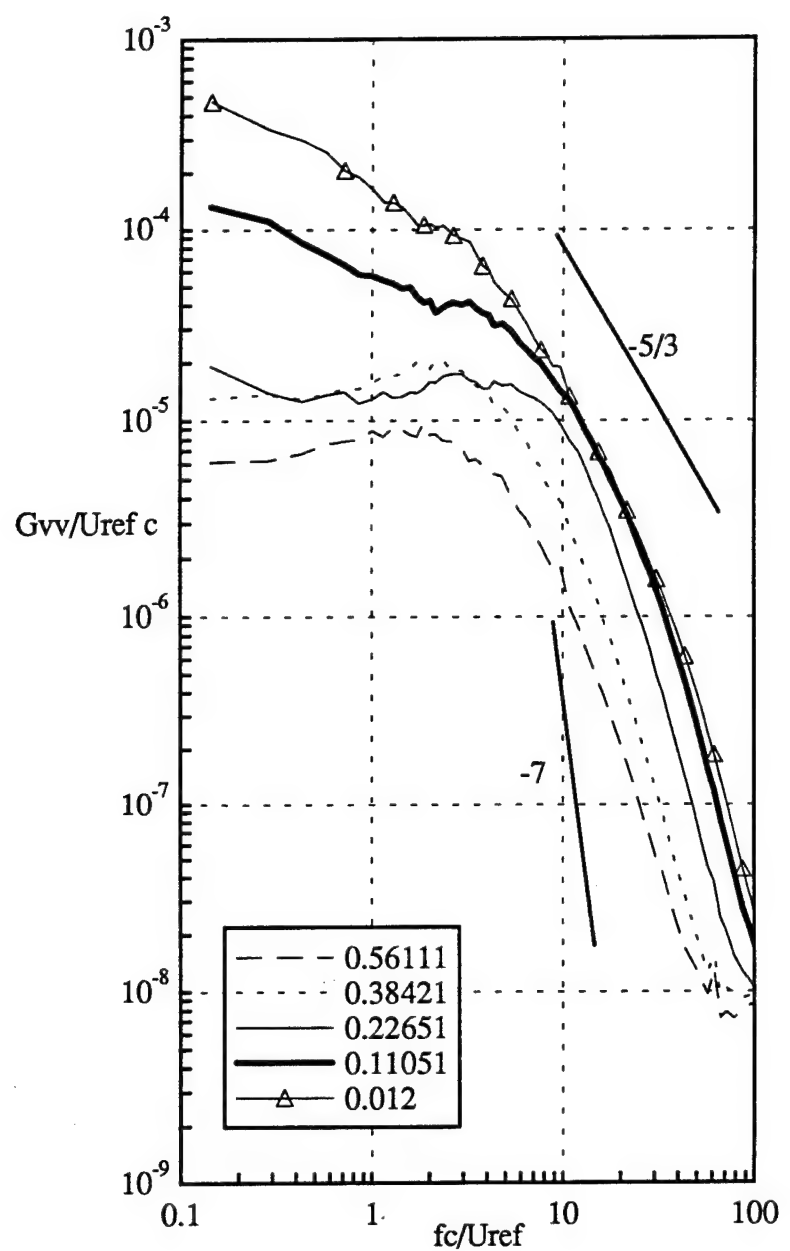


Figure 116. Autospectra of V velocity fluctuations at various spanwise locations along a horizontal profile through the core center indicated by dots in Figure 108 at $x/c=22$ of co-rotating pair. Locations relative to the core center at $y/c=0.033$.

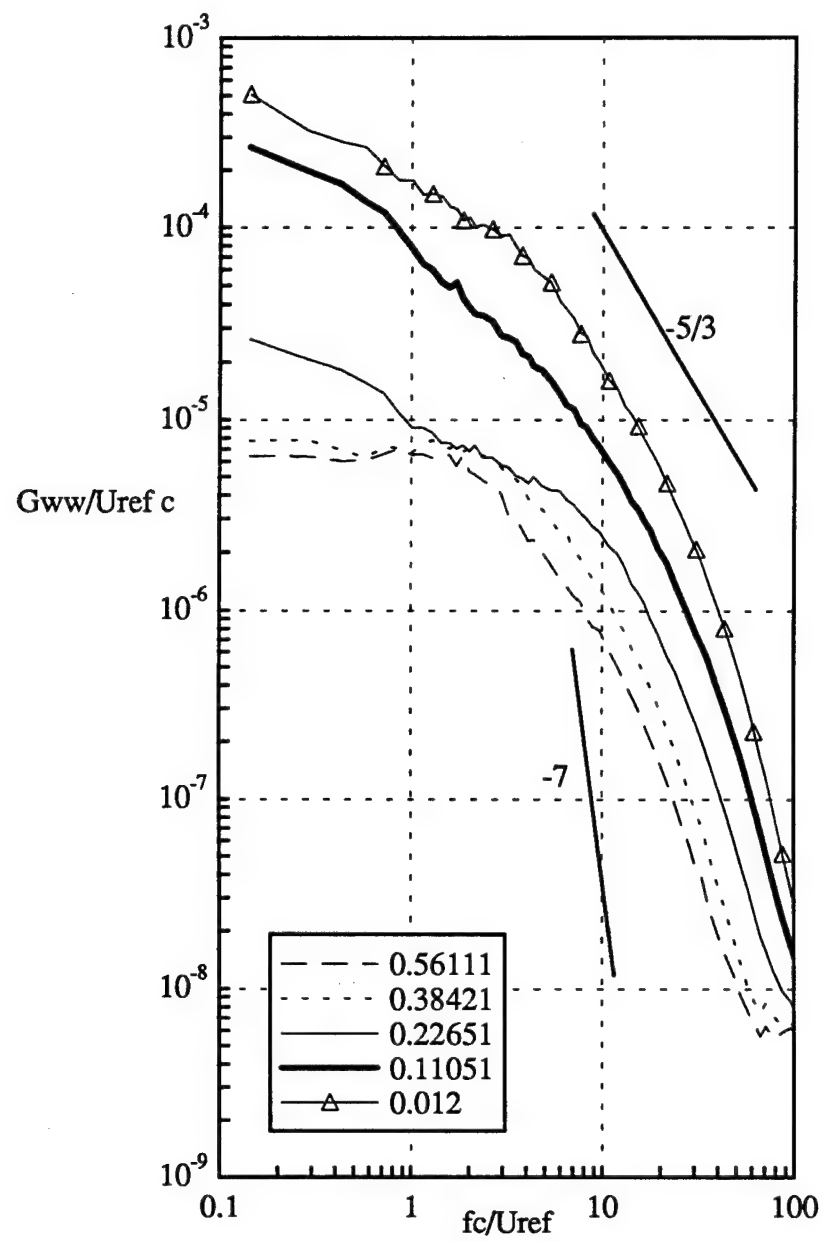


Figure 117. Autospectra of W velocity fluctuations at various spanwise locations along a horizontal profile through the core center indicated by dots in Figure 108 at $x/c=22$ of co-rotating pair. Locations relative to the core center at $y/c=0.033$.

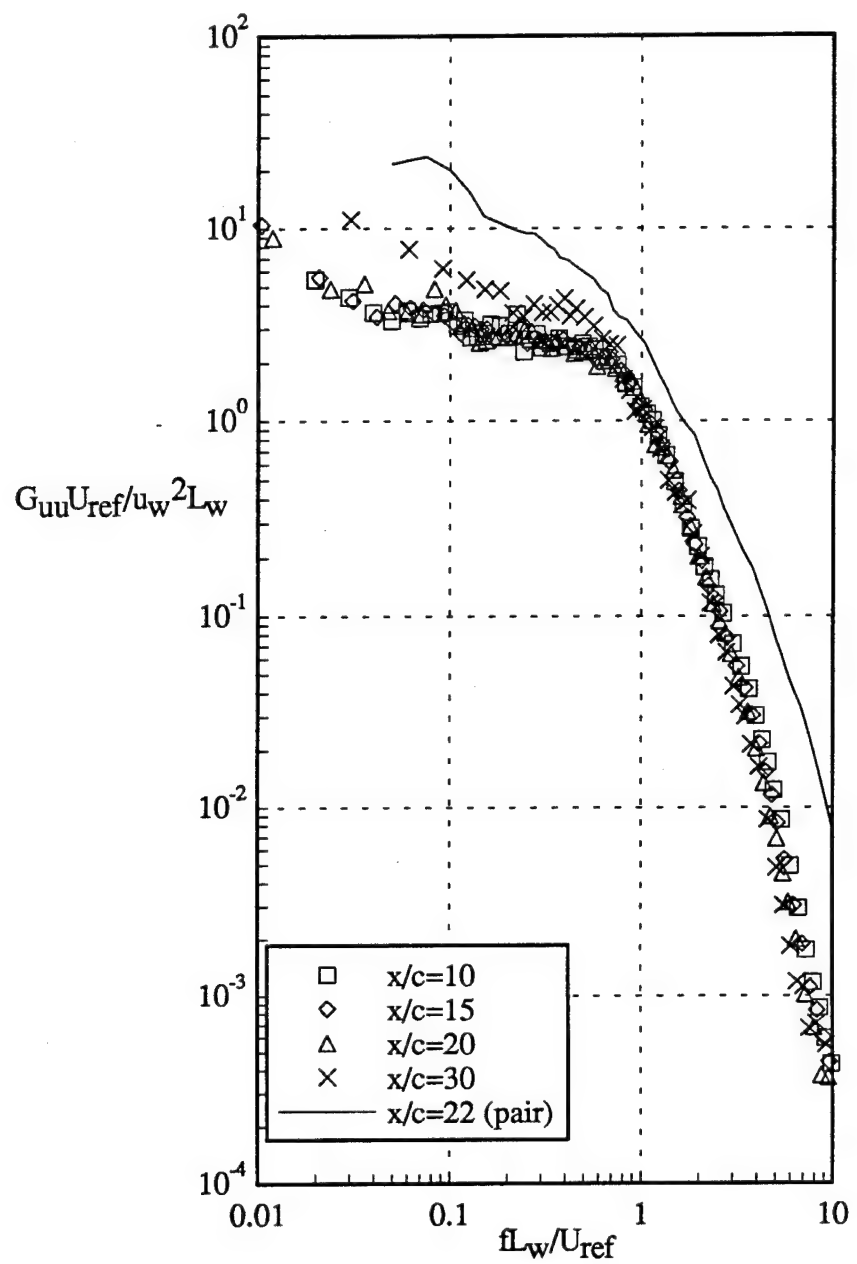


Figure 118. Autospectra of U velocity fluctuations at core center normalized on two-dimensional wake parameters for isolated vortex cases and co-rotating pair at $x/c=22$.

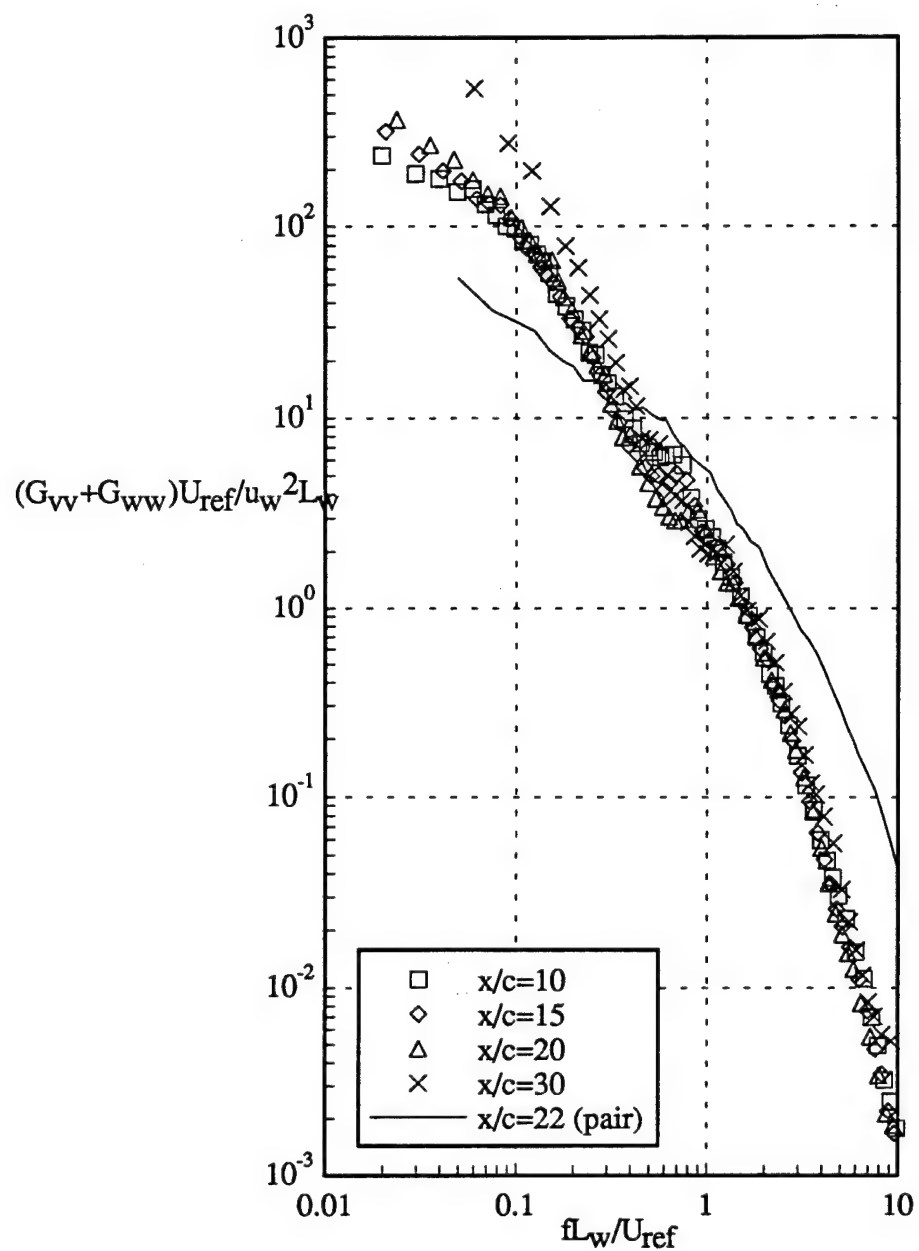


Figure 119. Autospectra of V+W velocity fluctuations at core center normalized on two-dimensional wake parameters for isolated vortex cases and co-rotating pair at $x/c=22$.

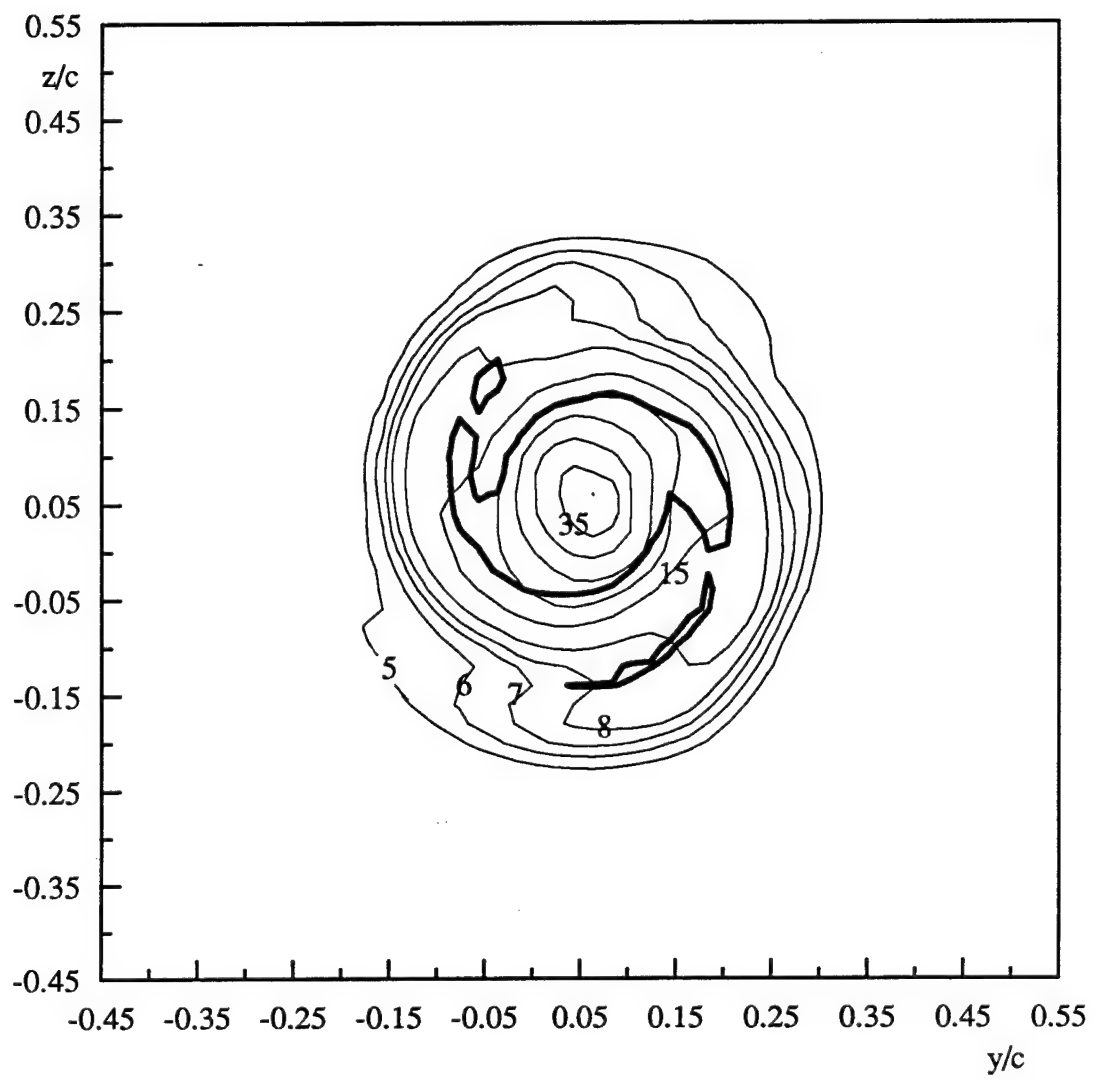


Figure 120. Contours of axial normal stress $\bar{u}^2/U_{\text{ref}}^2 \times 10^5$ filtered at $fc/U_{\text{ref}}=3$ at $x/c=22$ of co-rotating pair

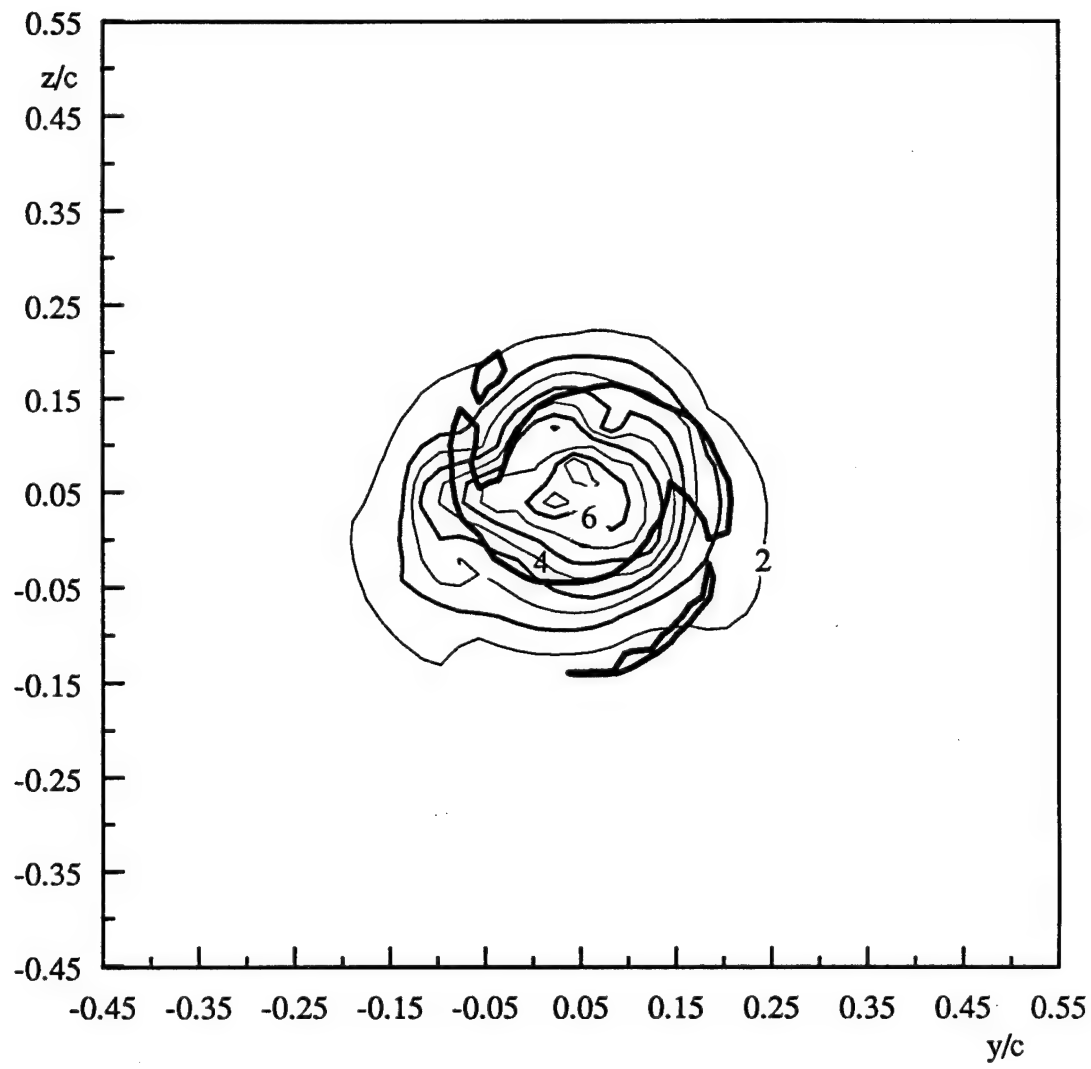


Figure 121. Contours of axial normal stress $\bar{u}^2/U_{\text{ref}}^2 \times 10^6$ filtered at $fc/U_{\text{ref}}=40$ at $x/c=22$ of co-rotating pair

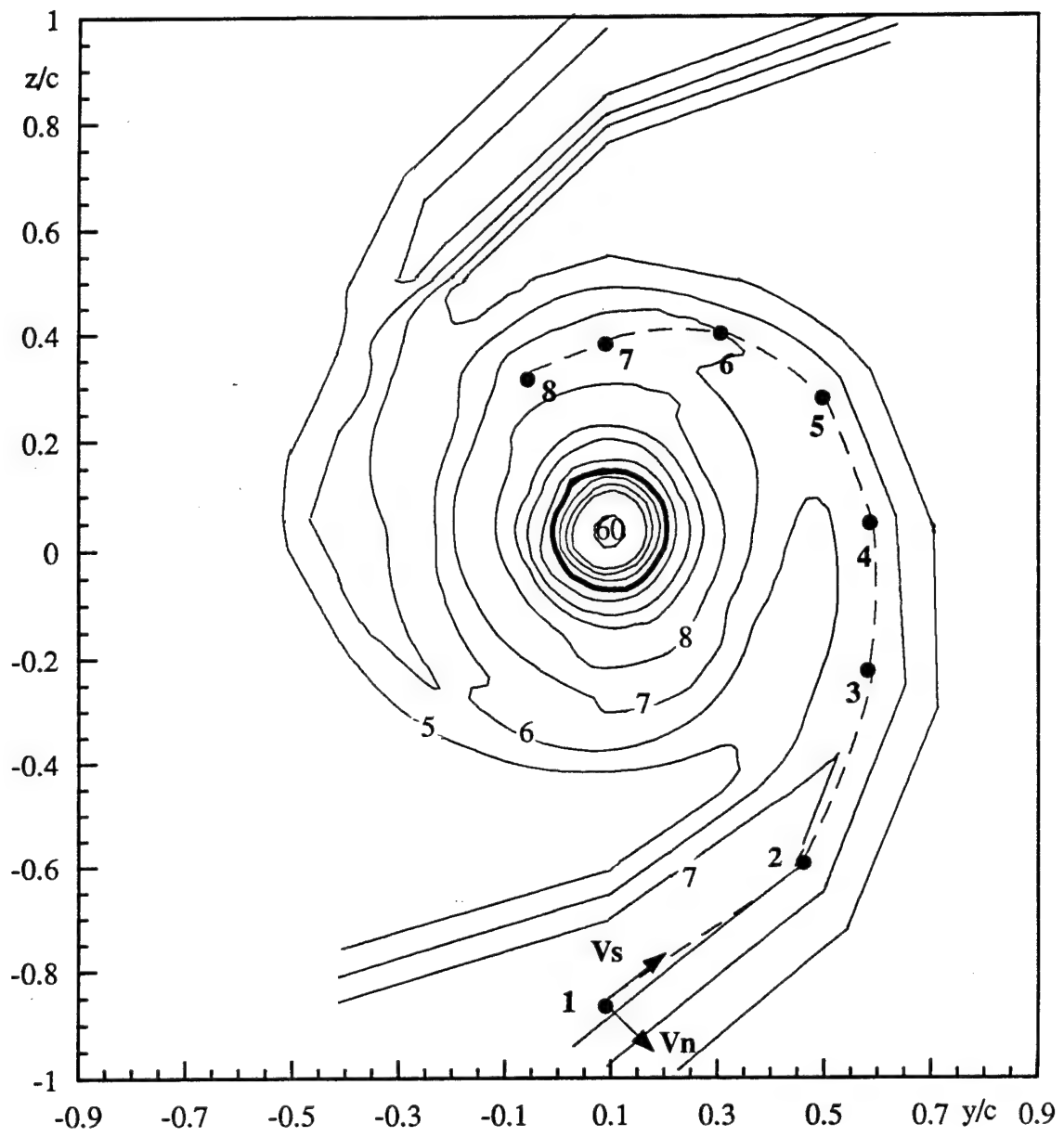


Figure 122. Contours of turbulence axial normal stress $\bar{u}^2/U_{ref}^2 \times 10^5$ at $x/c=30$ of co-rotating pair. Dashed line denotes spiral wake centerline in spiral wake tail. Dots indicate locations of profiles and autospectra in Figures 128-131.

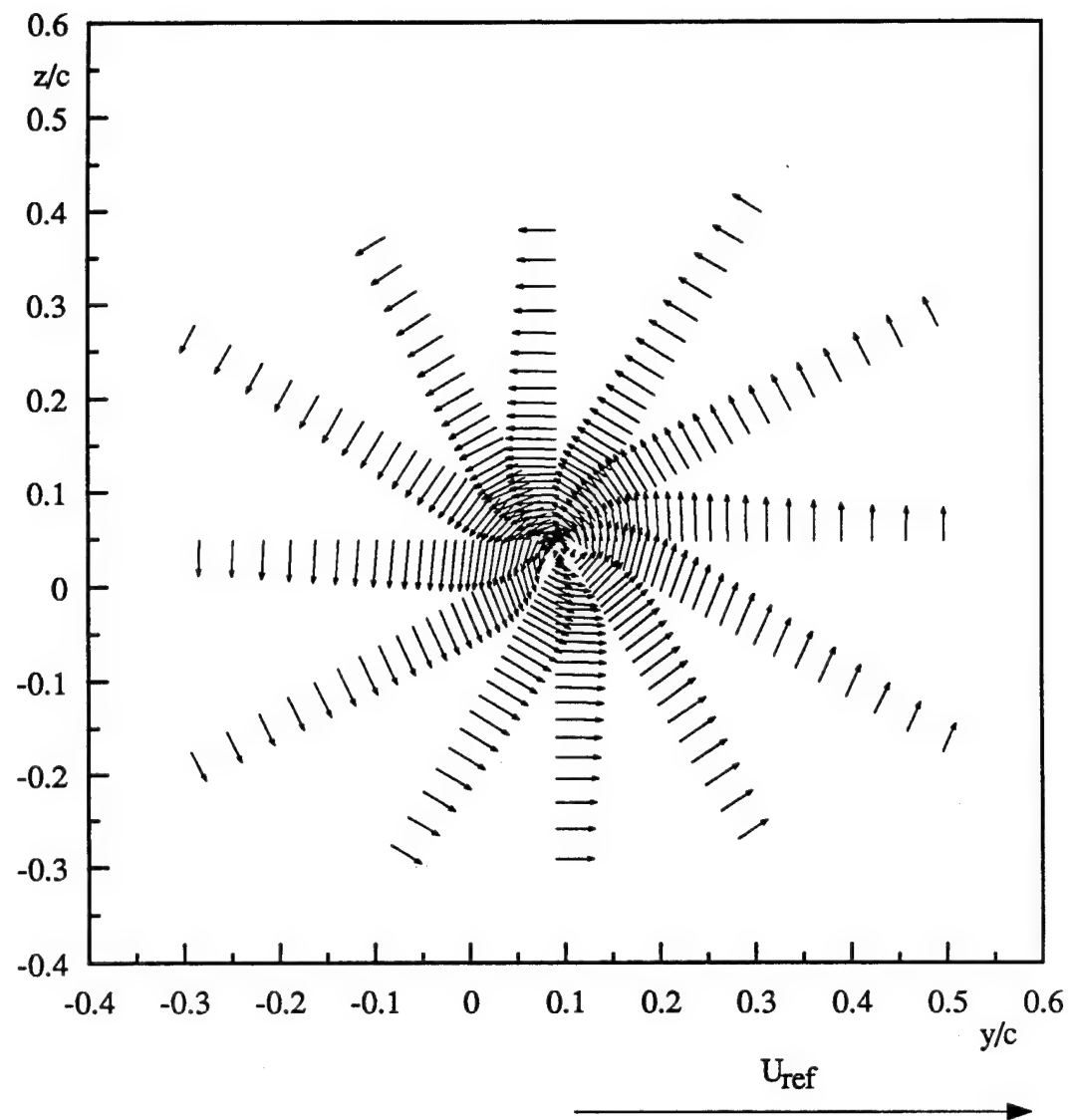


Figure 123. Mean cross-flow velocity vectors at $x/c=30$ of co-rotating pair

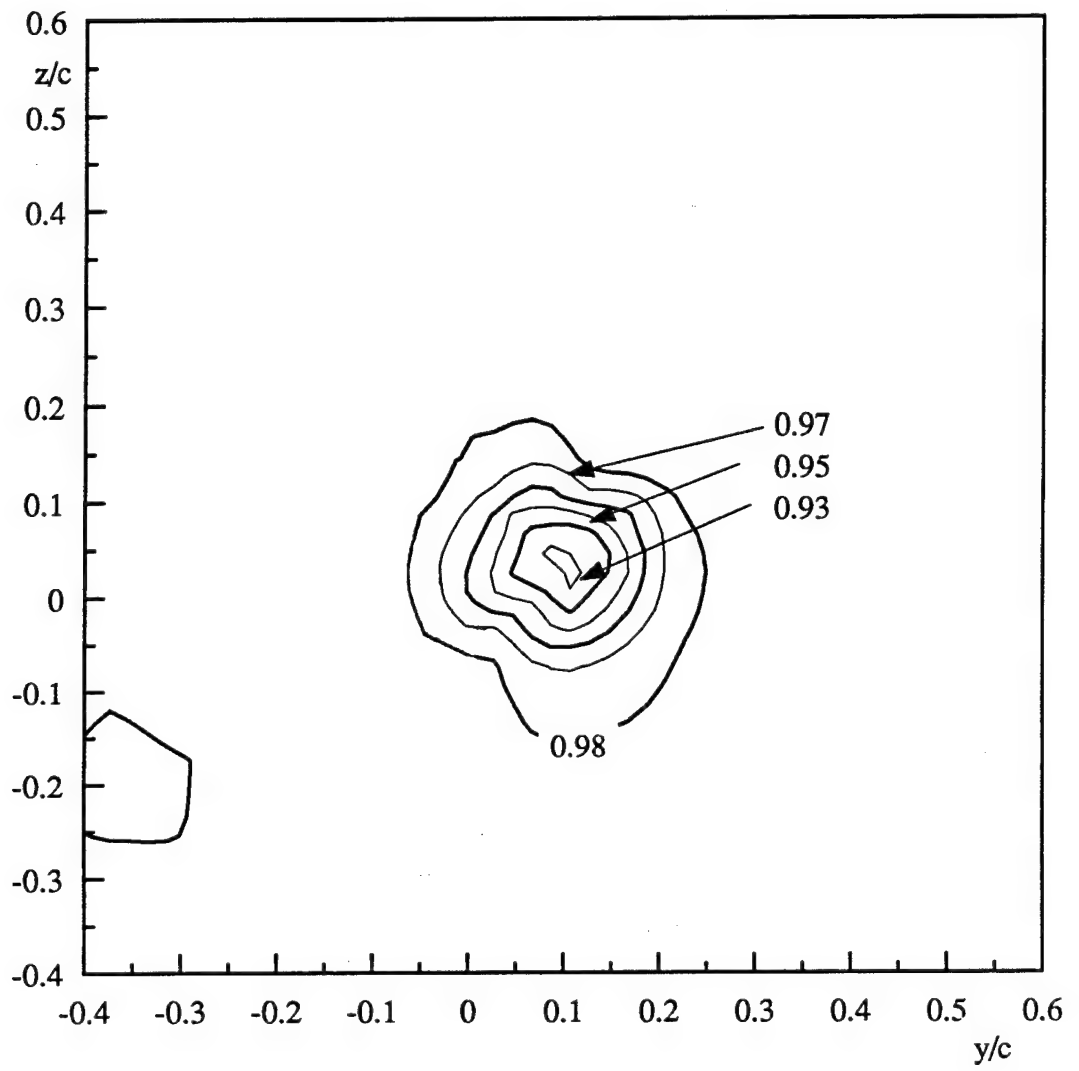


Figure 124. Contours of mean axial velocity U/U_{ref} at $x/c=30$ of co-rotating pair

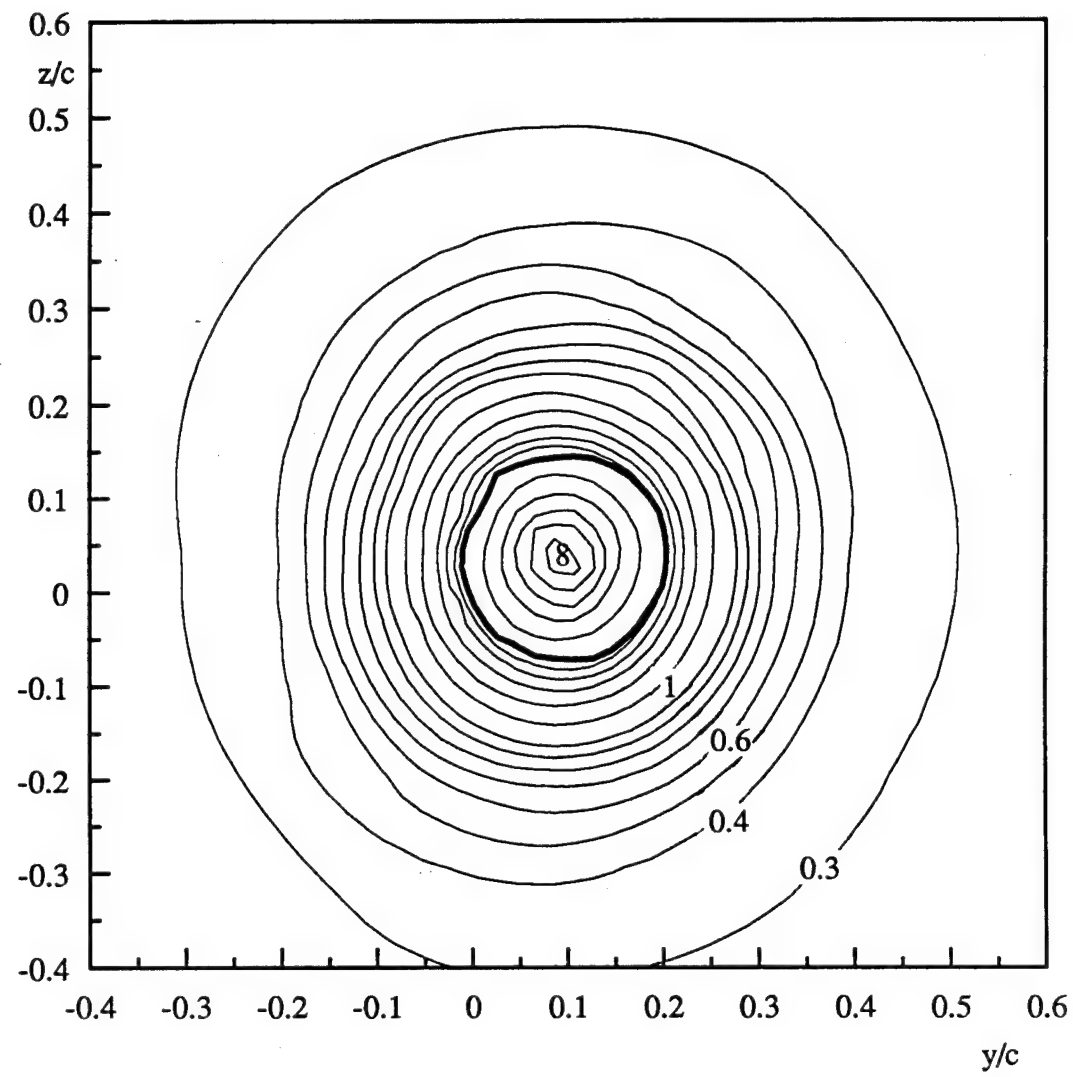


Figure 125. Contours of mean streamwise vorticity normalized on U_{ref} and c at $x/c=30$ of co-rotating pair

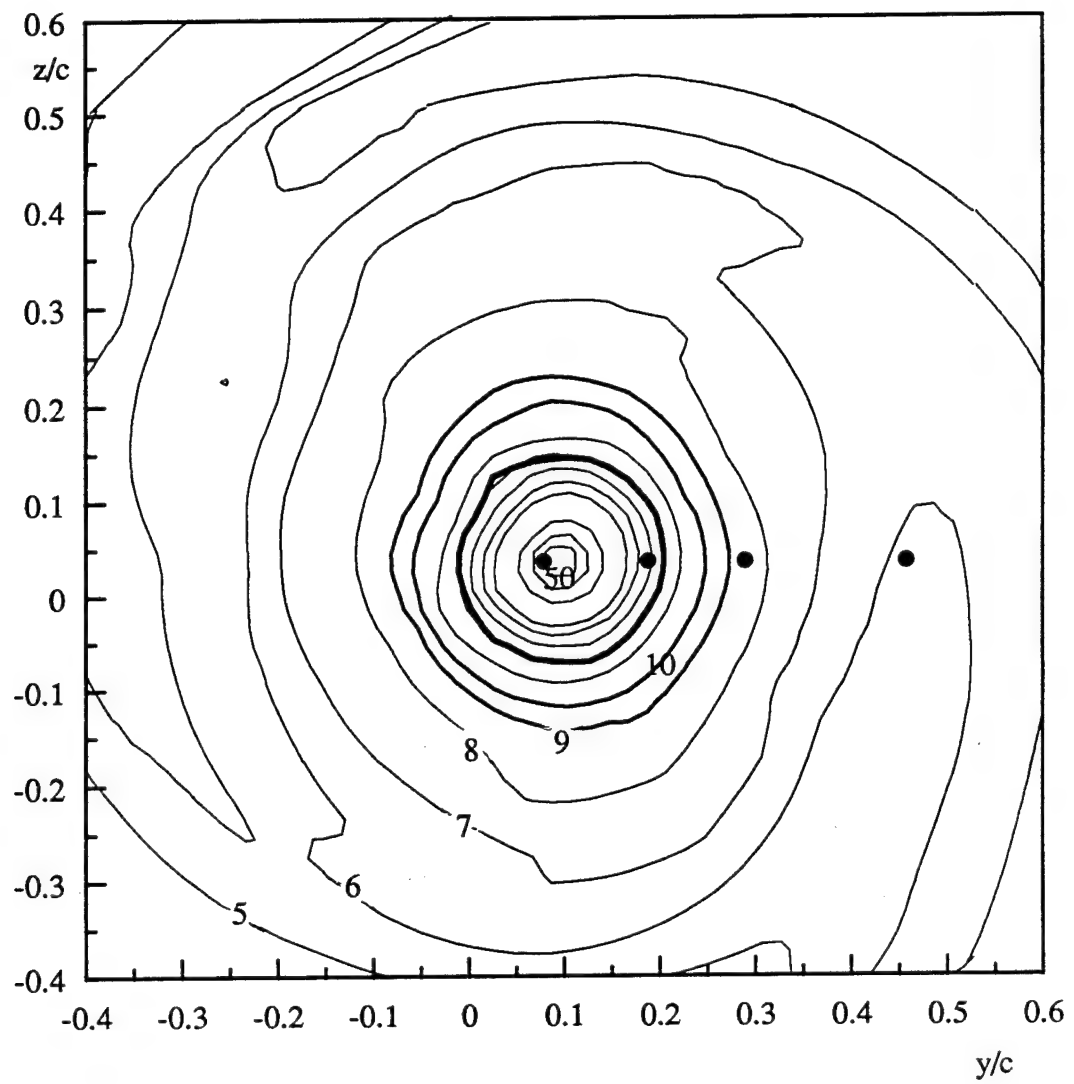


Figure 126. Contours of turbulence axial normal stress $\bar{u}^2/U_{ref}^2 \times 10^5$ at $x/c = 30$ of co-rotating pair. Dots show locations of autospectra in Figure 133-135.

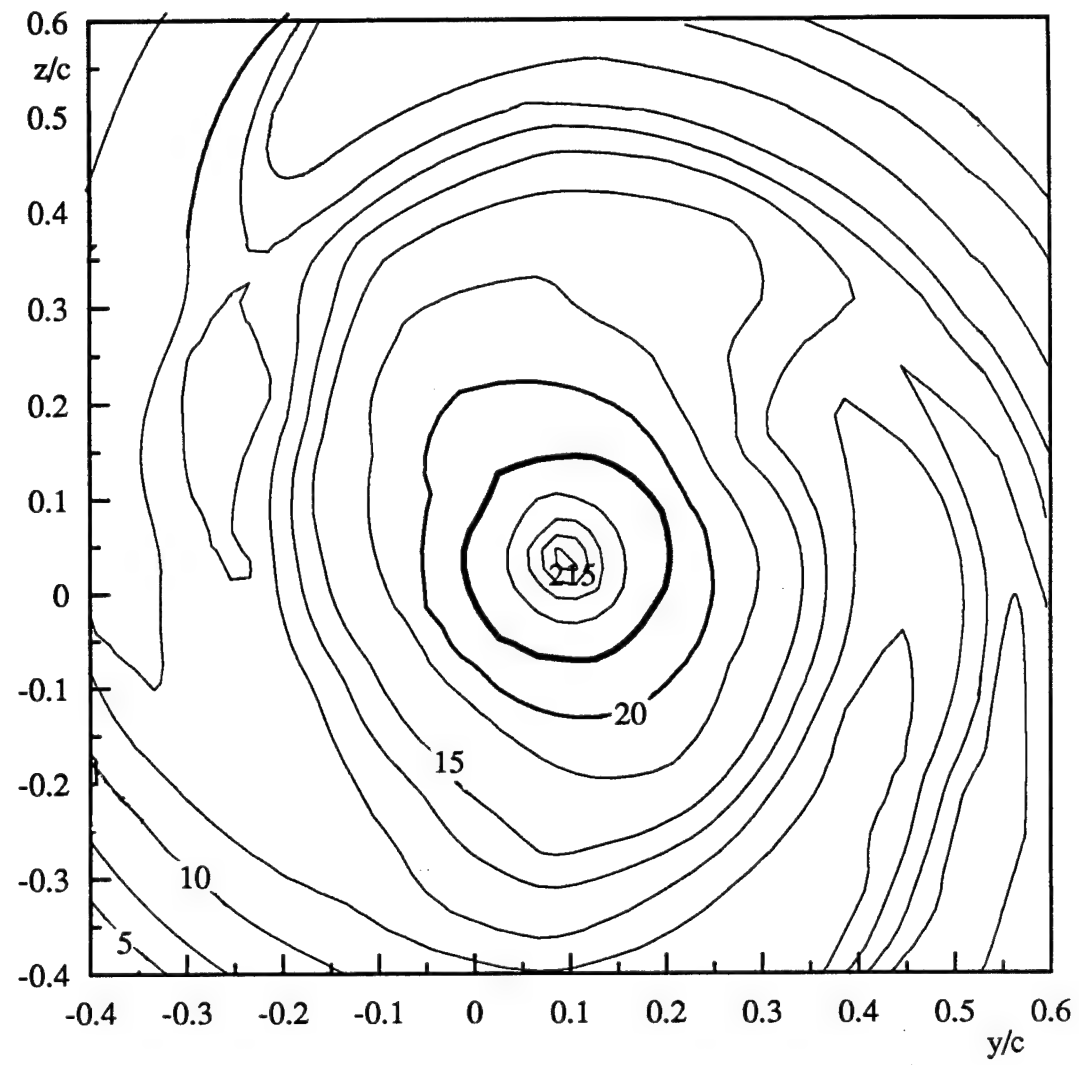


Figure 127. Contours of turbulence cross-flow normal stress sum $(\bar{v}^2 + \bar{w}^2)/U_{ref}^2 \times 10^5$ at $x/c = 30$ of co-rotating pair.

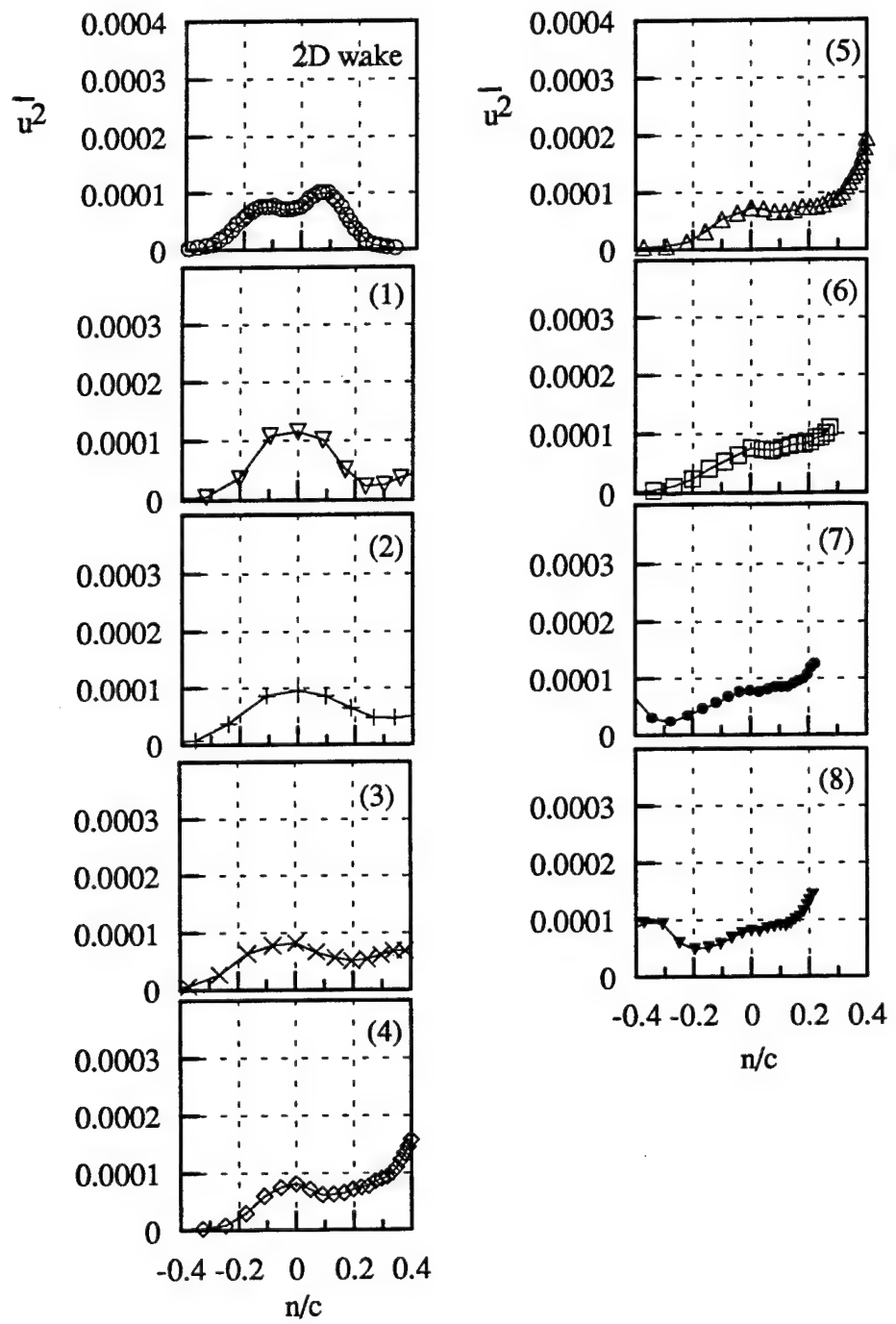


Figure 128. Profiles of axial normal stress $\bar{u}^2/U_{\text{ref}}^2$ at selected locations along the dashed line in Figure 122 at $x/c=30$ of co-rotating pair. Numbers indicate locations along this line.

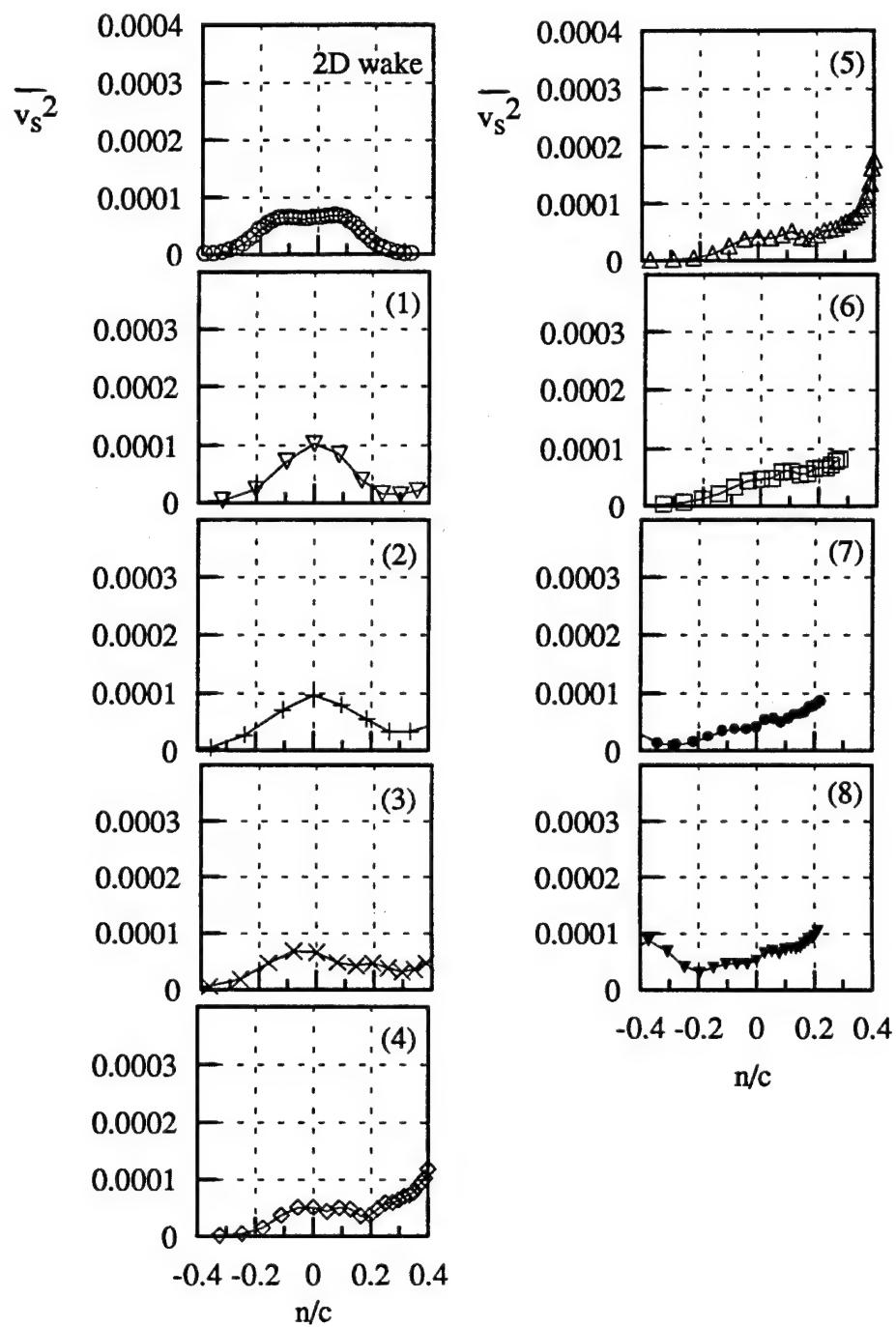


Figure 129. Profiles of normal stress \bar{v}_s^2/U_{ref}^2 parallel to spiral wake centerline in the spiral wake tail at selected locations along the dashed line in Figure 122 at $x/c=30$ of co-rotating pair. Numbers indicate locations along this line.

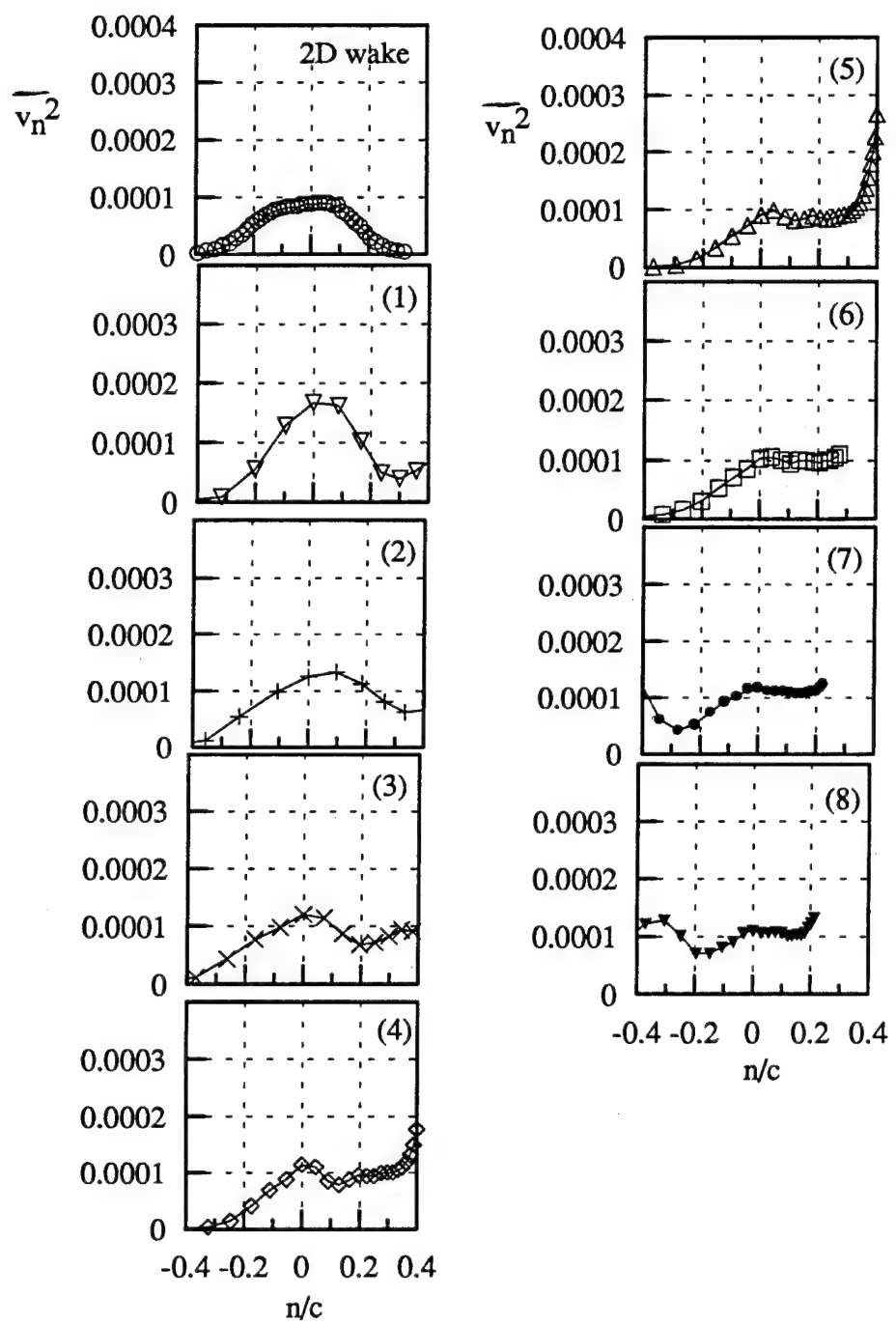


Figure 130. Profiles of normal stress \bar{v}_n^2/U_{ref}^2 normal to spiral wake centerline in the spiral wake tail at selected locations along the dashed line in Figure 122 at $x/c=30$ of co-rotating pair. Numbers indicate locations along this line.

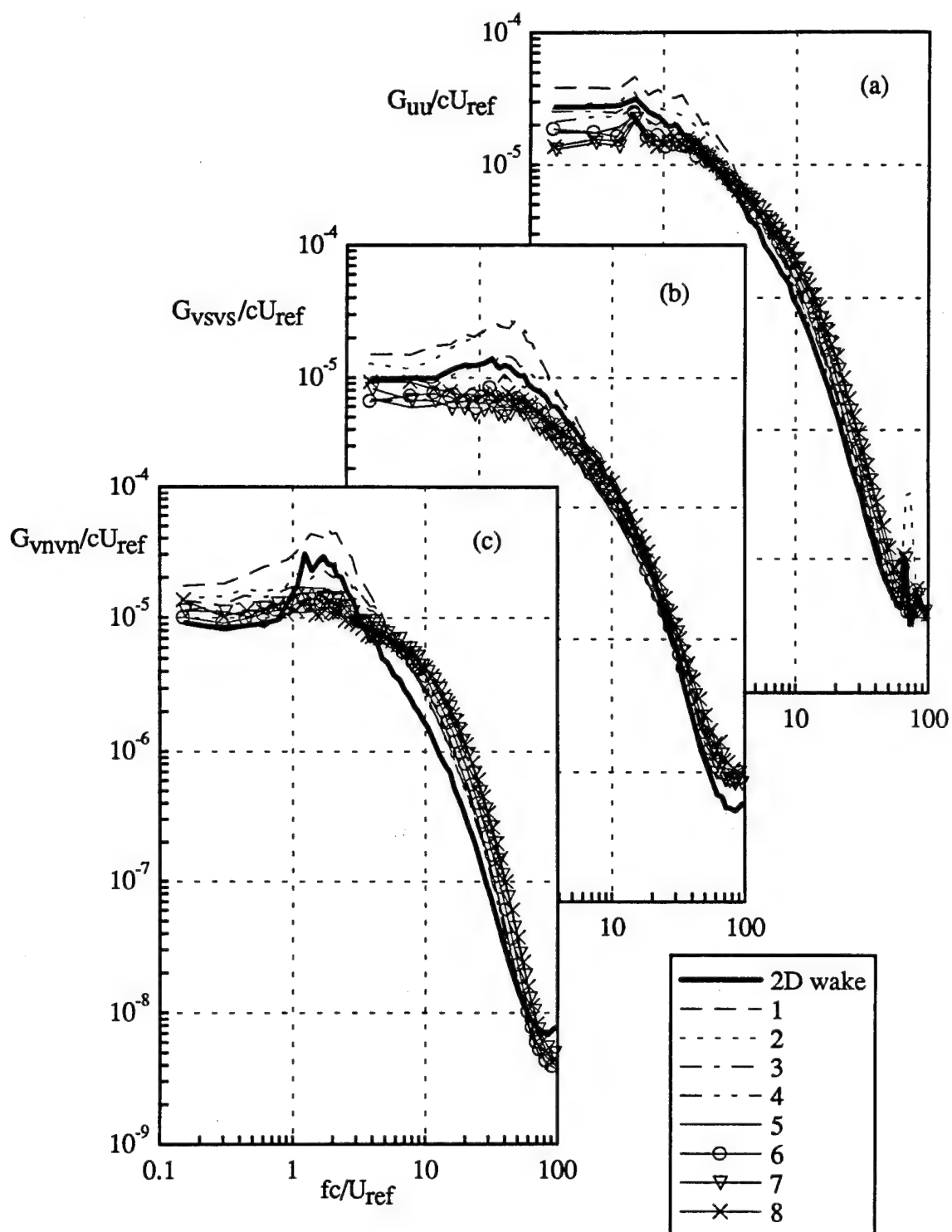


Figure 131 Velocity autospectra in coordinates aligned with the spiral wake centerline in the spiral wake tail at $x/c=30$ of co-rotating pair (a) U spectra, (b) V_s spectra, (c) V_n spectra. Locations indicated by dots in Figure 122.

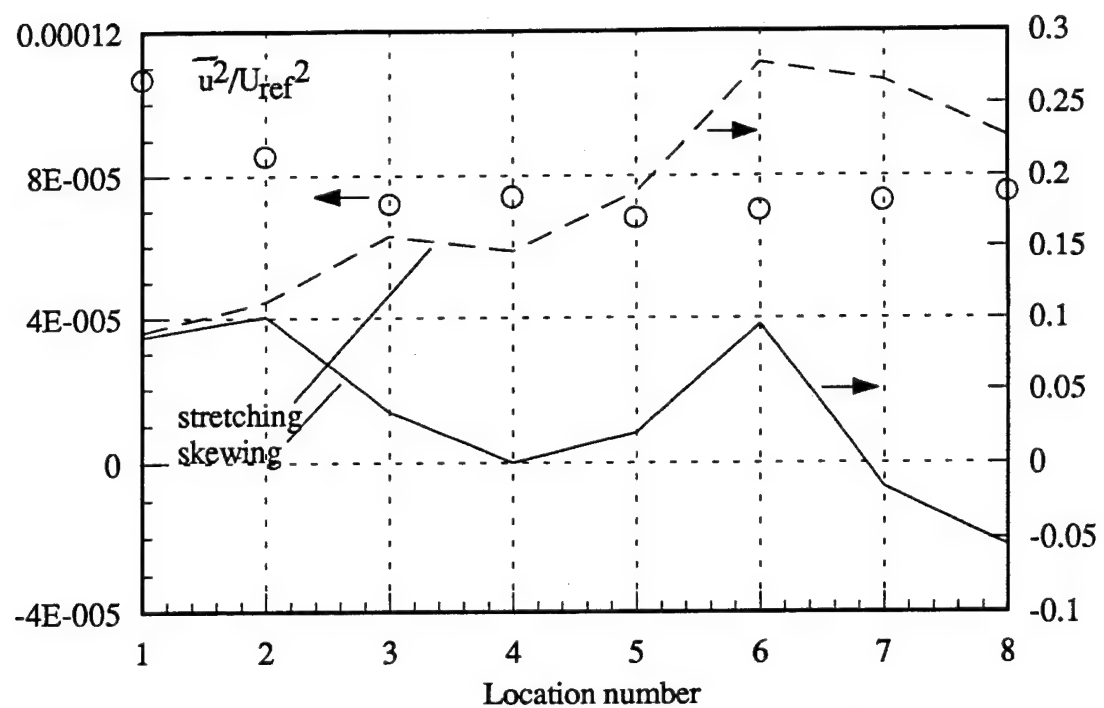


Figure 132. Rates of strain and turbulence stress on the dashed curve in Figure 122 at $x/c=30$ of co-rotating pair. Strain rates normalized on maximum axial velocity gradient in the two-dimensional portion of the wake.

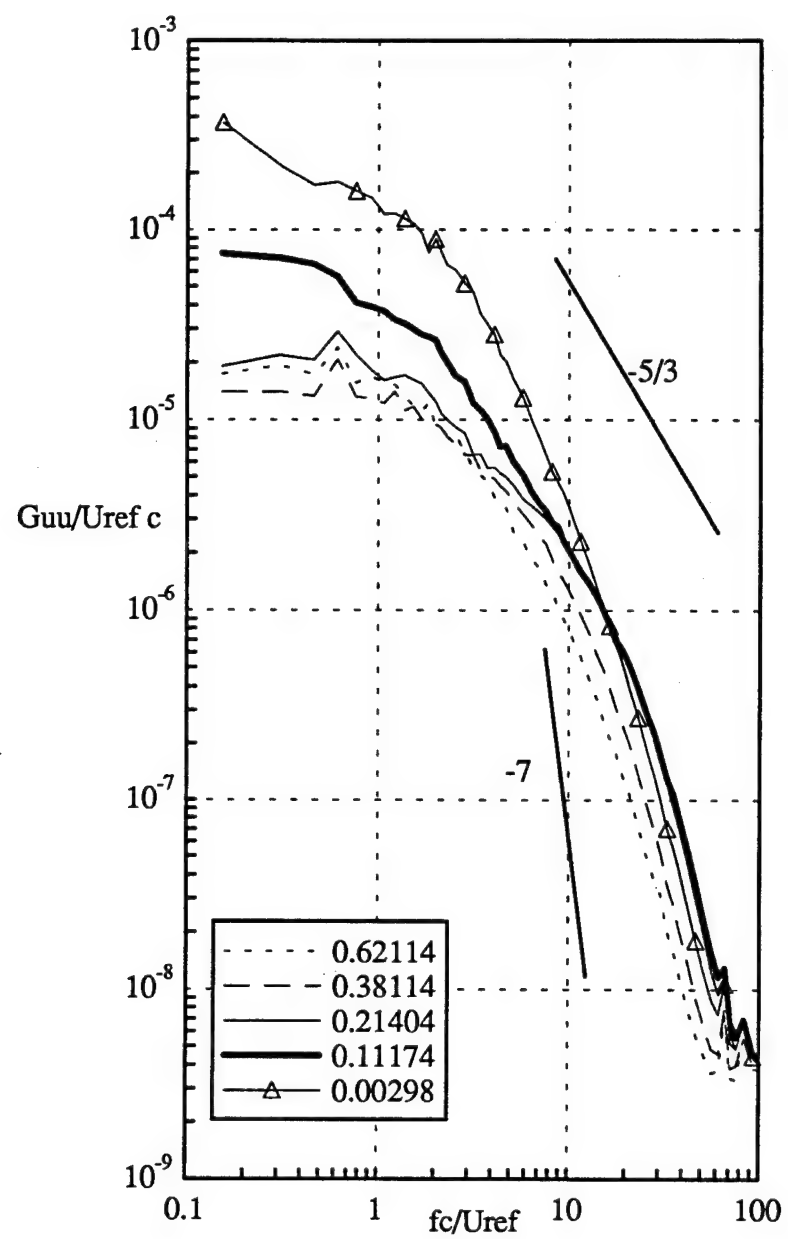


Figure 133. Autospectra of U velocity fluctuations at various spanwise locations along a horizontal profile through the core center indicated by dots in Figure 126 at $x/c=30$ of co-rotating pair. Locations relative to the core center at $y/c=0.0763$.

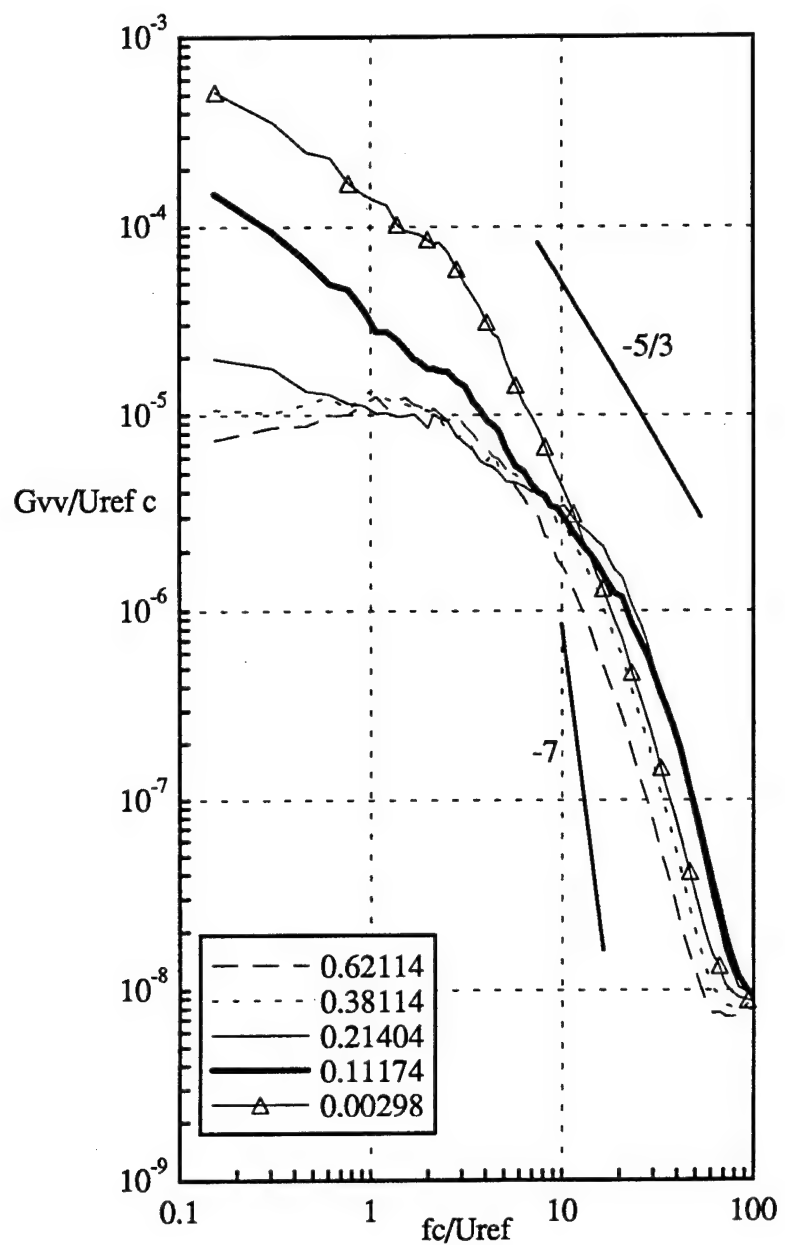


Figure 134. Autospectra of V velocity fluctuations at various spanwise locations along a horizontal profile through the core center indicated by dots in Figure 126 at $x/c=30$ of co-rotating pair. Locations relative to the core center at $y/c=0.0763$.

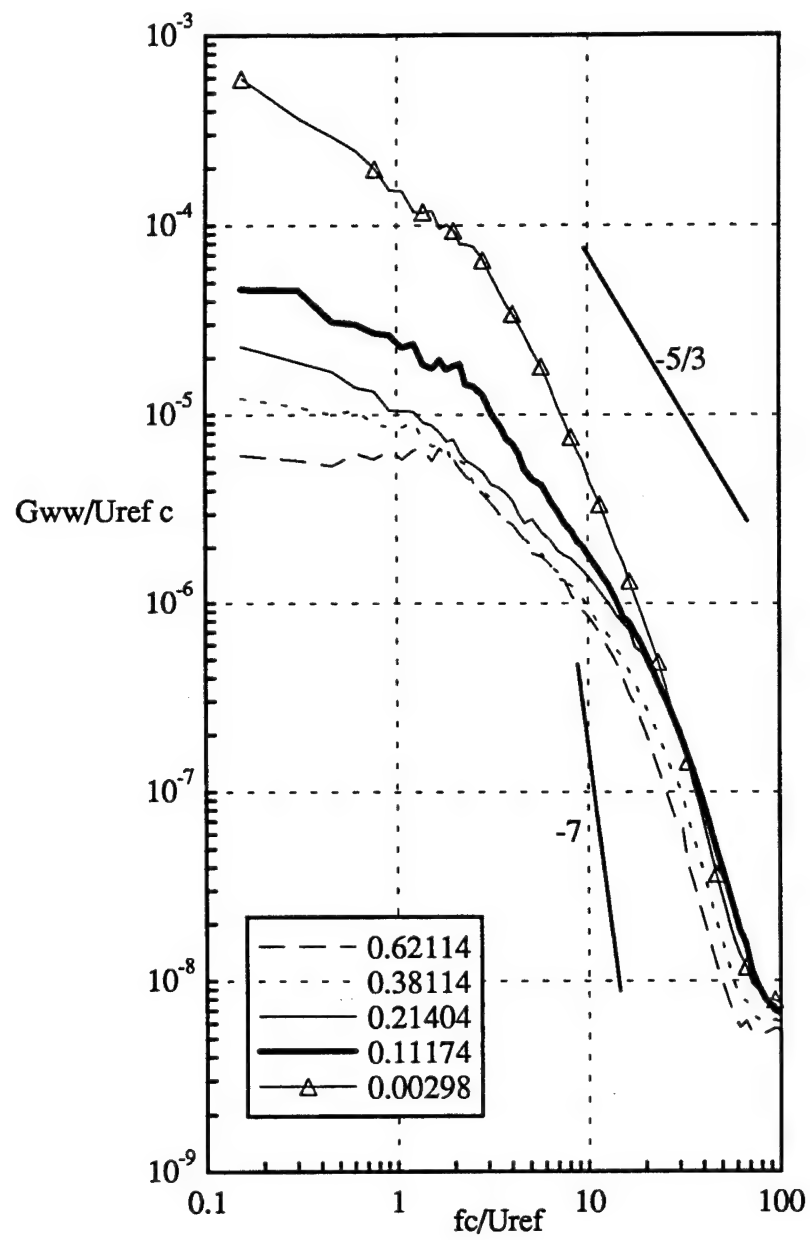


Figure 135. Autospectra of W velocity fluctuations at various spanwise locations along a horizontal profile through the core center indicated by dots in Figure 126 at $x/c=30$ of co-rotating pair. Locations relative to the core center at $y/c=0.0763$.

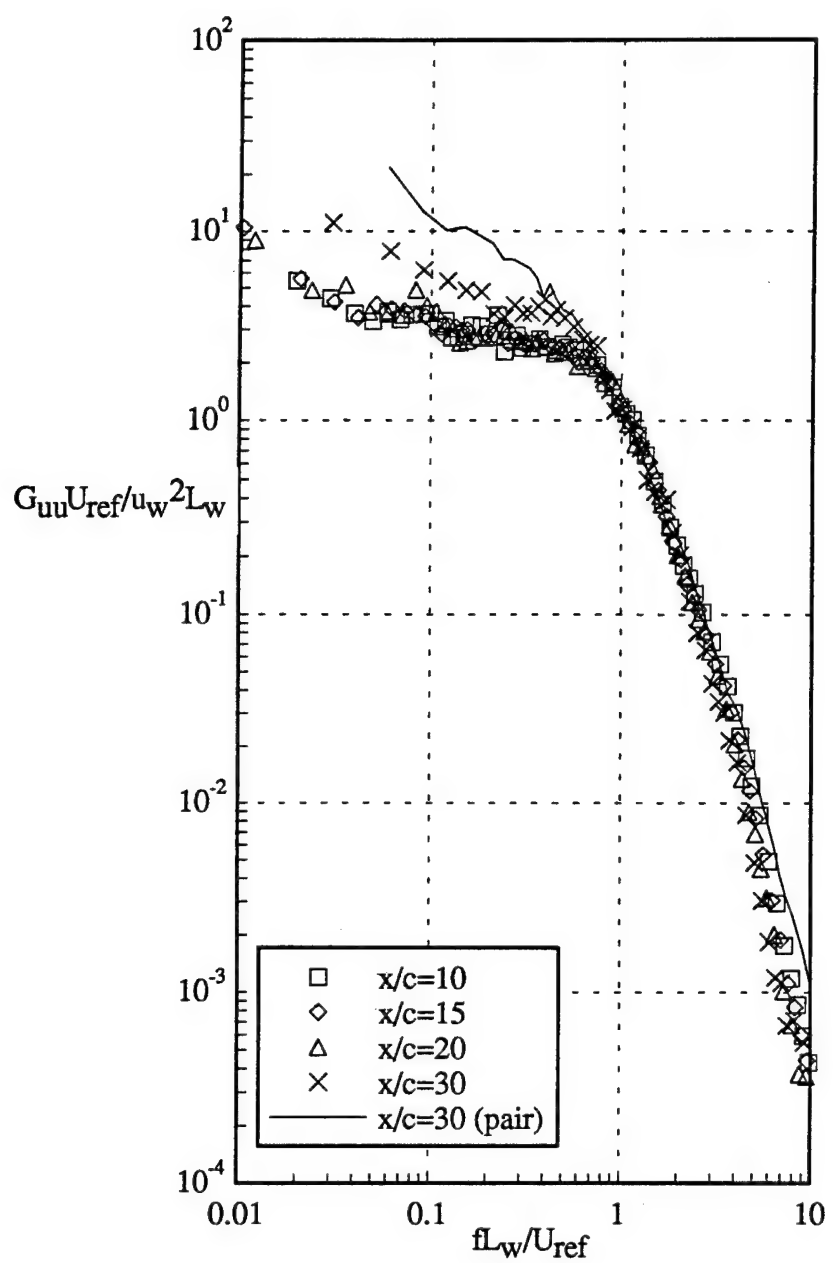


Figure 136. Autospectra of U velocity fluctuations of core center normalized on two-dimensional wake parameters for isolated vortex cases and co-rotating pair at $x/c=30$.

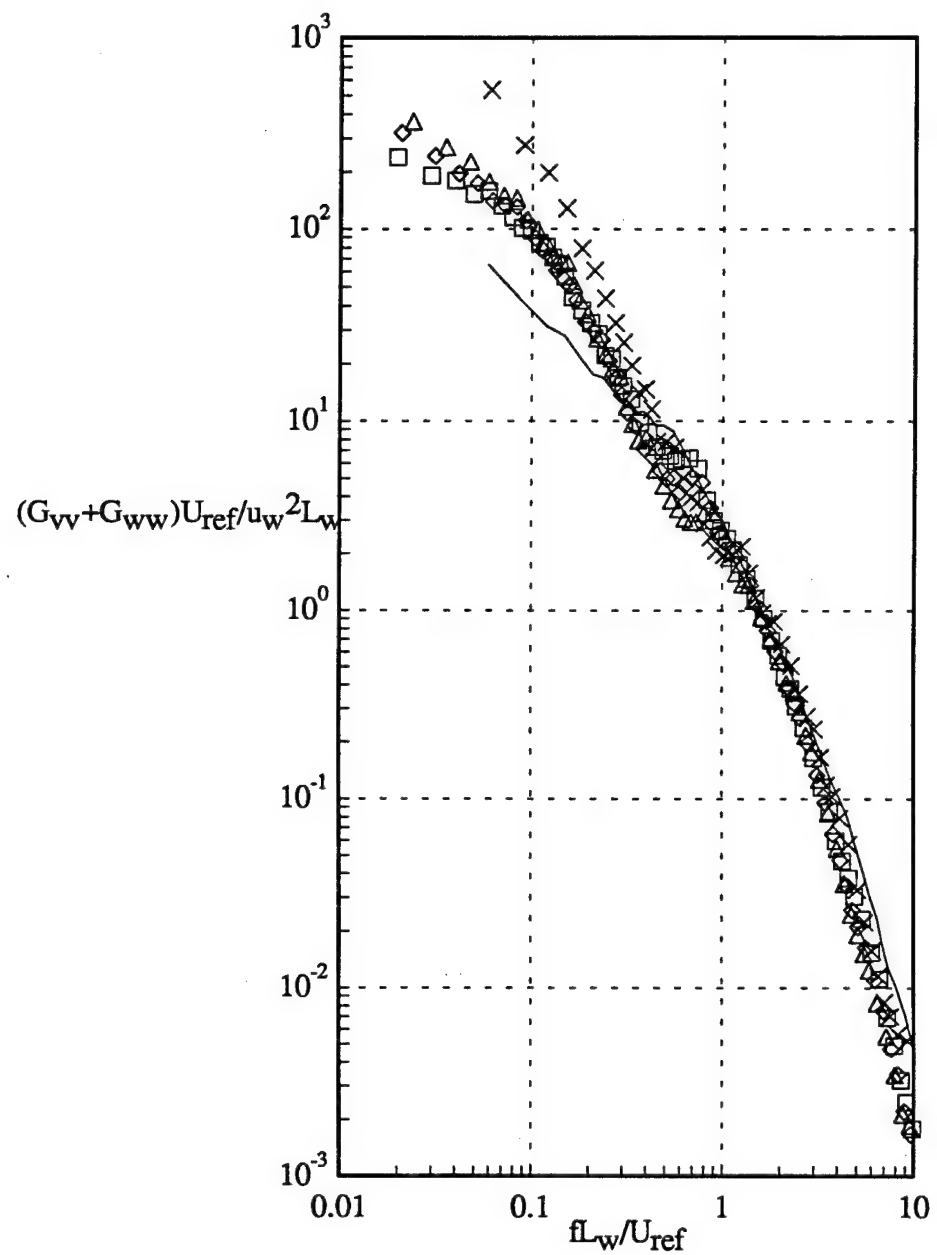


Figure 137. Autospectra of V+W velocity fluctuations of core center normalized on two-dimensional wake parameters for isolated vortex and co-rotating pair at $x/c=30$.

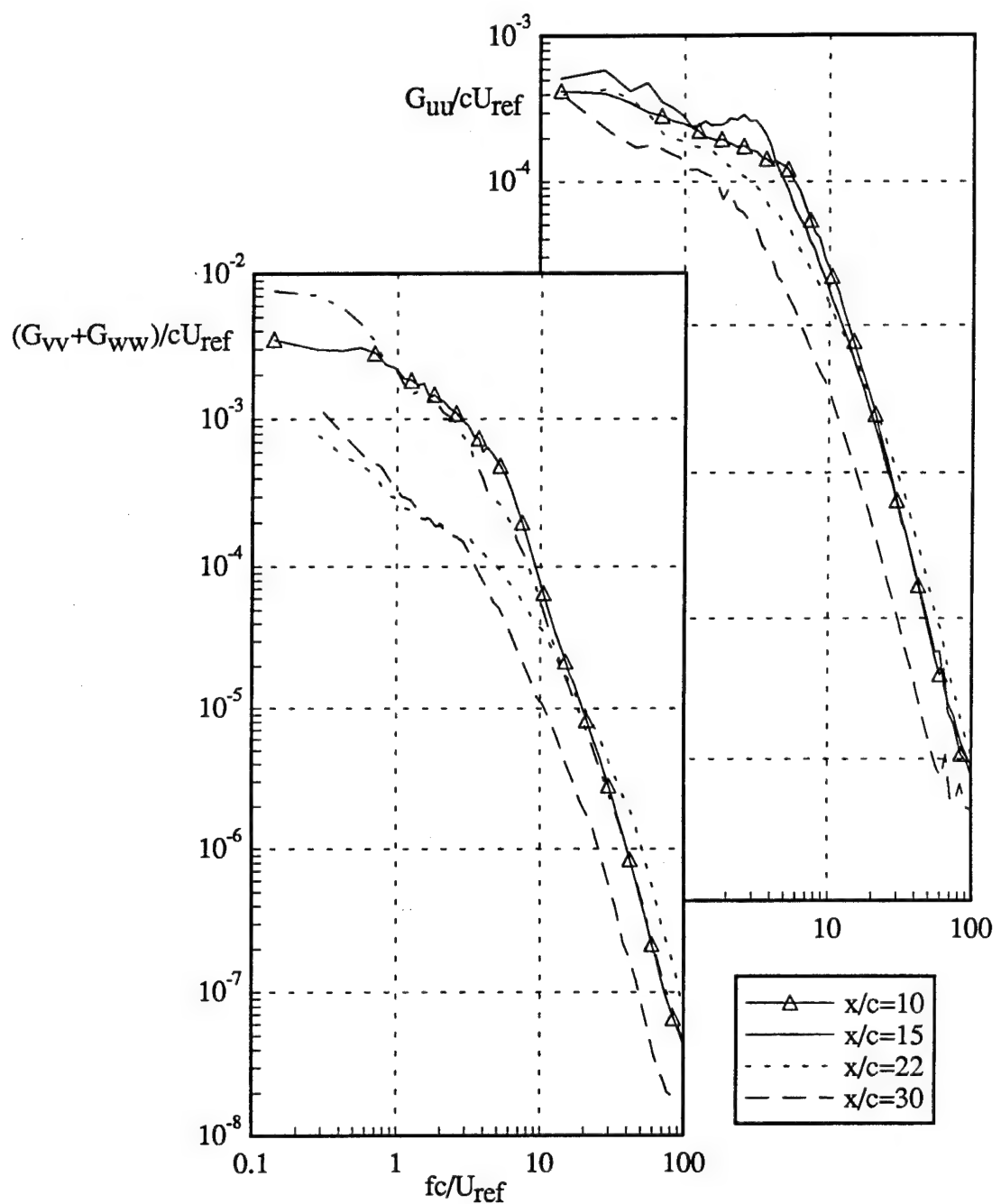


Figure 138 Variation of core center velocity autospectra with streamwise distance of co-rotating pair

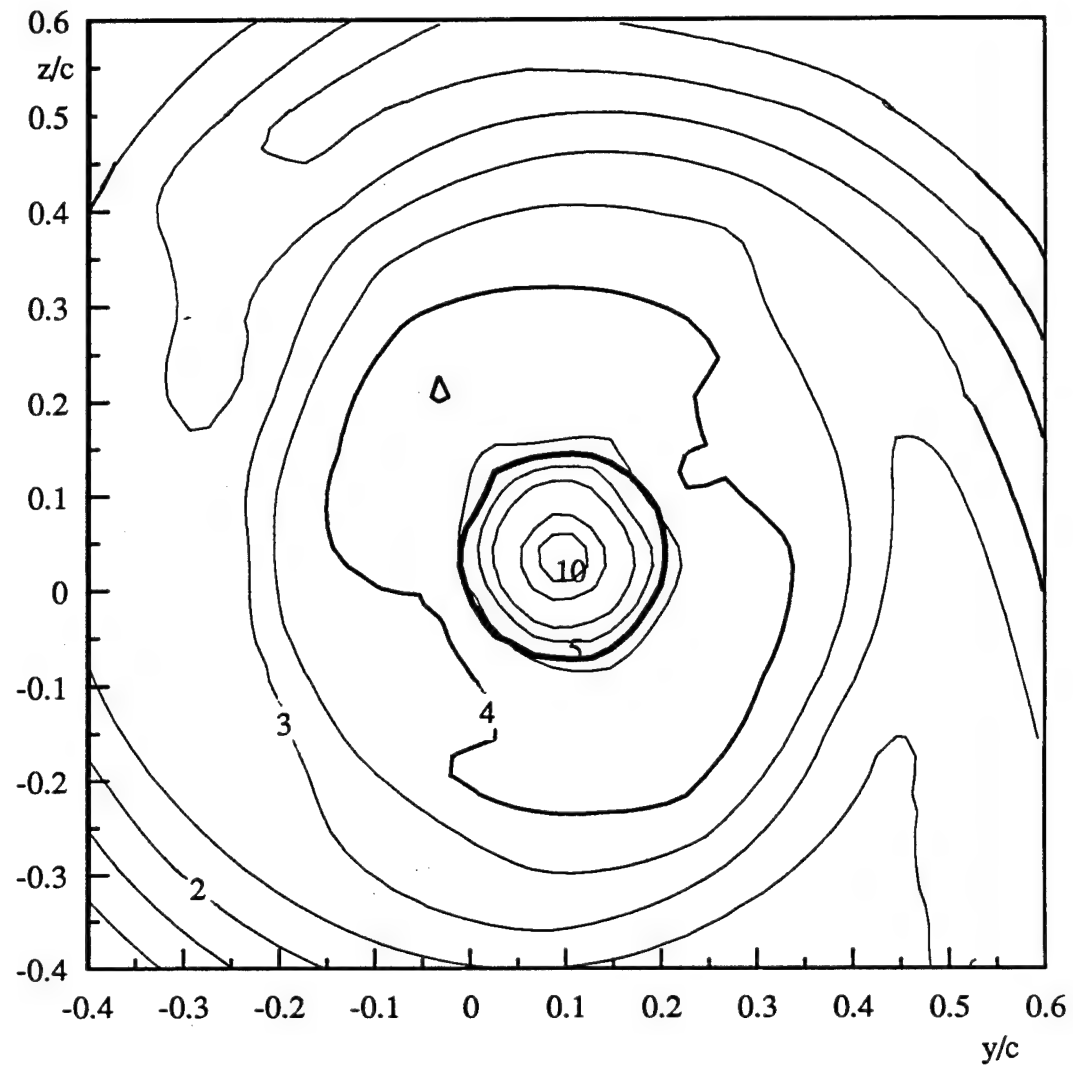


Figure 139. Contours of axial normal stress $\bar{u}^2/U_{\text{ref}}^2 \times 10^5$ filtered at $fc/U_{\text{ref}}=3$ at $x/c=30$ of co-rotating pair

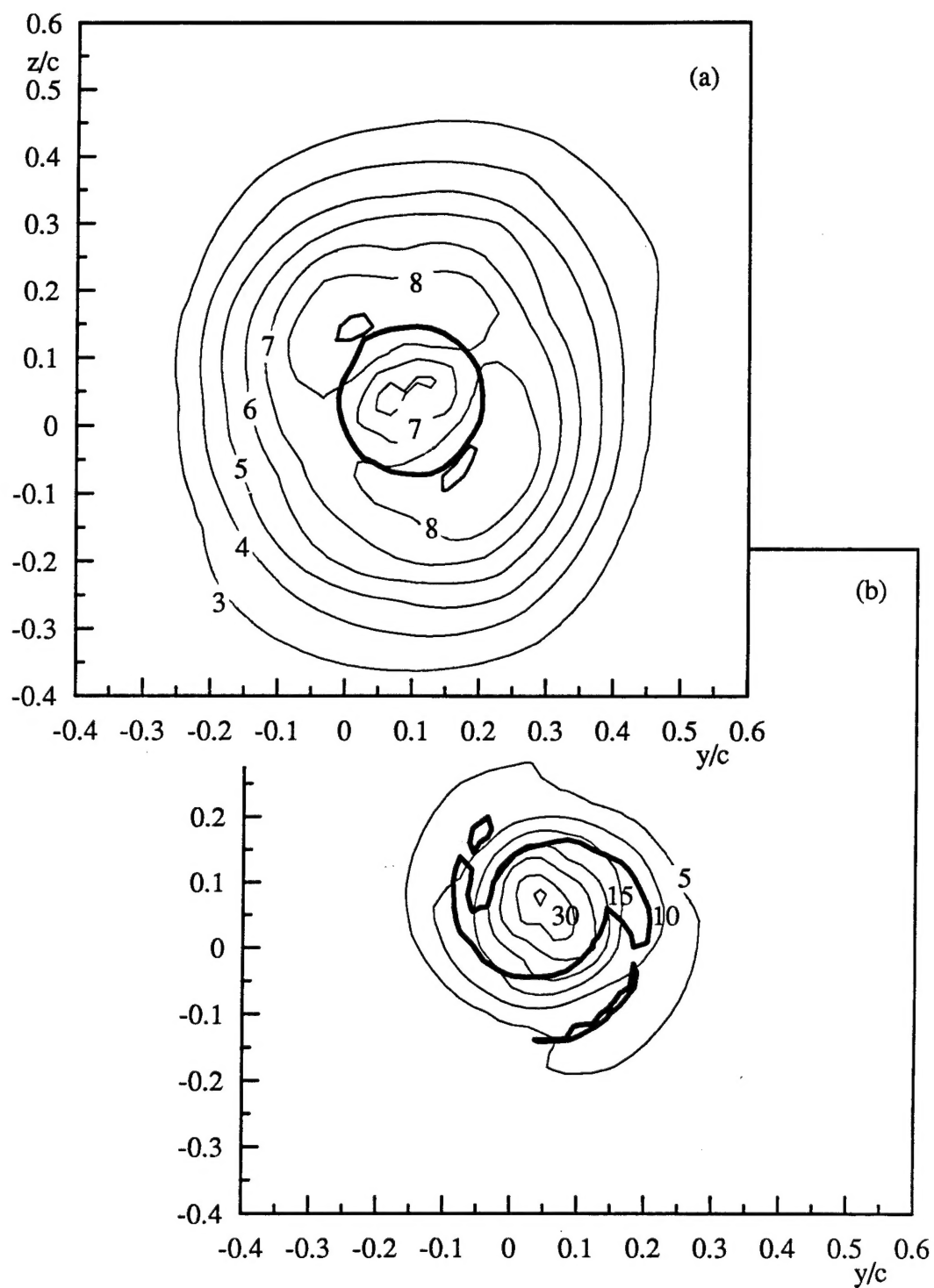


Figure 140. Contours of axial normal stress $\bar{u}^2/U_{ref}^2 \times 10^6$ filtered at (a) $fc/U_{ref} = 15.12$ at $x/c = 30$ and (b) $fc/U_{ref} = 18.24$ at $x/c = 22$ of co-rotating pair

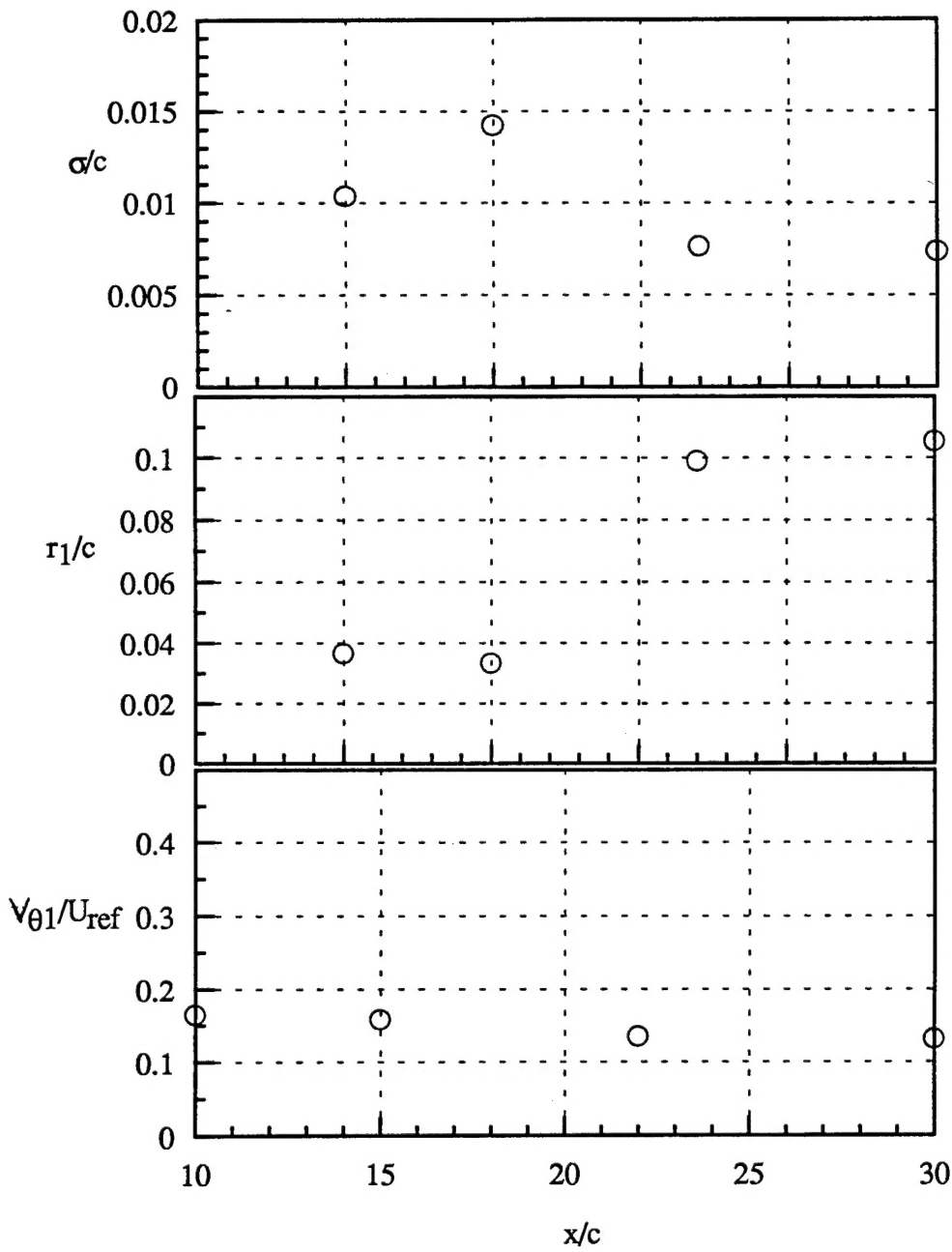


Figure 141. Variation in wandering amplitude, core radius, and peak tangential velocity with streamwise distance for co-rotating vortex.

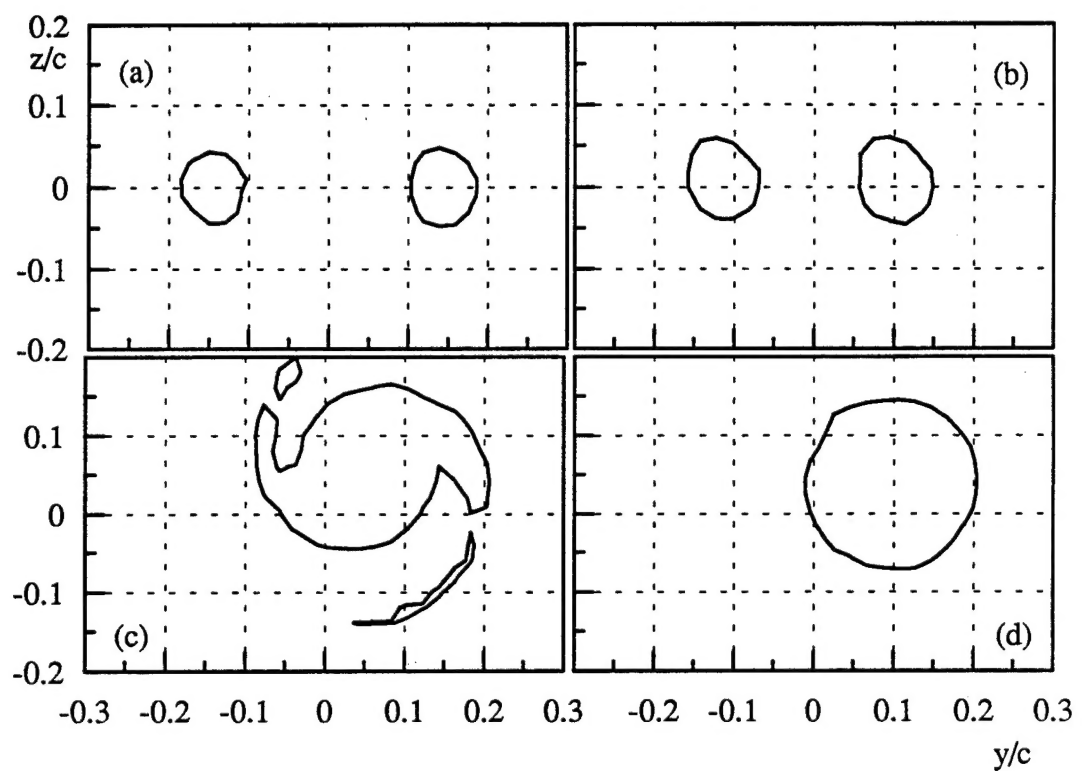


Figure 142 Variation of core size with streamwise distance for co-rotating pair
 (a) $x/c=10$, (b) $x/c=15$, (c) $x/c=22$, (d) $x/c=30$.

VITA

Christine M. Vogel is the daughter of Mr. and Mrs. Stephen L. Vogel who reside in Williamsville, New York. She graduated with honor from Holy Angels Academy in Buffalo, New York in 1989. In 1993, she received a bachelor of science degree in aerospace engineering from the University of Notre Dame in Indiana. She went on to study fluid mechanics at the graduate level at Virginia Polytechnic Institute and State University where she has completed a master of science degree in aerospace engineering in April of 1995.

Christine M Vogel

4/7/95